IMAGE PLANE FILTERS AND ADAPTIVE OPTICAL SYSTEMS

by

Anthony Joseph Seward

A dissertation submitted to the Graduate School

in partial fulfillment of the requirements

for the degree

Doctor of Philosophy, Engineering

Specialization: Electrical Engineering

New Mexico State University

Las Cruces, New Mexico

August, 2005

"Image plane filters and adaptive optical systems," a dissertation prepared by Anthony Joseph Seward in partial fulfillment of the requirements for the degree, Doctor of Philosophy, Engineering, has been approved and accepted by the following:

Linda Lacey
Dean of the Graduate School

Michael K. Giles
Chair of the Examining Committee

Date

Committee in charge:

Dr. Michael K. Giles, Chair

Dr. Paul M. Furth

Dr. Jon A. Holtzmann

Dr. David G. Voelz

DEDICATION

This dissertation is dedicated to Beulah, without whose love, encouragement and support I would not have finished.

ACKNOWLEDGMENT

First, I would like to thank my advisor, Dr. Michael Giles, for his patience, and for introducing me to the field of photonics. Second, I would like to thank Dr. François Lacombe and the rest of my compatriots at Bâtiment Lyot for their encouragement and probing questions. I also owe a great deal of gratitude to Dr. Mark Kramer for teaching me so much about field testing working adaptive optics systems.

VITA

March 1, 1968	Born WPAFB, Ohio
1986-1990	B.S.E.E., New Mexico State University
1990-1993	M.S.E.E., New Mexico State University
1994-1995	D.E.A. Optique et Photonique, Université de Paris VII
1998-1999	Instructor, New Mexico State University
2000-Present	Optical Engineer, MZA Associates Corporation
2003-Present	Lead Engineer, Optics Group
	Air Force Research Laboratory, North Oscura Peak Facility

Publications

[1] Anthony J. Seward, François Lacombe, and Michael K. Giles. Focal Plane Masks in Adaptive Optics Systems. *Adaptive Optics Systems and Technology*, volume 3762 of *Proc. SPIE*, pages 283–293, September 1999.

[2] Michael K. Giles, Anthony J. Seward, Mikhail A. Vorontsov, Jungtae Rha, and Ray Jimenez. Setting up a liquid crystal phase screen to simulate atmospheric turbulence. *High-Resolution Wavefront Control: Methods, Devices, and Applications II*, volume 4124 of *Proc. SPIE*, pages 89–97, November 2000.

[3] Michael K. Giles, Anthony J. Seward, and Todd M. Giles. Closed-loop phase contrast adaptive optics system using liquid crystal phase modulators: experimental results. *High-Resolution Wavefront Control: Methods, Devices, and Applications III*, volume 4493 of *Proc. SPIE*, pages 174–183, February 2002.

Field of Study

Major Field:	Electrical Engineering
	Optics and Photonics
	Adaptive Optics

ABSTRACT

IMAGE PLANE FILTERS AND ADAPTIVE OPTICAL SYSTEMS

by

Anthony Joseph Seward

Doctor of Philosophy, Engineering

New Mexico State University

Las Cruces, New Mexico, 2005

Dr. Michael K. Giles, Chair

Shack-Hartmann sensors are the most commonly used wavefront sensors in adaptive optics applications today. There are problems when using Shack-Hartmann wavefront sensors in the presence of strong scintillation. This dissertation investigates the use of focal plane filters as wavefront sensors in adaptive optics systems. Both simulation and experiment are used to explore the characteristics of focal plane filter wavefront sensors, the conclusion being that they are a viable alternative to Shack-Hartmann wavefront sensors.

CONTENTS

LIST OF TABLES xii

LIST OF FIGURES xxii

ACRONYMS xxiii

1 INTRODUCTION 1

PART I AN OVERVIEW OF ADAPTIVE OPTICS

2 WHAT IS ADAPTIVE OPTICS? 4

2.1 Why do I need adaptive optics 4

2.1.1 What are the effects of turbulence 4

2.1.2 Speckle interferometry 9

2.1.3 The adaptive optics solution 11

2.2 What are the components in an Adaptive optics system? . . . 11

2.2.1 Fine Tracker 12

2.2.2 Tip-Tilt Mirror 12

2.2.3 Wavefront corrector 13

2.2.4 Wavefront sensor 13

2.2.5 Wavefront calculator 13

3 DESIGNING ADAPTIVE OPTICS SYSTEMS 14

3.1 What are the goals of the design? 14

3.2 How bad is the turbulence? 16

4 CHOOSING THE COMPONENTS OF ADAPTIVE OPTICS SYSTEMS 20

4.1 How fast do I have to correct? 20

4.2 Calculating the dynamic range of the tip-tilt mirror 23

4.3 Choosing a wavefront corrector 24

4.3.1 Wavefront corrector types 24

4.3.2 Wavefront corrector constraints 26

4.4 How do I choose a wavefront sensor? 28

4.4.1 Wavefront sensor dimensions 29

4.4.2 Shack-Hartmann sensor 33

4.4.3 Curvature sensor 36

4.5 What does a wavefront calculator do? 37

5 OTHER CONSIDERATIONS 40

5.1 What is my limiting reference? 40

5.1.1 Limiting magnitude of the reference 41

5.1.2 Natural guide stars 46

5.1.3 What about laser guide stars? 47

5.2 What is anisoplanatism? 48

5.2.1 Angular anisoplanatism 48

5.2.2 Displacement anisoplanatism 51

5.2.3 Focus anisoplanatism 52

5.2.4 Conjugation at the turbulent layer 52

5.2.5 Multiconjugate adaptive optics 54

PART II FOCAL PLANE FILTERS AND ADAPTIVE OPTICS

6 THEORY OF FOCAL PLANE FILTERS 56

6.1 What are focal plane filters? 57

6.2 Recovery of the phase 67

6.2.1 Zernike Visibility 68

6.2.2 Three Bin 70

6.3 Examples 70

6.4 Wavefront calculation 73

6.4.1 Phase unwrapping 74

6.4.2 Pseudo Shack-Hartmann 76

7 COMPUTER SIMULATIONS: MATLAB 78

7.1 Turbulence 79

7.2 Corrector 79

7.3 Tip-Tilt 79

7.4 Detectors 79

7.5 Wave Front Sensor Filter 79

7.6 Simulations 80

7.7 Conclusions 83

8 COMPUTER SIMULATIONS: WAVETRAIN 84

8.1 The Simulation Layouts 85

8.1.1 Common Elements 85

8.1.2 Ideal Corrector 88

8.1.3 NOP Corrector 90

8.2 Results: Ideal Corrector 91
8.3 Results: NOP Corrector 92
8.4 Results: NOP Corrector and a brighter source 94
8.5 Results: NOP Corrector and a still brighter source 94
8.6 Single frames 95
8.7 Summary 98

9 EXPERIMENT 100
9.1 Layout 100
9.2 Technique 103
9.2.1 Computers 103
9.2.2 Turbulence 104
9.2.3 Focal Plane Filter 105
9.3 Results 105
9.4 Conclusion 112

10 CONCLUSION 114

APPENDICES

A IDEAL CORRECTOR PLOTS 116

B NOP CORRECTOR PLOTS I 136

C NOP CORRECTOR PLOTS II 192

D NOP CORRECTOR PLOTS III 200

E RESCALING 208

BIBLIOGRAPHY 212

LIST OF TABLES

6.1 The first six Zernike polynomials 71

8.1 Summary of *ideal corrector* simulations 92

8.2 Summary of NOP simulations 93

8.3 Summary of NOP simulations with double power beacon 94

8.4 Summary of NOP simulations with triple power beacon. 95

9.1 Test log summary 111

E.1 System constraints 208

LIST OF FIGURES

2.1 No turbulence 5

2.2 Weak turbulence ($D/r_0 = 2.5$) 6

2.3 Weak turbulence ($D/r_0 = 3.75$) 6

2.4 Moderate turbulence ($D/r_0 = 5$) 7

2.5 Moderate turbulence ($D/r_0 = 6.25$). 7

2.6 Strong turbulence ($D/r_0 = 8.\overline{3}$) 8

2.7 Strong turbulence ($D/r_0 = 12.5$) 8

2.8 Extreme turbulence ($D/r_0 = 25$) 9

2.9 System Block Diagram of an Adaptive Optics System 12

4.1 Strehl ratio vs. number of zones per coherence diameter. 30

4.2 RMS error in rad vs. number of zones per coherence diameter . . 31

4.3 Number of modes vs. number of zones for the same residual error 32

4.4 Shack-Hartmann and plane wave 34

4.5 Shack-Hartmann and aberrated wave. 34

4.6 Quad-cell detector 35

5.1 Angular anisoplanatism. 49

5.2 Displacement anisoplanatism 51

5.3 Focus anisoplanatism 53

6.1 General layout for focal plane filters 59

6.2 The focal plane filter 61

6.3 Zernike visibility 69

6.4 The first six Zernike polynomials 71

6.5 Application of the null filter 72

6.6 Application of the phase contrast filter 73

6.7 Zernike visibility of Zernike polynomials 74

7.1 Matlab simulation flowchart 78

7.2 145 photons per pixel per frame 81

7.3 7 photons per pixel per frame 81

7.4 4.5 photons per pixel per frame 82

7.5 3 photons per pixel per frame 82

8.1 Common elements in the simulations 86

8.2 DiagnosticPlane composite system 87

8.3 Closed loop simulation with ideal corrector 88

8.4 Closed loop simulation with NOP corrector 90

8.5 Three Bin with diffraction WFS single frame, r_0 = 12 cm, wind speed = 5 m/s, low power beacon 96

8.6 Three Bin with diffraction WFS single frame, r_0 = 12 cm, wind speed = 5 m/s, double power beacon 96

8.7 Three Bin with diffraction WFS single frame, r_0 = 12 cm, wind speed = 5 m/s, triple power beacon 97

9.1 Experimental layout 101

9.2 Phase screen 104

9.3 Open Loop 106

9.4 Closed Loop 106

9.5 Experiment results: peak value metric 107

9.6 Experiment results: moment of inertia metric 109

9.7 Single frame with all LCDs off 110

9.8 Single frame: Exposure length too small 112

A.1 Wrapped phase WFS, r_0 = 30 cm, wind speed = 5 m/s 116

A.2 Unwrapped phase WFS, r_0 = 30 cm, wind speed = 5 m/s 117

A.3 Ideal Three Bin WFS, r_0 = 30 cm, wind speed = 5 m/s 117

A.4 Three Bin with diffraction WFS, r_0 = 30 cm, wind speed = 5 m/s . 118

A.5 Wrapped phase WFS, r_0 = 30 cm, wind speed = 10 m/s 119

A.6 Unwrapped phase WFS, r_0 = 30 cm, wind speed = 10 m/s 119

A.7 Ideal Three Bin WFS, r_0 = 30 cm, wind speed = 10 m/s 120

A.8 Three Bin with diffraction WFS, r_0 = 30 cm, wind speed = 10 m/s 120

A.9 Wrapped phase WFS, r_0 = 20 cm, wind speed = 5 m/s 121

A.10 Unwrapped phase WFS, r_0 = 20 cm, wind speed = 5 m/s 122

A.11 Ideal Three Bin WFS, r_0 = 20 cm, wind speed = 5 m/s 122

A.12 Three Bin with diffraction WFS, r_0 = 20 cm, wind speed = 5 m/s . 123

A.13 Wrapped phase WFS, r_0 = 20 cm, wind speed = 10 m/s 124

A.14 Unwrapped phase WFS, r_0 = 20 cm, wind speed = 10 m/s 124

A.15 Ideal Three Bin WFS, r_0 = 20 cm, wind speed = 10 m/s 125

A.16 Three Bin with diffraction WFS, r_0 = 20 cm, wind speed = 10 m/s 125

A.17 Wrapped phase WFS, r_0 = 15 cm, wind speed = 5 m/s 126

A.18 Unwrapped phase WFS, r_0 = 15 cm, wind speed = 5 m/s 127

A.19 Ideal Three Bin WFS, r_0 = 15 cm, wind speed = 5 m/s 127

A.20 Three Bin with diffraction WFS, r_0 = 15 cm, wind speed = 5 m/s . 128

A.21 Wrapped phase WFS, r_0 = 15 cm, wind speed = 10 m/s 129

A.22 Unwrapped phase WFS, r_0 = 15 cm, wind speed = 10 m/s 129

A.23 Ideal Three Bin WFS, r_0 = 15 cm, wind speed = 10 m/s 130

A.24 Three Bin with diffraction WFS, r_0 = 15 cm, wind speed = 10 m/s 130

A.25 Wrapped phase WFS, r_0 = 12 cm, wind speed = 5 m/s 131

A.26 Unwrapped phase WFS, r_0 = 12 cm, wind speed = 5 m/s 132

A.27 Ideal Three Bin WFS, r_0 = 12 cm, wind speed = 5 m/s 132

A.28 Three Bin with diffraction WFS, r_0 = 12 cm, wind speed = 5 m/s . 133

A.29 Wrapped phase WFS, r_0 = 12 cm, wind speed = 10 m/s 134

A.30 Unwrapped phase WFS, r_0 = 12 cm, wind speed = 10 m/s 134

A.31 Ideal Three Bin WFS, r_0 = 12 cm, wind speed = 10 m/s 135

A.32 Three Bin with diffraction WFS, r_0 = 12 cm, wind speed = 10 m/s 135

B.1 Shack-Hartmann WFS, r_0 = 30 cm, wind speed = 0 m/s 136

B.2 Ideal Three Bin WFS, r_0 = 30 cm, wind speed = 0 m/s 137

B.3 Three Bin with diffraction WFS, r_0 = 30 cm, wind speed = 0 m/s . 137

B.4 Shack-Hartmann WFS, r_0 = 30 cm, wind speed = 5 m/s 138

B.5 Ideal Three Bin WFS, r_0 = 30 cm, wind speed = 5 m/s 139

B.6 Three Bin with diffraction WFS, r_0 = 30 cm, wind speed = 5 m/s . 139

B.7 Shack-Hartmann WFS, r_0 = 30 cm, wind speed = 10 m/s 140

B.8 Ideal Three Bin WFS, r_0 = 30 cm, wind speed = 10 m/s 141

B.9 Three Bin with diffraction WFS, r_0 = 30 cm, wind speed = 10 m/s 141

B.10 Shack-Hartmann WFS, r_0 = 30 cm, wind speed = 20 m/s 142

B.11 Ideal Three Bin WFS, r_0 = 30 cm, wind speed = 20 m/s 143

B.12 Three Bin with diffraction WFS, r_0 = 30 cm, wind speed = 20 m/s 143

B.13 Shack-Hartmann WFS, r_0 = 20 cm, wind speed = 0 m/s 144

B.14 Ideal Three Bin WFS, r_0 = 20 cm, wind speed = 0 m/s 145

B.15 Three Bin with diffraction WFS, r_0 = 20 cm, wind speed = 0 m/s . 145

B.16 Shack-Hartmann WFS, r_0 = 20 cm, wind speed = 5 m/s 146

B.17 Ideal Three Bin WFS, r_0 = 20 cm, wind speed = 5 m/s 147

B.18 Three Bin with diffraction WFS, r_0 = 20 cm, wind speed = 5 m/s . 147

B.19 Shack-Hartmann WFS, r_0 = 20 cm, wind speed = 10 m/s 148

B.20 Ideal Three Bin WFS, r_0 = 20 cm, wind speed = 10 m/s 149

B.21 Three Bin with diffraction WFS, r_0 = 20 cm, wind speed = 10 m/s 149

B.22 Shack-Hartmann WFS, r_0 = 20 cm, wind speed = 20 m/s 150

B.23 Ideal Three Bin WFS, r_0 = 20 cm, wind speed = 20 m/s 151

B.24 Three Bin with diffraction WFS, r_0 = 20 cm, wind speed = 20 m/s 151

B.25 Shack-Hartmann WFS, r_0 = 15 cm, wind speed = 0 m/s 152

B.26 Ideal Three Bin WFS, r_0 = 15 cm, wind speed = 0 m/s. 153

B.27 Three Bin with diffraction WFS, r_0 = 15 cm, wind speed = 0 m/s . 153

B.28 Shack-Hartmann WFS, r_0 = 15 cm, wind speed = 5 m/s 154

B.29 Ideal Three Bin WFS, r_0 = 15 cm, wind speed = 5 m/s. 155

B.30 Three Bin with diffraction WFS, r_0 = 15 cm, wind speed = 5 m/s . 155

B.31 Shack-Hartmann WFS, r_0 = 15 cm, wind speed = 10 m/s 156

B.32 Ideal Three Bin WFS, r_0 = 15 cm, wind speed = 10 m/s 157

B.33 Three Bin with diffraction WFS, r_0 = 15 cm, wind speed = 10 m/s 157

B.34 Shack-Hartmann WFS, r_0 = 15 cm, wind speed = 20 m/s 158

B.35 Ideal Three Bin WFS, r_0 = 15 cm, wind speed = 20 m/s 159

B.36 Three Bin with diffraction WFS, r_0 = 15 cm, wind speed = 20 m/s 159

B.37 Shack-Hartmann WFS, r_0 = 12 cm, wind speed = 0 m/s 160

B.38 Ideal Three Bin WFS, r_0 = 12 cm, wind speed = 0 m/s. 161

B.39 Three Bin with diffraction WFS, r_0 = 12 cm, wind speed = 0 m/s . 161

B.40 Shack-Hartmann WFS, r_0 = 12 cm, wind speed = 5 m/s 162

B.41 Ideal Three Bin WFS, r_0 = 12 cm, wind speed = 5 m/s 163

B.42 Three Bin with diffraction WFS, r_0 = 12 cm, wind speed = 5 m/s . 163

B.43 Shack-Hartmann WFS, r_0 = 12 cm, wind speed = 10 m/s 164

B.44 Ideal Three Bin WFS, r_0 = 12 cm, wind speed = 10 m/s 165

B.45 Three Bin with diffraction WFS, r_0 = 12 cm, wind speed = 10 m/s 165

B.46 Shack-Hartmann WFS, r_0 = 12 cm, wind speed = 20 m/s 166

B.47 Ideal Three Bin WFS, r_0 = 12 cm, wind speed = 20 m/s 167

B.48 Three Bin with diffraction WFS, r_0 = 12 cm, wind speed = 20 m/s 167

B.49 Shack-Hartmann WFS, r_0 = 9 cm, wind speed = 0 m/s 168

B.50 Ideal Three Bin WFS, r_0 = 9 cm, wind speed = 0 m/s 169

B.51 Three Bin with diffraction WFS, r_0 = 9 cm, wind speed = 0 m/s . 169

B.52 Shack-Hartmann WFS, r_0 = 9 cm, wind speed = 5 m/s 170

B.53 Ideal Three Bin WFS, r_0 = 9 cm, wind speed = 5 m/s 171

B.54 Three Bin with diffraction WFS, r_0 = 9 cm, wind speed = 5 m/s . 171

B.55 Shack-Hartmann WFS, r_0 = 9 cm, wind speed = 10 m/s 172

B.56 Ideal Three Bin WFS, r_0 = 9 cm, wind speed = 10 m/s 173

B.57 Three Bin with diffraction WFS, r_0 = 9 cm, wind speed = 10 m/s . 173

B.58 Shack-Hartmann WFS, r_0 = 9 cm, wind speed = 20 m/s 174

B.59 Ideal Three Bin WFS, r_0 = 9 cm, wind speed = 20 m/s 175

B.60 Three Bin with diffraction WFS, r_0 = 9 cm, wind speed = 20 m/s . 175

B.61 Shack-Hartmann WFS, r_0 = 6 cm, wind speed = 0 m/s 176

B.62 Ideal Three Bin WFS, r_0 = 6 cm, wind speed = 0 m/s 177

B.63 Three Bin with diffraction WFS, r_0 = 6 cm, wind speed = 0 m/s . 177

B.64 Shack-Hartmann WFS, r_0 = 6 cm, wind speed = 5 m/s 178

B.65 Ideal Three Bin WFS, r_0 = 6 cm, wind speed = 5 m/s 179

B.66 Three Bin with diffraction WFS, r_0 = 6 cm, wind speed = 5 m/s . 179

B.67 Shack-Hartmann WFS, r_0 = 6 cm, wind speed = 10 m/s 180

B.68 Ideal Three Bin WFS, r_0 = 6 cm, wind speed = 10 m/s 181

B.69 Three Bin with diffraction WFS, r_0 = 6 cm, wind speed = 10 m/s . 181

B.70 Shack-Hartmann WFS, r_0 = 6 cm, wind speed = 20 m/s 182

B.71 Ideal Three Bin WFS, r_0 = 6 cm, wind speed = 20 m/s 183

B.72 Three Bin with diffraction WFS, r_0 = 6 cm, wind speed = 20 m/s . 183

B.73 Shack-Hartmann WFS, r_0 = 3 cm, wind speed = 0 m/s 184

B.74 Ideal Three Bin WFS, r_0 = 3 cm, wind speed = 0 m/s 185

B.75 Three Bin with diffraction WFS, r_0 = 3 cm, wind speed = 0 m/s . 185

B.76 Shack-Hartmann WFS, r_0 = 3 cm, wind speed = 5 m/s 186

B.77 Ideal Three Bin WFS, r_0 = 3 cm, wind speed = 5 m/s 187

B.78 Three Bin with diffraction WFS, r_0 = 3 cm, wind speed = 5 m/s . 187

B.79 Shack-Hartmann WFS, r_0 = 3 cm, wind speed = 10 m/s 188

B.80 Ideal Three Bin WFS, r_0 = 3 cm, wind speed = 10 m/s 189

B.81 Three Bin with diffraction WFS, r_0 = 3 cm, wind speed = 10 m/s . 189

B.82 Shack-Hartmann WFS, r_0 = 3 cm, wind speed = 20 m/s 190

B.83 Ideal Three Bin WFS, r_0 = 3 cm, wind speed = 20 m/s 191

B.84 Three Bin with diffraction WFS, r_0 = 3 cm, wind speed = 20 m/s . 191

C.1 Shack-Hartmann WFS, r_0 = 12 cm, wind speed = 0 m/s 192

C.2 Ideal Three Bin WFS, r_0 = 12 cm, wind speed = 0 m/s 193

C.3 Three Bin with diffraction WFS, r_0 = 12 cm, wind speed = 0 m/s . 193

C.4 Shack-Hartmann WFS, r_0 = 12 cm, wind speed = 5 m/s 194

C.5 Ideal Three Bin WFS, r_0 = 12 cm, wind speed = 5 m/s 195

C.6 Three Bin with diffraction WFS, r_0 = 12 cm, wind speed = 5 m/s . 195

C.7 Shack-Hartmann WFS, r_0 = 12 cm, wind speed = 10 m/s 196

C.8 Ideal Three Bin WFS, r_0 = 12 cm, wind speed = 10 m/s 197

C.9 Three Bin with diffraction WFS, r_0 = 12 cm, wind speed = 10 m/s 197

C.10 Shack-Hartmann WFS, r_0 = 12 cm, wind speed = 20 m/s 198

C.11 Ideal Three Bin WFS, r_0 = 12 cm, wind speed = 20 m/s 199

C.12 Three Bin with diffraction WFS, r_0 = 12 cm, wind speed = 20 m/s 199

D.1 Shack-Hartmann WFS, r_0 = 12 cm, wind speed = 0 m/s 200

D.2 Ideal Three Bin WFS, r_0 = 12 cm, wind speed = 0 m/s 201

D.3 Three Bin with diffraction WFS, r_0 = 12 cm, wind speed = 0 m/s . 201

D.4 Shack-Hartmann WFS, r_0 = 12 cm, wind speed = 5 m/s 202

D.5 Ideal Three Bin WFS, r_0 = 12 cm, wind speed = 5 m/s 203

D.6 Three Bin with diffraction WFS, r_0 = 12 cm, wind speed = 5 m/s . 203

D.7 Shack-Hartmann WFS, r_0 = 12 cm, wind speed = 10 m/s 204

D.8 Ideal Three Bin WFS, r_0 = 12 cm, wind speed = 10 m/s 205

D.9 Three Bin with diffraction WFS, r_0 = 12 cm, wind speed = 10 m/s 205

D.10 Shack-Hartmann WFS, r_0 = 12 cm, wind speed = 20 m/s 206

D.11 Ideal Three Bin WFS, r_0 = 12 cm, wind speed = 20 m/s 207

D.12 Three Bin with diffraction WFS, r_0 = 12 cm, wind speed = 20 m/s 207

ACRONYMS

ABL Airborne Laser

ADU Analog to Digital Unit

AO Adaptive Optics

DM Deformable Mirror

DSP Digital Signal Processing

EORL Electro-Optics Research Lab

FPF Focal Plane Filter

FSM Fast Steering Mirror

LCD Liquid Crystal Display

LGS Laser Guide Star

NGS Natural Guide Star

NOP North Oscura Peak

OPD Optical Path Difference

OTF Optical Transfer Function

PIB Power-In-the-Bucket

SAR Synthetic Aperture Radar

SNR Signal to Noise Ratio

SORL Space Optics Research Lab

WFS Wave Front Sensor

Chapter 1
INTRODUCTION

This dissertation expands on earlier work [1, 2, 3] in presenting focal plane filters as candidates for adaptive optics wavefront sensors. The first part will present background material on adaptive optics in general and the second part will discuss the investigation of focal plane filters in the context of adaptive optics.

The background material starts (chapter 2) by motivating the use of adaptive optics. First, the effects of a turbulent atmosphere on images are presented and then the components of an adaptive optics system are introduced. Chapter 3 discusses factors that need to be considered at the early stages of system design, namely design goals and atmospheric characterization. The characterization of the atmosphere is then used to parameterize and constrain the choice of particular adaptive optics components in chapter 4. Part one concludes (chapter 5) with a discussion of several miscellaneous factor that can affect the final design of an adaptive optics system.

Next, the second part commences in chapter 6 with discussion and development of the theory behind focal plane filters. Expression are derived for the integrated intensity at the detector plane of a focal plane filter wavefront sensor. There are expressions applicable to the case where most diffractive effects are ignored, and also where diffractive effects are fully considered. Then, the results of some preliminary simulations are given in chapter 7. These simulations were limited in scope and modeled direct conjugation as if a segmented piston corrector. Further, more detailed simulations were preformed and the

results presented in chapter 8. This set of simulations modeled both direct grid level correction and a continuous facesheet deformable mirror. Lastly, chapter 9 presents the results of an experiment carried out to attempt to replicate the results of chapter 7.

PART I

AN OVERVIEW OF ADAPTIVE OPTICS

Chapter 2

WHAT IS ADAPTIVE OPTICS?

2.1 Why do I need adaptive optics

Astronomers have recognized for centuries that the fundamental limit to the resolving power of an optical system observing from the earth was atmospheric turbulence. In the frequently cited [4, 5] passage by Sir Isaac Newton from the first book of Optics (Proposition VIII. Problem II.)[6], he accurately noted several aspects of the problem: the effect of turbulence is to enlarge the 'size' of the observed stars (in the language of modern optical design, the effect of turbulence is to enlarge the effective point spread function of the system); the resolution of larger telescopes is limited by turbulence; the light gathering ability of large telescopes is not affected by turbulence; the effects of turbulence are reduced at higher altitudes (where there is less turbulence). It is an indication of the technical complexity of the problem that it can be so accurately described and yet require nearly two hundred and fifty years for viable solutions.

The remainder of this section gives an overview of the effects of turbulence and presents summaries of the two solutions: speckle interferometry and adaptive optics.

2.1.1 What are the effects of turbulence

To start with, let's look at the image of a point source if there were no aberrations. An example of such an image is shown in figure 2.1. One can see the first Airy ring in this simulated image.

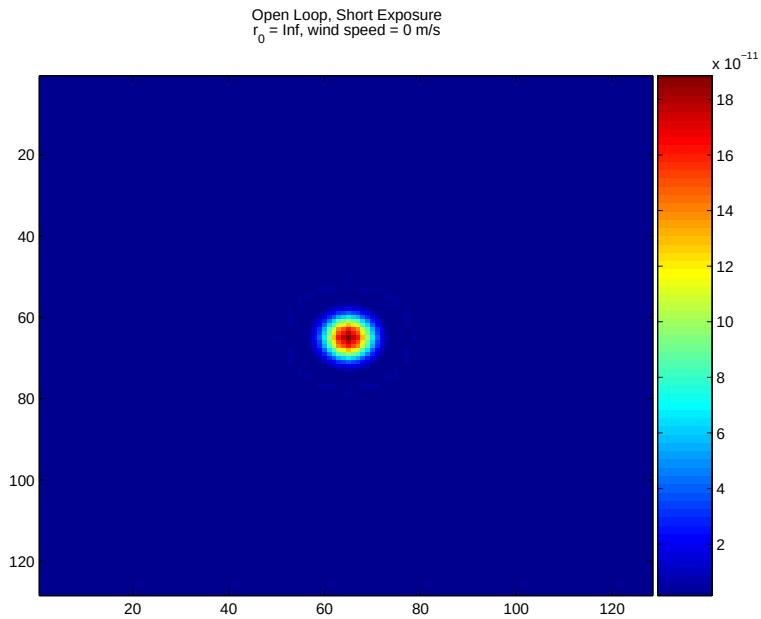

Figure 2.1: No turbulence

If we next add some turbulence to the simulation, the image will look something like figure 2.2. This figure shows the effects of weak turbulence, in this case an entrance pupil diameter (D) of 75 cm and a turbulence coherence diameter (r_0) of 30 cm for a D/r_0 of 2.5. The description and calculation of r_0 will be discussed in section 3.2, but suffice it to say that a larger r_0 is a good thing.

As the strength of the turbulence increases, the negative effects on image quality become more and more apparent. Figures 2.3 through 2.8 show the simulated effect of turbulence as we progress from mild turbulence ($D/r_0 = 3.75$) through extreme turbulence ($D/r_0 = 3.75$).

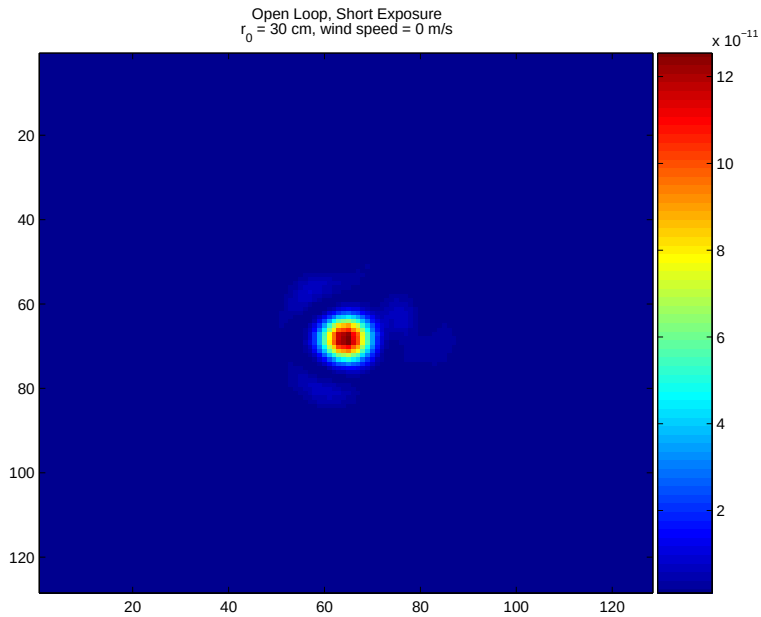

Figure 2.2: Weak turbulence ($D/r_0 = 2.5$)

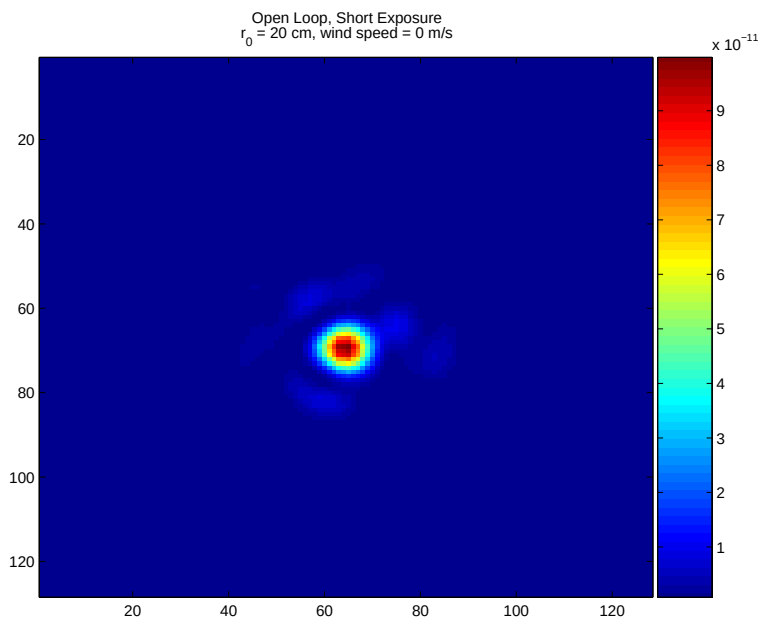

Figure 2.3: Weak turbulence ($D/r_0 = 3.75$)

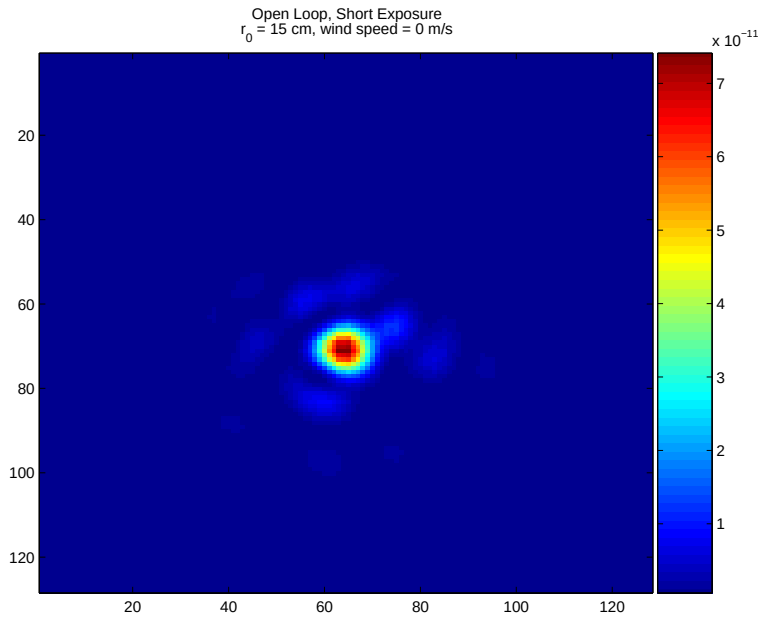

Figure 2.4: Moderate turbulence ($D/r_0 = 5$)

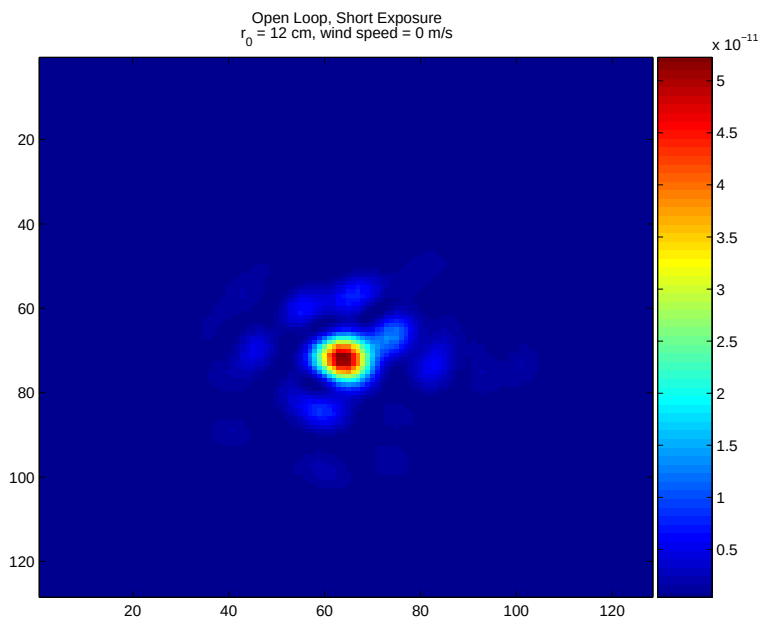

Figure 2.5: Moderate turbulence ($D/r_0 = 6.25$)

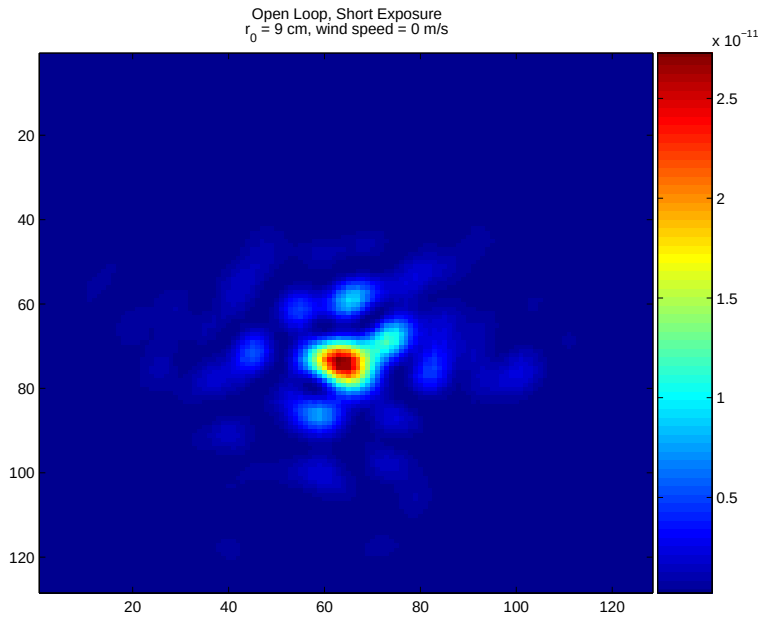

Figure 2.6: Strong turbulence ($D/r_0 = 8.\overline{3}$)

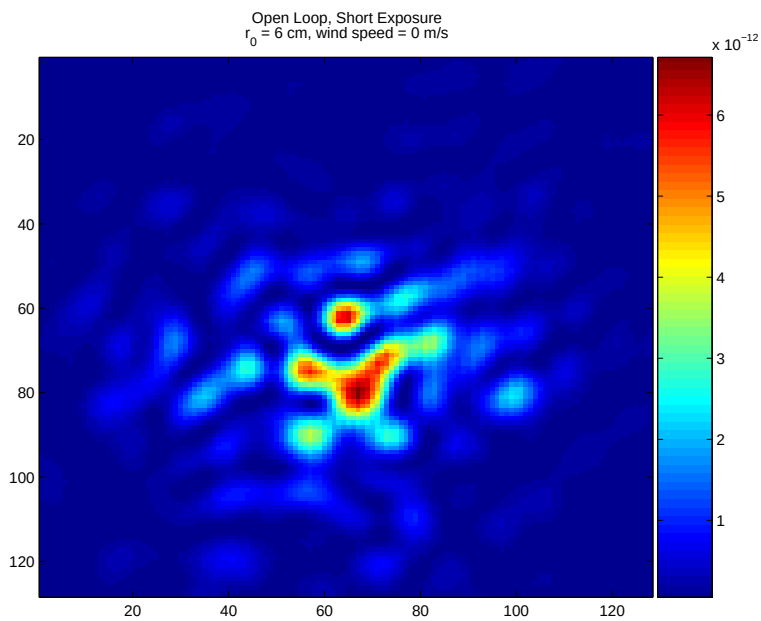

Figure 2.7: Strong turbulence ($D/r_0 = 12.5$)

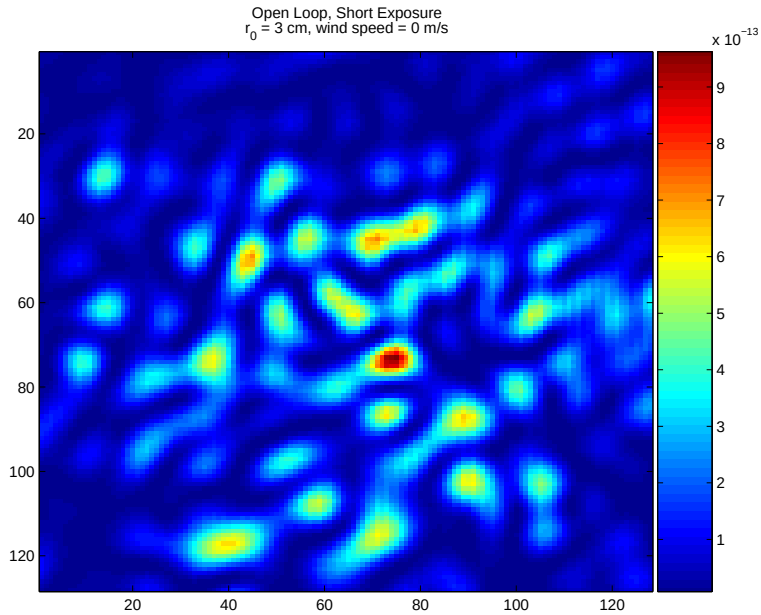

Figure 2.8: Extreme turbulence ($D/r_0 = 25$)

2.1.2 Speckle interferometry

The first method for correcting the effects of atmospheric turbulence to produce any significant results was the method of speckle interferometry. In 1970 Labeyrie [7] proposed a statistical method of reconstructing the image of an object from an image taken through turbulent aberrations. Since the dynamic changes of a degraded image due to turbulence will vary much more rapidly than changes in the object, it should be possible to separate the two effects with some sort of post-processing.

The form of the ensemble averaged optical transfer function for a short exposure image can be expressed analytically (see for example [8, section 8.7]) and contains more high frequency information than the long exposure optical transfer function. A simple method of removing the effects of turbulence

might therefore involve first taking a series of short-time exposures, averaging the results, and finally equalizing the filtering caused by the atmosphere. Since we have assumed that the telescope is perfect and that we can accurately characterize the severity of the turbulence, there is some room for improvement. If we use a reference star — one that we can accurately represent as a point source — to calculate an *ad hoc* Optical Transfer Function (OTF), we would be relieved of the task of measuring the strength of the turbulence and we could compensate for the optics of the telescope at the same time. The results, however would be less than ideal. The ensemble averaged short exposure OTF still causes significant suppression of higher frequencies. Direct inverse filtering will thus introduce a lot of noise at higher frequencies. One question might be why not use the OTF from the reference to correct for each image? The OTF for an individual short exposure image does contain a lot of high frequency information, but there are also significant spatial frequencies for which the OTF is very small. The problem thus remains the same: Inverse filtering from short exposure OTFs or their averages will introduce significant noise in the reconstructed image.

The method proposed by Labeyrie takes advantage of the fact that the ensemble averaged *power* spectrum for a short exposure image contains significant values out to the diffraction limit of the telescope. The procedure is then to take a series of short exposures of a reference and our object, calculate the power spectrum for each and over the entire series of images, average the power spectrum for the reference, and finally, use this to reconstruct the averaged power spectrum of the object. We are left with a power spectrum of the original object that has been corrected for atmospheric aberrations.

There remain two problems with this method. First of all, since we are taking short exposure images this method is only useful for relative bright objects. Faint objects will be lost in the noise of the detection process for short exposures. Secondly, a full reconstruction of the image of the object is not possible since we have lost all of the phase information from the image when calculating the power spectrum. While there are methods for reconstructing the phase spectrum from higher order moments of the Fourier transform of the images [9, 10], the restriction to bright objects stands.

2.1.3 The adaptive optics solution

Adaptive optics, on the other hand, is not limited in application to bright objects. The overall methodology of adaptive optics is to correct for the aberrations induced by the turbulence, all the while keeping the shutter to the imaging camera open. By keeping the shutter open, it is possible to obtain corrected images of faint objects.

2.2 What are the components in an Adaptive optics system?

Figure 2.9 shows the basic components of an Adaptive Optics (AO) system. The particulars of each subsystem will be touched upon below. Here it is noted that although the system block diagram implies that there is only incoming light, the components of an AO system do not change for systems that also include an outgoing beam.

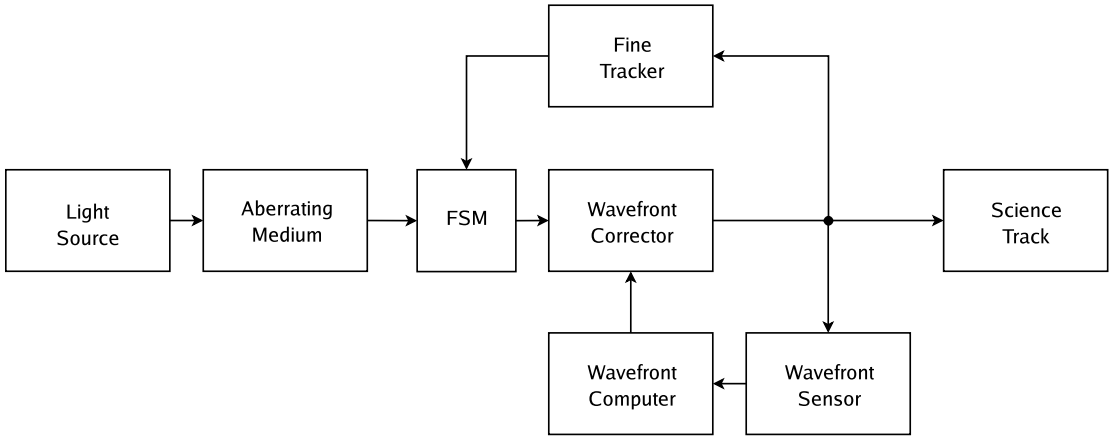

Figure 2.9: System Block Diagram of an Adaptive Optics System

2.2.1 Fine Tracker

The fine tracker is used to measure the fine mis-pointing of the system and to command the tip-tilt mirror. Together with the tip-tilt mirror, it comprises the heart of the tracker loop.

2.2.2 Tip-Tilt Mirror

Sometimes called the Fast Steering Mirror (FSM), the tip-tilt mirror is a flat mirror with a large dynamic range relative to the wavefront corrector. The tip-tilt mirror is used to correct the two lowest modes of aberrations induced by turbulence. These modes (tilt along the two lateral axes of the system) are the largest single contributors to the total aberrations due to turbulence.

2.2.3 Wavefront corrector

Even after the FSM has done its job, there remains a great deal of error in the wavefront. The wavefront corrector is tasked with reducing this error given commands received from the other components of the AO control loop. It is the means by which high resolution wavefront feedback is applied.

2.2.4 Wavefront sensor

In order for the wavefront corrector to know the amount of feedback to apply, the wavefront error must first be measured. This is the task of the wavefront sensor. The type of wavefront sensor can depend on the nature of the turbulence to be corrected for. Different devices will place different limitations on the performance of the AO loop when encountering different atmospheres.

2.2.5 Wavefront calculator

The job of translating the output of the wavefront sensor into something useful to the wavefront corrector belongs to the wavefront calculator. Depending on the specifics of the wavefront sensor, wavefront corrector and atmosphere, this can be simple or very intricate.

Chapter 3

DESIGNING ADAPTIVE OPTICS SYSTEMS

This chapter will present a cursory look at some of the decision processes involved in the first phase of AO system design. Space and scope preclude an in depth discussion here, but hopefully a sense of the problem will be conveyed.

3.1 What are the goals of the design?

Perfect correction of the effects of turbulence is not possible. The atmosphere is a thick medium but wavefront correctors will only correct at specific planes; the resolution of wavefront correctors is not sufficient to correct the smallest scales of turbulence; wavefront sensors that could sense at the finest scales of turbulence would require more light than is available in almost any situation. These are just some of the physical reasons that compromises must be made in designing an AO system.

The first stage in the design is therefore to prioritize the performance goals of the system. Using the three scenarios below will illustrate some of the issues.

Scenario I

When an astronomical telescope is placed on the top of a mountain, much of the atmospheric turbulence that degrades performance is avoided. Most of the turbulence can then be approximated as being constrained to a few distinct layers above the telescope (e.g. [11, 12]).

Typical of astronomical applications, the AO beacon is a bright star in the region of the star to be observed. This Natural Guide Star (NGS), though rel-

atively bright astronomically, is not very bright in an absolute sense. This will place a fundamental limit on the feasible dimensions of the AO system. These limits will in turn place a limit on the ability of the system to correct for turbulence. One factor of astronomical applications that relaxes the level of required correction somewhat is that the resulting corrected image can be post-processed. When used in conjunction with AO systems, these post-processing techniques preform better than when there is no AO system. There are two reasons for this. First, the image corrected by an AO system has a higher starting Signal to Noise Ratio (SNR) than would otherwise be the case. Second, the Wave Front Sensor (WFS) data can be used to constrain the statistics algorithms that form the post-processing methods[13].

The design priorities in this case would be to provide stable correction with as few degrees of freedom as possible (more degrees of freedom require more light with which to measure the degrees of freedom). By using few degrees of freedom, the system will be able to operate with dimmer NGSs and therefore correct over a larger portion of the sky. The results can then be improved by post-processing.

Scenario II

Propagating a laser horizontally through the atmosphere poses some interesting problems relative to the first scenario. First, the turbulence cannot be approximated as being isolated in distinct layers. This increases the scintillation observed. Second, the turbulence tends to be stronger, even for horizontal propagation at high altitudes.

Since the beacon is somewhat within our control, the AO beacon will be made brighter than the astronomical scenarios. This will allow for more degrees of freedom in the system. Since the atmosphere is thick, phase correction at a single plane is less effective than correction at a plane conjugate to a turbulent layer. This, coupled with the inherent increase in turbulence strength will require the increased degrees of freedom. In addition, the prospect for post-processing is not available. Thus, there are several reasons why the system needs to have more degrees of freedom and correct to a higher level.

Scenario III

The Hawaiian islands are located in a remote section of the Pacific ocean, but have mountain peaks that rise more than 4000 m above the surrounding terrain (the ocean). This produces very low levels of turbulence. It turns out however, that the turbulence layers are translated very quickly across the site[14].

In many respects this scenario is similar to the first, but there are a couple differences. The better turbulence conditions reduce the number of degrees of freedom needed to correct to a given Strehl ratio. The faster translation of the turbulence across the telescope, requires a faster response time for the AO system.

3.2 How bad is the turbulence?

From the preceding discussion, it is apparent that quantitative decisions regarding the parameters in an adaptive optics system will be directly related to quantitative characterization of the strength of turbulence for a given AO application. The remainder of this section is devoted to a discussion of the

quantization of atmospheric turbulence strength and the remaining chapters of this part are devoted to a discussion of using this description of turbulence strength to quantify the parameters of an AO system.

Without a doubt the most important parameter for the characterization of an AO system is the coherence length, r_0, of the aberrations. The value of r_0 relative to the entrance pupil diameter determines the dimensions of the wavefront sensor, and constrains the characteristics of the chosen wavefront corrector. Additionally, r_0 affects the response time required to achieve a given level of correction. Some understanding of the calculation of r_0 and its relation to system parameters is therefore useful when designing an AO application.

The definition of r_0 comes from an investigation into the maximum effective diameter of an optical system for a given level of atmospheric turbulence. In other words, at what entrance pupil diameter will the aberrations due to the atmosphere begin to be the limiting factor in determining the resolution of the system. After deriving an expression for the resolution of a system in terms of the entrance pupil diameter and the statistics of the aberrations, Fried [15] (see also Goodman [8, p.431]) found that turbulence would be the limiting factor for determining resolution if the entrance pupil had a diameter larger than

$$r_0 \triangleq \left(\frac{6.88}{2.905}\right)^{3/5} \left(\frac{1}{2\pi}\right)^{6/5} \left[\frac{\overline{\lambda}^2}{\int_0^L C_n^2\left(\xi\right) d\xi}\right]^{3/5} \tag{3.1}$$

or

$$r_0 = 0.185 \left[\frac{\overline{\lambda}^2}{\int_0^L C_n^2\left(\xi\right) d\xi}\right]^{3/5} \tag{3.2}$$

for the case where the wavefront is a plane before the turbulence is encountered[1]. The integrand in the denominator, C_n^2, is the refractive index structure constant[2]. When the input wavefront is spherical we have [16]

$$r_{0_{sph}} \triangleq \left(\frac{6.88}{2.905}\right)^{3/5} \left(\frac{1}{2\pi}\right)^{6/5} L \left[\frac{\overline{\lambda}^2}{\int_0^L C_n^2\left(\xi\right)\xi^{5/3} d\xi}\right]^{3/5} \tag{3.3}$$

or

$$r_{0_{sph}} = r_0 L \left[\frac{\int_0^L C_n^2\left(\xi\right) d\xi}{\int_0^L C_n^2\left(\xi\right)\xi^{5/3} d\xi}\right]^{3/5} \quad . \tag{3.4}$$

Here L is the distance from the entrance pupil to the source of the spherical wave.

This is a numeric characterization of the strength of the turbulence. While this parameter can be calculated using theoretical models of atmospheric turbulence, it is also possible to measure it with a scintillometer. Note also the dependence of r_0 on mean wavelength. Any reported value of r_0 is therefore relative to an associated wavelength. Although, since it can be assumed that the atmospheric fluctuations of refractive index are insensitive to wavelength [8], values at other wavelengths may be calculated by using

$$r_{0_{\lambda_{new}}} = r_{0_{\lambda_{old}}} \left(\frac{\overline{\lambda}_{new}}{\overline{\lambda}_{old}}\right)^{6/5} \quad . \tag{3.5}$$

---

[1]The constant term in front of the brackets can be expressed in several ways. The form given here facilitates some calculations of isoplanatic angle (equation (5.20)) and full aperture wavefront variance (equation (4.12)).

[2]C_n^2 is a function of distance along the propagation path but for historical reasons it is nevertheless referred to as the 'refractive index structure *constant*.'

Once one has an idea of the strength of the turbulence which will affect the optical system, the next logical question is 'how much of the degradation can I correct?' This is a complicated question and the answer depends upon several factors including:

- How many zones or modes will be measured by the wavefront sensor? In other words, how many degrees of freedom will the wavefront sensor have?
- How quickly will the system respond?
- Can the wavefront corrector handle the amplitude of the aberrations?

Other factors such as the quality of the reference, type of wavefront sensor and corrector, *et cetera*, will obviously affect the performance of the system, but the considerations above can all be treated rather straightforwardly simply by knowing r_0 and D (the entrance pupil diameter of the optical system).

The Strehl ratio after correction will be given by

$$S = e^{-\sigma^2_{total}} \tag{3.6}$$

where σ^2_{total} is the sum of the correction errors in the system.

Chapter 4

CHOOSING THE COMPONENTS OF ADAPTIVE OPTICS SYSTEMS

4.1 How fast do I have to correct?

Since the aberrations the system is trying to correct are in constant motion, the system temporal response has a direct effect on overall performance. Aberrations are often modeled as phase screens which are translated across the entrance pupil at the characteristic wind speed. This is a result of Taylor's Hypothesis [8] which states that under the right conditions turbulence can be modeled as 'frozen', but being carried along by a local wind. This proves to be a reasonable model of atmospheric turbulence as it applies to optical propagation.

Because of the time required to measure and analyze the turbulence induced aberrations and then apply a correction to a wavefront corrector, we are always correcting for old aberrations. The system must operate quickly enough so as to limit the errors introduced by this time lag. Before deciding how fast that might be, it is necessary to calculate the error introduced by the system response time.

Greenwood [17] studied the problem and came up with the expression

$$\sigma_t^2 = \int_0^\infty |1 - H(f)|^2 A(f)\, df \quad , \tag{4.1}$$

where $H(f)$ is the temporal system transfer function of the entire system, and $A(f)$ is the temporal spectrum of the atmospheric turbulence. The temporal spectrum of the turbulence depends upon the turbulence model, and for Kol-

mogorov type turbulence it is expressed as

$$A(f) = 0.0326k^2 f^{-8/3} \int_0^L C_n^2(z)\, v_w^{5/3}(z)\, dx \quad . \tag{4.2}$$

Here k is the reference optical wavenumber, f is temporal frequency, v_w is the wind velocity, and z is the length along the propagation path.

Typical transfer functions for adaptive optics systems approximate a simple RC filter and so, for the purposes of calculating the constraints on the system,

$$H(f) = \frac{1}{1 + j\frac{f}{f_c}} \tag{4.3}$$

will specify the system transfer function. This leads to a minimum 3dB cutoff frequency of

$$f_c = 0.586 \left[\frac{1}{\lambda^2 \sigma_t^2} \int_0^L C_n^2(z)\, v_w^{5/3}(z)\, dz \right]^{3/5} \tag{4.4}$$

in terms of maximum acceptable temporal error σ_t^2.

For astronomical applications it is often possible to model the turbulence in the upper atmosphere as one or more layers of turbulence each with a given r_0 and translated with a velocity v_w. In this case we can for convenience assume that the wind velocity profile for each layer is constant and then equation (4.4) becomes

$$f_c = \frac{0.426 \cdot v_w}{r_0 \left(\sigma_t^2\right)^{3/5}} \tag{4.5}$$

for each turbulent layer. For order of magnitude calculations, add the contribution of each layer:

$$f_c = \frac{.426}{\left(\sigma_t^2\right)^{3/5}} \sum_{l=1}^{layers} \frac{v_{wl}}{r_{0l}} \quad . \tag{4.6}$$

Once a value for f_c has been calculated for a given σ_t, there is a reasonably simple formula for finding the new value of f_c in terms of a new σ_t, assuming that the site parameters (r_{0l} and v_{wl}) do not change. Collecting the constant parameters

$$f_{c_1} = \frac{1}{\sigma_{t_1}^{6/5}} A \tag{4.7}$$

$$f_{c_2} = \frac{1}{\sigma_{t_2}^{6/5}} A \tag{4.8}$$

and combining the two equations

$$f_{c_1} \sigma_{t_1}^{6/5} = f_{c_2} \sigma_{t_2}^{6/5} \tag{4.9}$$

yields the relatively simple result

$$f_{c_{new}} = f_{c_{old}} \left(\frac{\sigma_{t_{old}}}{\sigma_{t_{new}}} \right)^{6/5} \quad . \tag{4.10}$$

Conversely, the effect on the error due to a change in system cutoff frequency (with the site parameters remaining unchanged) is

$$\sigma_{t_{new}} = \sigma_{t_{old}} \left(\frac{f_{c_{old}}}{f_{c_{new}}} \right)^{5/6} \quad . \tag{4.11}$$

4.2 Calculating the dynamic range of the tip-tilt mirror

subject]tip-tilt In atmospheric adaptive optics, tip-tilt aberrations are by far the dominant aberrations to be corrected. Since tip-tilt is so large it is often corrected in a separate system and will therefore be characterized by itself. By correcting tip-tilt separately it is possible to considerably relax the specifications of the wavefront corrector used on the remaining modes. Another consideration is that laser guide star references are insensitive to tip-tilt (see p. 47). As a consequence wavefront sensors using laser guide stars as a reference will not be able to measure tip-tilt without making use of special techniques: another reason for which tip-tilt correction is normally assigned to a separate system.

It is possible to characterize the statistics of the turbulence across the aperture both with and without tip-tilt. Roddier [18] investigated the statistics of Kolmogorov turbulence as a function of Zernike modes. The mean square phase difference for the two end points of a pupil diameter are

$$\sigma_{tt}^2 = 6.88 \left(\frac{D}{r_0}\right)^{5/3} \quad . \tag{4.12}$$

Two standard deviations will cover 95.5% of possible cases. We then have

$$\Delta_{tt} = 5.25 \left(\frac{D}{r_0}\right)^{5/6} \text{ rad} \quad . \tag{4.13}$$

It would be convenient if

$$\Delta_{tt} = 6.28 \left(\frac{D}{r_0}\right)^{5/6} \text{ rad} \approx 2\pi \left(\frac{D}{r_0}\right)^{5/6} \text{ rad} \tag{4.14}$$

because we would then have

$$\Delta_{tt} = \lambda \left(\frac{D}{r_0} \right)^{5/6} \mathrm{m} \quad . \tag{4.15}$$

This would be the result if we had used 2.4 standard deviations above — in the process covering 98.4% of cases — rather than the common two standard deviations. Using this estimate for the tip-tilt deflection gives even more design safety and at the same time provides a convenient expression.

4.3 Choosing a wavefront corrector

4.3.1 Wavefront corrector types

There are many types of wavefront correctors available for adaptive optics systems. The following short descriptions are more to introduce terminology than to provide a detailed treatment.

Discrete actuator deformable mirror

This type of corrector is formed by bonding an array of discrete actuators (thus the name) to the back of a reflective surface. The actuators act for the most part independently. There is some coupling between actuators, however, due to the finite elasticity of the reflective surface and finite actuator spacing.

Bimorph mirror

A bimorph mirror is constructed by bonding a thin metal mirror on top of a conducting electrode layer, on top of a piezoelectric layer, with an array of discrete electrodes bonded on the back. A voltage applied to the discrete electrodes will cause a local curvature on the mirror. The radius of this curvature has the form[5, p.191]

$$R = \frac{V \cdot d}{t^2} \tag{4.16}$$

where V is the applied voltage, d is a parameter of the piezoelectric material, and t is the thickness of the piezoelectric layer plus the mirror layer. The bimorph mirror is well matched with the curvature sensor described in section 4.4.3.

Segmented mirror

Segmented mirrors are formed by assembling a large array of tiny mirrors over the area to be corrected. Each of these mirrors corrects for the local piston at a particular location. It does so by moving in or out based on commands from the wavefront controller. There is no attempt to deal with the discontinuity between adjacent segments. There is a natural correspondence between a segmented mirror and an interferometric wavefront sensor.

Liquid Crystal Display

In many ways a Liquid Crystal Display wavefront corrector can be considered a special case of a segmented mirror. The main differences are that with an Liquid Crystal Display (LCD) there are no mechanical moving parts and there are chromatic effects. Another important consideration is that LCDs are much cheaper than segmented mirrors.

4.3.2 Wavefront corrector constraints

The two main concerns regarding the wavefront corrector are that it can respond quickly enough and that it can correct all of the aberrations detected. The former applies to system response time, which is treated in section 4.1, while the latter is treated here. There are two parameters of importance when considering how well the wavefront corrector can accomplish its task, namely its dynamic range and its resolution.

The dynamic range describes the largest difference in phase across the wavefront corrector aperture which the system will be expected to correct and the resolution defines the difference in phase between two actuators or pixels.

Full aperture stroke

Assuming that tip-tilt has been corrected by the system, the residual mean square phase difference has a maximum value of (again from Roddier [18])

$$\sigma_{ap}^2 = 0.34 \left(\frac{D}{r_0}\right)^{5/3} \quad . \tag{4.17}$$

Again using a tolerance of 2.4 standard deviations, we have

$$\Delta_{ap} = 1.4 \left(\frac{D}{r_0}\right)^{5/6} \quad \text{rad} \tag{4.18}$$

which can be expressed as

$$\Delta_{ap} = .22 \cdot 2\pi \left(\frac{D}{r_0}\right)^{5/6} \quad \text{rad.} \tag{4.19}$$

Expressing this result in terms of wavelength gives

$$\Delta_{ap} = .22 \cdot \lambda \left(\frac{D}{r_0}\right)^{5/6} \quad \text{m} \tag{4.20}$$

or equivalently

$$\Delta_{ap} = .22 \cdot \Delta_{tt} \ \ \text{m} \quad . \tag{4.21}$$

INTER-ACTUATOR STROKE

For separation distances up to a third of the entrance pupil diameter, the phase structure function after tip-tilt correction can be approximated as (from the plots in Roddier [18])

$$\mathcal{D}\left(\vec{r}\right) \approx 0.9 \frac{\vec{r}}{D} \left(\frac{D}{r_0}\right)^{5/3} \quad . \tag{4.22}$$

If there are N_0 actuators on the active portion of the wavefront corrector, then $\vec{r}$ (the distance between two actuators) is

$$\vec{r} \approx \frac{D}{\sqrt{N_0}} \quad . \tag{4.23}$$

This leads to

$$\sigma_{IA}^2 = \frac{.9}{\sqrt{N_0}} \left(\frac{D}{r_0}\right)^{5/3} \tag{4.24}$$

and once again we take 2.4 standard deviations to obtain

$$\Delta_{IA} = \frac{2.28}{\sqrt[4]{N_0}} \left(\frac{D}{r_0}\right)^{5/6} \quad \text{rad} \tag{4.25}$$

for the inter actuator stroke. Following the same procedure that was used above for the full-aperture tip-tilt we proceed from

$$\Delta_{IA} = \frac{.36 \cdot 2\pi}{\sqrt[4]{N_0}} \left(\frac{D}{r_0}\right)^{5/6} \quad \text{rad} \tag{4.26}$$

to

$$\Delta_{IA} = \frac{.36 \cdot \lambda}{\sqrt[4]{N_0}} \left(\frac{D}{r_0}\right)^{5/6} \quad \text{m} \tag{4.27}$$

and finally

$$\Delta_{IA} = \frac{.36}{\sqrt[4]{N_0}} \Delta_{tt} \quad \text{m.} \tag{4.28}$$

4.4 How do I choose a wavefront sensor?

Since the atmospheric aberrations are encoded as a phase modulation of the incoming light field, a device is needed to extract this phase information before detection. There are several methods available for doing this. The most common uses a Shack-Hartmann lens array to sample the pupil plane while the next most common records two images of the reference; one inside and one outside the focal plane. The wavefront sensors deriving from these two methods are referred to respectively as Shack-Hartmann wavefront sensors and

curvature wavefront sensors. This dissertation presents another method which uses phase and amplitude filters in the image plane.

4.4.1 Wavefront sensor dimensions

Before discussing the effect of r_0 on the dimensions of the wavefront sensor, a distinction should be made between zonal and modal wavefront sensing. In a modal wavefront sensor the incoming wavefront is reconstructed in terms of the Zernike modes across the entrance pupil of the system, whereas in a zonal wavefront sensor the reconstructed wavefront is spatially sub-divided into 'zones' and the phase is given for each zone. The number of modes or zones in the reconstructed wavefront then limits the accuracy of the reconstruction for a given turbulence strength.

Since there is a limited amount of light reaching the system, the degrees of freedom in the wavefront sensor should not be too great. Otherwise, any theoretical gains in performance will be offset by sensor errors due to noise.

For a zonal wavefront sensor, the mean square residual wavefront error in terms of zone size (r_s) is given by Wincour [19]

$$\sigma^2_{zonal} = 0.31583 \left(\frac{r_s}{r_0}\right)^{5/3} \quad . \tag{4.29}$$

The zone size is related to the entrance pupil diameter by

$$r_s = \frac{D}{\sqrt{Z}} \quad , \tag{4.30}$$

where Z is the number of zones. This yields

$$\sigma^2_{zonal} = 0.31583 \left(\frac{Z}{N_0} \right)^{-5/6} \quad , \tag{4.31}$$

where $N_0 = (D/r_0)^2$, or the ratio of the entrance pupil area to the area of the turbulence equivalent aperture.

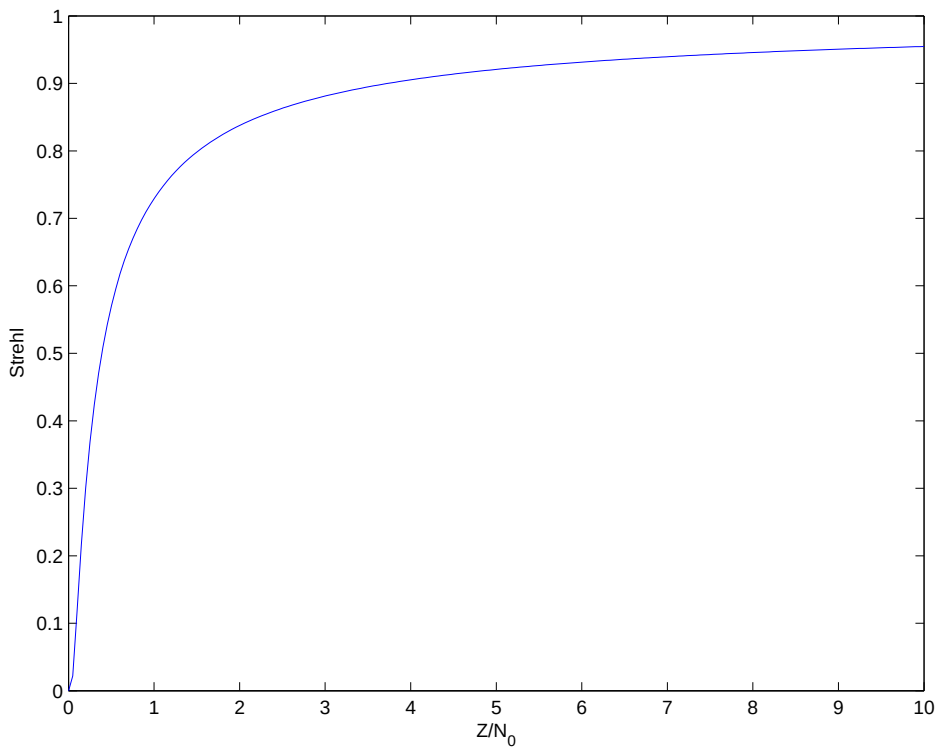

Figure 4.1: Strehl ratio vs. number of zones per coherence diameter

A plot of the Strehl ratio due to this error is given in figure 4.1. The Strehl ratio is plotted against Z/N_0. It can be seen that there is probably no justification for the number of zones to exceed about $4N_0$ and in many cases it would

probably suffice that the number of zones be equal to N_0. A plot of the error itself appears in figure 4.2

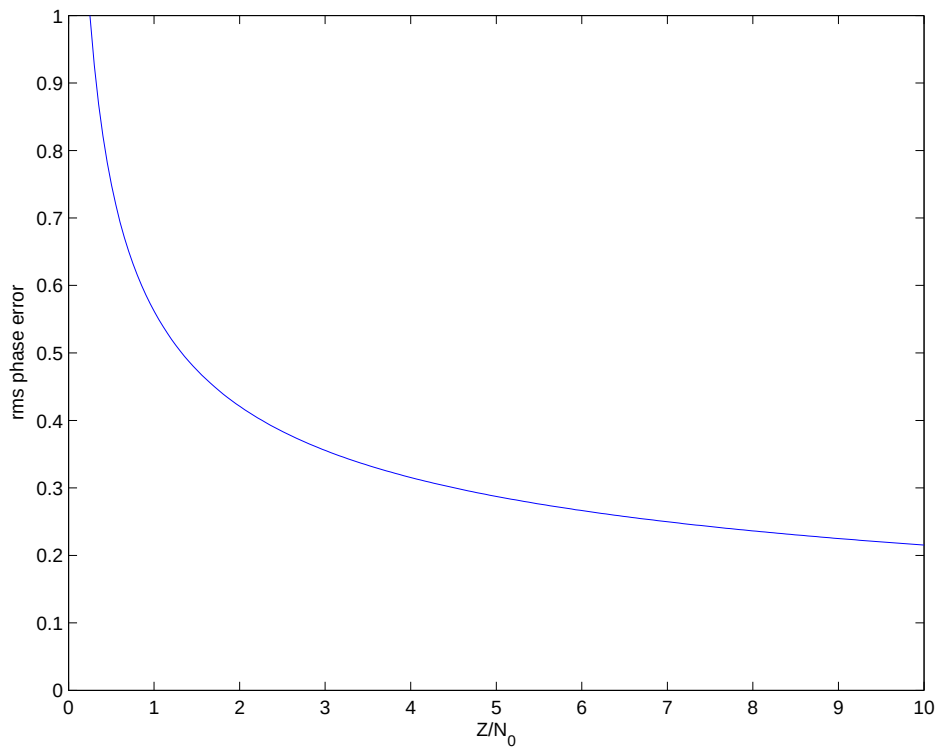

Figure 4.2: RMS error in rad vs. number of zones per coherence diameter

For modal correction the residual error is given as [20]

$$\sigma^2_{modal} = 0.2944 M^{-\sqrt{3}/2} \left(\frac{D}{r_0}\right)^{5/3} \tag{4.32}$$

or

$$\sigma^2_{modal} = 0.2944 M^{-\sqrt{3}/2} {N_0}^{5/6} \quad , \tag{4.33}$$

Where M is the number of modes. Combining equation (4.31) and equation (4.33) gives an expression for the minimum number of modes to correct in order to

produce the same level of correction obtained using a given number of zones:

$$M = \text{ceil}\left(0.92217 Z^{5/3\sqrt{3}}\right) \quad . \tag{4.34}$$

Here ceil() is a function that always rounds up to the next higher integer.

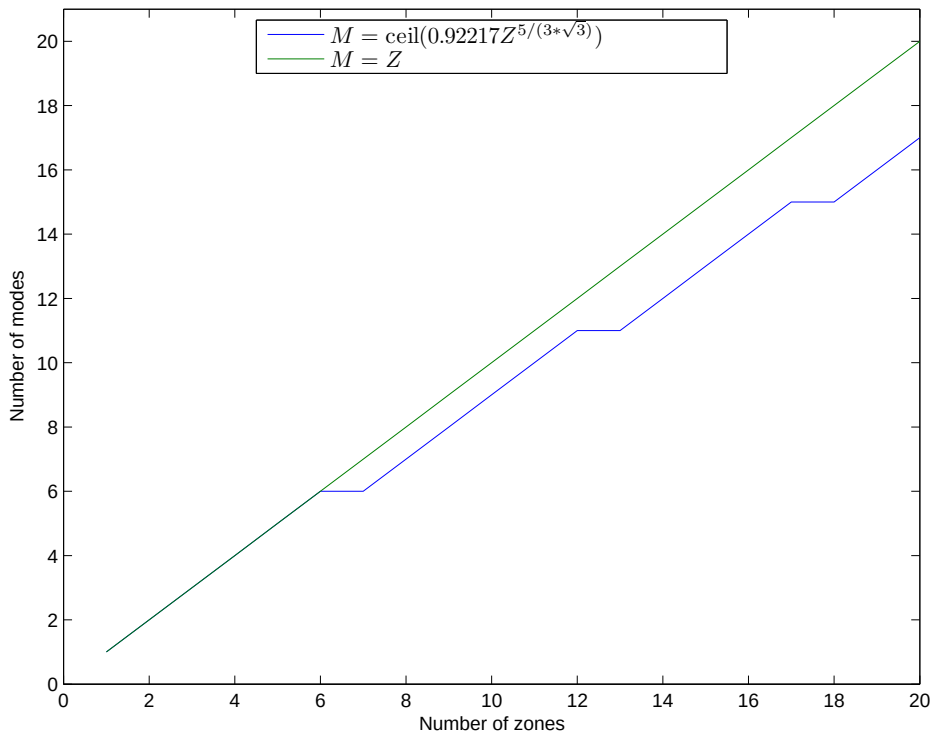

Figure 4.3: Number of modes vs. number of zones for the same residual error

This expression is plotted in figure 4.3 along with the expression $M = Z$ and it can be seen that for the lower numbers of zones and modes there are slightly more zones required, but that the number of modes or zones required for a given level of correction is essentially equal.

For an adaptive optics system of any size, the wavefront sensor will be a zonal sensor since direct detection of the higher order Zernike modes is not evident. Sometimes the sensor is actually of mixed type, as is the case when a Shack-Hartmann (zonal) sensor is used in conjunction with a quad-cell detector to directly measure the sub-aperture tip-tilt. For the most part, in what follows it will be assumed that the wavefront sensor is, for all intents and purposes, zonal.

Although it was stated above that there was probably no reason for choosing more than $4N_0$ degrees of freedom in the wavefront sensor there is a good reason for choosing fewer. If there are too many degrees of freedom, then there will not be enough photons in the system to overcome noise (see 5.1.1). For this reason N_0 is usually chosen as the number of degrees of freedom in the wavefront sensor.

4.4.2 Shack-Hartmann sensor

The basic function of a Shack-Hartmann wavefront sensor is to sample small regions of the pupil and form images of the reference from these sub-pupils. The local tip-tilt over a sub-pupil can then be calculated from the lateral displacement of the image of the reference. The local tip-tilts can then be used together to calculate a piecewise linear reconstruction of the wavefront across the entire pupil.

To better understand the process, first look at figure 4.4. This figure shows the effect of placing a lenslet array in the image plane of an aberration free pupil. The result is a mosaic of regularly spaced images of the reference. If, however, the field at the pupil contains aberrations (see figure 4.5) then the ref-

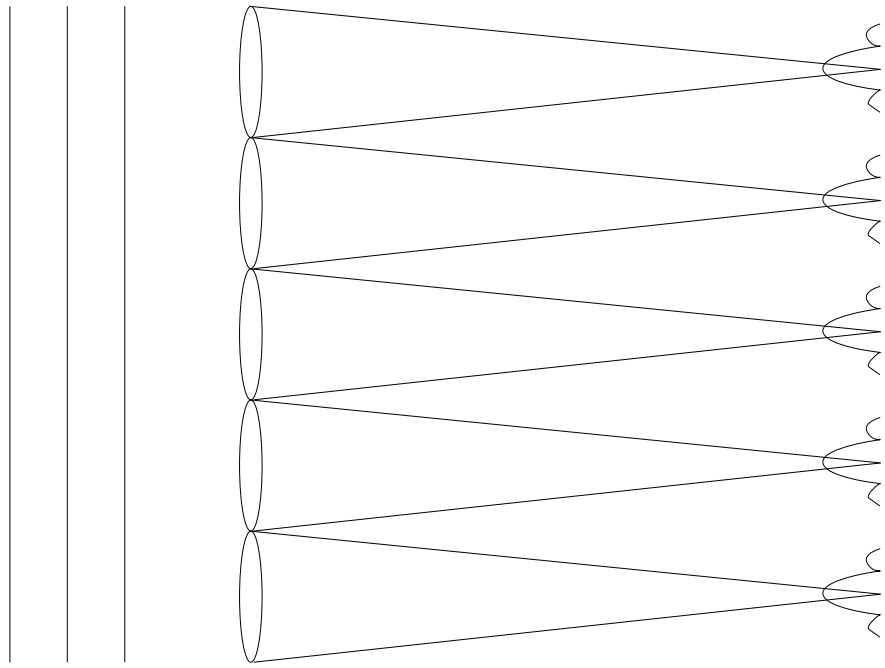

Figure 4.4: Shack-Hartmann and plane wave

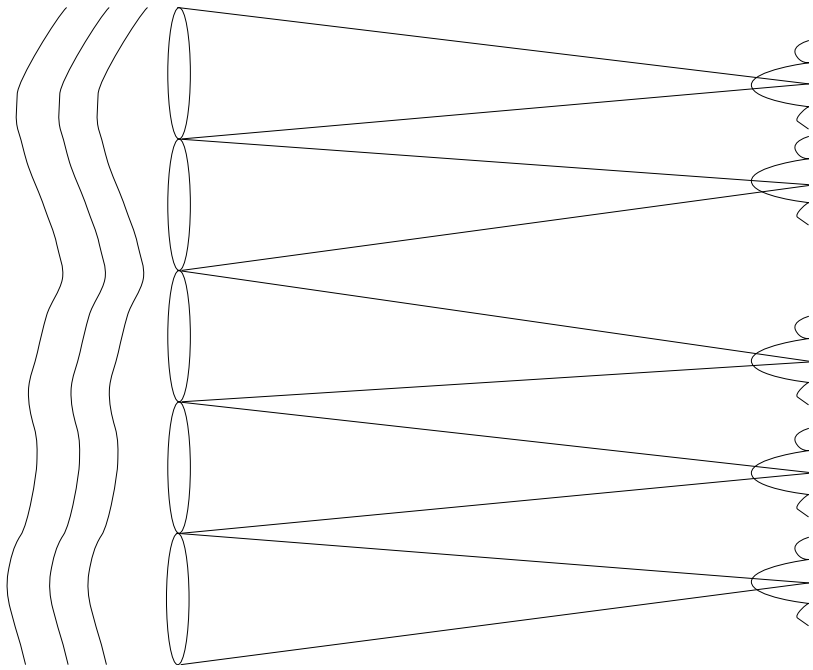

Figure 4.5: Shack-Hartmann and aberrated wave

erence images in the mosaic are aberrated. Since each sub-pupil (the sub-part of the pupil as seen by each lens in the lenslet array) is only affected by the aberrations local to itself, each of the multiple reference images contain information relating to the aberrations across the corresponding sub-pupil. If the lateral displacement of each reference image relative to its position for an unaberrated pupil is calculated, it is possible to calculate the tip-tilt across the sub-pupil. If these are then combined for all of the sub-pupils, the result is a piecewise linear fit to the wavefront over the entire pupil.

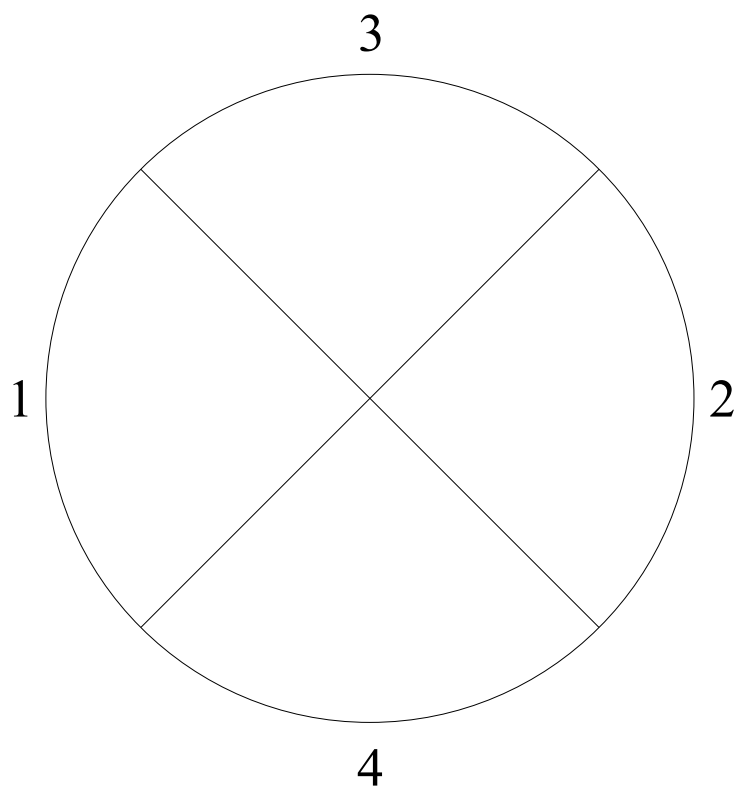

Figure 4.6: Quad-cell detector

One way to calculate the displacement of the reference images is to use a quad cell detector as in figure 4.6. The displacement of the image in the

x-axis direction is calculated by subtracting the irradiance in quadrant 1 from the irradiance in quadrant 2, normalized by the sum of the two. The same process is used to calculate the displacement along the *y-axis*.

The more common and more accurate method is to project the mosaic of reference images onto a pixellated detector and then calculate the centroids

$$\begin{aligned} x_{\text{cent}} &= \sum_{\forall x, \forall y} I(x,y) \cdot x \\ y_{\text{cent}} &= \sum_{\forall x, \forall y} I(x,y) \cdot y \end{aligned} \tag{4.35}$$

for each image. This method is more robust but also more computationally intensive.

4.4.3 Curvature sensor

Another common wavefront sensor, and one gaining popularity, is the curvature wavefront sensor. This type of wavefront sensor is based on the fact that by comparing two images, one in front of an image of the pupil and one behind an image of the pupil, it is possible to calculate the aberrations across the pupil. This is accomplished through the irradiance transport equation [14, p.30]

$$\frac{\partial I}{\partial z} = -\frac{\lambda}{2\pi}\left(\nabla I \cdot \nabla \phi + I \nabla^2 \phi\right) \quad . \tag{4.36}$$

From this equation, it appears that the computation of the wavefront aberrations is quite a daunting task and probably not useful in an adaptive optics scenario. The curvature sensor capitalizes on some symmetries of equation (4.36) to make the problem tractable.

When coupled with a bimorph mirror, whose response parallels equation (4.36), the contrast between the intra-focal and extra-focal images is proportional to the voltage to apply to the bimorph mirror and can be expressed as

$$\frac{I_1(\vec{r}) - I_2(-\vec{r})}{I_1(\vec{r}) + I_2(-\vec{r})} = \frac{f(f - \Delta z)}{\Delta z} \frac{V d_{xy}}{t^2} \quad . \tag{4.37}$$

Here t is the mirror thickness, V is the voltage to be applied and d is a coefficient of the piezoelectric tensor. f is the effective focal length of the system that forms the pupil around which the intra- and extra-focal images are taken and Δz is the distance from the pupil plane to the intra- and extra-focal planes.

4.5 What does a wavefront calculator do?

The wavefront calculator, or wavefront computer or wavefront reconstructor, basically takes wavefront sensor measurements as input and computes commands to the wavefront corrector as output. The methods which it uses to do so are varied, sometimes highly dependent on the types of the wavefront sensor and wavefront corrector

For systems in which the wavefront sensor and corrector are closely matched, the wavefront calculator can in theory be trivial. Cases in which this is true are, for example a curvature sensor and a bimorph mirror or an interferometric sensor and a piston type corrector.

MODAL FILTERING

Once the output of the wavefront sensor is collected, it needs to be converted into commands for the wavefront corrector. This process can be represented in three conceptual steps. First the output of the wavefront sensor is represented as an output vector of a linear system. Second the inversion of this system gives a vector of commands to send to the wavefront corrector. Optionally the inverse system can be passed through a modal filter so as to maximize the signal to noise ratio.

For both the Shack-Hartmann sensor and the Curvature sensor, it is possible to describe the wavefront sensing process as the linear system

$$\vec{s} = \boldsymbol{D}\vec{c} \quad . \tag{4.38}$$

In this equation $\vec{s}$ is the output of the wavefront sensor. The term $\vec{c}$ at first glance might be thought of as the incoming wavefront sampled at certain points. While this vector is directly related to the incoming wavefront, it is more instructive to see how $\vec{c}$ relates to the wavefront corrector. Each element in $\vec{c}$ corresponds to an actuator or pixel in the wavefront corrector. It is now possible to define $\boldsymbol{D}$ in the following way: apply a unit deflection to element i of the wavefront corrector; now read the output from the wavefront sensor; this output vector is then used as column i of the matrix $\boldsymbol{D}$. What we have just defined is, in effect, a heuristic for measuring the transformation matrix $\boldsymbol{D}$ used to take a description of the incoming wavefront in the $\vec{c}$ coordinate system and convert it to one in the $\vec{s}$ coordinate system.

It would seem that a more intuitive description would be

$$\vec{c} = \boldsymbol{E}\vec{s} \quad , \tag{4.39}$$

or a system description which translates the output of the wavefront sensor into inputs to the wavefront corrector. After all, that is the operation which we wish to perform. The above discussion shows, however, that $\boldsymbol{D}$ can be directly measured in such a way that errors in control of the wavefront corrector are minimized; something which is not true of the system in equation (4.39)

It is obvious that if $\boldsymbol{D}$ is invertible then $\boldsymbol{D}^{-1}$ is just $\boldsymbol{E}$. If this is not the case — $\boldsymbol{D}$ is maybe not square, e.g. fewer correction actuators than sensor zones — then the generalized inverse

$$\boldsymbol{D}^{+} = \left(\boldsymbol{D}^{\mathrm{T}}\boldsymbol{D}\right)^{-1}\boldsymbol{D}^{\mathrm{T}} \tag{4.40}$$

is computed.

Gendron [21](also Gendron and Léna [22]) showed that the performance of an adaptive optics system could be improved if the commands to the wavefront corrector were passed through a conditioning filter. This filter makes use of knowledge of the statistical characteristics of the atmosphere to ensure that the commands to the wavefront controller are sensible. The overall effect is to reduce the harm done by noise in the detection of some of the higher turbulence modes.

Chapter 5

OTHER CONSIDERATIONS

5.1 What is my limiting reference?

In astronomical adaptive optics there are two types of point sources that are used. The first, and most common, is a bright star that is close to the object to be observed. The second is an artificial 'star' created by aiming a laser at a point near the object to be observed. The sodium atoms high in the atmosphere are put into an excited state by the laser. As the atoms return to their unexcited state, they radiate and produce an artificial 'star' in the neighborhood of the observed object.

The reference must be near the object so that light from the reference and object undergo the same aberrations. If the aberrations seen by the reference are significantly different from those seen by the object, the adaptive optics system will be correcting the wrong aberrations from the point of view of the object. This could easily be worse than no correction at all. Just how close must the reference be to the object? This is determined by the strength of the turbulence as measured by the optical coherence length, r_0, defined by Fried. This parameter is probably the most useful quantity from the theoretical analysis of turbulence. It will be useful in specifying the dimensions of many components in the system.

5.1.1 Limiting magnitude of the reference

Before moving on to discussions of the characteristics of laser guide stars and natural guide stars, it will be useful to determine just how weak the radiation of the reference can be. Since we are dealing with astronomical applications the strength of the reference will be expressed in terms of stellar magnitude.

The magnitude of a celestial object in terms of its spectral photon flux density is

$$M = -2.5\left(\log_{10} E_{p,\lambda} - b_\lambda\right) \quad . \tag{5.1}$$

In this equation, b_λ is a normalizing constant for the observation band and $E_{p,\lambda}$ is the spectral photon flux density whose units are $photons/\mathrm{s}\cdot\mathrm{cm}^2\cdot\text{Å}$. The subscript λ here indicates that E is a spectral quantity while the subscript p indicates the it is in terms of photons. This notation will be used in the following discussion. When calculating the limiting magnitude for a wavefront sensor, the area will be given in terms of the entrance pupil diameter. Since this diameter is most conveniently given in units of meters, it is convenient to define magnitude as (the 4 accounts for the conversion from $\mathrm{m}^2$to cm^2

$$M = -2.5\left(\log_{10} E_{p,\lambda} - b_\lambda - 4\right) \tag{5.2}$$

where the units of $E_{p,\lambda}$ are now $photons/\mathrm{s}\cdot\mathrm{m}^2\cdot\text{Å}$.

If we define the total noise (in units of photons per frame) in the system as seen at the end of the wavefront sensor detection process as σ_{tot_p}, then the

minimum spectral flux density can be expressed as

$$E_{p,\lambda_{min}} = S^*_{p,\lambda} \cdot \sigma_{tot_p} \quad . \tag{5.3}$$

In this equation $S^*_{p,\lambda}$ is a kind of minimal signal to noise ratio. It is different from a normal signal to noise ratio in that its units for the signal ($photons/\mathrm{s} \cdot \mathrm{m}^2 \cdot \text{Å}$) are very different from the units for the noise (photons). In order to reconcile this and to find an expression for $S^*_{p,\lambda}$ we start by making use of one of the properties of a wavefront sensor. The measurement noise for a given type of wavefront sensor can be expressed in terms of the input signal to noise ratio. Inverting this equation yields an expression for the minimum signal to noise ratio required to measure the incoming wavefront to within a given error. For example, a Shack-Hartmann sensor using quad-cell detectors has a measurement error expressed in Tyson [5] as

$$\sigma^2_{WFS_{S-H}} = \frac{0.0875 \cdot \pi^2}{SNR^2} \quad . \tag{5.4}$$

This leads to

$$SNR_{S-H}\left(\sigma_{WFS}\right) = \frac{0.2958 \cdot \pi}{\sigma_{WFS}} \tag{5.5}$$

as an expression for the SNR.

This SNR is for an entire observation band. If the input signal spectrum were flat, the spectral SNR would become just

$$\frac{SNR\left(\sigma_{WFS}\right)}{\Delta\lambda} \quad , \tag{5.6}$$

with $\Delta\lambda$ the bandwidth in Angstroms. In order to accommodate other input spectra we use

$$\frac{SNR\left(\sigma_{WFS}\right)}{f_\lambda \Delta\lambda} \tag{5.7}$$

where f_λ is the normalized input spectrum.

Since σ_{tot_p} is evaluated after having traversed the entire system to the detector of the wavefront sensor, while $E_{p,\lambda}$ is evaluated before it has encountered any part of the system, we need to account for the optical transmission through the system. Thus we have

$$\frac{SNR\left(\sigma_{WFS}\right)}{T_{sys_\lambda} \cdot f_\lambda \Delta\lambda} \quad . \tag{5.8}$$

Similarly we need to divide by the frame rate, t_f, for

$$S^*_{p,\lambda} = \frac{SNR\left(\sigma_{WFS}\right)}{t_f \cdot T_{sys_\lambda} \cdot f_\lambda \Delta\lambda} \quad , \tag{5.9}$$

and account must be taken for the area of the wavefront sensor zone (at the entrance pupil):

$$S^*_{p,\lambda} = \frac{SNR\left(\sigma_{WFS}\right)}{\frac{\pi D^2}{4N_z} \cdot t_f \cdot T_{sys_\lambda} \cdot f_\lambda \Delta\lambda} \quad , \tag{5.10}$$

where D is the entrance pupil diameter. We now have

$$S^*_{p,\lambda} = \frac{SNR\left(\sigma_{WFS}\right)}{\beta} \tag{5.11}$$

where

$$\beta = \frac{\pi D^2}{4N_z} \cdot t_f \cdot T_{sys_\lambda} \cdot f_\lambda \Delta\lambda \quad . \tag{5.12}$$

So, $S^*_{p,\lambda}$ is the minimum SNR required to achieve a wavefront sensor measurement error of σ_{WFS} after SNR has been normalized by a factor β. This β converts

from photons per frame at the wavefront sensor to spectral photon flux density in front of the entrance pupil. Lastly, the noise is the combination of photon noise and the noise due to the detector system of the wavefront sensor:

$$\sigma_{tot_p} = \sigma_{ph}^2 + \left(\frac{\sigma_{sys_{e^-}}}{\mathcal{R}_{ph-e^-{}_\lambda}} \right)^2 \quad , \tag{5.13}$$

In this expression, $\sigma_{sys_{e^-}}$ is the total system noise expressed in units of electrons per frame and $\mathcal{R}_{ph-e^-{}_\lambda}$ is the spectral photo-electric responsitivity. Using these results in equation (5.3) gives

$$\begin{aligned}
E_{p,\lambda_{min}} &= S^*_{p,\lambda} \left[\sigma_{ph}^2 + \sigma_{sys_p}^2 \right]^{1/2} \\
&= S^*_{p,\lambda} \left[\beta E_{p,\lambda_{min}} + \sigma_{sys_p}^2 \right]^{1/2} \\
\tfrac{1}{S^*_{p,\lambda}{}^2} E^2_{p,\lambda_{min}} &= \beta E_{p,\lambda_{min}} + \sigma_{sys_p}^2 \\
\tfrac{1}{S^*_{p,\lambda}} E^2_{p,\lambda_{min}} &= SNR\left(\sigma_{WFS}\right) E_{p,\lambda_{min}} + S^*_{p,\lambda} \sigma_{sys_p}^2
\end{aligned} \tag{5.14}$$

which, after application of the quadratic equation, yields the expression

$$E_{p,\lambda_{min}} = \frac{S^*_{p,\lambda}}{2} \left(SNR\left(\sigma_{WFS}\right) + \sqrt{SNR^2\left(\sigma_{WFS}\right) + 4\,\sigma_{sys_p}^2} \right) \tag{5.15}$$

for the minimum spectral photon flux density. Applying this result to the equation for stellar magnitude (equation (5.2)) produces an equation for the mini-

mum reference magnitude, namely

$$M_{limit} = -2.5 \left(\log_{10} \left[\frac{S^*_{p,\lambda}}{2} \left(SNR\left(\sigma\right) + \sqrt{SNR^2\left(\sigma\right) + 4\,\sigma^2_{sys_p}} \right) \right] - b_\lambda - 4 \right) \tag{5.16}$$

Throughout this derivation several of the terms in these expressions have remained in a spectral form, that is, wavelength dependent. If we wanted to calculate the exact limiting magnitude for a given set of conditions, it would be necessary for us to take the wavelength dependence of the source into consideration. This, however would mean that the final calculation was only valid for a particular reference spectrum. This is not practical as two references could have the same magnitude over a given band yet not have the same spectrum over the band. We are thus forced to somewhat simplify the analysis. First, assume that f_λ is one over the band, second we will take T_{sys} to be a constant. In addition the responsivity in equation (5.13) will become wavelength independent. If the effective values used for these parameters maintain the same area over the bandwidth $\Delta\lambda$ as before then the overall photon flux density should not be too adversely affected by these simplifications.

As an example, let's take a Shack-Hartmann wavefront sensor with a quad-cell detector for each sub-aperture. If we settle on an error value of 0.416 radians, then the SNR is 2 (this would correspond to a Strehl ratio of 80% if other errors are negligible). Suppose also that the system error is ten photons per frame and that we operate in the visible band (where b_λ is approximately 3), and equation (5.16) will simplify to

$$M_{limit} = -2.5 \left(\log_{10} \frac{22}{\beta} - 7 \right) \tag{5.17}$$

or

$$M_{limit} = -2.5 \left(\log_{10} \frac{22}{\frac{\pi D^2}{4N_z} \cdot t_f \cdot T_{sys} \cdot \Delta\lambda} - 7 \right) \quad . \tag{5.18}$$

Using the system on a telescope with a 1m diameter, a frame rate of 10ms, a bandwidth of 5000Å, 16 sub-pupils and a transmission of 20% yields a theoretical limiting magnitude of 13.4.

5.1.2 Natural guide stars

A NGS system has many advantages over a system employing laser guide stars. First and foremost is the fact that there is no need to design a system for creating the Laser Guide Star (LGS). This alone can reduce the complexity of the overall design considerably. In addition, NGS systems do not suffer from focus anisoplanatism section 5.2.3; the reference wavefront samples the entire depth of the atmosphere, and they are not blind to tip-tilt aberration modes. NGS systems do, however, suffer from one very serious problem and it is one for which there is effectively no solution, namely finding a reference that is both bright enough and near enough to the object being observed. The observer must accept the references which providence has seen fit to provide, and hopefully one exists which will allow the adaptive optics system to be used in the observation of the object of interest. Olivier and Gavel [23] show a plot of the probability of finding a natural guide star (in the visible) of a given magnitude within a given angular separation of the observation star. For an angular separation of 10 μrad there is only a 1% chance of there being a magnitude 16 or brighter reference near a given object. This is also only for an object near the

relatively dense galactic plane, and the odds are much worse as the observation object is closer to the galactic pole.

5.1.3 What about laser guide stars?

The most common artificial guide star is created by using a laser to excite the gaseous sodium layer that exists in the upper atmosphere about 90 to 100 kilometers above the earth. With this method, it is possible to create a reference beacon with a consistent intensity anywhere in the field of view of the telescope. It is thus possible to reduce the angular anisoplanatism of a system simply by adjusting the configuration of the pumping laser for the artificial guide star.

Laser beacons, however, suffer from other problems. The major problem is a blindness to tip-tilt. As the pumping laser beam passes up through the atmosphere it encounters a certain amount of turbulence. The distortions to the shape of the beam profile are not of great concern since the purpose of the laser is simply to deliver energy to the sodium layer in the upper atmosphere. This energy is used to place the sodium atoms in an excited state so that when they return to the ground state they will emit radiation which will serve as a beacon. The beacon is effectively a point source (approximately 1 m in diameter at an altitude of 90 km) and any variations in the beam profile will not be seen from the ground. Beacon location, on the other hand, will be. The overall tip-tilt aberration induced on the beam during its passage upward to the sodium layer will change the location of the beacon on the stellar background. Since the transition from ground state to excited state and back to ground state is rapid (on the order of 16 ns Happer et al. [24]) the return beacon will see the same

overall tip-tilt aberrations as on the trip up, this time in reverse. The tip-tilt term of the return wave will thus cancel the turbulence induced displacement of the pumping beam.

5.2 What is anisoplanatism?

Except for the rare cases where the object and the reference are one and the same, light from the reference will not follow the same path to the wavefront sensor as does light from the object. Since the wavefront sensor can only measure the wavefront errors as seen by the reference, there will necessarily be errors when the system tries to observe the object after correcting for the turbulence traversed by light from the reference. These errors are called isoplanatic errors or anisoplanatism. There are a variety of reasons for the appearance of anisoplanatism, not all of which are present in every system configuration. The sections below discuss the origins of the more common classifications of anisoplanatism and the systems to which they apply, and in addition some solutions are presented.

5.2.1 Angular anisoplanatism

When using a natural guide star, the light from the reference will arrive at the entrance pupil of the telescope from a different angle than that from the object. This is referred to as angular anisoplanatism (figure 5.1). Angular anisoplanatism is the most common form of isoplanatic error and can be quantified by the expression, due to Fried [25],

$$\sigma_{iso}^2 = 2.905\,(2\pi)^2\,\frac{\int_0^L C_n^2\,(\theta\xi)^{5/3}\,d\xi}{\overline{\lambda}^2} \tag{5.19}$$

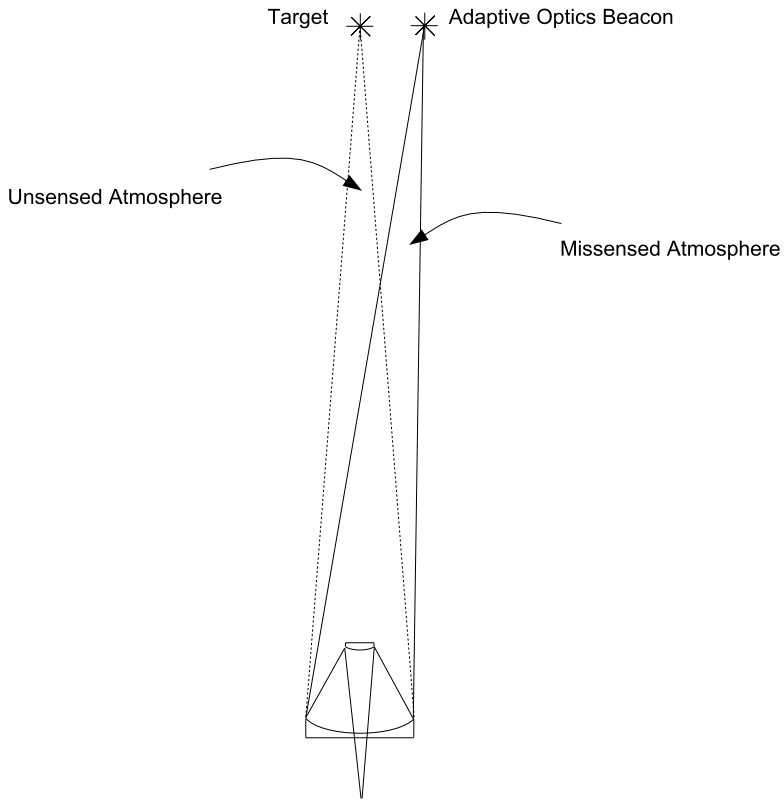

Figure 5.1: Angular anisoplanatism

where L is the total length of the propagation path and θ is the angular separation between the reference and the object. Fried also defined an *isoplanatic angle* θ_0 as

$$\theta_0 \triangleq \left(\frac{1}{2.905}\right)^{3/5} \left(\frac{1}{2\pi}\right)^{6/5} \left[\frac{\overline{\lambda}^2}{\int_0^L C_n^2\left(\xi\right)\xi^{5/3} d\xi}\right]^{3/5} \tag{5.20}$$

which is simply the separation angle at which the mean-square error due to anisoplanatism is 1 rad^2. With this definition equation (5.19) can be written

$$\sigma_{iso}^2 = \left(\frac{\theta}{\theta_0}\right)^{3/5} \quad . \tag{5.21}$$

It should be noted that the value for the squared isoplanatic error given in equation (5.19) assumes $D/r_0 \gg \theta/\theta_0$. While this may seem somewhat restrictive, the general case is very complicated and unwieldy. In compensation for the limited validity of equation (5.19) we can calculate, in most situations of interest (large D/r_0), the separation angle at which point isoplanatic error becomes significant. For smaller values of D/r_0 the true isoplanatic angle will be larger than that predicted by equation (5.20).

With the help of equation (3.3), the calculation of the isoplanatic angle can be simplified to

$$\theta_0 = \frac{r_{0sph}}{L\,(6.88)^{3/5}} = \frac{r_0}{3.181} \cdot \left[\frac{\int_0^L C_n^2\,(\xi)\,d\xi}{\int_0^L C_n^2\,(\xi)\,\xi^{5/3} d\xi} \right]^{3/5} \quad . \tag{5.22}$$

If we model the turbulence at a particular site as a thin layer at a certain altitude then the second term in equation (5.22) simplifies to

$$\left[\frac{\int_0^L C_n^2\,(\xi)\,d\xi}{\int_0^L C_n^2\,(\xi)\,\xi^{5/3} d\xi} \right]^{3/5} = \frac{(8/3)^{3/5}}{L} \tag{5.23}$$

and the expression for the isoplanatic angle becomes

$$\theta_0 = \left(\frac{8}{3 \cdot 6.88} \right)^{3/5} \frac{r_0}{L} = 0.566\,\frac{r_0}{L} \quad . \tag{5.24}$$

Suppose that at a site there is a single turbulent layer at a height of 6.5 km, and of the value of r_0 is 15 cm in the visible, then in this case $\theta_0 = 13.1$ μrad or about 2.7 arcseconds.

5.2.2 Displacement anisoplanatism

Another source of isoplanatic error occurs when the system to be corrected is not used to collect the light from the reference. In this case the wavefront sensor optics are laterally displaced relative to the imaging system but with an optic axis that is parallel to that of the main system. For this reason this type of error is referred to as displacement anisoplanatism (Tyson [5]). This configuration is fairly uncommon.

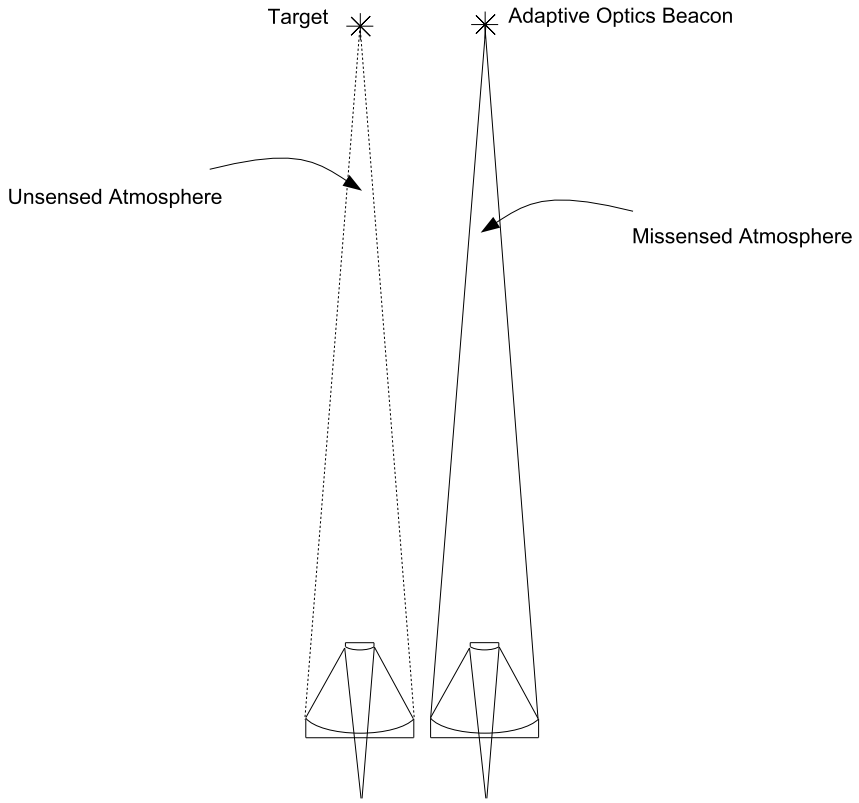

Figure 5.2: Displacement anisoplanatism

5.2.3 Focus anisoplanatism

Artificial guide stars also suffer from angular isoplanatism, but suffer additionally from other types of anisoplanatism. All artificial guide stars are physically close to the observer compared to celestial objects. The light from celestial objects is nearly a perfect plane wave before it arrives at the aberrating atmosphere. Artificial guide stars are usually not considered to be plane reference waves, but rather point sources originating somewhere in the atmosphere (laser guide stars) or just above it (artificial satellites). Since the reference does not have the same radius of curvature as the object, and therefore has a different conjugate plane, this kind of anisoplanatism is called focus anisoplanatism (figure 5.3).

5.2.4 Conjugation at the turbulent layer

One proposed solution for anisoplanatism is to place the wavefront corrector at the conjugate plane of the turbulent layer rather than at the exit pupil. The observation that this might help to enlarge the size of the isoplanatic patch comes from the limits inherent in the application of a linear system approximation to an optical train. Even in a well corrected optical system the optical point spread function will vary somewhat over the field of view. This effect (anisoplanatism) is increased if a filter is placed in the system at a plane other than a pupil or image plane. When the turbulence of the atmosphere is modeled as a thin phase screen at a given altitude, this phase screen (a phase filter) is neither at an image plane nor at a pupil plane. Correcting for the phase screen at the exit pupil will therefore not account for the anisoplanatism due to the location

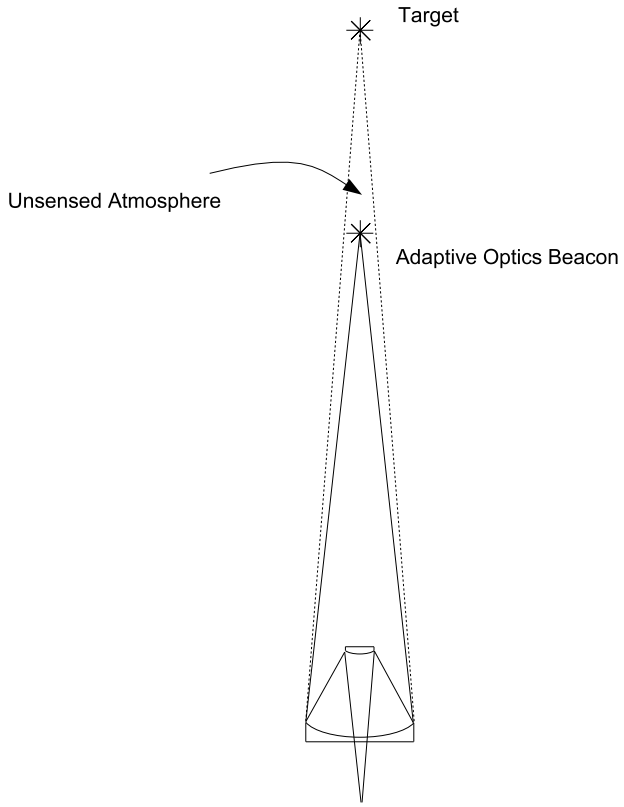

Figure 5.3: Focus anisoplanatism

of the screen in the system. If, on the other hand, the aberrations are conjugated in an image plane of the phase screen then the turbulence will not be seen by the rest of the system and its location is irrelevant. This analysis assumes that the atmospheric disturbances are indeed localized at one thin layer and since this is not the case, the effectiveness of conjugating at the turbulent layer is not perfect.

5.2.5 Multiconjugate adaptive optics

An extension of the concept of conjugation at one single turbulent layer is called multiconjugate adaptive optics. As the name implies, the system uses several wavefront correctors to conjugate the aberrations. The idea is to assign a layer of the atmosphere to a specific wavefront corrector and to place this wavefront corrector at the conjugate point of the corresponding layer of the atmosphere .If there are enough layers then each one can be modeled as a thin phase screen. As long as the support of the wavefront correctors at each turbulent layer includes the object, the effect of angular anisoplanatism can be reduced. Normally, for a thick atmosphere, a tradeoff would need to be made between the number of wavefront correctors and losses due to the extra optical components along the optical path. If, however, the atmospheric effects at a particular site can be well modeled by just a few distinct layers of turbulence, then there is a potential for significant improvement in performance with only a few wavefront correctors [12]. Naturally there will need to be a wavefront sensing system for each layer to be corrected.

PART II

FOCAL PLANE FILTERS AND ADAPTIVE OPTICS

Chapter 6

THEORY OF FOCAL PLANE FILTERS

Focal plane filters are a class of adaptive optics wavefront sensors that generalize several techniques that have seen wide use in the testing of optical elements. The method is fundamentally simple: given an optical system that forms an image of a transparent object, if a properly designed complex valued filter is placed at the aperture stop it is possible to transform variations in phase at the object into variations in irradiance at the image. The challenge is in designing the plate to best make use of the characteristics of the system or object at hand. When applying the method to adaptive optics systems, the turbulence is identified with the transparent object. A plane which forms an image of the reference object, whether a natural or artificial guide star, becomes a Fourier plane for the atmospheric turbulence. This plane then becomes a natural candidate for the aperture stop of the wavefront sensor's optical system. Once the location of the plate is known the next step is the design of the form of the plate. Three special cases of focal plane filters have seen wide use as wavefront sensors in optical testing: the Smartt point diffraction interferometer, phase contrast imagery, and dark ground imagery.

The plate used in a Smartt point diffraction interferometer has a low transmission over most of its surface, but at its center there is a small region which has a much higher transmission. The image of the reference object is placed over this high transmission zone and this creates a spherical reference wave which interferes with the rest of the wavefront in the image of the turbulence.

Since this method blocks most of the light that passes through the plate, it is only useful for high power applications.

In phase contrast imagery, a transparent plate is used and thus is very frugal in terms of power from the reference. The plate is entirely transparent, but in a small region its thickness is either slightly less or slightly more than the rest of the plate. The plate is placed such that the image of the reference object passes through this region. This method is used in biology in the construction of microscopes that can observe transparent cells. It is also sometimes called the Zernike method of observation.

The third method, dark ground imagery, is less widely used. It is essentially the opposite of the point diffraction interferometer. The plate is entirely transparent except for a small opaque region, and the image of the reference is focused on this zone. We will see below that this method has potential as a wavefront sensor in adaptive optics.

6.1 What are focal plane filters?

Most discussions of focal plane filters present them as two beam interferometers. The treatment in Born and Wolf [26, sec. 8.6c] of phase contrast microscopy follows Abbe's view of image formation. They begin by looking at the special case of a periodic phase grating and then the formulation is generalized to include non-periodic objects. In this treatment, the filter core acts to either block or retard the central diffraction order of the object. This central diffraction order is light that has not been affected by passage through the phase object, or in terms more familiar to adaptive optics, it is light that has not been aberrated by atmospheric turbulence. For the case of phase contrast microscopy,

this light is allowed to pass through a retarding plate. The retarding plate is chosen so that the central order is delayed by one quarter wavelength relative to the higher orders. Now the unaberrated light is in phase quadrature with the aberrated light and creates an interference pattern when an image of the phase object is formed. This interference pattern in the image plane of the phase object is directly related to the amount of aberration caused by the corresponding point on the phase object. The articles by Golden [27] and Ojeda-Castañeda [28] treat phase contrast observations as interferometers, but start from the point of view of Fourier optics. This viewpoint has the advantage of making it clear from the beginning that the results are not confined to the case of small aberrations in the phase object.

The derivation below will in general follow Golden's treatment, but without placing too much emphasis on the point of view that the process is an interferometric one. When looking at phase contrast imagery, it is convenient to regard the process as an interferometric one, however, when dealing with dark ground imagery this can cause problems. Dark ground imagery does not have an identifiable reference wave, even though it can be viewed as a special case of the Zernike method. The most general way of considering focal plane filters is as complex valued filters in the frequency plane of the phase object.

In what follows we refer to Fig. 6.1 for our terminology. For the moment we assume that the turbulence is represented as a phase screen at the pupil of the telescope as this simplifies the presentation of the mathematics. The adaptive optics reference is assumed to be at infinity, and thus the image plane of the telescope is at the back focal plane. This is where the filter is placed. A

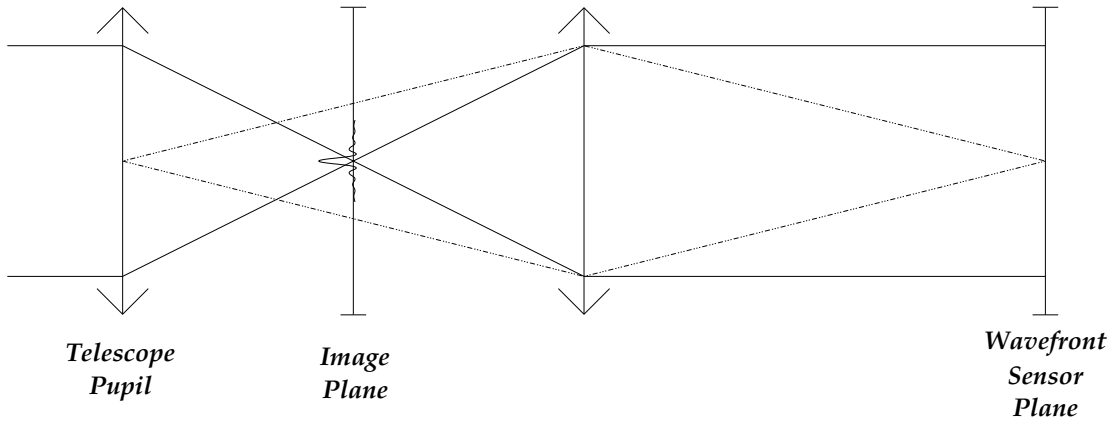

Figure 6.1: General layout for focal plane filters

secondary lens is used to re-image the turbulent layer (in this case the pupil of the telescope) onto a detector in the wavefront sensor plane.

The turbulent wavefront at the pupil of the telescope can be expressed as

$$T(x,y) = P(x,y) \cdot \exp[j\phi(x,y)] \tag{6.1}$$

where $P(x,y)$ is the field in the pupil plane in the absence of turbulence and $\phi(x,y)$ is the phase error in the pupil plane due to turbulence. Included in the term $P(x,y)$ is the pupil shape and the field irradiance. For example, if the reference source is an on-axis point source located at infinity, then the input field is a plane wave with constant incident irradiance. If we further suppose that the telescope pupil is annular with an external diameter D and a central obscuration with a diameter ϵD, then $P(x,y)$ is given by

$$P(x,y) = P_0 \left[\mathrm{cyl}\left(\frac{r}{D}\right) - \mathrm{cyl}\left(\frac{r}{\epsilon D}\right) \right] \quad . \tag{6.2}$$

In Eq. (6.2) we have followed the notation found in Gaskill [29] for representing the telescope pupil. The constant factor P_0 is the field amplitude incident on the telescope pupil.

For the sake of simplicity, we will assume that the reference is a point source aligned with the axis of the telescope. This is not a requirement for the sensor to function, but it will avoid some additional complications in the mathematics.

In the focal plane of the telescope, and before passing through the filter, the optical field is obtained from the two-dimensional Fourier transform of the field at the pupil multiplied by a complex constant:

$$K_1 \, \mathcal{FF}\left\{T(x,y)\right\} = K_1 \tilde{T}\left(\frac{x}{\lambda f}, \frac{y}{\lambda f}\right) \quad . \tag{6.3}$$

The constant K_1 comes from the mathematics of diffraction and in this case $K_1 = 1/j\lambda f \cdot \exp[j2\pi^2 r^2/\lambda]$, where f is the focal length of the telescope.

At the image plane we place a filter. This filter has a support with a real transmission coefficient α_s and a central filter core with a real transmission coefficient α_c and a real relative phase lag of δ (see Fig. 6.2). The filter core must be located over the image of the reference source. In our case this is the center of the field of view, but if the reference is located elsewhere in the field, the filter core must be placed at the corresponding location in the image plane. If the diameter of the filter core is given as d_c and the support diameter as d_s, the filter is given by

$$H(x,y) = \alpha_s \left[\mathrm{cyl}\left(\frac{r}{d_s}\right) - \mathrm{cyl}\left(\frac{r}{d_c}\right)\right] + \alpha_c e^{j\delta} \mathrm{cyl}\left(\frac{r}{d_c}\right) \quad . \tag{6.4}$$

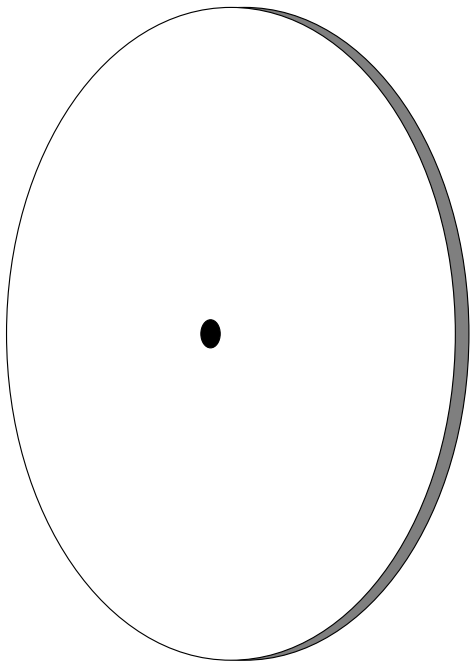

Figure 6.2: The focal plane filter

This is a very general expression for the focal plane filter and includes several special cases: phase contrast imagery ($\alpha_s = \alpha_c$, $\delta = \pm\pi/2$); the Smartt point diffraction interferometer ($\alpha_s \ll \alpha_c$, $\delta = 0$); and dark ground imagery ($\alpha_c = 0$). The diameter of the filter core should be about the size of the Airy disk formed by the telescope and the diameter of the filter support should cause the filter to be the aperture stop for the wavefront sensor system. If the filter support is not the aperture stop of the wavefront sensing system then there will be an extra quadratic factor in the phase at the wavefront sensor plane, and this will cause additional anisoplanatism in the wavefront sensing system (see for example Gaskill [29, p. 451]). Passage through the filter simply multiplies the field before

the filter by H, producing

$$K_1 H(x,y) \cdot \tilde{T}\left(\frac{x}{\lambda f}, \frac{y}{\lambda f}\right) \tag{6.5}$$

as the representation of the field after the filter.

After traversing the filter the field passes through a lens which is placed so as to form an image of the turbulence on a detector. The field at the detector (the wavefront sensor plane) is then the Fourier transform of the field at the image plane multiplied by a complex constant:

$$u(x,y) = K_2\, \mathcal{FF}\left\{H(x,y) \cdot \tilde{T}\left(\frac{x}{\lambda f}, \frac{y}{\lambda f}\right)\right\} \quad . \tag{6.6}$$

After some manipulation, Eq. 6.6 yields

$$u(x,y) = K_2 \cdot \frac{1}{m} T\left(\frac{x}{m}, \frac{y}{m}\right) ** \frac{1}{p^2} \tilde{H}\left(\frac{x}{p}, \frac{y}{p}\right) \tag{6.7}$$

where $p = \lambda z'/m'$. The value of z' is the distance from the image of the focal plane filter as seen from the wavefront sensor to the wavefront sensor detector, and m' is the lateral magnification of this image. The factor m is the magnification of the image of the pupil at the detector. In these equations K_2 is a constant that accounts for losses in the optical system. By expanding and rearranging the terms above, we arrive at the expression

$$u(x,y) = \alpha_s a_s S(x,y) e^{j\sigma(x,y)} + \left[\alpha_c a_c e^{j\delta} - \alpha_s a_c\right] M(x,y) e^{j\mu(x,y)} \tag{6.8}$$

for the optical field, where

$$S(x,y)e^{j\sigma(x,y)} = \left[T\left(\frac{x}{m},\frac{y}{m}\right) ** \text{ somb}\left(\frac{r}{p/d_s}\right)\right] \quad , \tag{6.9}$$

$$M(x,y)e^{j\mu(x,y)} = \left[T\left(\frac{x}{m},\frac{y}{m}\right) ** \text{ somb}\left(\frac{r}{p/d_c}\right)\right] \quad , \tag{6.10}$$

$$a_s = d_s^2 \frac{K_2\pi}{4mp^2} \quad , \tag{6.11}$$

and

$$a_c = d_c^2 \frac{K_2\pi}{4mp^2} \tag{6.12}$$

Equation (6.9) represents an optical field whose effects are governed by the filter support. Its square modulus, $S^2(x,y)$, is in essence the image of the telescope pupil that would be obtained if the filter were replaced by a clear aperture of the same diameter as the filter support. Equation (6.10) is the field due to the filter core, and acts as the reference wave for an interferometer.

With this expression for the field, it is a simple matter to calculate the irradiance incident upon the detector:

$$I(x,y) = |u(x,y)|^2 \tag{6.13}$$

$$\begin{aligned} I(x,y) = \alpha_s^2 a_s^2 S^2(x,y) + & \left[\alpha_s^2 a_c^2 + \alpha_c^2 a_c^2 - 2\alpha_s\alpha_c a_c^2 \cos(\delta)\right] M^2(x,y) \\ & + [2\alpha_s\alpha_c a_c a_s \cos(\sigma(x,y) - \mu(x,y) - \delta) \\ & - 2\alpha_s^2 a_c^2 \cos(\sigma(x,y) - \mu(x,y))\Big] \cdot S(x,y)M(x,y) \quad . \end{aligned} \tag{6.14}$$

The full form of Eq. (6.14) is necessary to account for all the effects of diffraction, but by making a few observations, it is possible to perform a reasonable simplification to this expression. In the paragraphs above it was noted that the diameter of the filter core d_c should be about the size of the diameter of the Airy disk of the telescope. This would cause $\mathrm{somb}(\frac{r}{p/d_c})$ in Eq. (6.10) to be very wide and as a result $\mu(x,y)$ would be very nearly a constant value equal to the average phase across the telescope pupil, i.e. zero. Additionally, the support of the filter is the aperture stop for the wavefront sensor system. As a result, $\mathrm{somb}(\frac{r}{p/d_s})$ is very narrow and $\sigma(x,y)$ is approximately equal to the phase aberration in the telescope pupil plane. The light due to the reference wave should have a uniform phase of very nearly zero since the light passing through the filter core was not diffracted by the turbulence. Thus, if the diameter of the filter support, d_s, is large enough and the diameter of the filter core, d_c, is small enough, then

$$\sigma(x,y) - \mu(x,y) \approx \phi(x/m, y/m) \quad . \tag{6.15}$$

This yields

$$\begin{aligned} I(x,y) = \alpha_s^2 a_s^2 S^2(x',y') + & \left[\alpha_s^2 a_c^2 + \alpha_c^2 a_c^2 - 2\alpha_s\alpha_c a_c^2 \cos(\delta)\right] M^2(x',y') \\ & + \left[2\alpha_s\alpha_c a_c a_s \cos(\phi(x',y') - \delta)\right. \\ & \left. -2\alpha_s^2 a_c^2 \cos(\phi(x',y'))\right] \cdot S(x',y') M(x',y') \end{aligned} \tag{6.16}$$

for the irradiance at the detector, where $x' = x/m$ and $y' = y/m$. For heuristic purposes, it is useful to neglect some of the effects of diffraction. When doing so, it is assumed that the filter core diameter is made infinitesimally small and

yet all of the light undiffracted by the turbulence passes through the filter core. The resulting expression for the irradiance at the wavefront sensor detector is

$$\begin{aligned} I(x',y') = \Big[&2\alpha_s^2 + \alpha_c^2 - 2\alpha_s\alpha_c\cos(\delta) + 2\alpha_s\alpha_c\cos(\phi(x',y') - \delta) \\ &-2\alpha_s^2\cos(\phi(x',y'))\Big] \cdot c^2P^2(x',y') \end{aligned} \tag{6.17}$$

where $P(x',y')$ is again the telescope pupil function from Eq. (6.1) and c is a constant to ensure conservation of energy. Equation (6.17) is essentially that given by Born and Wolf [26] as their Eq. (8.72).

We now simplify our results for two special cases of focal plane filters. When creating a phase contrast wavefront sensor, the two amplitude transmission coefficients of the filter α_s and α_c are equal and δ is equal to $\pi/2$ or $-\pi/2$. For the case where $\delta = \pi/2$ Eq. (6.16) reduces to

$$\begin{aligned} I(x',y') =& \alpha^2a_s^2S^2(x',y') + 2\alpha^2a_c^2M^2(x',y') \\ &+ \Big[2\alpha^2a_ca_s\sin(\phi(x',y')) \\ &-2\alpha^2a_c^2\cos(\phi(x',y'))\Big] \cdot S(x',y')M(x',y') \end{aligned} \tag{6.18}$$

and Eq. (6.17) to

$$I(x',y') = \Big[3\alpha^2 + 2\alpha^2\sin(\phi(x',y')) - 2\alpha^2\cos(\phi(x',y'))\Big]\, c^2P^2(x',y') \tag{6.19}$$

where $\alpha = \alpha_s = \alpha_c$. When $\delta = -\pi/2$ we have

$$\begin{aligned} I(x',y') = \alpha^2 a_s^2 S^2(x',y') + 2\alpha^2 a_c^2 M^2(x',y') \\ + \Big[-2\alpha^2 a_c a_s \sin(\phi(x',y')) \\ - 2\alpha^2 a_c^2 \cos(\phi(x',y'))\Big] S(x',y') M(x',y') \end{aligned} \tag{6.20}$$

and Eq. (6.17) becomes

$$I(x',y') = \Big[3\alpha^2 - 2\alpha^2 \sin(\phi(x',y')) - 2\alpha^2 \cos(\phi(x',y'))\Big] c^2 P^2(x',y') \quad . \tag{6.21}$$

The first case is called bright phase contrast and the second dark phase contrast.

For a dark ground wavefront sensor, the amplitude transmission for the filter core, α_c, is set to zero. This results in

$$\begin{aligned} I(x',y') = \alpha_s^2 a_s^2 S^2(x',y') + \alpha_s^2 a_c^2 M^2(x',y') \\ -2\alpha_s^2 a_c^2 \cos(\phi(x',y')) S(x',y') M(x',y') \end{aligned} \tag{6.22}$$

for the more general case and

$$I(x',y') = \big[1 - \cos(\phi(x',y'))\big] 2\alpha_s^2 c^2 P^2(x',y') \tag{6.23}$$

for the simplified case.

6.2 Recovery of the phase

In all of the special cases above, the irradiance in the WFS plane is expressed as a trigonometric function of the phase in the pupil plane multiplied by a scaled pupil image. The form of the trigonometric function depends on the values of the transmission and relative phase delay of the filter support and core.

In order to extract a meaningful expression of the phase in the pupil plane, we will be manipulating several expressions of the irradiance in the WFS plane. We will now introduce a convenient shorthand for equation (6.17):

$$\begin{aligned} I_{\alpha_s;\alpha_c;\delta}(x',y') = \Big[&2\alpha_s^2 + \alpha_c^2 - 2\alpha_s\alpha_c\cos(\delta) + 2\alpha_s\alpha_c\cos(\phi(x',y') - \delta) \\ &-2\alpha_s^2\cos(\phi(x',y'))\Big] \cdot c^2P^2(x',y') \quad . \end{aligned} \tag{6.24}$$

The shorthands for equation (6.19), equation (6.21) and equation (6.23) are then $I_{\alpha;\alpha;\frac{\pi}{2}}(x',y')$, $I_{\alpha;\alpha;\frac{3\pi}{2}}(x',y')$ and $I_{\alpha;0;-}(x',y')$ respectively.

The case of a null filter causes the WFS camera to image the scintillation directly. Using the new notation:

$$I_{\alpha;\alpha;0}(x',y') = \left[\alpha^2\right] c^2P^2(x',y') \quad . \tag{6.25}$$

6.2.1 Zernike Visibility

To illustrate the use of this notation, we now present a derivation of the Zernike visibility of a phase object.

$$
\begin{aligned}
V &= \frac{I_{\alpha;\alpha;\frac{\pi}{2}}(x',y') - I_{\alpha;\alpha;\frac{3\pi}{2}}(x',y')}{I_{\alpha;\alpha;\frac{\pi}{2}}(x',y') + I_{\alpha;\alpha;\frac{3\pi}{2}}(x',y')} \\
&= \frac{\left[3\alpha^2 + 2\alpha^2 S - 2\alpha^2 C\right] c^2 P^2\left(x',y'\right) - \left[3\alpha^2 - 2\alpha^2 S - 2\alpha^2 C\right] c^2 P^2\left(x',y'\right)}{\left[3\alpha^2 + 2\alpha^2 S - 2\alpha^2 C\right] c^2 P^2\left(x',y'\right) + \left[3\alpha^2 - 2\alpha^2 S - 2\alpha^2 C\right] c^2 P^2\left(x',y'\right)} \quad ,
\end{aligned}
$$

where $S = \sin(\phi(x',y'))$ and $C = \cos(\phi(x',y'))$.

$$
V = \frac{\left[4\alpha^2 S\right] c^2 P^2\left(x',y'\right)}{\left[6\alpha^2 - 4\alpha^2 C\right] c^2 P^2\left(x',y'\right)} = \frac{2\sin(\phi(x',y'))}{3 - 2\cos(\phi(x',y'))} \tag{6.26}
$$

This Zernike visibility is independent of intensity fluctuations in the pupil (scintillation). Though it is not easily invertible, it is, however, a well behaved function as shown in figure 6.3 Taking advantage of the expression for Zernike visibility requires two images from the WFS camera. Using two WFS cameras in parallel (spatial configuration) requires twice as much light as a single WFS exposure. The alternative, changing the relative phase lag between the core and filter with alternating WFS frames (temporal configuration), does not require more light to calculate a phase field, but it does introduce some temporal anisoplanatism.

Although the expression for Zernike visibility is well behaved, there is an ambiguity in the recovery of the phase. Looking a the region of plot shown in figure 6.3 ranging from about one radian to about five and a quarter (i.e. minus one) radians it is observed that this covers the majority of the domain of the

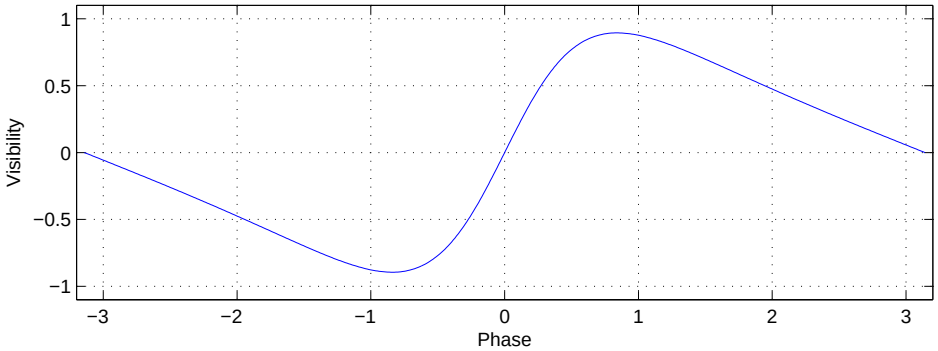

Figure 6.3: Zernike visibility

problem and is the most linear. If it is assumed that the phase to be recovered by the visibility calculation lies within this region then direct application of the visibility as feedback will drive the system to a piston value of π. Piston error is not an issue, but there will be some error when the true phase values from minus one to one. When the phase lies in this region then the feedback applied will cause the phase at that location to be miscorrected. The phase measured at the next frame will, however fall in the linear region of feedback. The simulations in chapter 6 are an examination of this form of direct feedback and the errors in the resulting correction.

6.2.2 Three Bin

When an application is not as light starved, a third WFS exposure (in either a temporal or spatial configuration) can be used to calculate the tangent of the phase:

$$\frac{I_{\alpha;\alpha;\frac{\pi}{2}}(x',y') - I_{\alpha;\alpha;\frac{3\pi}{2}}(x',y')}{6 \cdot I_{\alpha;\alpha;0}(x',y') - I_{\alpha;\alpha;\frac{\pi}{2}}(x',y') - I_{\alpha;\alpha;\frac{3\pi}{2}}(x',y')} = \frac{\sin(\phi(x',y'))}{\cos(\phi(x',y'))} \quad . \tag{6.27}$$

This expression can be used to calculate the phase directly using the arctangent routines available in any programming language.

6.3 Examples

This section will present examples of what the detector plane of a Focal Plane Filter (FPF) WFS can look like. First, we look at the first six Zernike modes. These modes will then form the phase field input to a FPF WFS. Ta-

i	n	m	Polynomial	Name
1	0	0	1	Piston
2	1	1	$2r\cos(\theta)$	Tip-Tilt
3	1	1	$2r\sin(\theta)$	
4	2	0	$2\sqrt{3}r^2 - \sqrt{3}$	Focus
5	2	2	$\sqrt{3}\sqrt{2}r^2\sin(2\theta)$	Astigmatism
6	2	2	$\sqrt{3}\sqrt{2}r^2\cos(2\theta)$	

Table 6.1: The first six Zernike polynomials

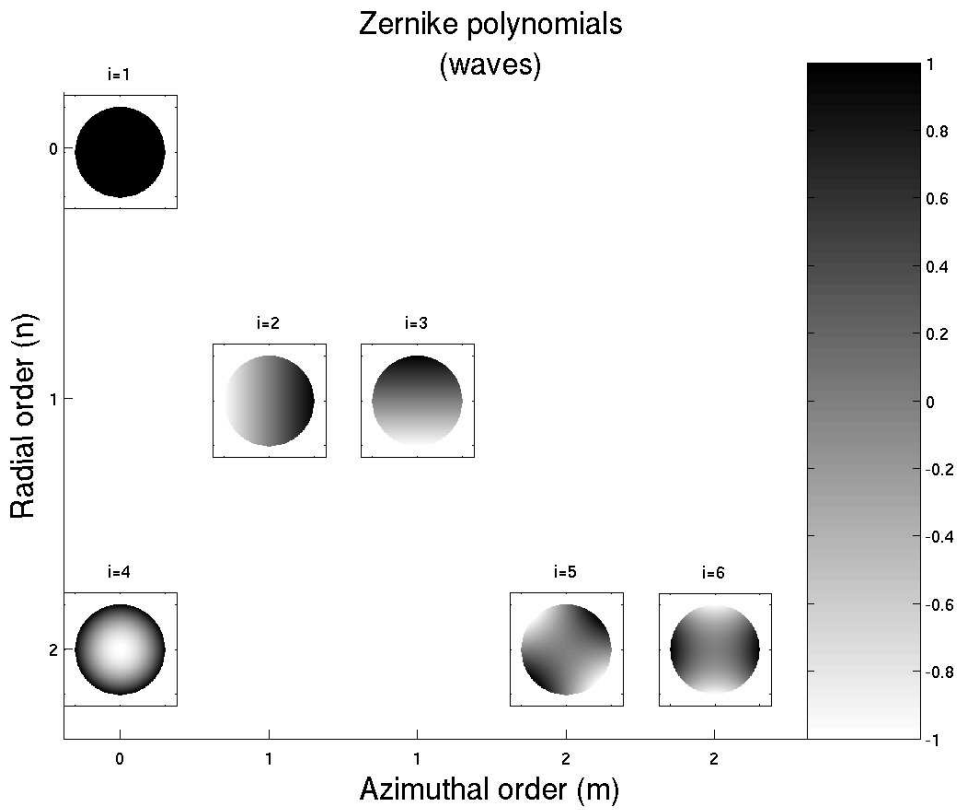

Figure 6.4: The first six Zernike polynomials

ble 6.1 shows the expressions for these first six modes using the normalization given by Noll [20] [see also 4, sec. 3.6.1] and figure 6.4.

Now let's modulate the phase of a plane wave impingent upon an imaging system. The plane wave is modulated at the entrance pupil and an ideal FPF WFS senses the wavefront at the pupil. In other words, we will directly evaluate equation (6.24) using the Zernike polynomials as the true phase values.

First, use of the null filter $I_{\alpha;\alpha;0}(x', y')$ (equation (6.25)) yields the normalized irradiances shown in figure 6.5. Notice that there are no intensity variations.

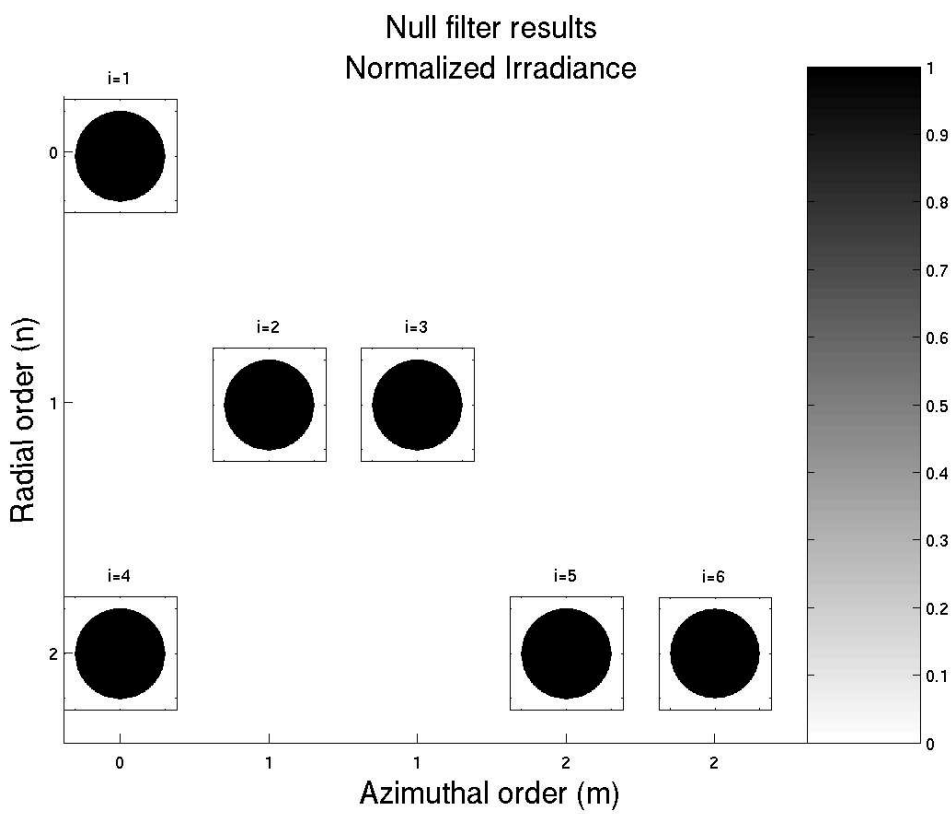

Figure 6.5: Application of the null filter

This is an illustration that there is no scintillation when the aberrations are in a wavefront sensor plane. Second, use of the phase contrast filter $I_{\alpha;\alpha;\pi/2}(x', y')$ (equation (6.21)) yields the normalized irradiances shown in figure 6.6. The

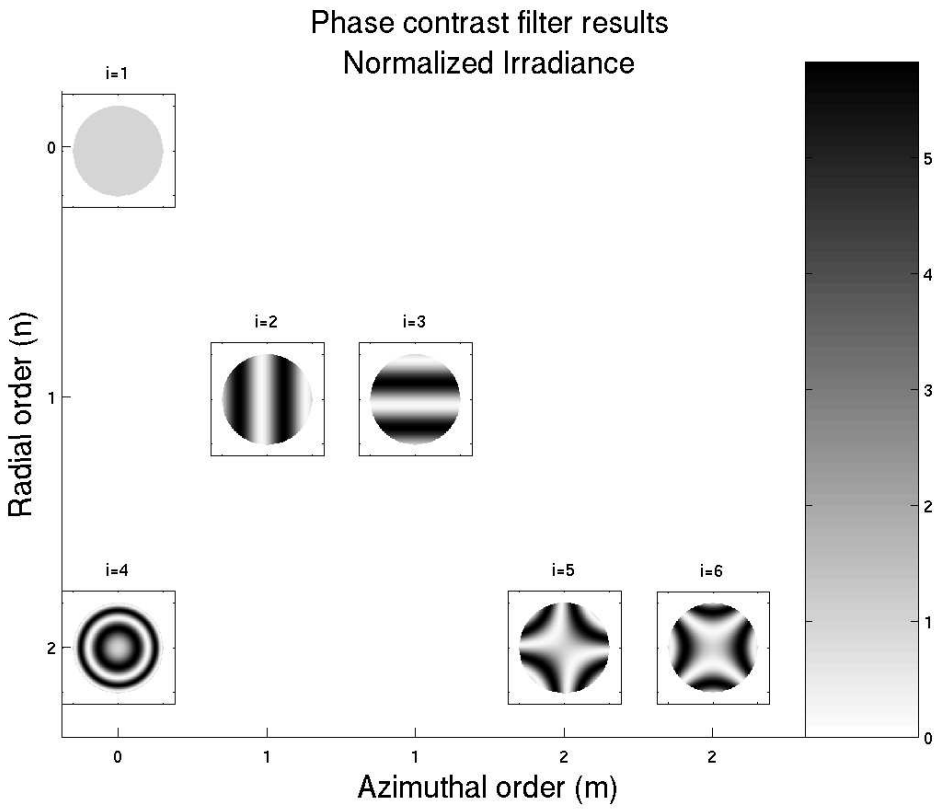

Figure 6.6: Application of the phase contrast filter

energy is constant in all of the WFS images. Lastly, calculation of the Zernike contrast (equation (6.26)) yields the phase maps shown in figure 6.7.

6.4 Wavefront calculation

Now that we have recovered the phase of the wavefront, it needs to be converted into something that can be used by the wavefront corrector. The method used is somewhat dependent on the type of wavefront corrector used. We will discuss two methods. The first, phase unwrapping, is more useful for piston type correctors and the second, pseudo Shack-Hartmann, is a natural interface to existing systems that currently use a Shack-Hartmann WFS.

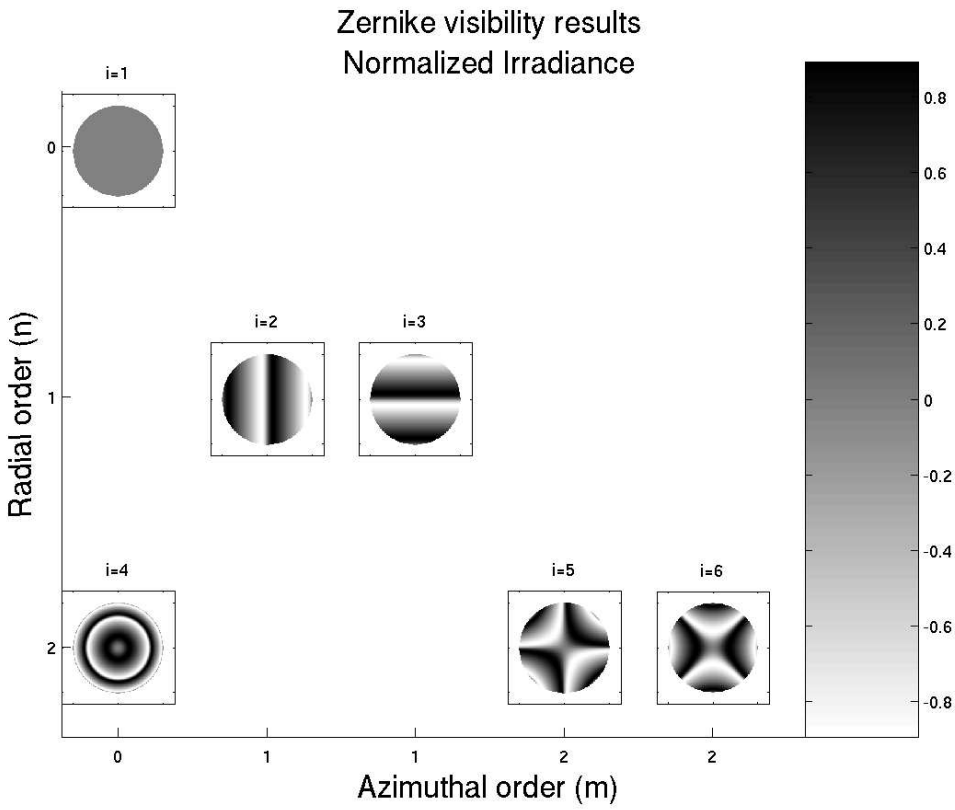

Figure 6.7: Zernike visibility of Zernike polynomials

6.4.1 Phase unwrapping

The subject of phase unwrapping is a very complex topic. It is widely used in radar remote sensing in order to accurately interpret the data from Synthetic Aperture Radar (SAR) and calculate terrain maps. There is a wide body of literature on the subject in the remote sensing journals and conferences. A very good book length survey of various algorithms has been written by Ghiglia and Pritt [30].

Fundamentally, phase unwrapping is the process of taking a field of phase data modulo 2π and estimating the field of phase data without the 2π wrap-

ping caused by the modulo operation. There are two basic stumbling blocks in unwrapping the phase in a two-dimensional optical field. The first is that there may be true discontinuities in the phase. These discontinuities introduce more ambiguities in the unwrapping problem. In adaptive optics, this problem is usually not encountered. It occurs more often in the reduction of SAR data. The second obstacle is the appearance of phase residues.

When unwrapping a grid of phase values, if the order or direction in which one passes through the grid affects the final result then the field cannot be unambiguously unwrapped. The cause of this ambiguity is the existence of points called *phase residues*. These phase residues are points in the phase field around which a path integral is an integer multiple of 2π. These phase residues often occur when the integrated irradiance of the optical field is zero. This happens in the presence of strong scintillation.

Because of the residues in a phase field in the condition of strong scintillation, the phase unwrapping algorithm must make some assumptions about the original field. Those algorithms that work better when handling discontinuities in the original phase field (e.g. a cliff or overhang in SAR data) do not necessarily work well for adaptive optics. There are a class of algorithms that use so called 'quality maps' which take into account the fact that there are some regions of a phase field in which one has more confidence in the accuracy of the measurements. A WFS exposure in which the null filter ($I_{\alpha;\alpha;0}(x', y') = \left[\alpha^2\right] c^2 P^2(x', y')$)) is used, gives a good measure of this confidence.

6.4.2 Pseudo Shack-Hartmann

In developing the simulations of deploying a FPF based WFS at North Oscura Peak (NOP) (chapter 8.1.3), it was necessary to process the output of the FPF WFS into commands for the continuous facesheet Deformable Mirror (DM). Since a model of the DM that took slopes as input and produced actuator commands as output had already been developed and validated against many experiments, it seemed prudent to produce tilts from the FPF WFS output. The original plan was to unwrap the phase as discussed above and to numerically calculate the tilts that corresponded to the inputs of the DM model.

After trying various unwrapping algorithms with limited success, it was observed that the tilt computations were failing when the unwrapping algorithm was not completely successful. Upon reflection it was noticed that the FFT of a complex field is the same whether the phase was unwrapped or not. Thus, if the output of a FPF WFS were passed to 'numeric' Shack-Hartman, the problem of unwrapping the phase field could be avoided. In a real system this could be accomplished by passing the phase field to a Digital Signal Processing (DSP) based dedicated computer. This computer would compute the FFT of a complex field based on these input phase values. The result of the FFT would then pass to the same centroiding algorithms that are in use in existing Shack-Hartmann based AO systems.

At NOP there are two cameras that have been used as the WFS camera in its Shack-Hartmann WFS. One camera has much better noise performance, but was acquired after the rest of the system had been deployed. It was determined that it would be simpler and not a performance hit to place a box that converted

the output of the low noise camera into something that looked like it came from the original camera. A similar procedure could be used for the output of a FPF WFS. The output of this pseudo Shack-Hartman (or 'numeric' Shack-Hartman) WFS would have a very high signal to noise ratio from the point of view of the centroiding algorithms.

In the simulations developed in chapter 8.1.3, the output of the FPF WFS was used to modulate a plane wave source and this source was then used as input to the standard Shack-Hartmann model for NOP, but with the noise turned off. The resulting simulations were more stable than the simulations which relied on phase unwrapping as part of the calculations of the DM commands.

Chapter 7

COMPUTER SIMULATIONS: MATLAB

As a proof of concept, some simple MATLAB simulations were created. Many simplifications were necessary in order to develop the algorithms that could then be implemented as WAVETRAIN systems (see chapter 8) or in a table top experiment (see chapter 9). Since the purpose of this dissertation was not to develop a simulation framework or algorithms for the many other AO components besides the WFS, the simulation of these other components suffered the most at this stage of simulation. A flowchart illustrating the methodology used in the simulation is shown in figure 7.1. The three main goals of these sim-

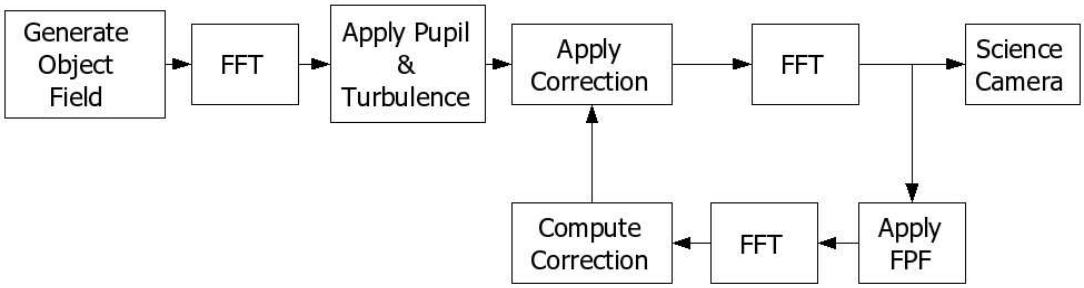

Figure 7.1: Matlab simulation flowchart

ulation were to develop the fundamental algorithms necessary for using FPF WFSs in an adaptive optics system; to learn some of the basic charastics of this class of WFSs; to find a acsnr threshold for a stable closed loop system.

7.1 Turbulence

A single phase screen was used for the simulation of the turbulence. Since it was modeled as at the pupil, there was no scintillation. This single phase screen was generated with Kolmorogorov statistics and scaled so that its strength was such that D/r_0 was 12. To simulate wind, the screen was translated across the pupil at a rate of two pupil diameters per second.

7.2 Corrector

The model for the corrector was that of a segmented piston corrector. It was laid out on a rectangular geometry and the total stroke was 2π. This simple model is adequate for simulating a LCD used as a wavefront corrector.

7.3 Tip-Tilt

No upstream tip-tilt correction was included in the model. All of the tilt was corrected using the AO system

7.4 Detectors

The wavelength use for the simulations was 1.5 μm. Photon noise was simulated, but no detector noise.

7.5 Wave Front Sensor Filter

The desired location of the phase filter core was determined by first computing a long exposure image of the reference and then selecting the location of the peak value as the location of the filter core.

A dynamic focal plane filter was used in the simulations. The relative phase of the filter core was alternated between $\pi/2$ and $-\pi/2$ for each frame and the Zernike visibility calculation (see equation (6.26) in section 6.2.1) was then carried out for each frame:

$$V = \frac{\left[4\alpha^2 S\right] c^2 P^2\left(x', y'\right)}{\left[6\alpha^2 - 4\alpha^2 C\right] c^2 P^2\left(x', y'\right)} = \frac{2\sin(\phi(x', y'))}{3 - 2\cos(\phi(x', y'))} \tag{7.1}$$

This allows for a calculation of the phase error that is independent of possible spatial fluctuations in the irradiance at the detector plane. The result of this visibility calculation was then used as a direct feedback to the wavefront corrector.

7.6 Simulations

The simulations were carried out at four photon flux rates: 145, 7, 4.5 and 3 photons per wavefront sensor pixel per frame. All of the simulations used the same phase screen and the phase screen was started at the same location. The screen was translated across the pupil at the same rate and in the same direction

The respective plots of the Strehl ratio as a function of time are given in Figures (7.2-7.5). The dip in level of correction near the one second mark is likely due to the existence of a particularly strong tip-tilt component during that segment of the phase screen.

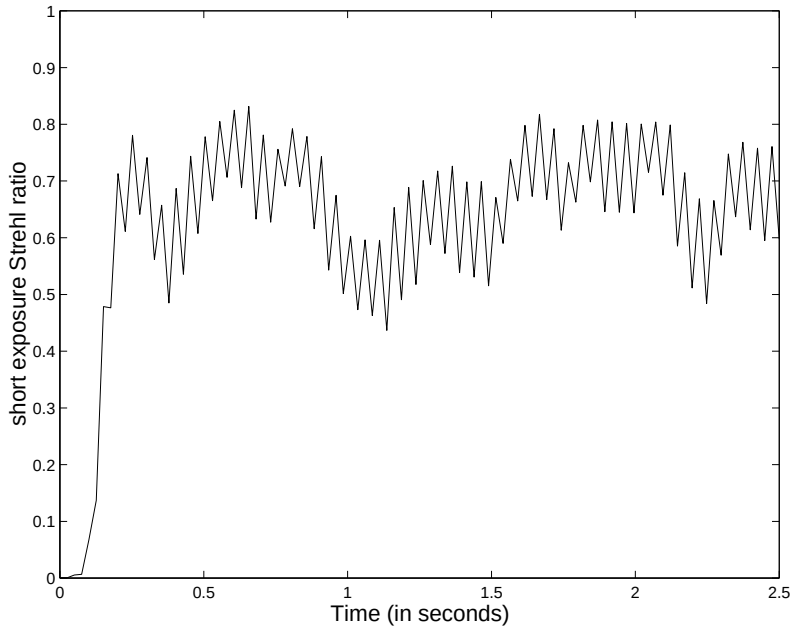

Figure 7.2: 145 photons per pixel per frame

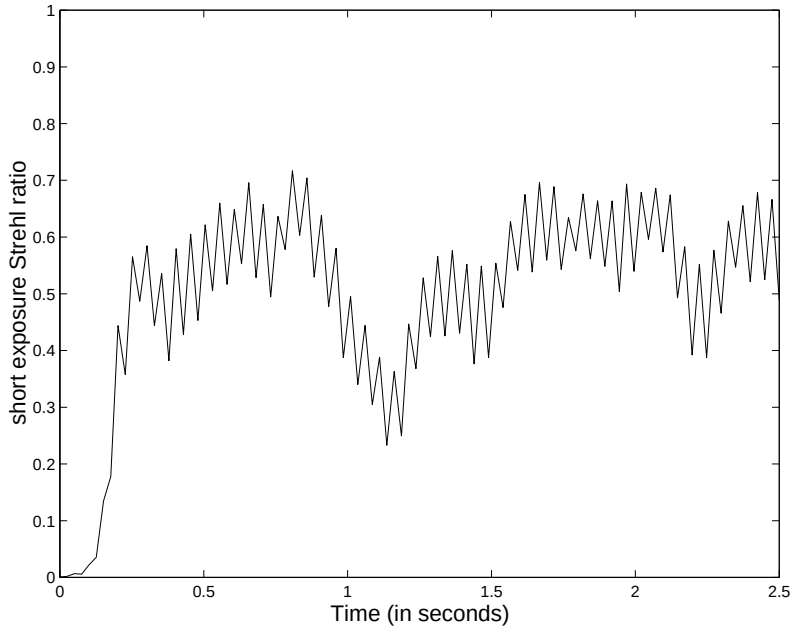

Figure 7.3: 7 photons per pixel per frame

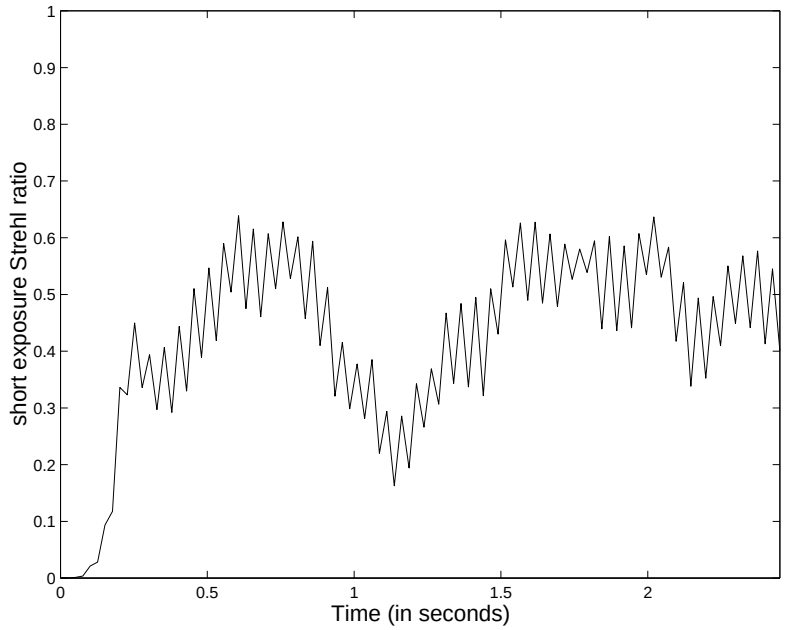

Figure 7.4: 4.5 photons per pixel per frame

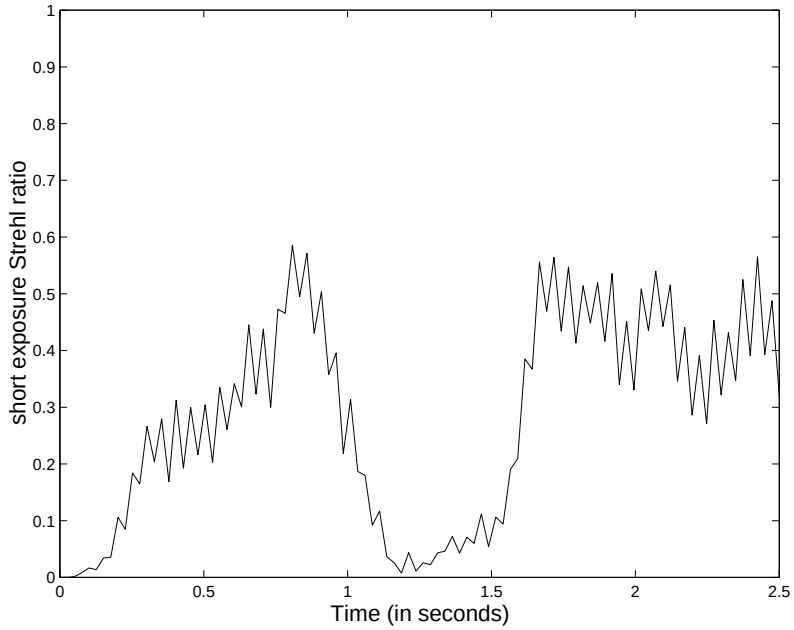

Figure 7.5: 3 photons per pixel per frame

7.7 Conclusions

The simulations demonstrate that, with no scintillation, using the direct application of Zernike visibility as the feedback for a cloosed loop AO system wirks well. In addition a SNR threshold was found of around three to five photodetector events per pixel per frame (averaged over the pupil). The inability of the simulation to maintain closed loop correction when the large tip-tilt component appears indicates that the system would preform better is a fast tracking loop was included.

Chapter 8

COMPUTER SIMULATIONS: WAVETRAIN

In order to simulate the performance of focal plane filters in adaptive optics systems, the WAVETRAIN [31] simulation framework was chosen. WAVETRAIN has been used to simulate parts of the Air Force's Airborne Laser (ABL) system and the NOP facility. The ABL is an anti-ballistic missile system that uses a laser to destroy missiles in the boost phase. It uses a sophisticated adaptive optics system to correct for atmospheric disturbances before the laser is sent out of the airplane.

The NOP test facility is a facility for testing components and algorithms in various directed energy systems before final development. It has been used to test many aspects of the Airborne Laser program. At the site there is a fully functional adaptive optics system. The wavefront corrector for the system is a 241 actuator continuous facesheet DM mirror. The model of this DM was used in the simulations described below.

In the simulations, no fine track system was used to remove the tip-tilt terms in the turbulence spectrum. The removal of tip-tilt was all done by the wavefront corrector. This was done to isolate the preformance of the several WFSs. A thick atmosphere was modeled. Four phase screens evenly spaced along the propagation path were able to produce realistic scintillation.

There were four goals to these simulations. First, to compare the SNR threshold estimated in the preliminary simulations (chapter 7). Second, to investigate the performance and reconstruction methods of FPF WFSs in the presence of scintillation. Third, to investigate the performance of FPF WFSs in conjunction

with continuous facesheet DMs. Lastly, to compare the performance of FPF WFSs with Shack-Hartmann WFSs in low light conditions.

8.1 The Simulation Layouts

Several configurations were created in order to investigate various aspects of the wavefront sensor. The configurations were grouped into two configurations. The first configuration consists of closed loop AO systems that use what will be termed an *ideal corrector*. This corrector is an attempt to perfectly correct a wavefront at a given location. It is implemented by applying an array of phase correction values directly to the incident array of complex numbers that represent the wavefront. This correction array is on the same sampling mesh as the wavefront array. As such it is the best correction that can be applied numerically in a single plane.

The second configuration groups several closed loop AO systems that use a model of the DM that is installed at NOP. This DM is a 241 actuator continuous facesheet deformable mirror. The outer ring of actuators is not used. The model of this DM was developed as part of the simulation of the ABL testing done at NOP and has been well validated. This DM model was used in anticipation of implementing a prototype at NOP.

8.1.1 Common Elements

The elements of the simulations that are common to both groups are shown in figure 8.1. These elements constitute an open loop imaging system. All of the data runs in this dissertation were configured so as to simulate an engagement between Salinas Peak and NOP. This is a common scenario at the NOP facility.

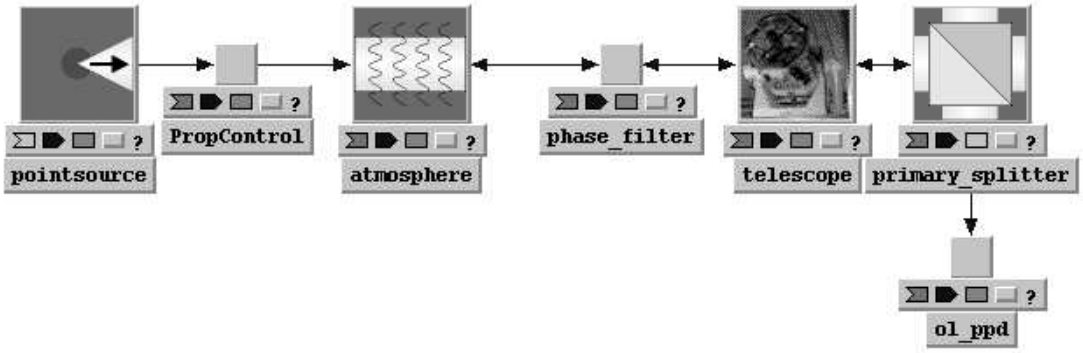

Figure 8.1: Common elements in the simulations

A point source beacon is turned on at Salinas Peak, a distance of 52 km and is imaged at NOP. The exposure interval of all of the WFS cameras is 0.5 ms. So as to minimize the effect of systems not under study, it was decided to correct for tip-tilt errors using the AO systems.

pointsource

This subsystem models a point source radiating into a hemisphere. The total power impingent upon the entrance pupil is this geometry is approximately 4 μW.

PropControl

PropControl is a system whose purpose it is to modify the propagation parameters in order to efficiently run the simulations.

atmosphere

This atmosphere model is configured for four phase screens, evenly spaced along the propagation path. Four phase screens was sufficient to produce significant scintillation along the propagation path while not overtaxing computational resources.

phase_filter

This system is used during debugging and diagnosis to apply a known phase at the entrance pupil of the telescope.

telescope

The telescope system models an ideal lens with an aperture. The size of the entrance pupil is 0.75 m.

ol_ppd

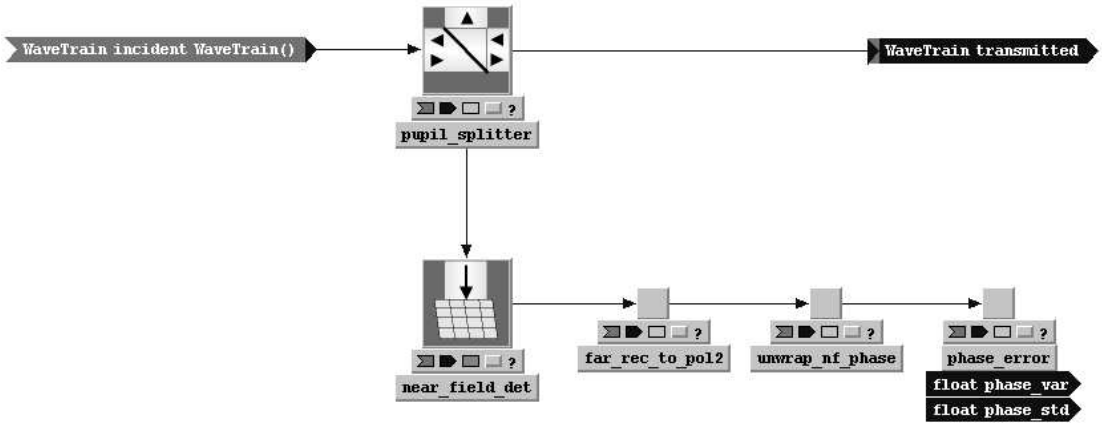

Figure 8.2: DiagnosticPlane composite system

In the closed loop systems there are several diagnostic subsystems. These are all instances of the DiagnosticPlane system class. The ol_ppd system in figure 8.1 is also an instance of this class. DiagnosticPlane is a composite system and its internal structure is shown in figure 8.2.

Since this subsystem is placed at a pupil plane of the system to be modeled, the near field calculations are appropriate for analyzing a pupil plane.

For the near field, the phase and square modulus can be recorded. In addition, the phase error can be calculated and recorded. This is important because saving raw images of a Monte Carlo analysis can take enormous amounts of disk space. Instead, just the standard deviation of the phase can be recorded, saving a great amount of space. The phase is unwrapped before the standard deviation is calculated.

8.1.2 Ideal Corrector

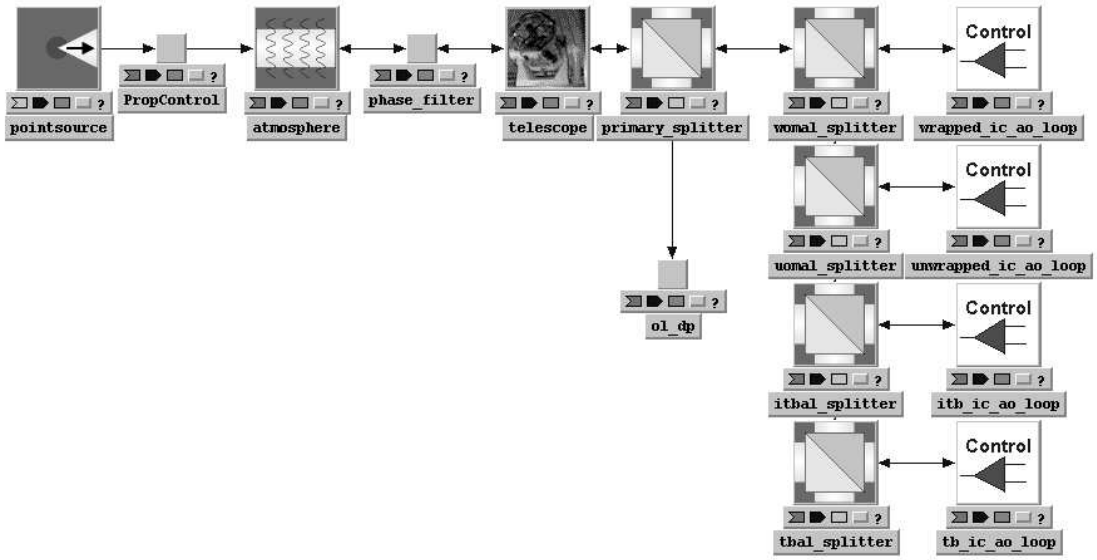

Figure 8.3: Closed loop simulation with ideal corrector

In order to investigate the performance of the FPF WFSs without regard to the effects introduced by the wavefront corrector, a set of closed loop AO systems that made use of a so-called ideal corrector were created. This corrector was implemented as a system that applies grid-level direct phase conjugation of an incoming wave.

wrapped_ic_ao_loop

This loop used a system that extracted the phase from the incoming wave by means of a simple rectangular to polar calculation on the complex valued grid that represented the wave. The result was then fed back into the ideal corrector in order to close the loop.

unwrapped_ic_ao_loop

The unwrapped_ic_ao_loop subsystem is very similar to the wrapped_ic_ao_loop, the only difference being that the phase field is passed to a phase unwrapping system before closing the loop through the ideal corrector.

itb_ic_ao_loop

As a next step toward a more realistic closed loop, the Optical Path Difference (OPD) of the wavefront was calculated by direct application of equation (6.27). Recall that this equation does not include all of the effects of diffraction. It is therefore referred to as an *ideal* three bin WFS.

tb_ic_ao_loop

For yet another level of realism, diffraction was added to the tb_ic_ao_loop system. It also uses the three bin expression for phase recovery, but rather than use analytic expressions for the field at the detector plane, the input wave to the WFS is first propagated to an image plane, then multiplied by the appropriate complex filter, then propagated to a pupil plane, where it encounters a detector. The WFS in the simulations uses the spatial configuration, i.e. there are three WFS detectors in parallel.

8.1.3 NOP Corrector

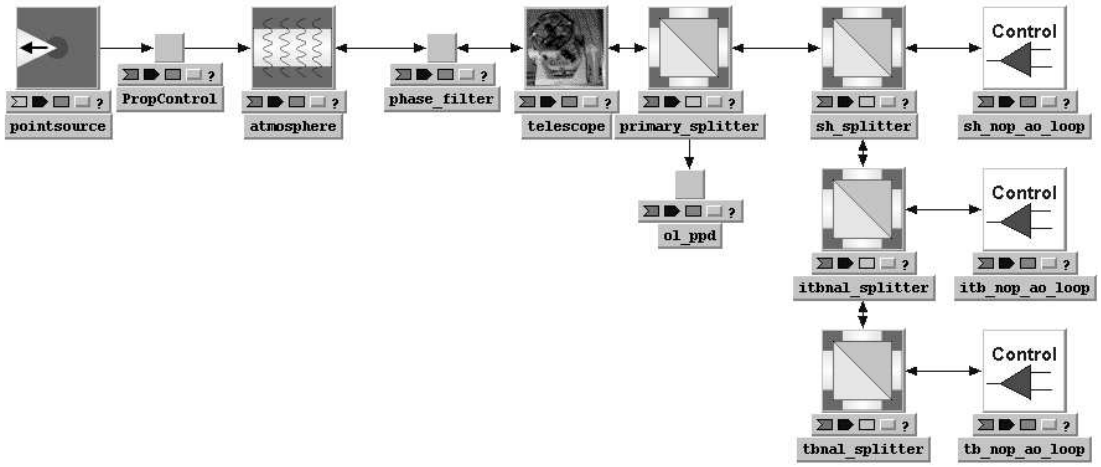

Figure 8.4: Closed loop simulation with NOP corrector

After having investigated the WFSs without regard to corrector effects, a set of closed loop systems using the NOP deformable mirror were created. The first one is a Shack-Hartmann WFS. The parameters for this WFS match those of the real system installed at NOP and thus the comparisons of the other WFSs to this one are in essence comparisons to current NOP performance.

The separation between DM actuators at the telescope primary is 4.5 cm. Thus, if the value of r_0 is less than this, the turbulence is under sampled.

8.2 Results: Ideal Corrector

Appendix A shows the results of some Monte Carlo case studies of the FPF WFS systems using the ideal corrector model. There were ten random seeds used to generate the phase screens, and the errorbars in the plots derive from these ten independent runs. Table 8.1 sumarizes these plots.

The turbulence strength in terms of r_0 ranges from 30 cm to 12 cm and the wind speed blowing across the propagation path is either 5 m/s or 10 m/s. The table shows the comparative levels of correction produced when using each of the four WFSs. The results are given in terms of a steady state residual phase error.

The ideal three bin WFS compares favorably with the two ideal wavefront sensors and actually tracks the unwrapped phase measurements very closely. The three bin WFS with diffraction has a steady state limit of about $1\frac{1}{2}$ rad RMS residual phase error. In these simulations, the filter core size is on the order of twice the diffraction limit.

These results show that simulations using the ideal three bin FPF WFS are representative of best case sensing of turbulence using a single wavefront sensor.

r_0	**Wind Speed** (m/s)	**rms phase error** (rad)			
		Wrapped	Unwrapped	Ideal FPF	FPF
30	5	< 0.1	< 0.1	< 0.1	1.5
	10	< 0.1	< 0.1	< 0.1	1.5
20	5	< 0.1	< 0.1	< 0.1	1.5
	10	< 0.1	< 0.1	< 0.1	1.5
15	5	< 0.1	< 0.1	< 0.1	1.5
	10	< 0.2	< 0.2	< 0.2	1.5
12	5	< 0.2	< 0.2	< 0.2	1.5
	10	< 0.25	< 0.25	< 0.25	1.5

Table 8.1: Summary of *ideal corrector* simulations

8.3 Results: NOP Corrector

Now we presents the results of a set of Monte Carlo runs under varying atmospheric conditions using a model of the NOP DM. The turbulence strength in terms of r_0 ranges from a weak 30 cm to an extreme 3 cm. The system at NOP was designed to operate at typical r_0 values of from 15 cm to 5 cm. The wind speed across the telescope aperture was varied from 0 m/s to a strong 20 m/s. There were 10 Monte Carlo seed values per set of atmospheric conditions. It was from these 10 runs that the error bars were calculated. The reconstructor for the DM is conditioned to eliminate waffle, so this is not a factor in these simulations. The full results are plotted in appendix B. Table 8.2 sumarizes these plots.

r_0	**Wind Speed** (m/s)	**rms phase error** (rad)		
		Shack-Hartmann	Ideal FPF	FPF
30	0	1.1	0.3	0.5
	5	1.1	0.3	0.5
	10	1.1	0.4	0.75
	20	1.1	0.4	0.6
20	0	1.1	0.4	0.6
	5	1.1	0.4	0.6
	10	1.1	0.4	1
	20	1.1	0.4	1
15	0	1.25	0.4	unstable
	5	1.25	0.4	unstable
	10	1.25	0.4	unstable
	20	1.25	0.4	unstable
12	0	1.5	0.75	unstable
	5	1.5	0.5	unstable
	10	1.5	0.5	unstable
	20	1.5	0.6	unstable
9	0	2	1	unstable
	5	2	1	unstable
	10	2	1	unstable
	20	2.5	1.25	unstable
6	0	3.25	2	unstable
	5	3.25	2	unstable
	10	3.25	2.25	unstable
	20	3.25	2.5	unstable
3	0	3.5	3	unstable
	5	3.5	3	unstable
	10	3.5	3	unstable
	20	3.5	3	unstable

Table 8.2: Summary of NOP simulations

8.4 Results: NOP Corrector and a brighter source

Because some of the results in the previous section were a bit surprising, it was decided to create some trial runs with a brighter beacon. It was hoped that this might confirm the hypothesis that the beacon was set too low to illustrate the differences between the WFSs at the stronger turbulence levels. This section shows the results of doubling the beacon power relative to the previous two sections. The Shack-Hartmann WFS is now performing more as expected and the three bin WFS with diffraction is also a bit more stable. Table 8.3 sumarizes these plots.

8.5 Results: NOP Corrector and a still brighter source

To further investigate the issue of beacon power as it relates to Shack-Hartmann performance and FPF WFS stability, the power was increased yet again. This section shows the resulting plots. One thing to note is that the three bin model with diffraction is starting to track closer to the ideal three bin model at the higher wind speeds. Table 8.4 sumarizes these plots.

r_0	**Wind Speed** (m/s)	**rms phase error** (rad)		
		Shack-Hartmann	Ideal FPF	FPF
12	0	1	0.5	0.75
	5	1	0.25	3
	10	1	0.4	0.5
	20	1	0.4	unstable

Table 8.3: Summary of NOP simulations with double power beacon

r_0	**Wind Speed** (m/s)	**rms phase error** (rad)		
		Shack-Hartmann	Ideal FPF	FPF
12	0	0.9	0.4	1.0
	5	0.75	0.25	2
	10	1	0.4	0.6
	20	0.75	0.4	0.75

Table 8.4: Summary of NOP simulations with triple power beacon

8.6 Single frames

Figures 8.5-8.7 show individual frames from a single FPF WFS camera. The first frame (figure 8.5) is representative of frames from the Monte Carlo runs performed in sections 8.2 and 8.3, the second (figure 8.6) is a frame from the run in section 8.4 and the third (figure 8.7) from section 8.5.

The runs in sections 8.2 and 8.3 had a low power AO beacon and the net power on the detector of about 4 μW. This low of a power was chosen in order to illustrate the performance of the FPF WFS at a critical point in the parameter study. During the preliminary runs for the systems, the various WFSs appeared to preform better than the Monte Carlo runs finally indicated. This was mostly because, due to limited computer resources, the preliminary runs were for shorter periods of time. As can be seen from the plots, the three bin FPF WFS only became unstable later in the runs.

The run plotted in section 8.4 had a beacon with double the power, or 8 μW, and the run in section 8.5 had a beacon producing about 13.5 μW.

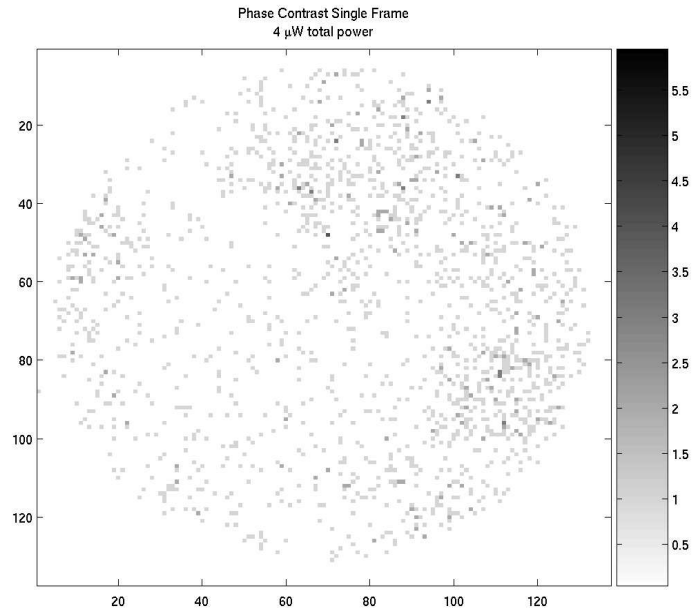

Figure 8.5: Three Bin with diffraction WFS single frame, r_0 = 12 cm, wind speed = 5 m/s, low power beacon

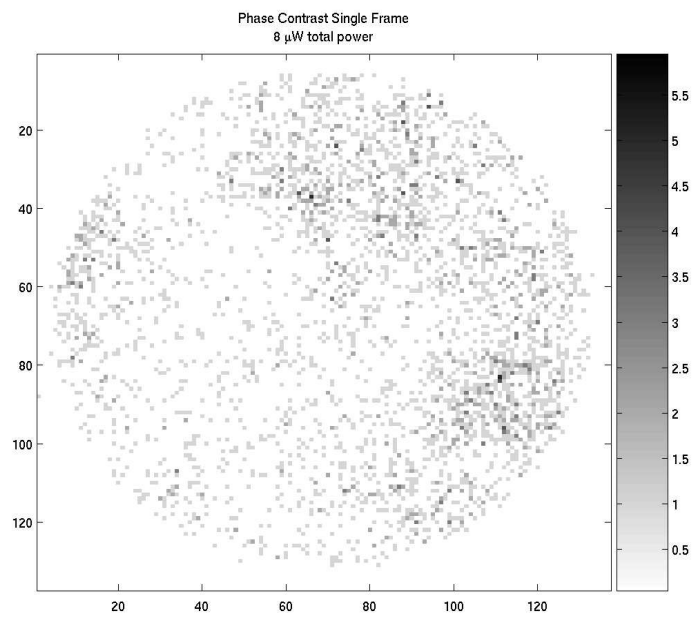

Figure 8.6: Three Bin with diffraction WFS single frame, r_0 = 12 cm, wind speed = 5 m/s, double power beacon

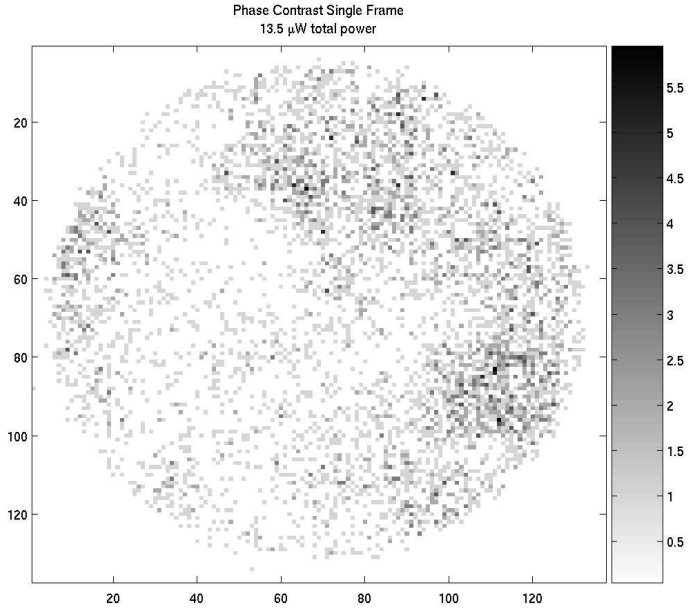

Figure 8.7: Three Bin with diffraction WFS single frame, r_0 = 12 cm, wind speed = 5 m/s, triple power beacon

8.7 Summary

One thing to consider with these results is that they show a worst case performance relative to the existing NOP system. These simulations were more light starved than the normal operating conditions for NOP. This is the main cause for the poor performance of the Shack-Hartmann loop. The FPF WFS based loops do better for mild turbulence, but they too perform poorly as the atmosphere degrades.

It appears that the error rejection for the FPF WFS configuration chosen was poor. There are two things that could improve this. First, the diameter of the FPF filter core could be adjusted from twice the Airy disk diameter to closer to the size of the Airy disk diameter. This is known to improve performance of phase contrast imaging systems in other applications. The limit of the ideal FPF loop indicates that this might also improve performance in this adaptive optics application. In addition, the FPF loops might benefit more from a modal filter, as they are clearly sensing modes that are in fact noise. Comparison of the results presented here with simulations that include a tip-tilt loop would also prove useful.

Something else that would be profitable to investigate is changing the detector size. The FPF WFS camera was 128 pixels by 128 pixels, the same as the Shack-Hartmann WFS camera. Since the reconstructed phase from the FPF WFS was passed to a pseudo-Shack-Hartmann reconstructor, this seemed reasonable. However, since the pseudo-Shack-Hartmann reconstructor is not a real wavefront sensor, this may not be the optimum configuration. If, for example, the 'detector' plane of the pseudo-Shack-Hartmann is much higher resolution there is no penalty for noise and it would be possible to have larger

guard bands in the Shack-Hartmann sub-apertures. All of this while reducing the array size of the FPF WFS camera and thereby increasing the photon flux rate per pixel.

Chapter 9

EXPERIMENT

In order to investigate some of the properties of FPF AO systems in a more realistic context, a closed loop system was assembled from parts that were on hand at the Electro-Optics Research Lab (EORL). This closed loop system made use of LCDs both to generate and to correct for simulated turbulence. In addition an LCD was used to create the focal plane filter. The main goal of the experiment was to replicate the results of the simulations presented in chapter 7. This motivated the use of the phase screen from the simulations in the experiment.

9.1 Layout

The optical layout of the experiment can be seen in figure 9.1. The point source was created by spatially filtering a HeNe laser. This light is then collimated by a well corrected lens manufactured by Space Optics Research Lab (SORL). This lens is designed for optical correlation experiments and is well suited to collimating light from point sources.

The collimated light then impinges on an LCD. This LCD will act as a turbulence generator. Since there is only one screen of simulated turbulence, this layout is not able to simulate the effects of scintillation. This LCD has a twisted nematic geometry. Since the LCD to be used for correction is also a twisted nematic device, it was necessary to place a half wave plate between the two devices.

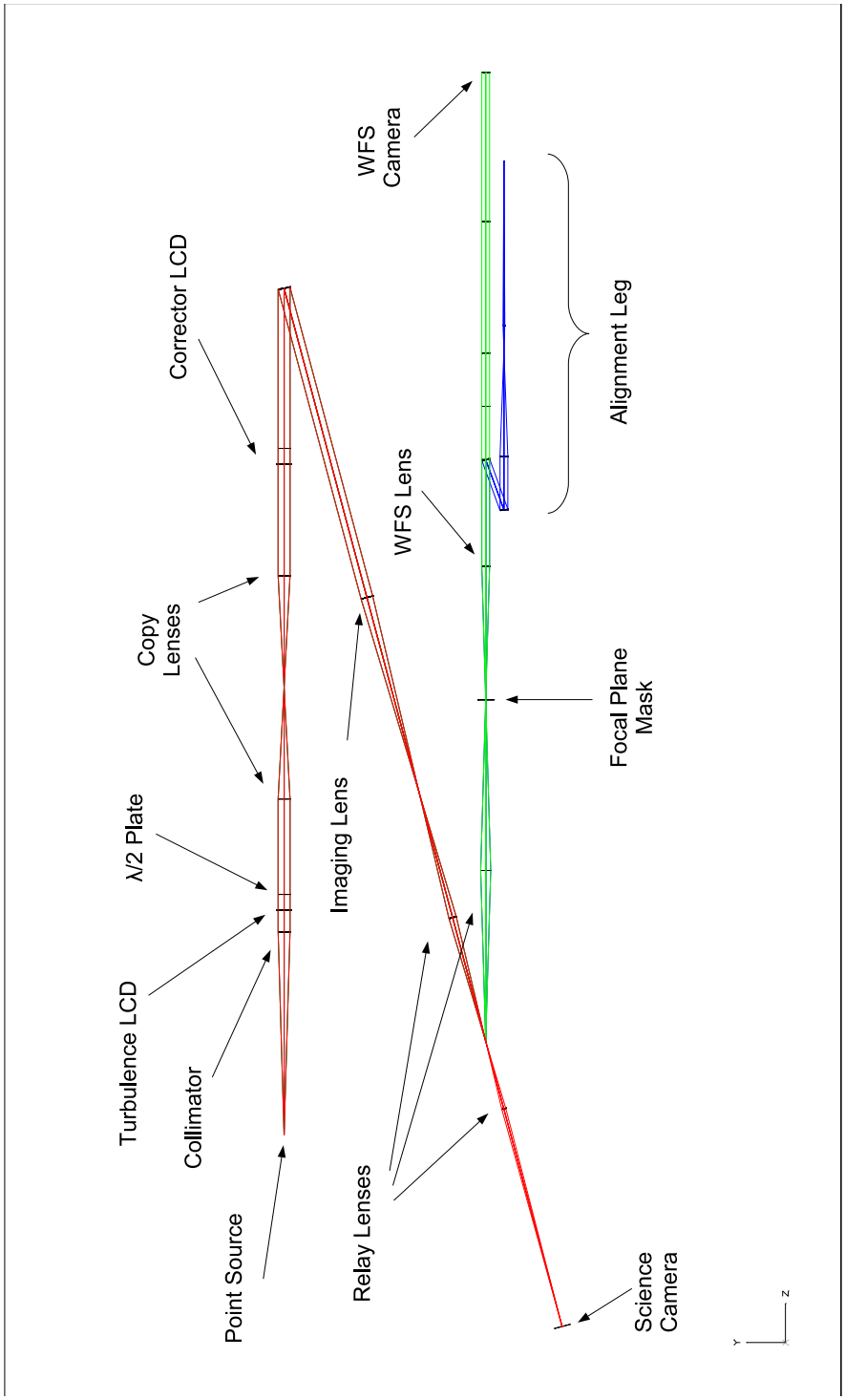

Figure 9.1: Experimental layout

The LCDs were placed in mounts that could be adjusted with high precision along all three axes. In addition, some control of the rotation about the *z-axis* was necessary. This was because the experiment was designed so that a pixel on the corrector LCD corresponded exactly to a pixel on the turbulence LCD. It is because of this also that the half wave plate was necessary. The pixels on the LCDs are not square and so it would not have been possible to rotate one of the LCDs by 90 degrees about the *z-axis* in order to line up the polarization of the light to the director of the LCD.

Since the pixels on an LCD form a regular grid, there will be multiple diffraction orders in the far field. In order to avoid sampling issues, an iris that filters out all but the central diffraction order is placed at the focus formed by a lens placed directly after the LCD. Since an image of the turbulence LCD is to be formed on the corrector LCD after the central order is filtered, a $4f$ system is placed between the two LCDs and the iris is placed in the filter plane.

For filtering the central order after the corrector LCD another SORL lens was chosen. It was placed after a turning flat that was located at the end of the optical table. The central diffraction order is a potentially corrected image of the point source, but it is not the proper size for evaluation nor the proper location on the table for use in a FPF WFS. As such, it is necessary to relay this image. The first relay lens brings the image further down the table , but at the same magnification. At this point a beam splitter is placed in the path. The reflection is used for the WFS and the transmitted beam is sent to the science camera.

The science camera image needs to be magnified a bit so the lens placed behind the splitter was adjusted to produce a magnification of about 3.

The WFS path is formed from the light reflected off of the beam splitter in front of the science camera. Since the image formed at the beam splitter was the correct size for the WFS we just need to relay it with unit magnification to a plane at which we can place the FPF. The filter LCD is of the same type as that used to generate the turbulence and the correction upstream. The size of the image at the LCD is such that it fills a two pixel by two pixel area of the LCD. A lens (called the WFS lens) was then placed after the LCD in order to form an image of the turbulence and corrector LCDs on the WFS camera. This image has been passed through a complex valued filter and is an interferometric measure of the closed loop phase after the application of the corrector LCD. The exact form of this interferometer pattern depends on the particular filter generated by the filter LCD.

In order to make sure that the spot formed by the relay lens is located at the proper place in the filter plane, an alignment leg was formed. A pellicle beam splitter was placed after the WFS lens in order to align the FPF LCD without modifying the WFS path. An initial lens forms an image of the WFS LCD before a microscope objective is used to image the LCD with high enough precision on the alignment camera.

9.2 Technique

9.2.1 Computers

The minimal setup for the experiment would require controlling three LCD drivers and digitizing two cameras. The boards used to control the LCD drivers were custom made at the EORL. The boards used to digitize the camera images were made by Imagenation. Due to a combination of hardware and software

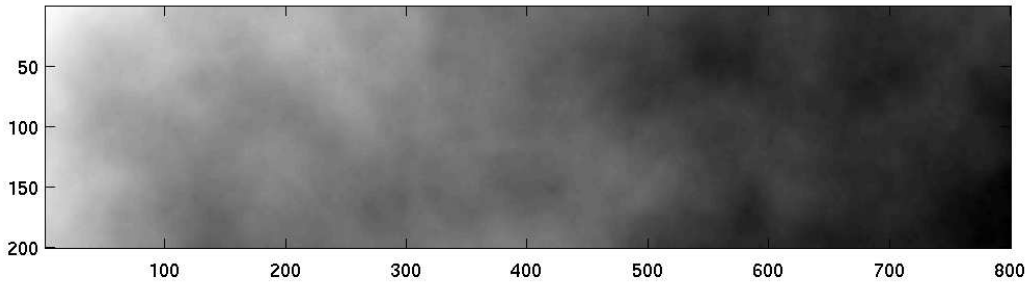

Figure 9.2: Phase screen

limitations, it was not possible to control the experiment with just one computer. Since the WFS camera and the LCD controllers for the filter LCD and the corrector LCD needed to be the same computer, it was decided that the second computer would control the turbulence LCD. Since the first computer could also handle the science camera it was set up to do so. The turbulence computer was capable of controlling another LCD and so for the runs in which ideal correction was tested, it controlled both the turbulence LCD and the corrector LCD.

9.2.2 Turbulence

In order to implement the turbulence, a phase screen was created using Kolmogorov statistics (figure 9.2). The screen values were then scaled for each run. So that wind could be simulated, an over sized screen was generated in order to be translated across the LCD.

9.2.3 Focal Plane Filter

Since twisted nematic LCDs can be used in phase modulation mode and amplitude modulation mode, but not both at the same time, it was decided that the experiment would be set up so that the FPF LCD operated in phase mode. This allowed testing of the Zernike contrast method of phase calculation. The phase retardation of the filter was alternated between plus and minus $\pi/2$ and the contrast calculated after each frame. Since the system was aligned so that a pixel on the WFS camera corresponded to a pixel on the corrector, there was no real need for a reconstructor. The accumulated correction was then applied directly to the LCD.

9.3 Results

During the taking of experimental data, a TV monitor was used to view the output of the camera in real time. It was clear during the experiment that when the loop was closed that the system was correcting a significant amount of the phase from the turbulence LCD. When the data was analyzed, it became obvious that the recorded level of correction did not correspond to the observed level of correction. For example, figure 9.3 shows a typical open loop frame and figure 9.4 shows a typical closed loop frame. There is obviously some correction, yet a comparison of the peak values in the two runs shows almost no correction. The peak values of the runs are shown in figure 9.5. The open loop and closed loop runs are nearly identical despite the obvious differences in the images. The labels for the figure come from the summary of the data log in table 9.1. These digitized still frames show even less evidence of correction than

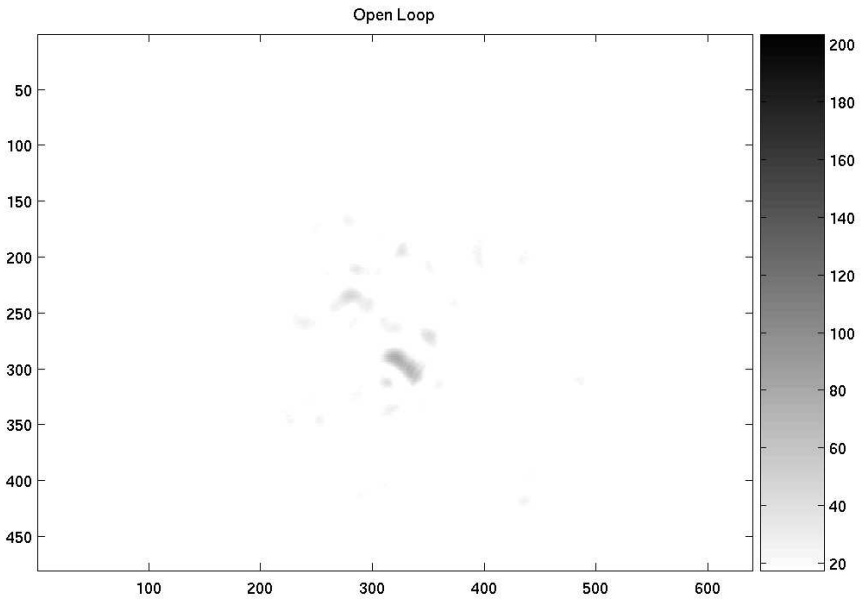

Figure 9.3: Open Loop

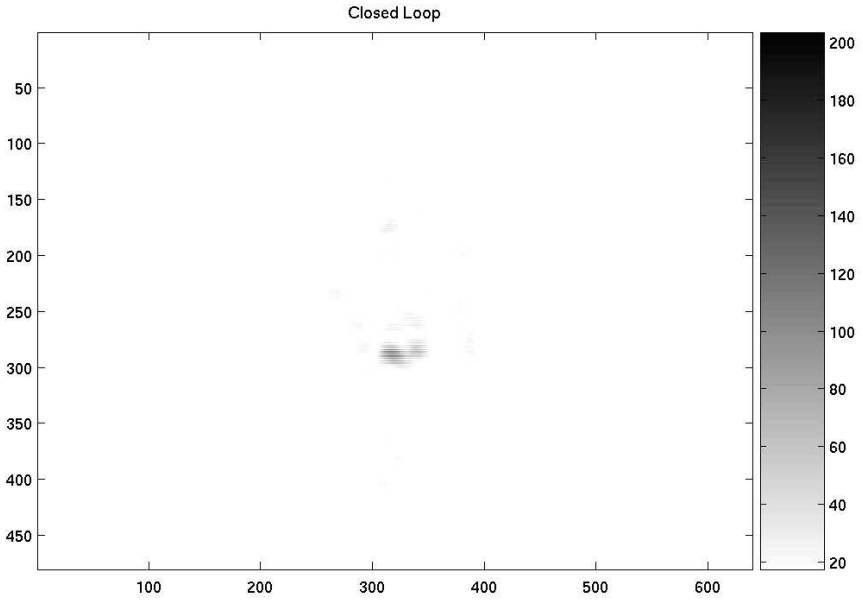

Figure 9.4: Closed Loop

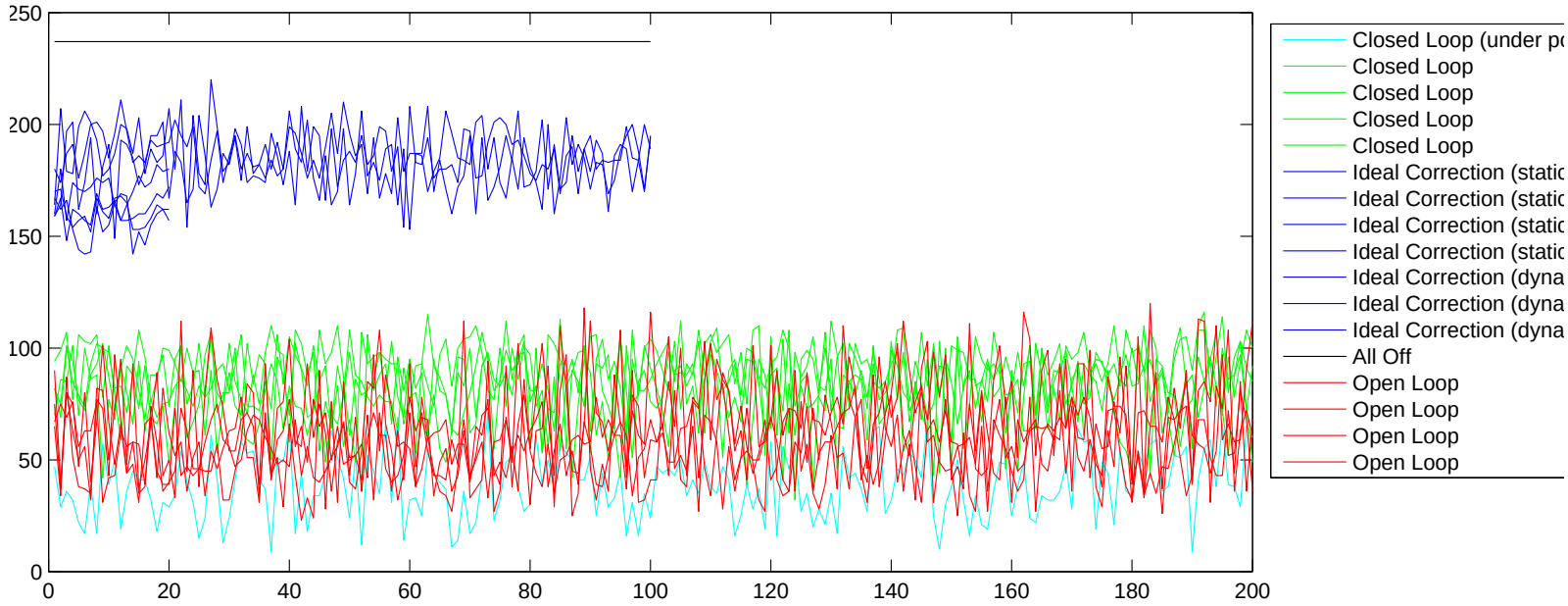

Figure 9.5: Experiment results: peak value metric

the real time TV output of the cameras.

In trying to determine a valid metric for correction, a major problem was that digitized values below 16 Analog to Digital Units (ADUs) are recorded as 16 with the hardware for the experiment. This made it impossible to normalize the images based on conservation of energy. Each image appeared to vary in responsivity when the loop was closed so what was needed was a self normalizing metric that measured the spread of energy in a frame. It was decided to use a moment of inertia calculation:

$$\begin{aligned} x_{\text{moi}} &= \sum_{\forall x, \forall y} I(x,y) \cdot (x - x_{\text{cent}})^2 \\ y_{\text{moi}} &= \sum_{\forall x, \forall y} I(x,y) \cdot (y - y_{\text{cent}})^2 \end{aligned} \tag{9.1}$$

where

$$\begin{aligned} x_{\text{cent}} &= \sum_{\forall x, \forall y} I(x,y) \cdot x \\ y_{\text{cent}} &= \sum_{\forall x, \forall y} I(x,y) \cdot y \end{aligned} \tag{9.2}$$

(i.e. the centroid). This metric gave a quantitative measure that corresponded reasonably with the qualitative observations.

A plot showing the summary results is shown in figure 9.6. The scalar metric for the plot is

$$\text{metric} = r_{\text{moi}} = \sqrt{x_{\text{moi}}^2 + y_{\text{moi}}^2} \tag{9.3}$$

There are a couple of anomalies to note first. When all of the LCDs are turned off, there is a much higher throughput. As a result, the image is strongly sat-

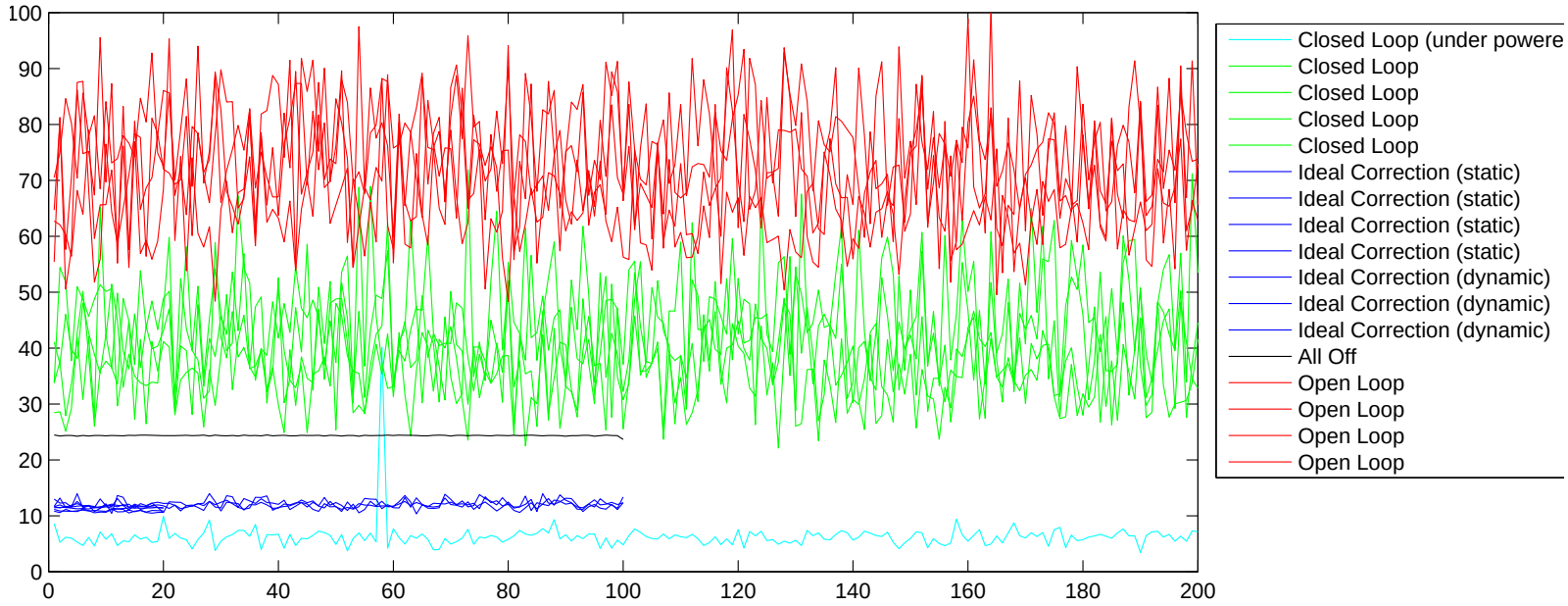

Figure 9.6: Experiment results: moment of inertia metric

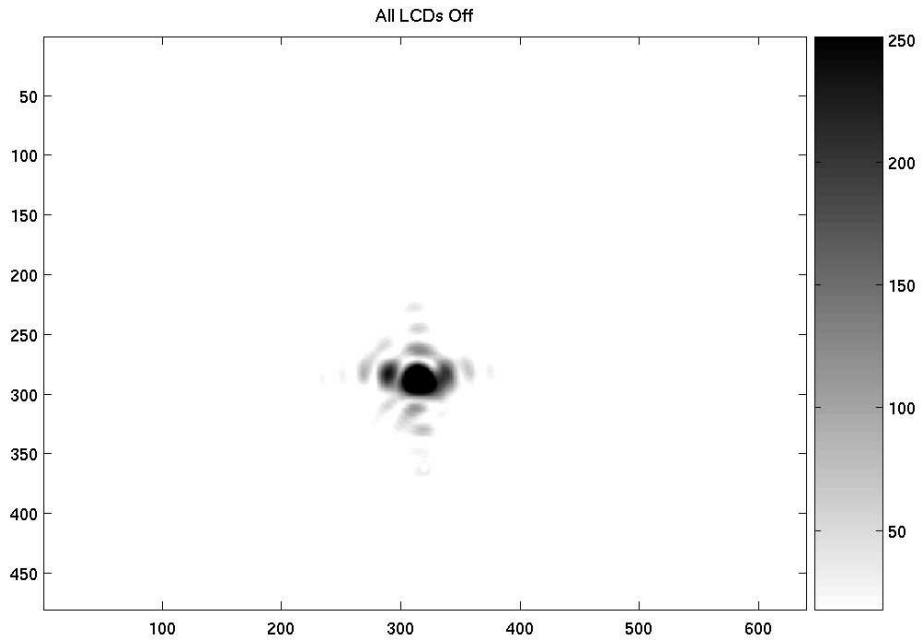

Figure 9.7: Single frame with all LCDs off

urated (see figure 9.7). This caused the moment of inertia to be larger than it should have been. At the other extreme, the first run of closed loop simulations had too short an exposure length (figure 9.8). As a result, the moment of inertia calculation was too small: All of the light that had not been corrected was under the 16 ADU threshold. The open loop runs in figure 9.6 show a larger moment of inertia than the closed loop runs. This corresponds to the broader versus narrower spot in the images.

Table 9.1 shows the pertinent details of the experiment log. The first column describes the state of the loop. There were several "ideal" runs. These were runs where the turbulence and corrector were run by the turbulence computer and the phase applied to the corrector LCD was of equal and opposite sign to that applied to the turbulence LCD. This was to verify alignment and an

Loop State	**Exposure Length (ms)**	**Turbulence Scale Factor**
All Off	1	N/A
Ideal Correction (static)	1	20
Ideal Correction (static)	1	10
Ideal Correction (static)	1	5
Ideal Correction (static)	1	1
Ideal Correction (dynamic)	1	20
Ideal Correction (dynamic)	1	10
Ideal Correction (dynamic)	1	5
Closed Loop (under powered)	1	20
Closed Loop	2	20
Closed Loop	2	10
Closed Loop	2	5
Closed Loop	2	1
Open Loop	2	20
Open Loop	2	10
Open Loop	2	5
Open Loop	2	1

Table 9.1: Test log summary

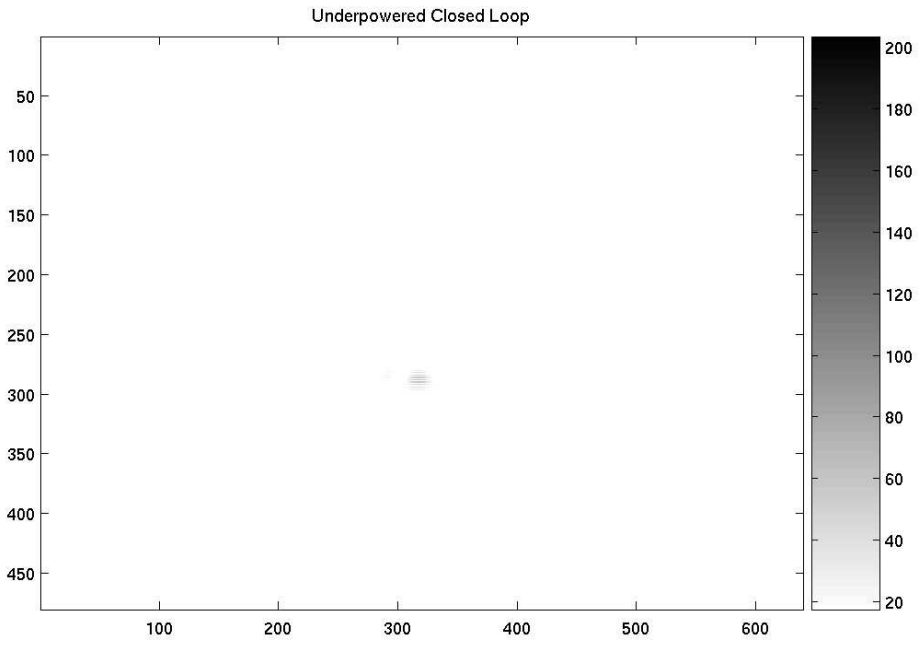

Figure 9.8: Single frame: Exposure length too small

attempt to provide a reference for correction. A data run was also taken with all of the LCDs off. The second column gives the exposure length of the science camera in ms. The final column gives the scale factor applied to the phase screen before being written to the turbulence LCD.

9.4 Conclusion

Fundamentally the problem with the experiment was one of finding a proper reference with which to judge success. The throughput of the system varied depending on whether the LCDs were on or not and whether the turbulence LCD and corrector LCD were controlled by the same computer. This lack of quantifiability made standard AO metrics like Strehl ratio or Power-In-the-Bucket (PIB) useless.

Using the moment of inertia of the image as the performance metric gave quantitative results that corresponded reasonably with qualitative observations of the recorded science camera images. This metric should map well to 3 dB PIB for well corrected images or gaussian beams, but it seems to be more appropriate for poorly corrected or open loop cases.

The experiment did demonstrate that Zernike visibility method of direct feedback can be used to close the loop in a hardware adaptive optics. It was not possible to replicate the results of the simulations in chapter 7. There were several obstacles to achieving this goal. The 16 ADU threshold meant that it would not be possible to replicate the search for a SNR threshold: the threshold would be below the 16 ADU cutoff. The synchronization problems meant that quantitative comparisons with the simulations' use of single frame Strehl was not possible. Without better hardware, quantitative comparisons between the simulations and experiment would be very difficult.

Chapter 10
CONCLUSION

The proposal that a wavefront sensor based on focal plane filters could be used effectively in an adaptive optics system was first proposed in Seward et al. [1]. This dissertation has expanded on that original work and has demonstrated that they are viable candidates.

The discussion of the theory of FPF WFSs in chapter 6 gives a unified view of a large class of interferometric techniques. This presentation is unique in that it allows for a generalization to filters that are either dynamic or continuously varying in form.

In addition, the proposal to use a numeric implementation of a Shack-Hartmann WFS both eases the integration path for FPF WFS systems and improves the performance when using a continuous facesheet DM for correction. The pseudo-Shack-Hartmann reconstructor eases the integration by exploiting any existing infrastructure or knowledge based on the Shack-Hartmann WFS in AO systems.

APPENDICES

Appendix A

IDEAL CORRECTOR PLOTS

This appendix collects the detailed plots resulting from the simulations run with the *ideal corrector*. The text in section 8.1.2 describes the simulations and section 8.2 sumarizes these results.

A.1 r_0 = 30 cm

A.1.1 wind speed = 5 m/s

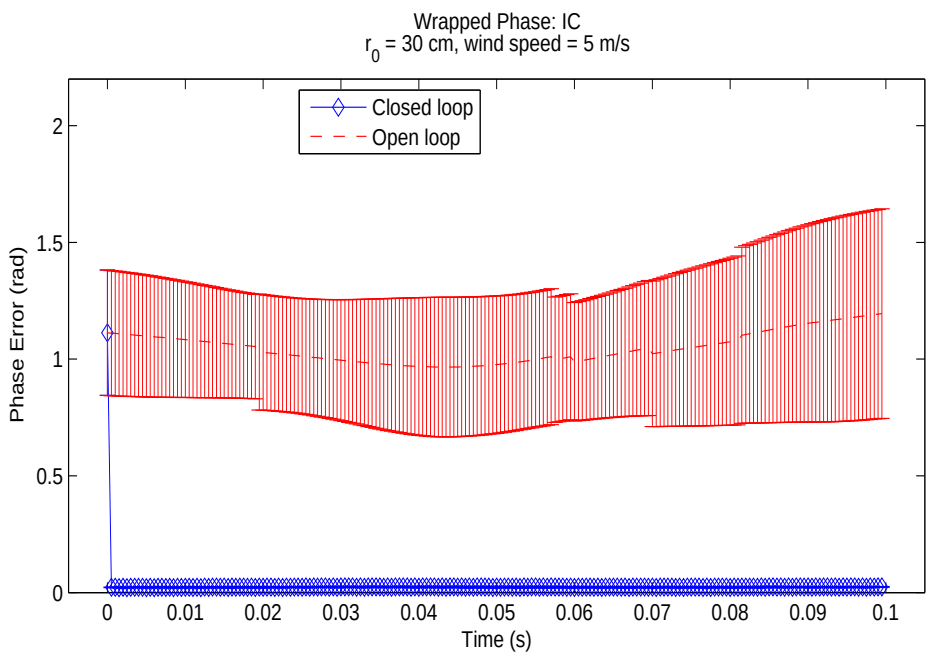

Figure A.1: Wrapped phase WFS, r_0 = 30 cm, wind speed = 5 m/s

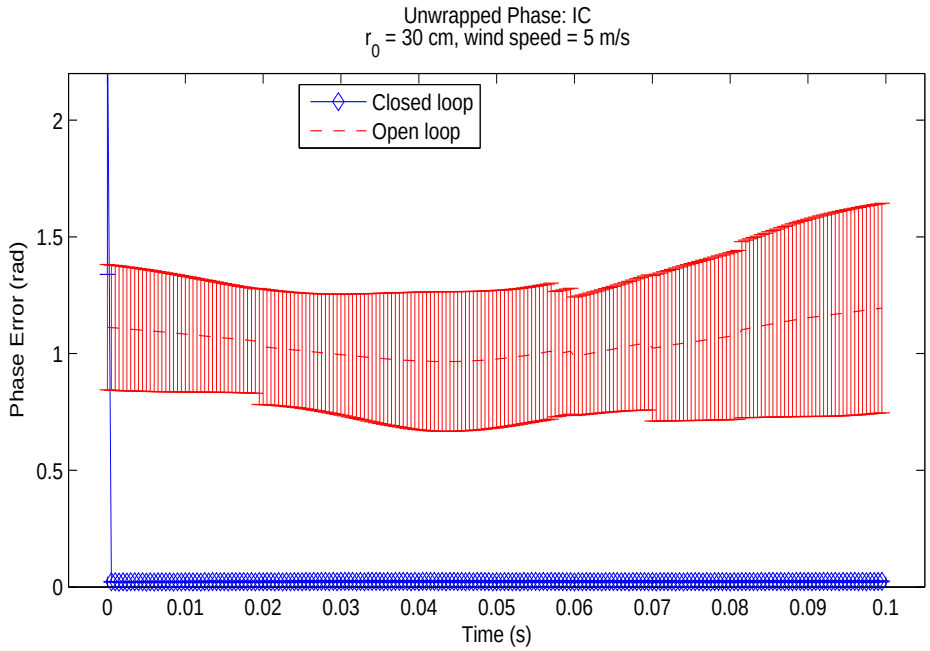

Figure A.2: Unwrapped phase WFS, r_0 = 30 cm, wind speed = 5 m/s

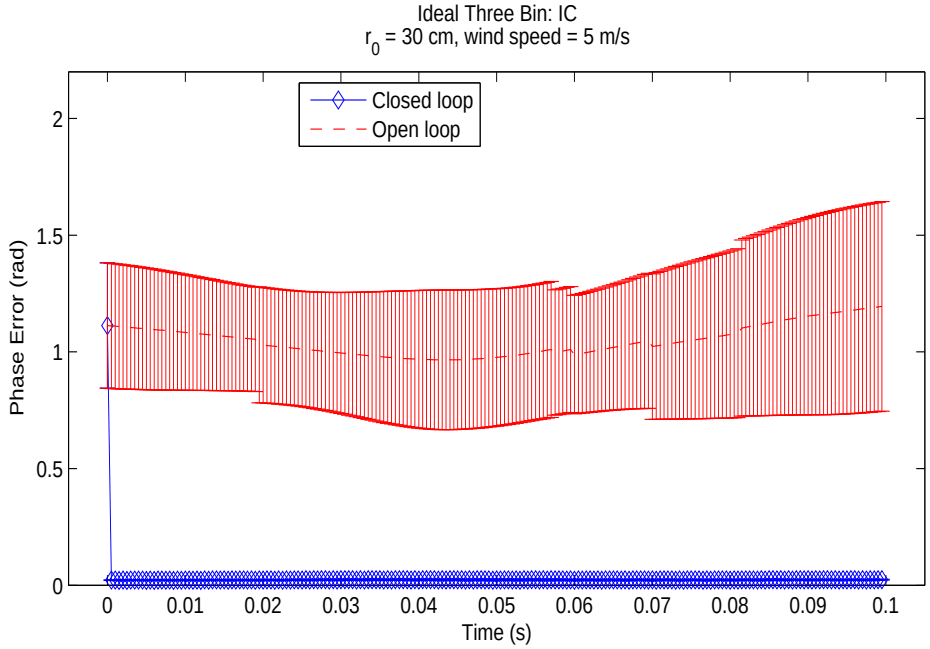

Figure A.3: Ideal Three Bin WFS, r_0 = 30 cm, wind speed = 5 m/s

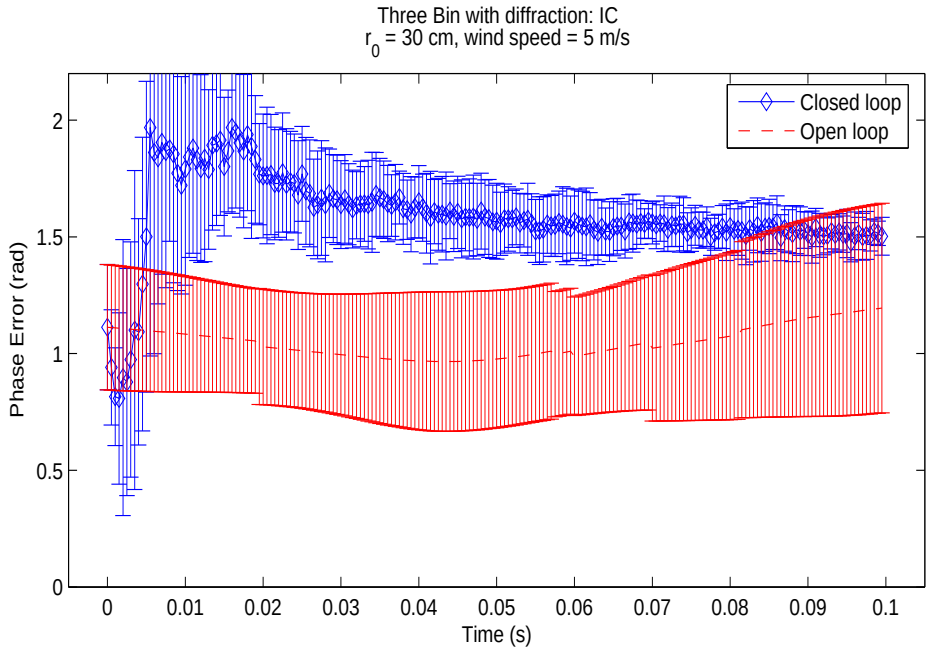

Figure A.4: Three Bin with diffraction WFS, r_0 = 30 cm, wind speed = 5 m/s

A.1.2 wind speed = 10 m/s

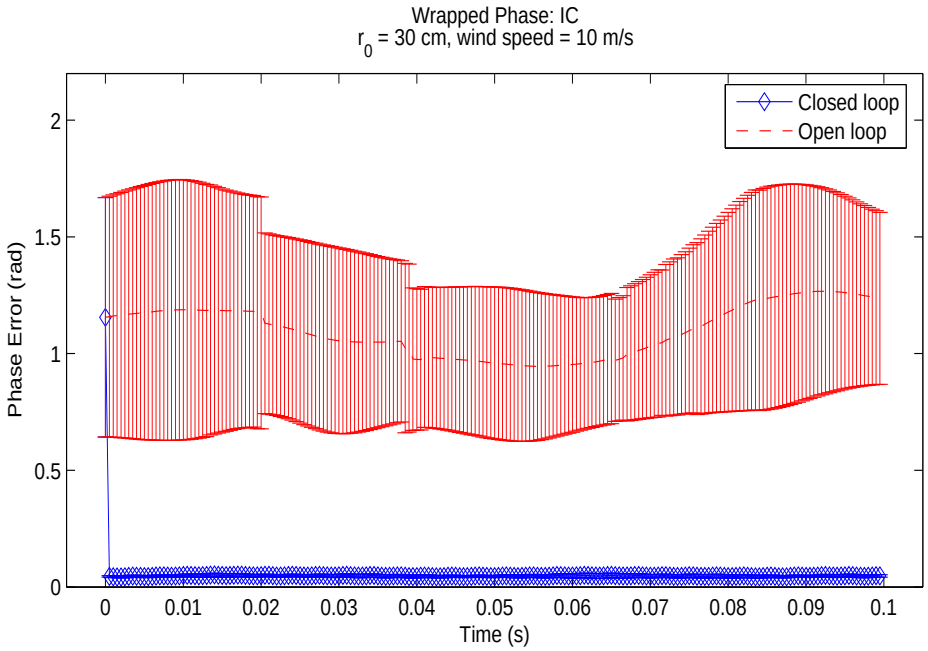

Figure A.5: Wrapped phase WFS, r_0 = 30 cm, wind speed = 10 m/s

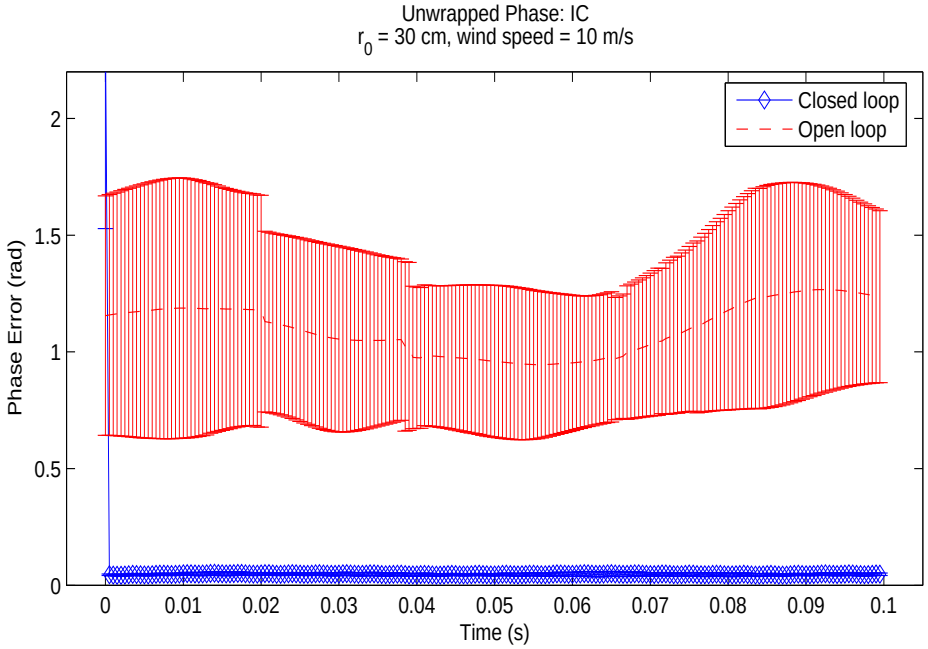

Figure A.6: Unwrapped phase WFS, r_0 = 30 cm, wind speed = 10 m/s

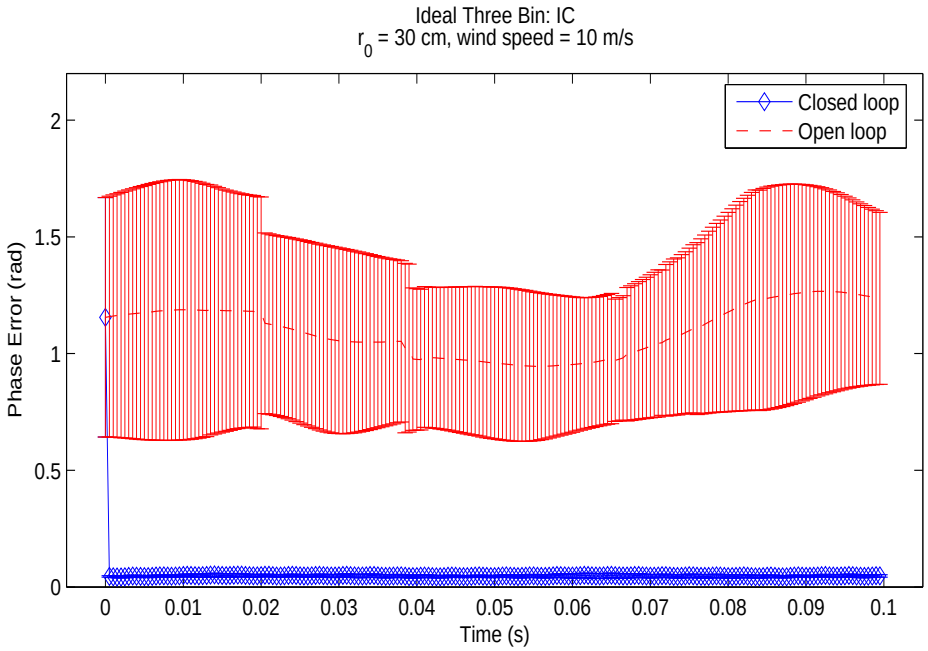

Figure A.7: Ideal Three Bin WFS, r_0 = 30 cm, wind speed = 10 m/s

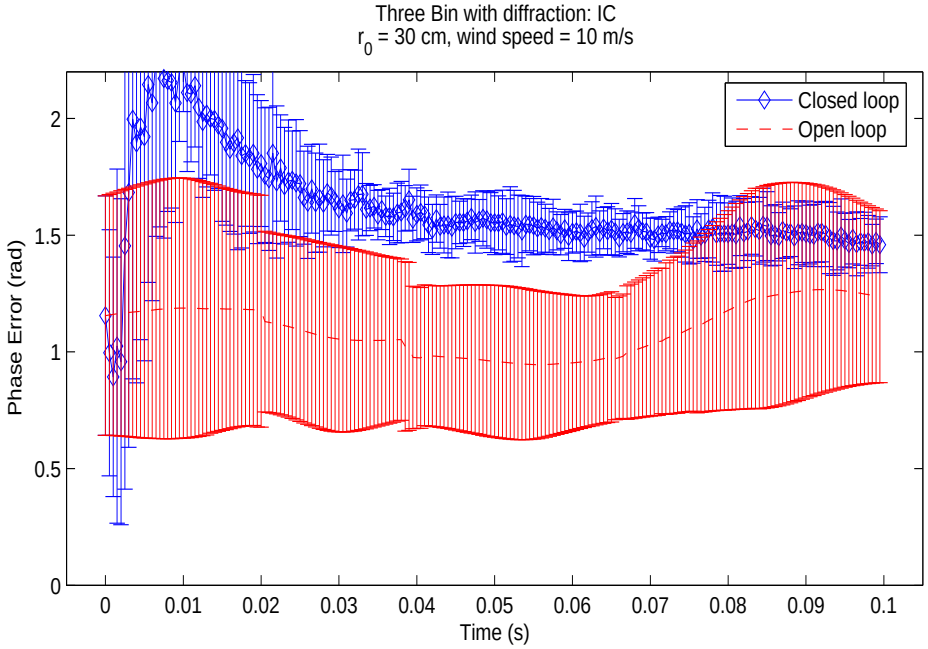

Figure A.8: Three Bin with diffraction WFS, r_0 = 30 cm, wind speed = 10 m/s

A.2 r_0 = 20 cm

A.2.1 wind speed = 5 m/s

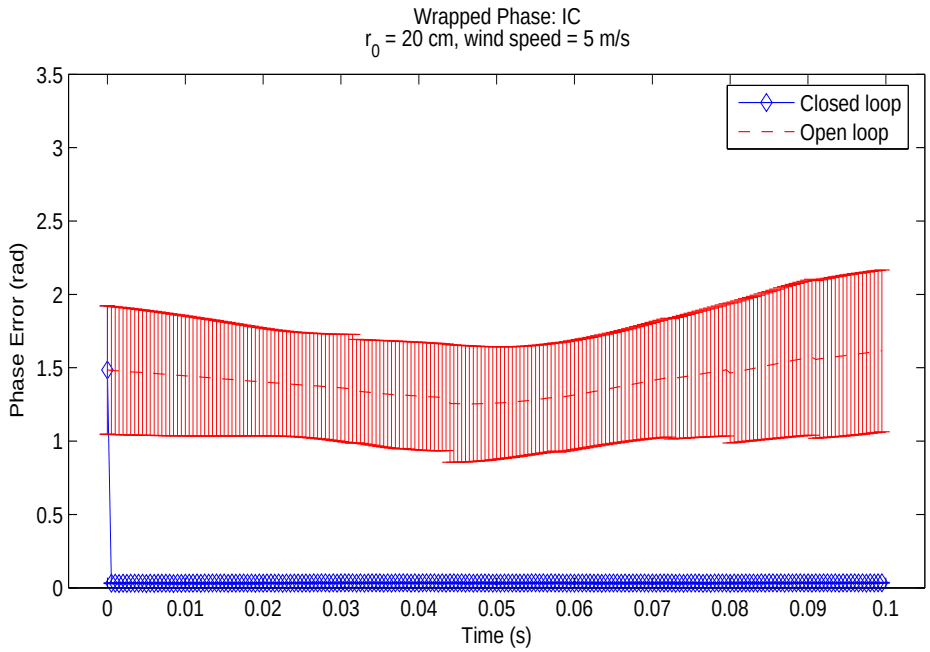

Figure A.9: Wrapped phase WFS, r_0 = 20 cm, wind speed = 5 m/s

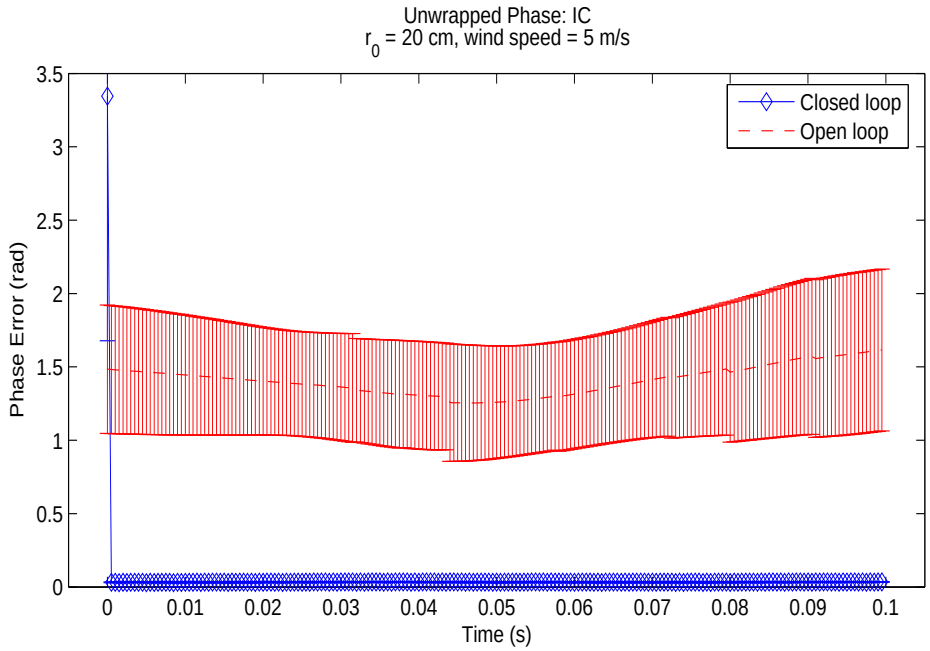

Figure A.10: Unwrapped phase WFS, r_0 = 20 cm, wind speed = 5 m/s

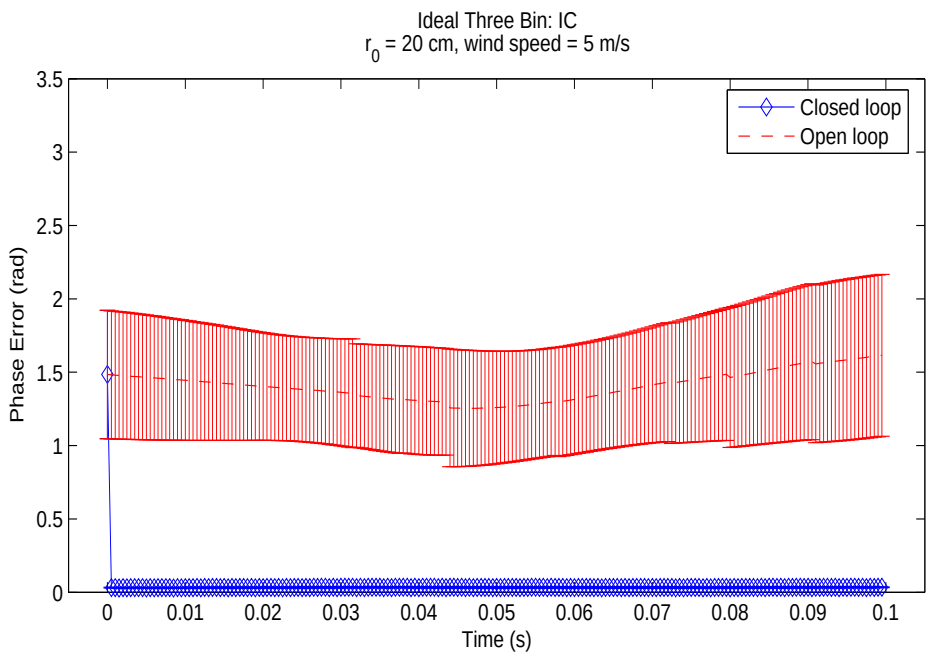

Figure A.11: Ideal Three Bin WFS, r_0 = 20 cm, wind speed = 5 m/s

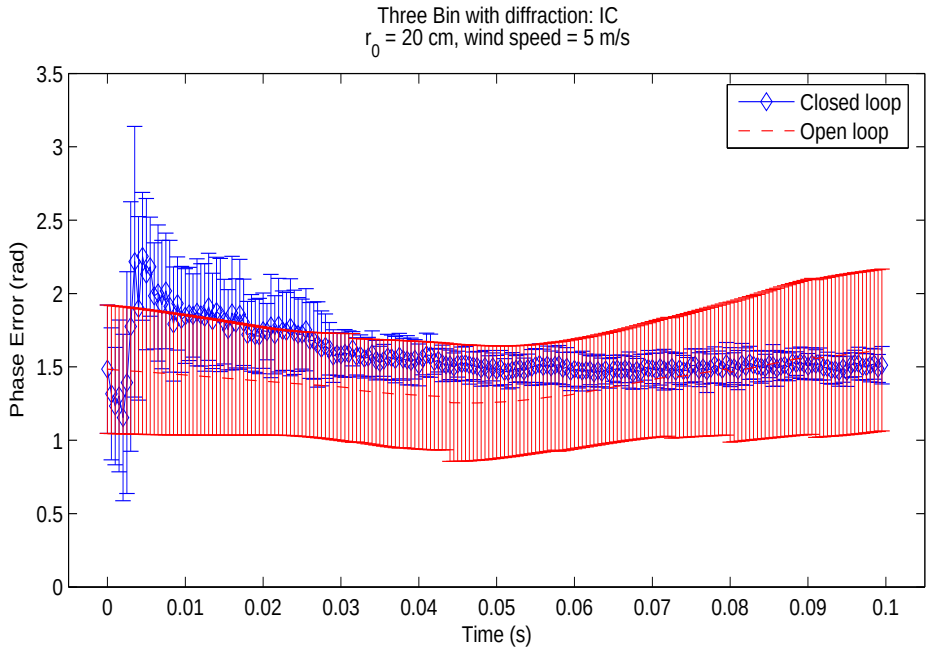

Figure A.12: Three Bin with diffraction WFS, r_0 = 20 cm, wind speed = 5 m/s

A.2.2 wind speed = 10 m/s

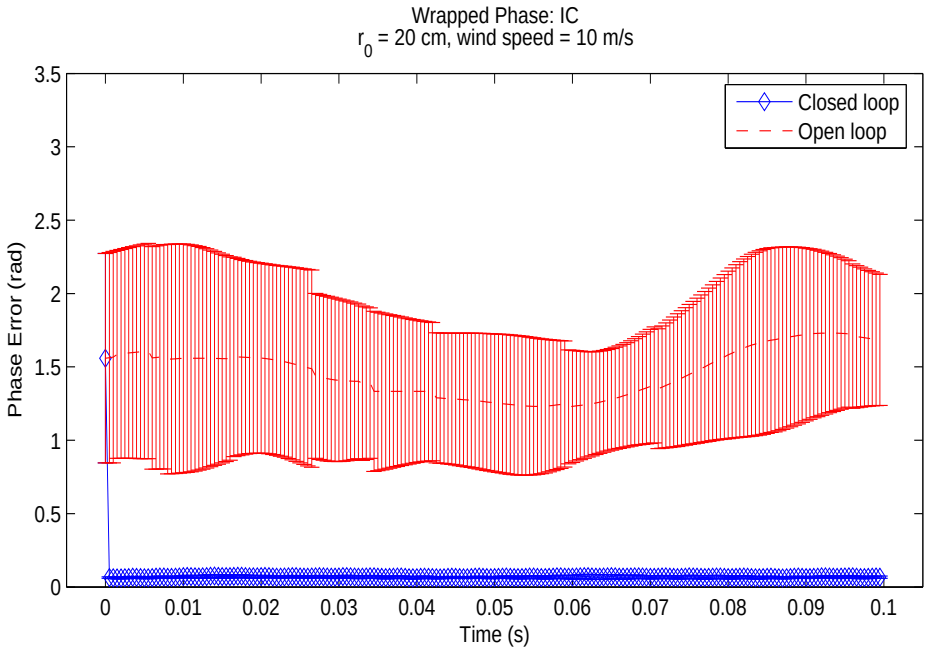

Figure A.13: Wrapped phase WFS, r_0 = 20 cm, wind speed = 10 m/s

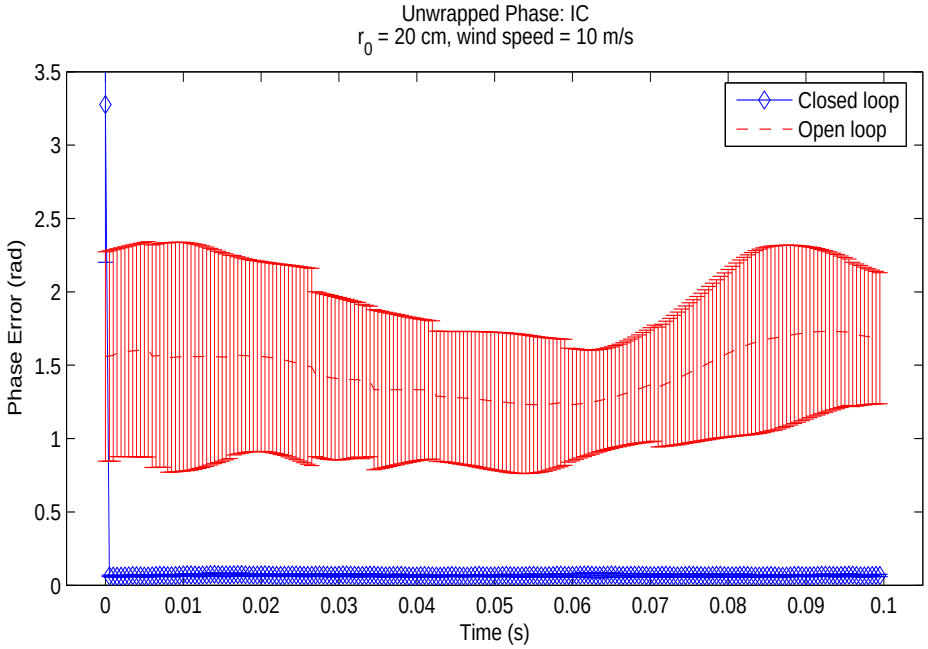

Figure A.14: Unwrapped phase WFS, r_0 = 20 cm, wind speed = 10 m/s

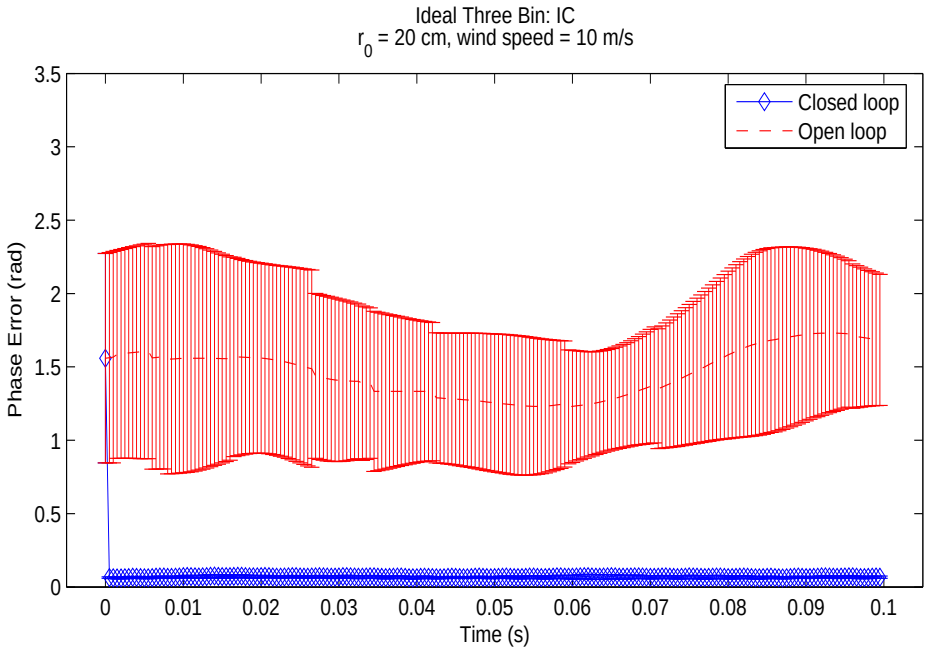

Figure A.15: Ideal Three Bin WFS, r_0 = 20 cm, wind speed = 10 m/s

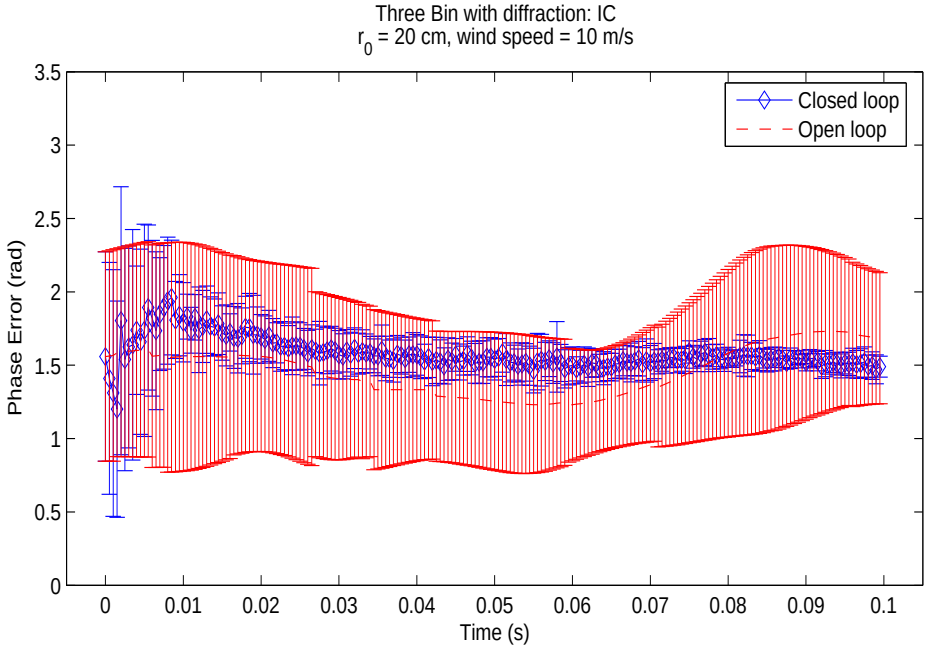

Figure A.16: Three Bin with diffraction WFS, r_0 = 20 cm, wind speed = 10 m/s

A.3 r_0 **=** 15 cm

A.3.1 wind speed = 5 m/s

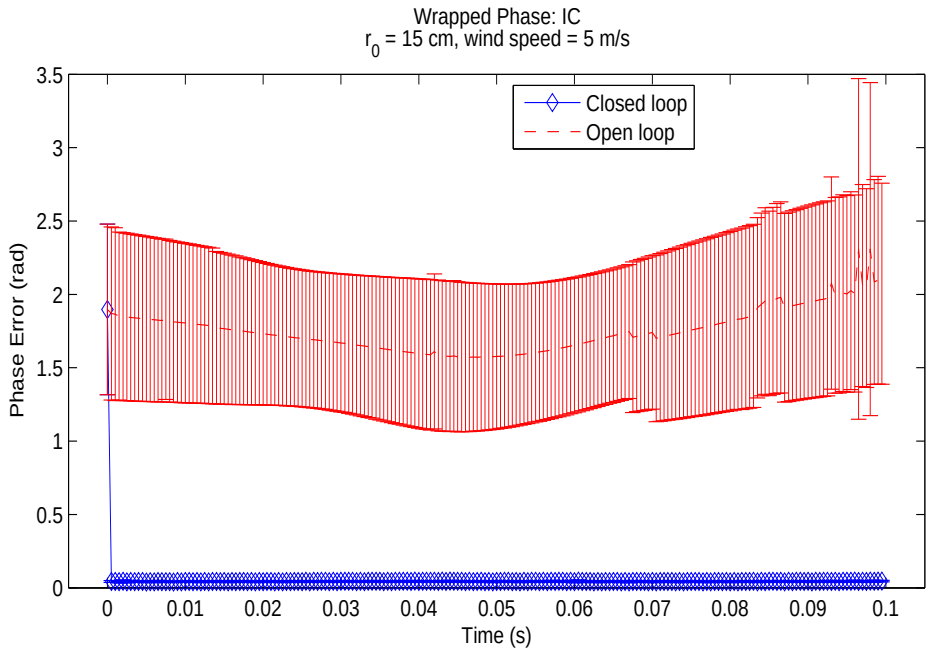

Figure A.17: Wrapped phase WFS, r_0 = 15 cm, wind speed = 5 m/s

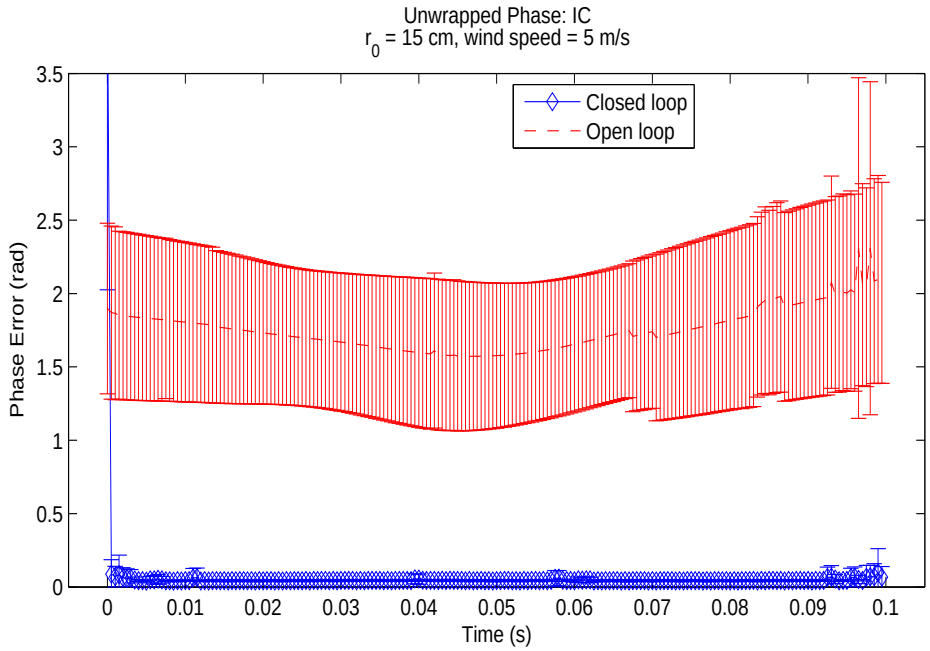

Figure A.18: Unwrapped phase WFS, r_0 = 15 cm, wind speed = 5 m/s

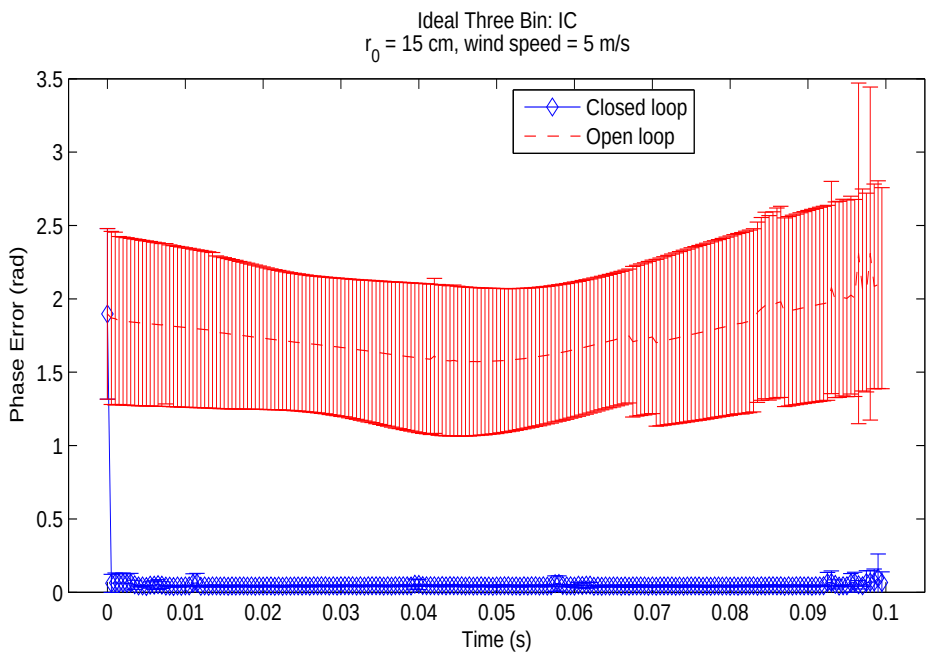

Figure A.19: Ideal Three Bin WFS, r_0 = 15 cm, wind speed = 5 m/s

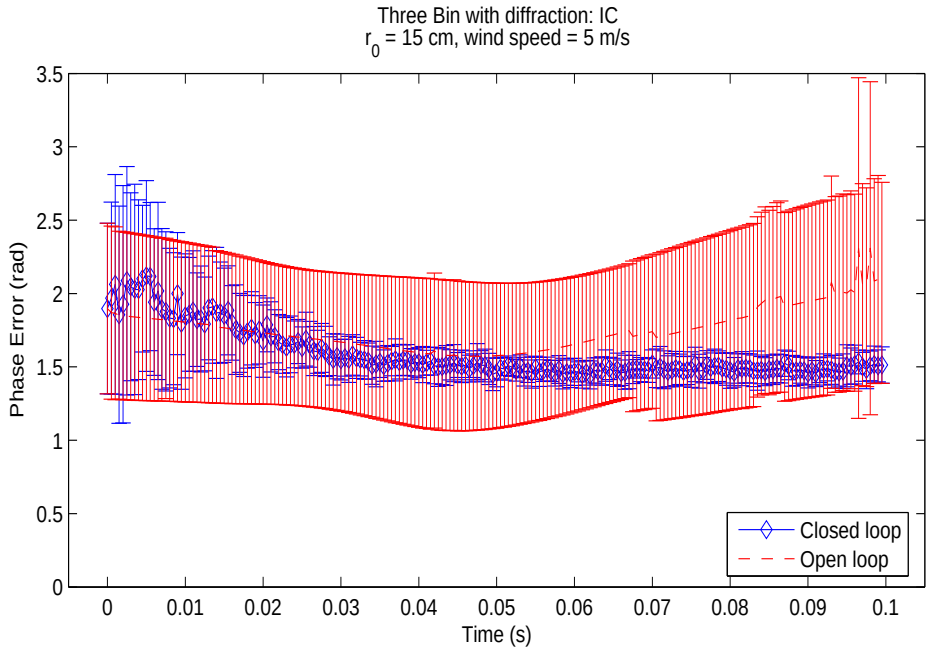

Figure A.20: Three Bin with diffraction WFS, r_0 = 15 cm, wind speed = 5 m/s

A.3.2 wind speed = 10 m/s

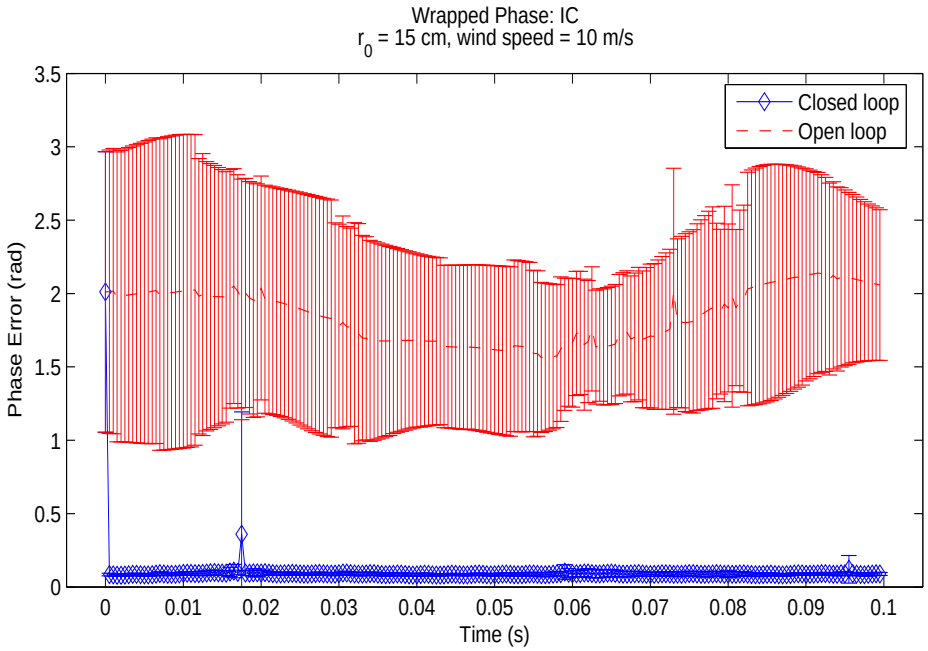

Figure A.21: Wrapped phase WFS, r_0 = 15 cm, wind speed = 10 m/s

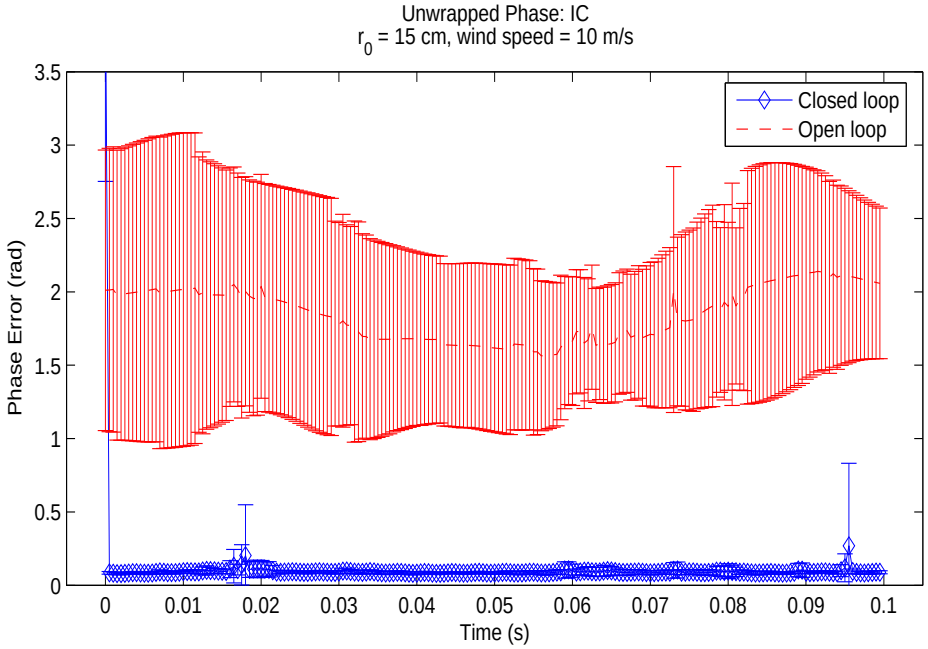

Figure A.22: Unwrapped phase WFS, r_0 = 15 cm, wind speed = 10 m/s

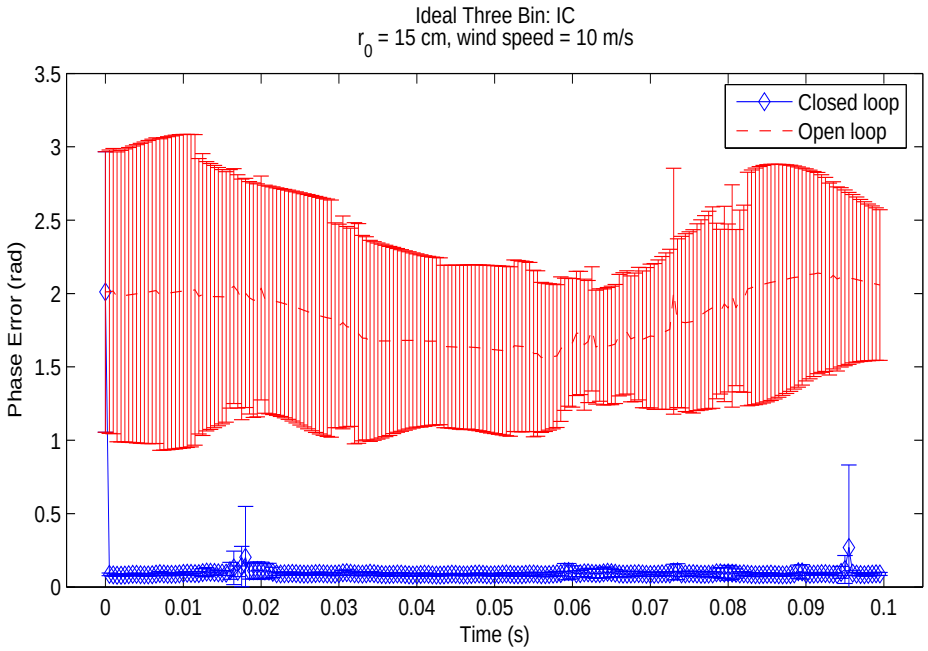

Figure A.23: Ideal Three Bin WFS, r_0 = 15 cm, wind speed = 10 m/s

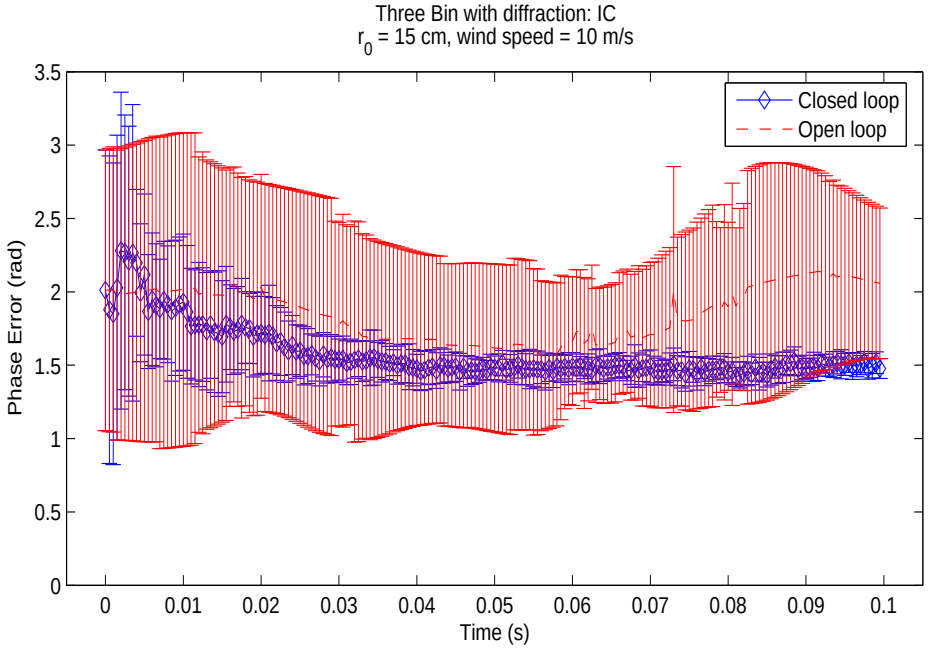

Figure A.24: Three Bin with diffraction WFS, r_0 = 15 cm, wind speed = 10 m/s

A.4 r_0 = 12 cm

A.4.1 wind speed = 5 m/s

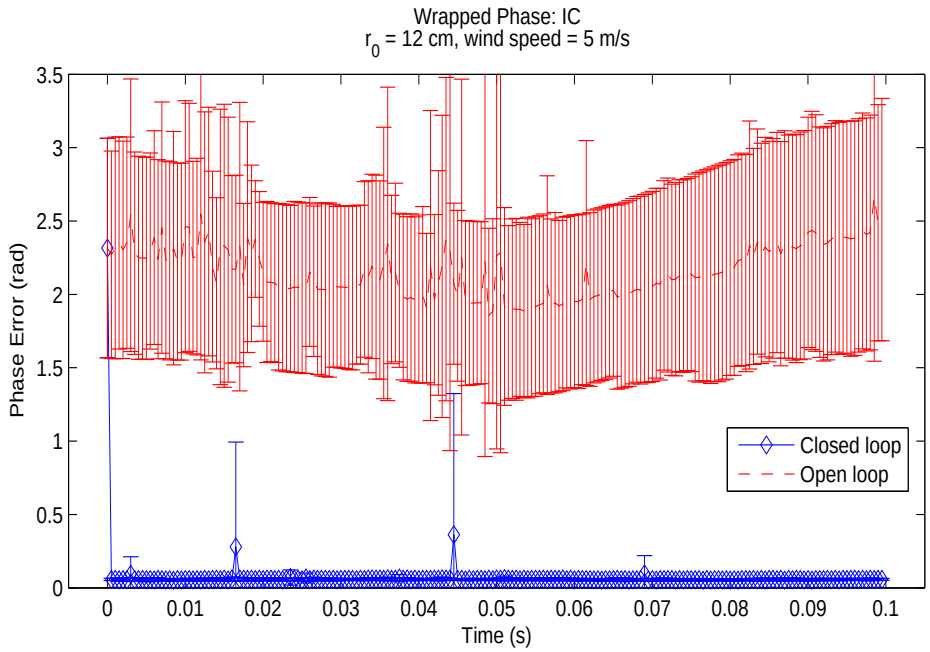

Figure A.25: Wrapped phase WFS, r_0 = 12 cm, wind speed = 5 m/s

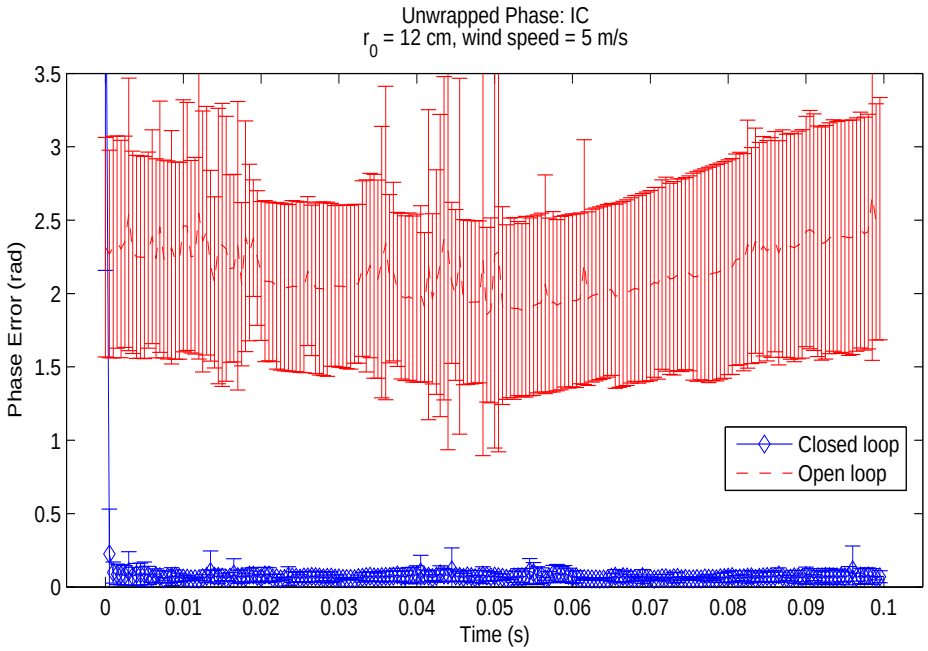

Figure A.26: Unwrapped phase WFS, r_0 = 12 cm, wind speed = 5 m/s

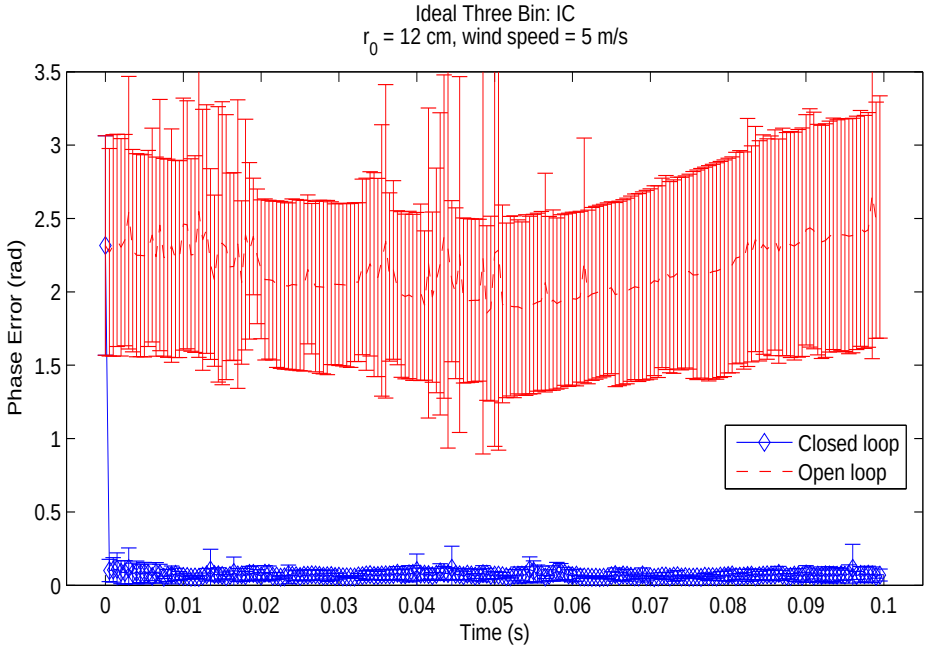

Figure A.27: Ideal Three Bin WFS, r_0 = 12 cm, wind speed = 5 m/s

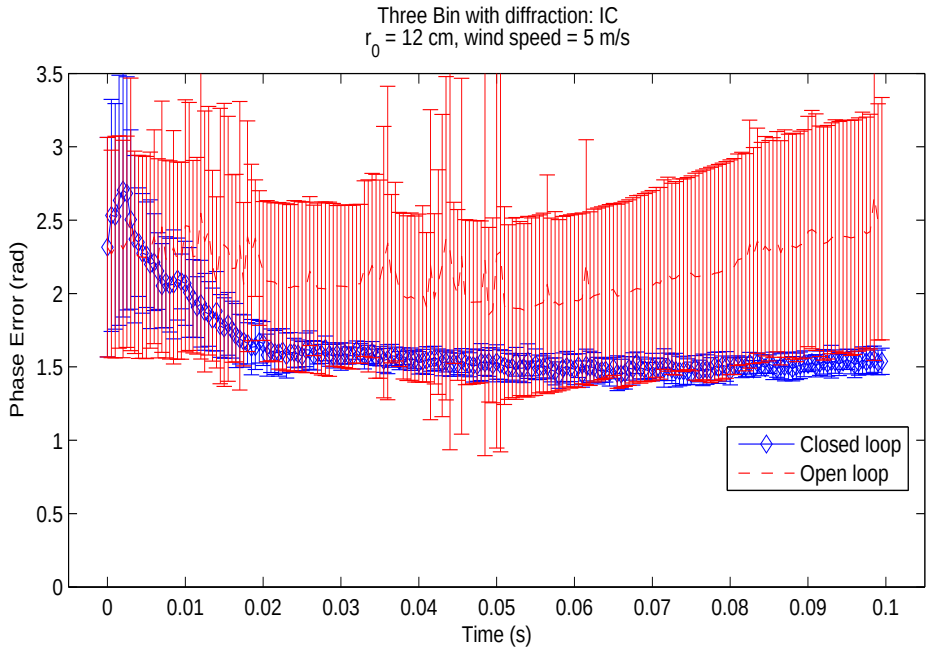

Figure A.28: Three Bin with diffraction WFS, r_0 = 12 cm, wind speed = 5 m/s

A.4.2 wind speed = 10 m/s

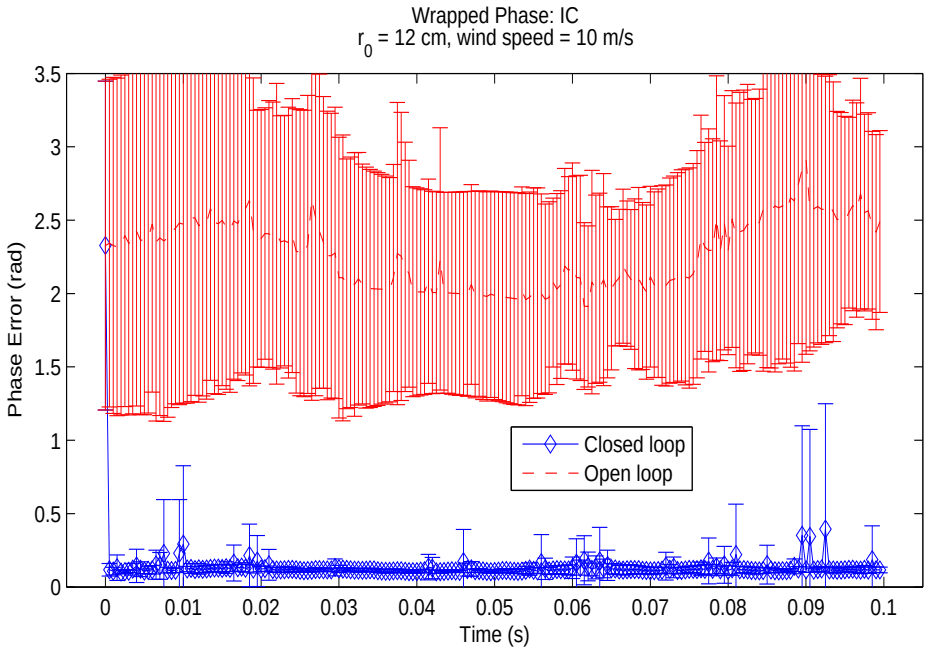

Figure A.29: Wrapped phase WFS, r_0 = 12 cm, wind speed = 10 m/s

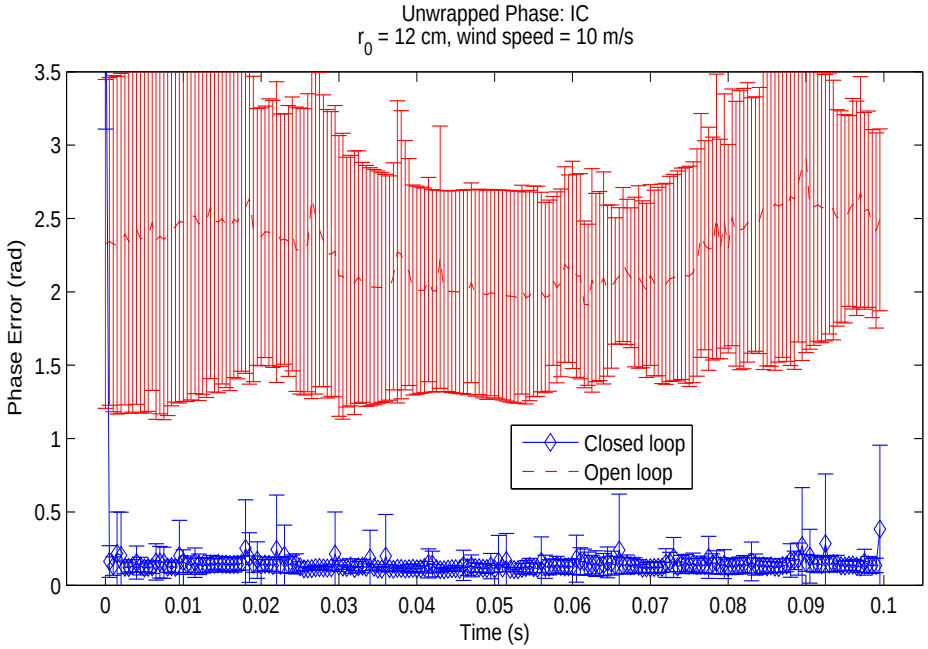

Figure A.30: Unwrapped phase WFS, r_0 = 12 cm, wind speed = 10 m/s

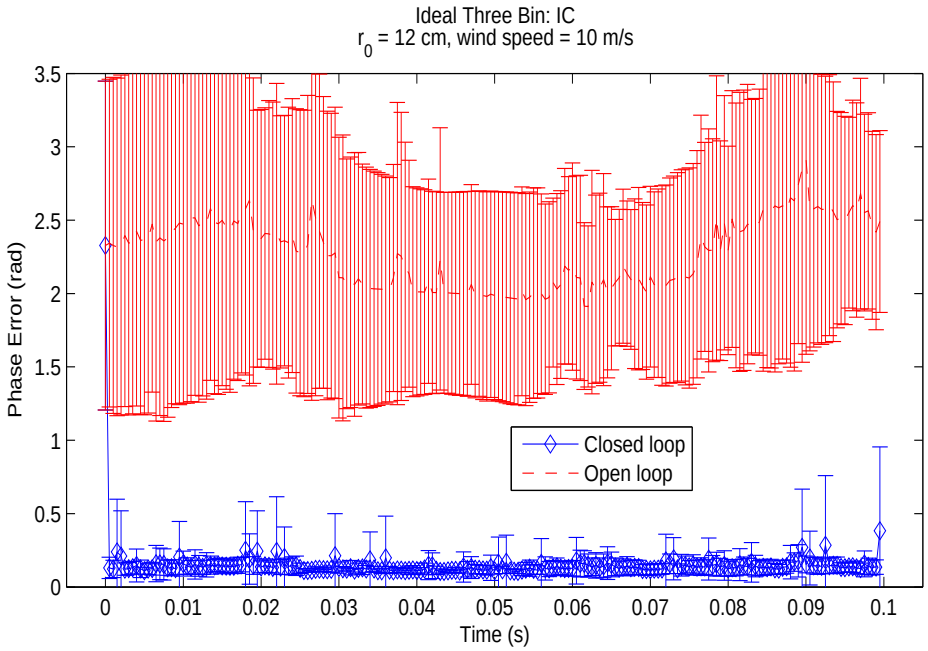

Figure A.31: Ideal Three Bin WFS, r_0 = 12 cm, wind speed = 10 m/s

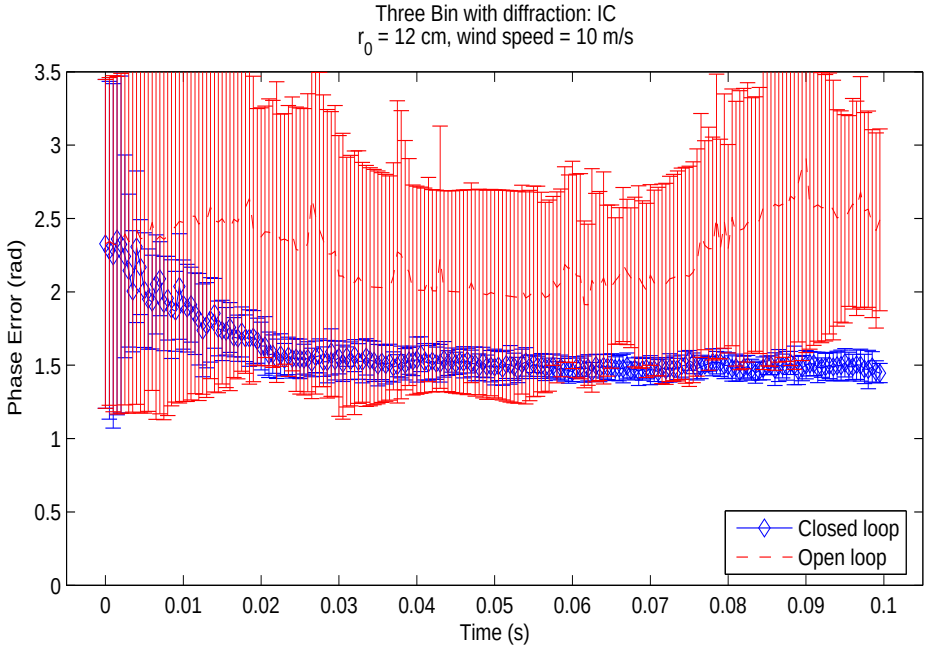

Figure A.32: Three Bin with diffraction WFS, r_0 = 12 cm, wind speed = 10 m/s

Appendix B

NOP CORRECTOR PLOTS I

This appendix collects the detailed plots resulting from the simulations run with the model of the continuous facesheet DM at NOP and with an aperture averaged power over the pupil of 4 μW. The text in section 8.1.3 describes the simulations and section 8.3 sumarizes these results.

B.1 r_0 = 30 cm

B.1.1 wind speed = 0 m/s

With such low turbulence and wind, all three of the loops preform well. The Shack-Hartman loop is operating at its limits of performance. For the same light levels, the FPF WFSs do a better job.

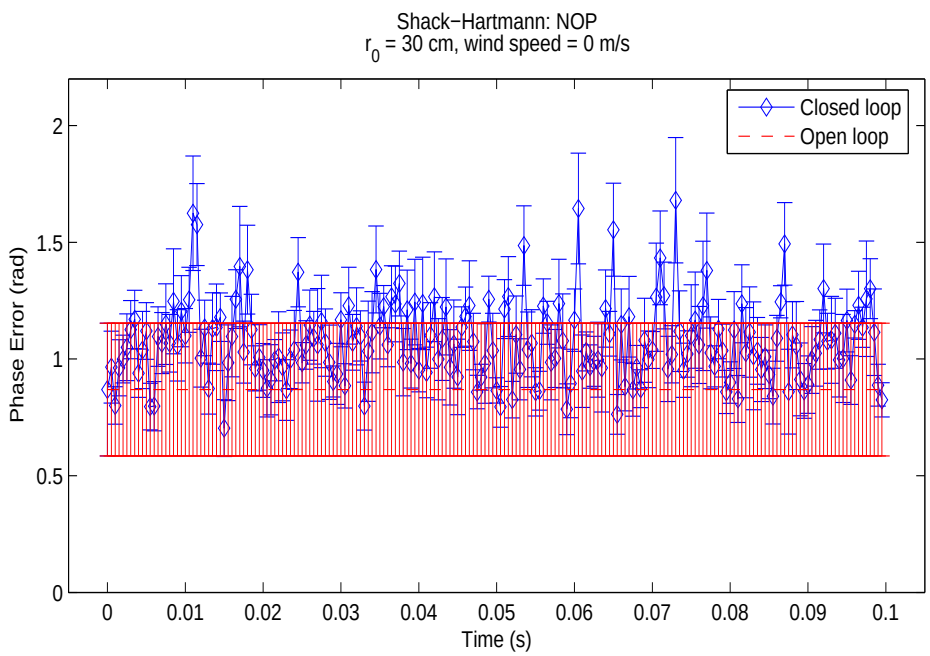

Figure B.1: Shack-Hartmann WFS, r_0 = 30 cm, wind speed = 0 m/s

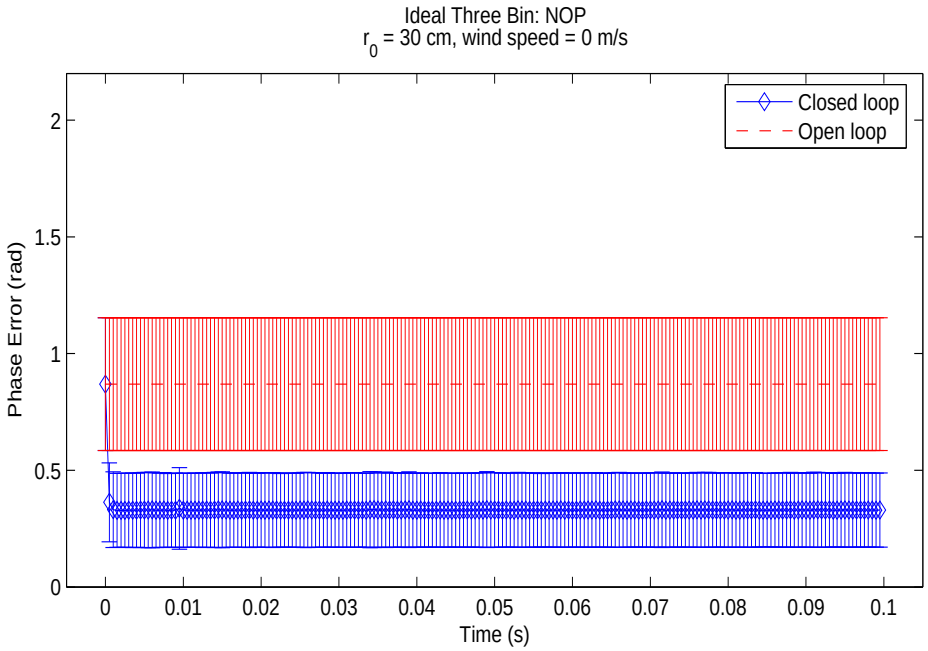

Figure B.2: Ideal Three Bin WFS, r_0 = 30 cm, wind speed = 0 m/s

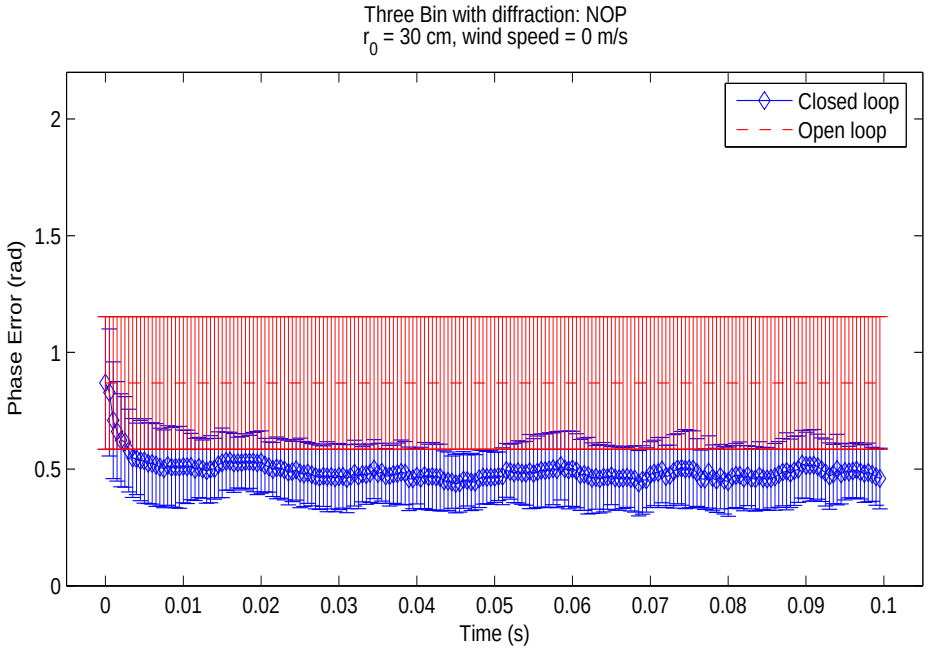

Figure B.3: Three Bin with diffraction WFS, r_0 = 30 cm, wind speed = 0 m/s

B.1.2 wind speed = 5 m/s

As a moderate wind blowing across the propagation path is added, the improvements observed in the FPF WFS systems is still evident.

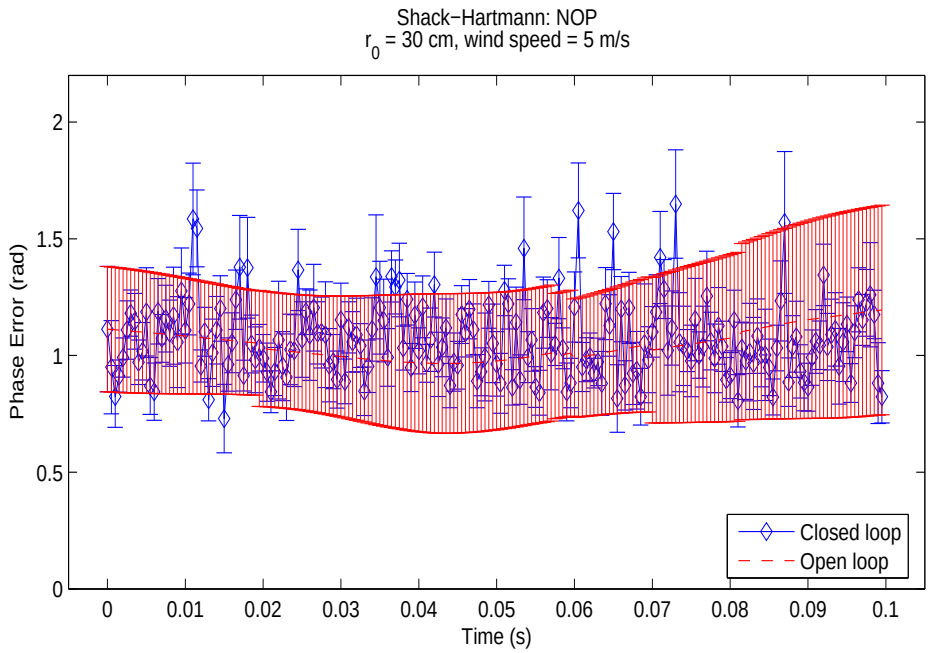

Figure B.4: Shack-Hartmann WFS, r_0 = 30 cm, wind speed = 5 m/s

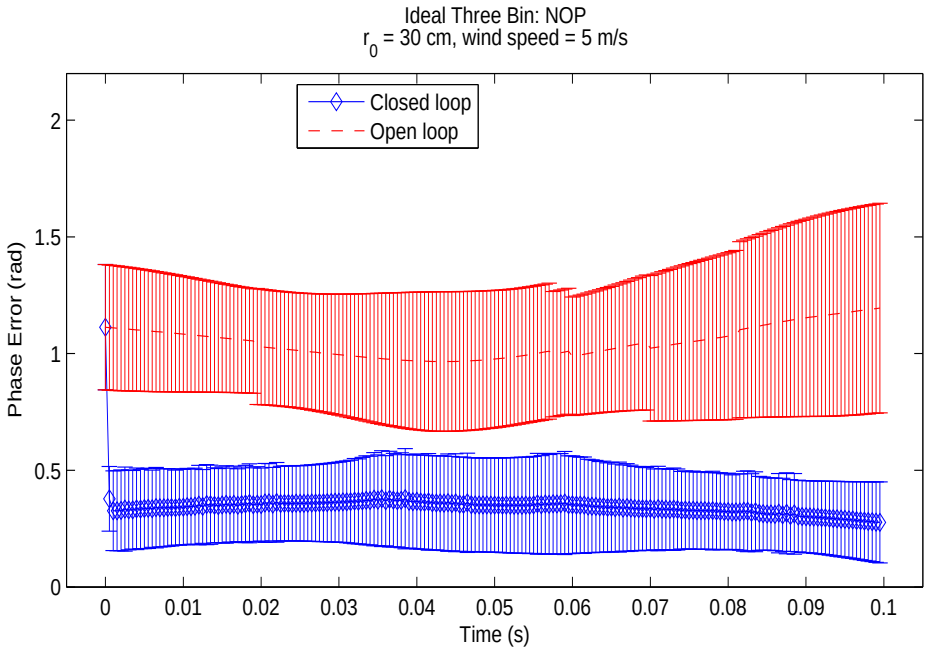

Figure B.5: Ideal Three Bin WFS, r_0 = 30 cm, wind speed = 5 m/s

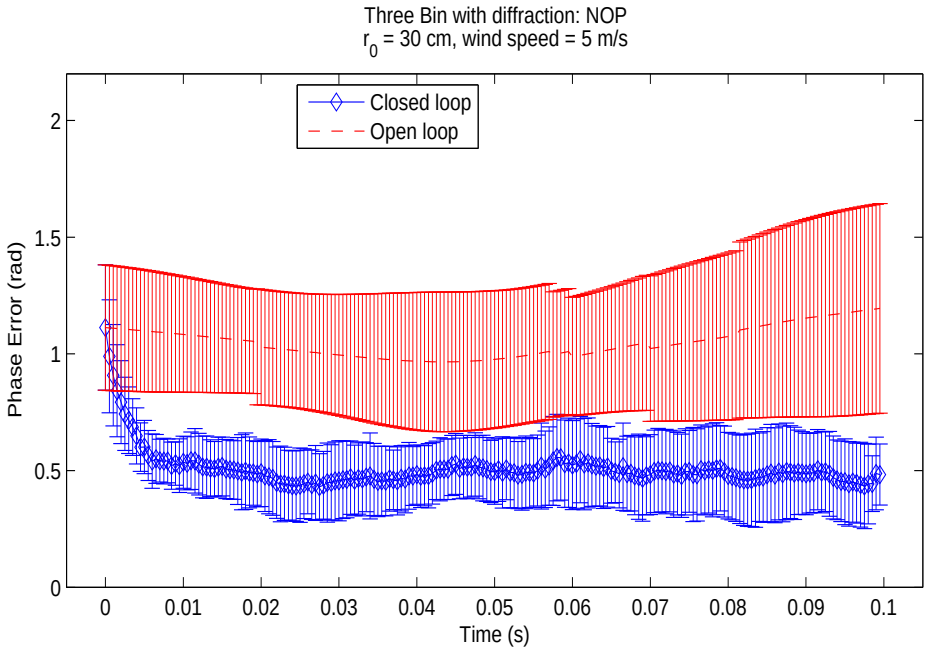

Figure B.6: Three Bin with diffraction WFS, r_0 = 30 cm, wind speed = 5 m/s

B.1.3 wind speed = 10 m/s

With the 10 m/s wind, the FPF WFS that includes diffractive effects shows a marked degradation in performance. The cause of this is unclear since the next set of runs with a stiffer (20 m/s) wind do not exhibit the same behavior.

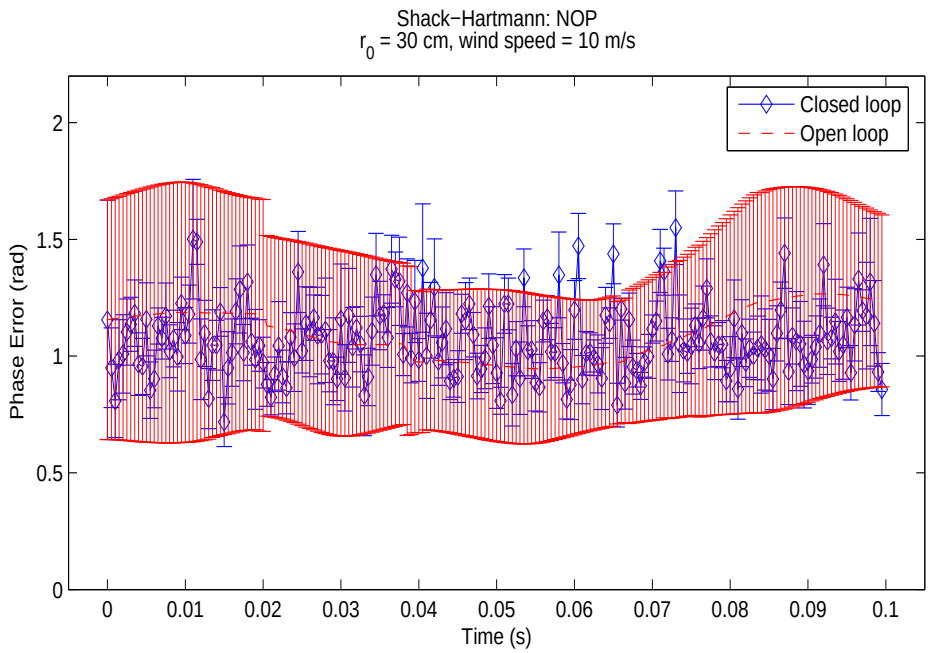

Figure B.7: Shack-Hartmann WFS, r_0 = 30 cm, wind speed = 10 m/s

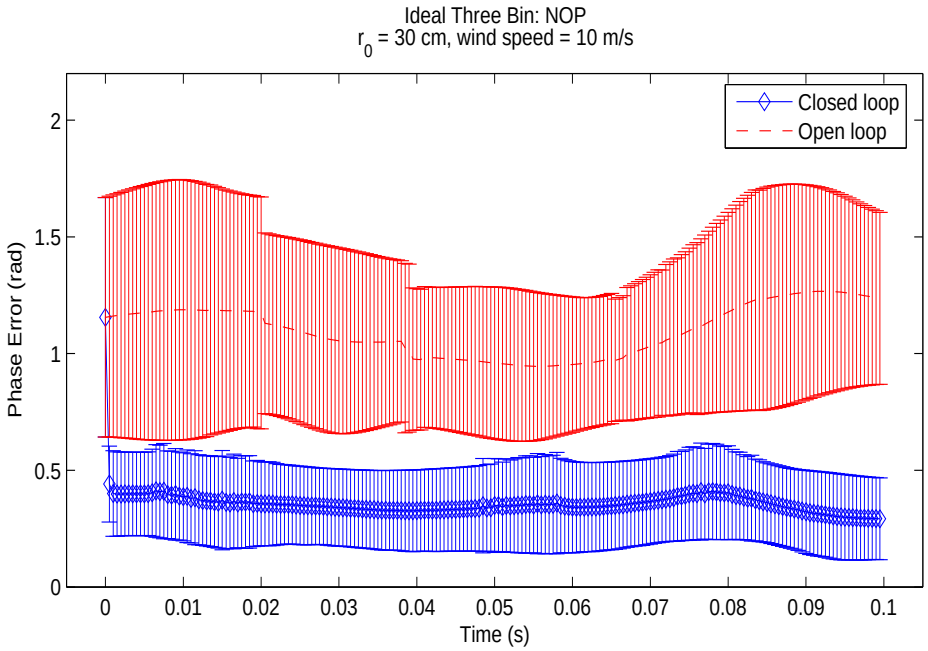

Figure B.8: Ideal Three Bin WFS, r_0 = 30 cm, wind speed = 10 m/s

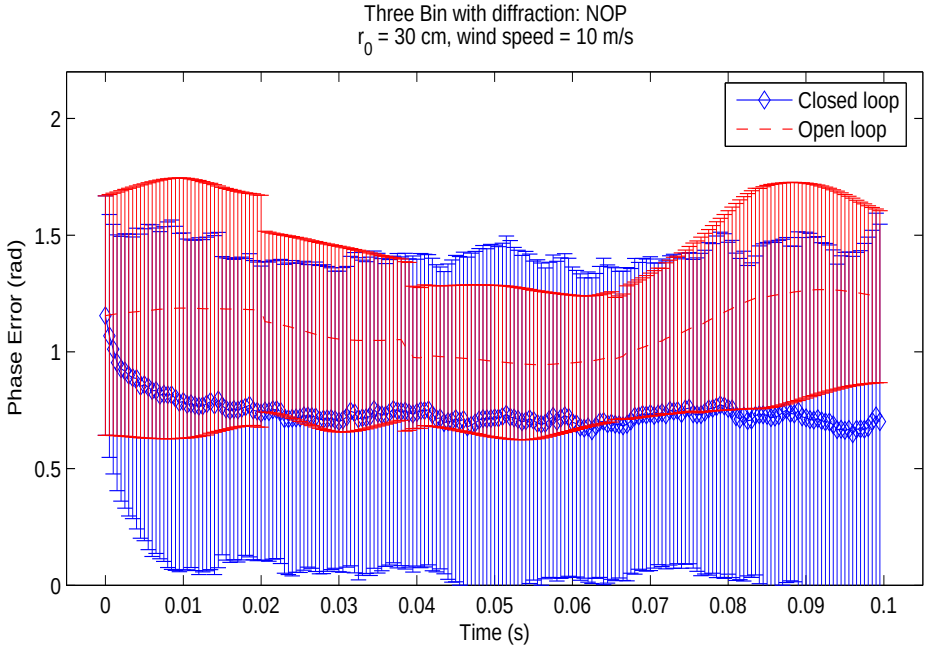

Figure B.9: Three Bin with diffraction WFS, r_0 = 30 cm, wind speed = 10 m/s

B.1.4 wind speed = 20 m/s

With a stiff wind the model of the FPF WFS again shows performance on par with the ideal system. Both outperform the Shack-Hartmann.

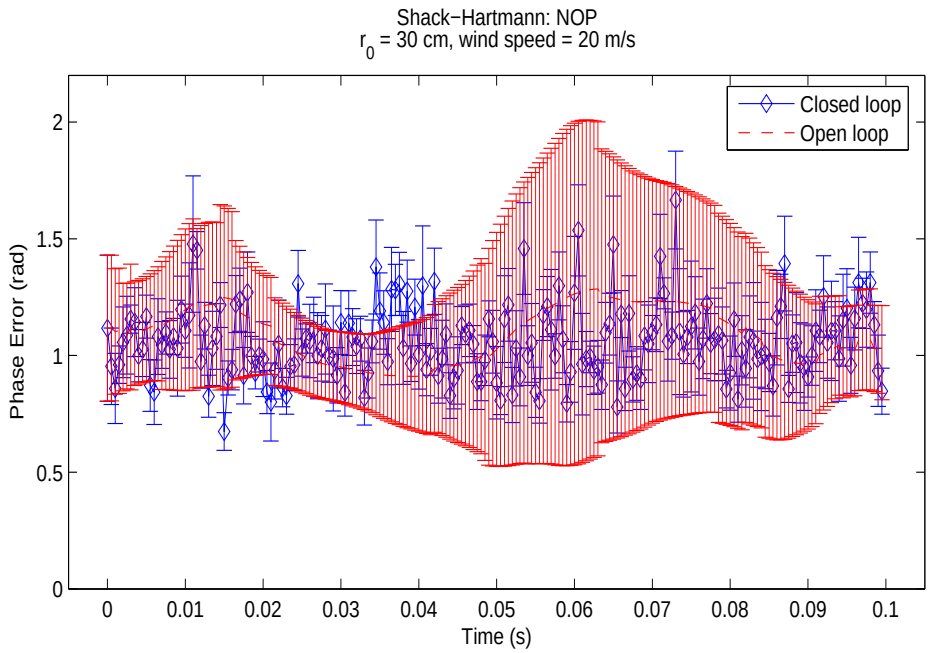

Figure B.10: Shack-Hartmann WFS, r_0 = 30 cm, wind speed = 20 m/s

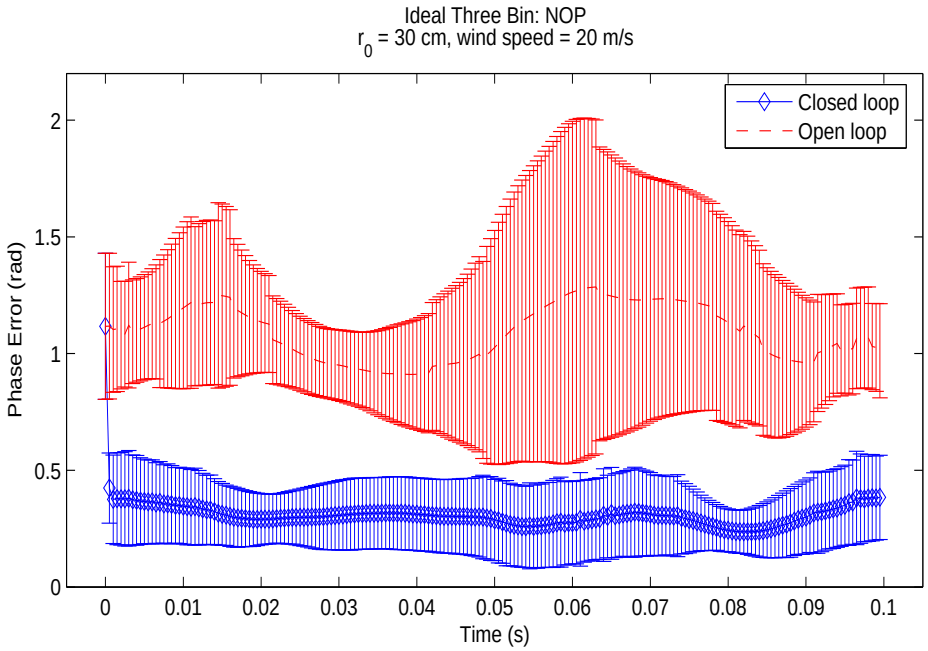

Figure B.11: Ideal Three Bin WFS, r_0 = 30 cm, wind speed = 20 m/s

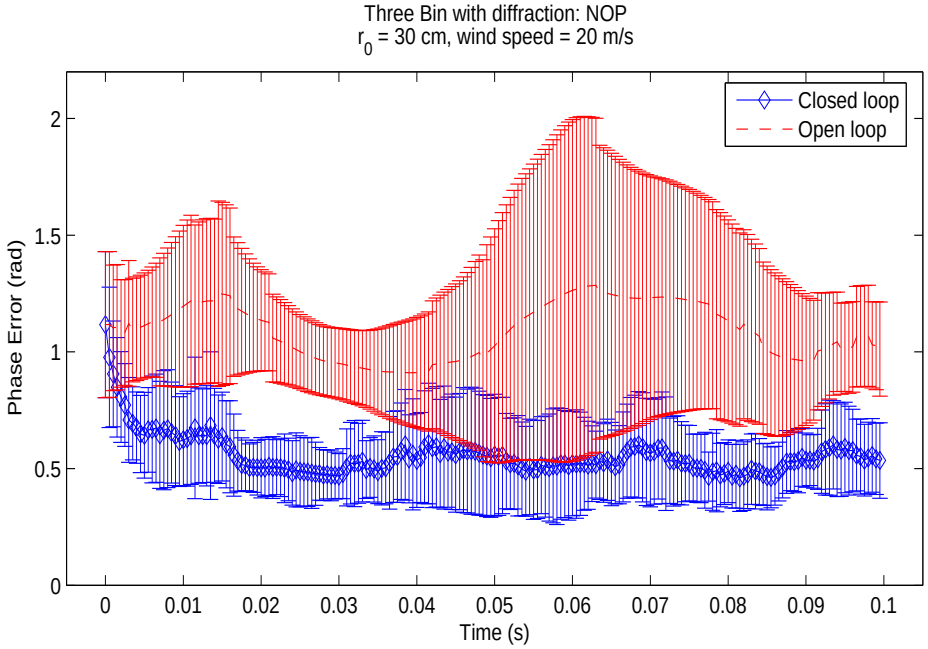

Figure B.12: Three Bin with diffraction WFS, r_0 = 30 cm, wind speed = 20 m/s

B.2 r_0 **=** 20 cm

For these next several series the turbulence strength is increased to a still moderate r_0 = 20 cm. The low wind speed cases still show marked improvement with the FPF WFS systems.

B.2.1 wind speed = 0 m/s

There is not much change between this case and the case of r_0 = 30 cm, with wind speed = 0 m/s.

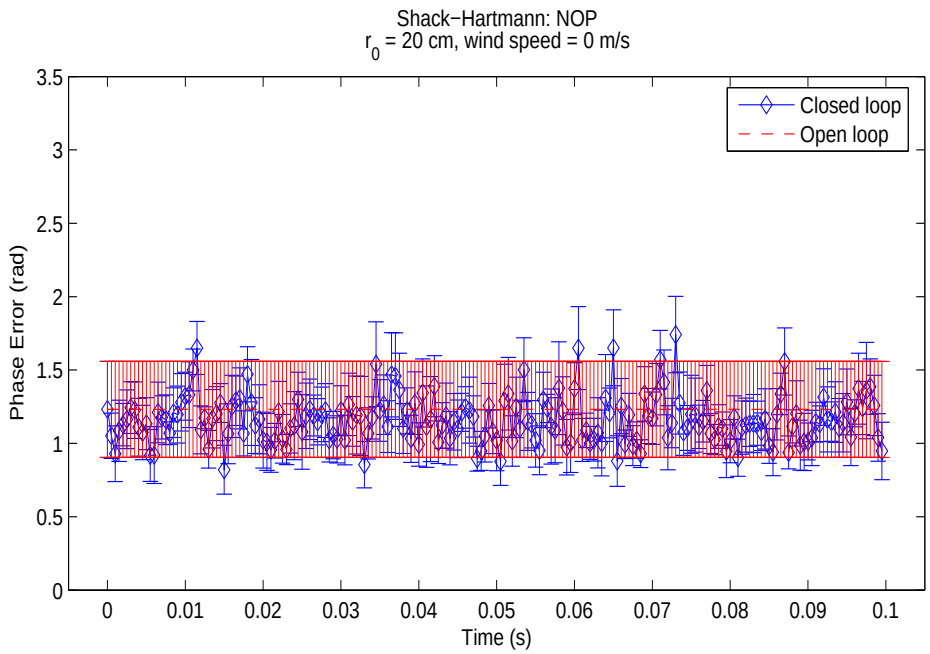

Figure B.13: Shack-Hartmann WFS, r_0 = 20 cm, wind speed = 0 m/s

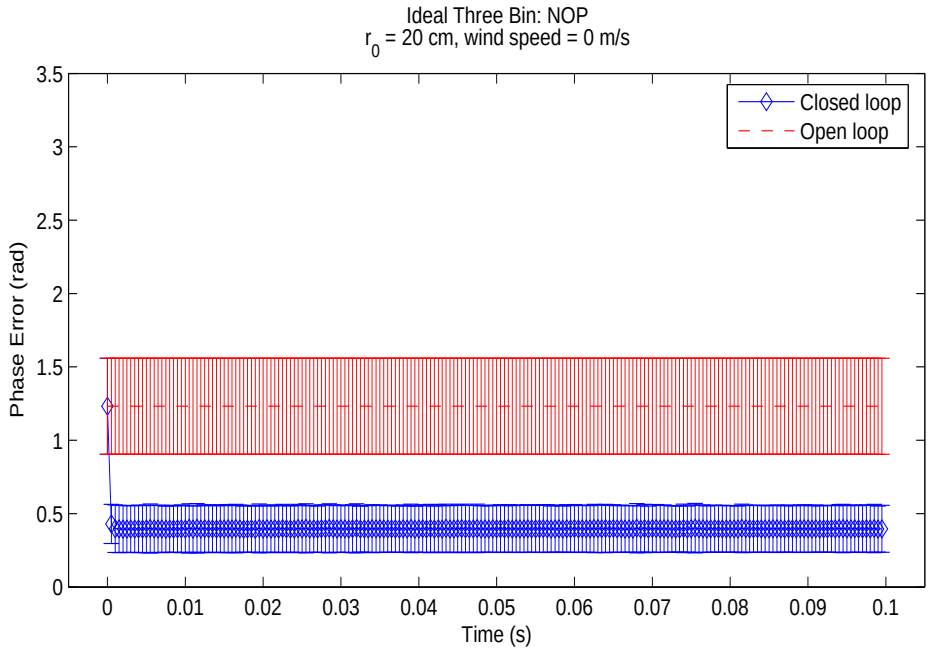

Figure B.14: Ideal Three Bin WFS, r_0 = 20 cm, wind speed = 0 m/s

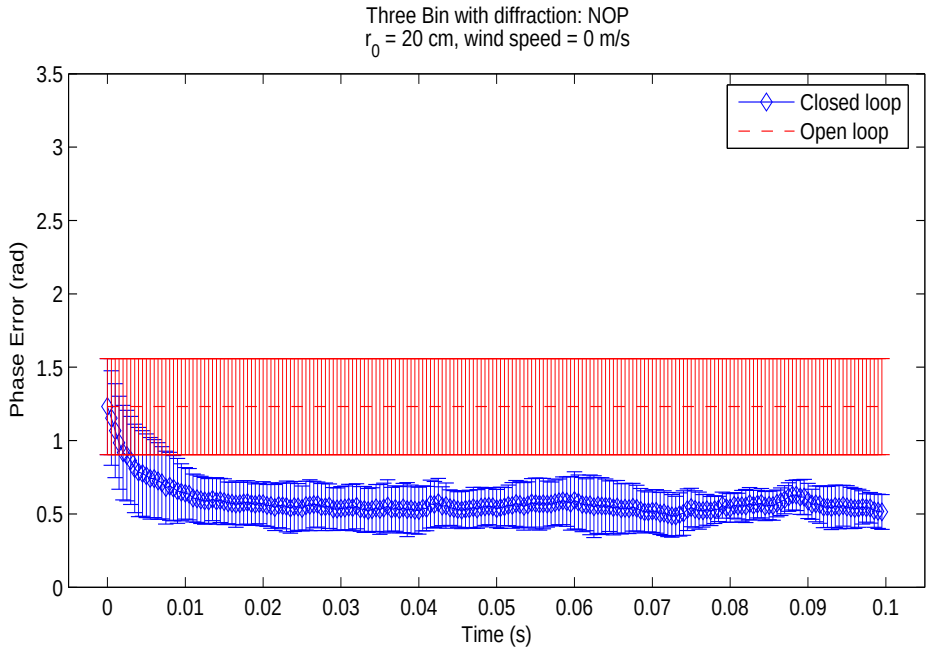

Figure B.15: Three Bin with diffraction WFS, r_0 = 20 cm, wind speed = 0 m/s

B.2.2 wind speed = 5 m/s

For these runs, the FPF WFSs still show significant improvement, but the diffractive case is starting to show some strain.

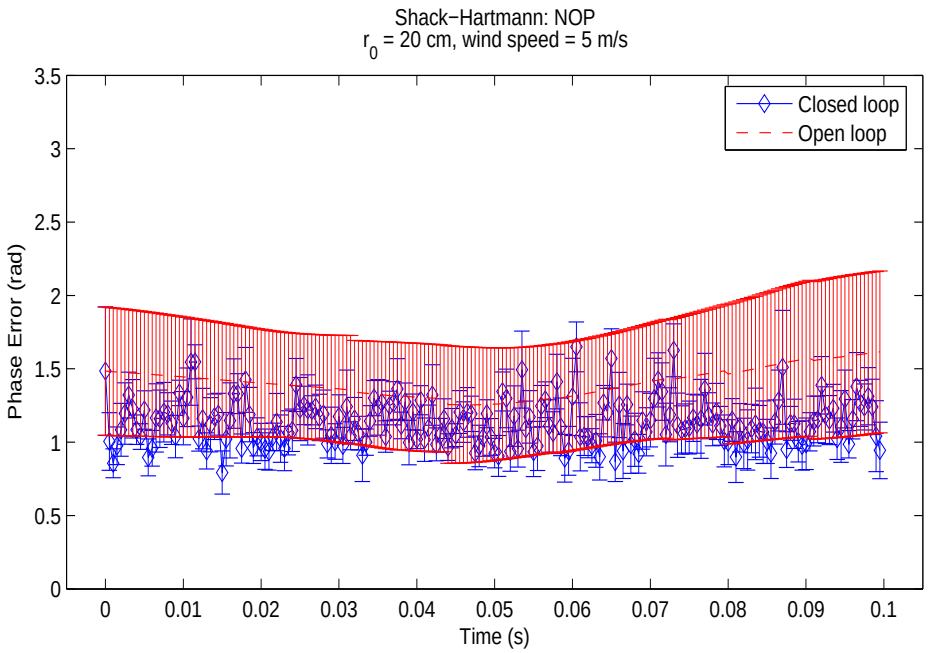

Figure B.16: Shack-Hartmann WFS, r_0 = 20 cm, wind speed = 5 m/s

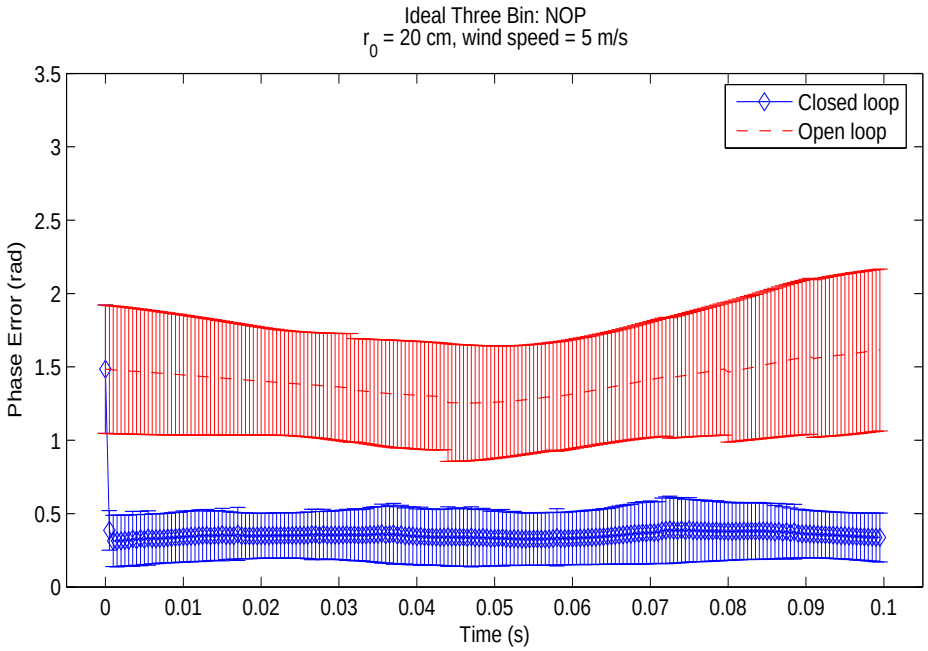

Figure B.17: Ideal Three Bin WFS, r_0 = 20 cm, wind speed = 5 m/s

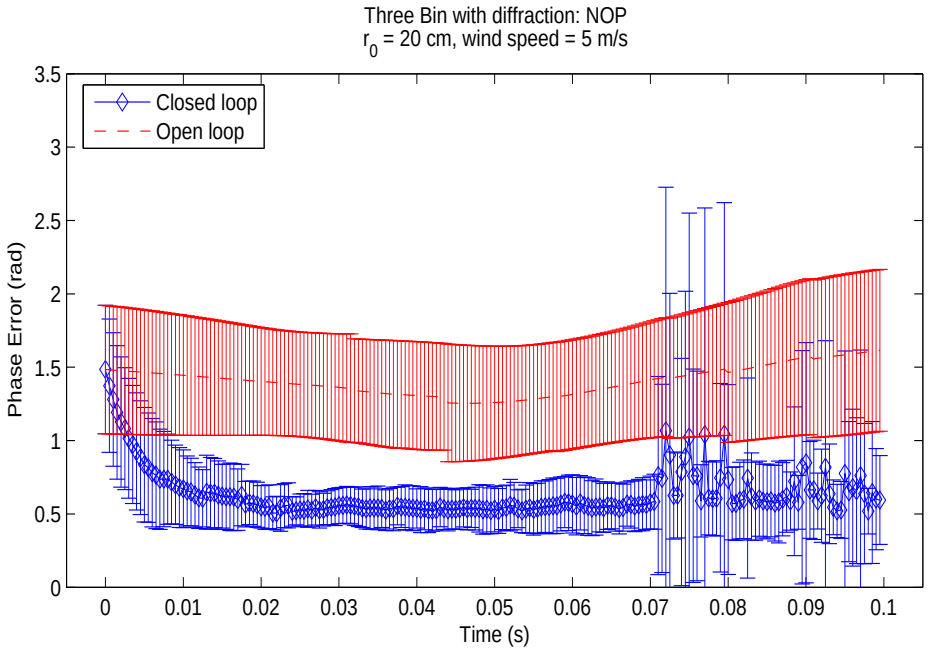

Figure B.18: Three Bin with diffraction WFS, r_0 = 20 cm, wind speed = 5 m/s

B.2.3 wind speed = 10 m/s

As with the runs in figure B.9, the FPF loop with diffraction is not stable. Unlike that case, the system does not return to stability in the stiffer wind.

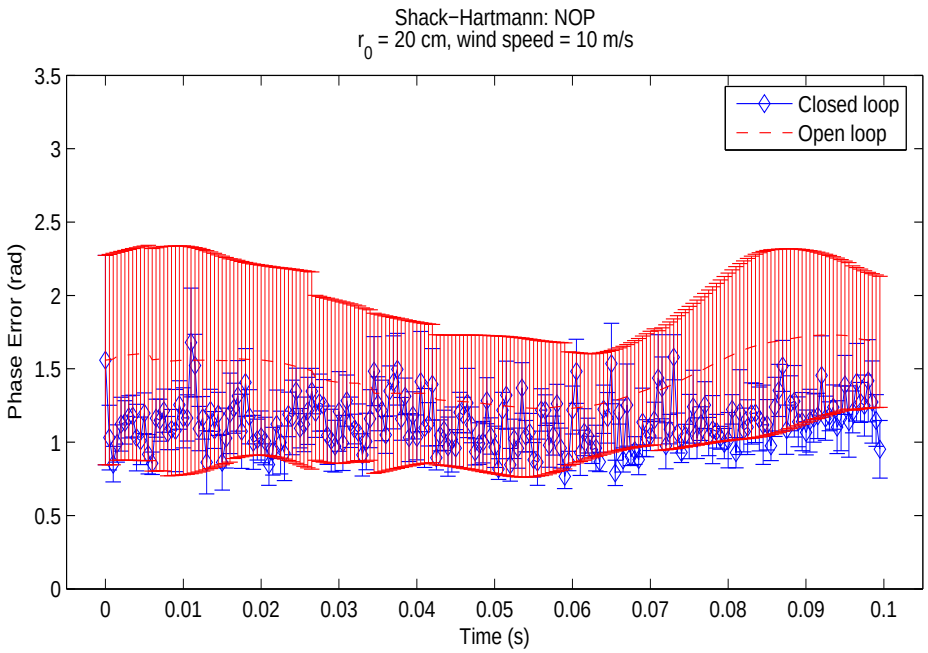

Figure B.19: Shack-Hartmann WFS, r_0 = 20 cm, wind speed = 10 m/s

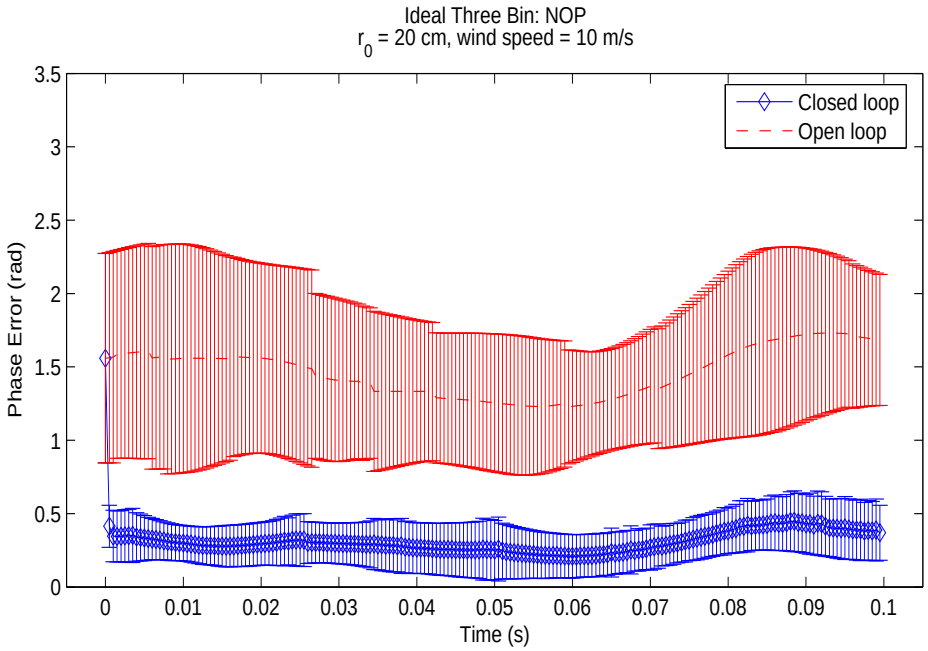

Figure B.20: Ideal Three Bin WFS, r_0 = 20 cm, wind speed = 10 m/s

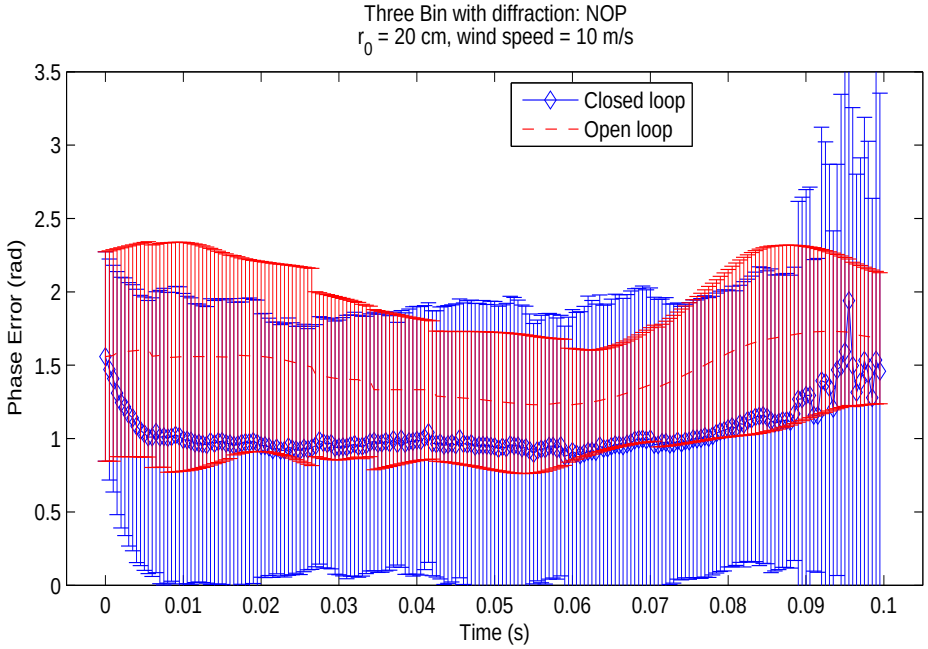

Figure B.21: Three Bin with diffraction WFS, r_0 = 20 cm, wind speed = 10 m/s

B.2.4 wind speed = 20 m/s

Here, while the ideal three bin loop is still showing excellent performance, the diffractive three bin loop is growing more unstable. It appears that it is sensing noise as wavefront perturbations.

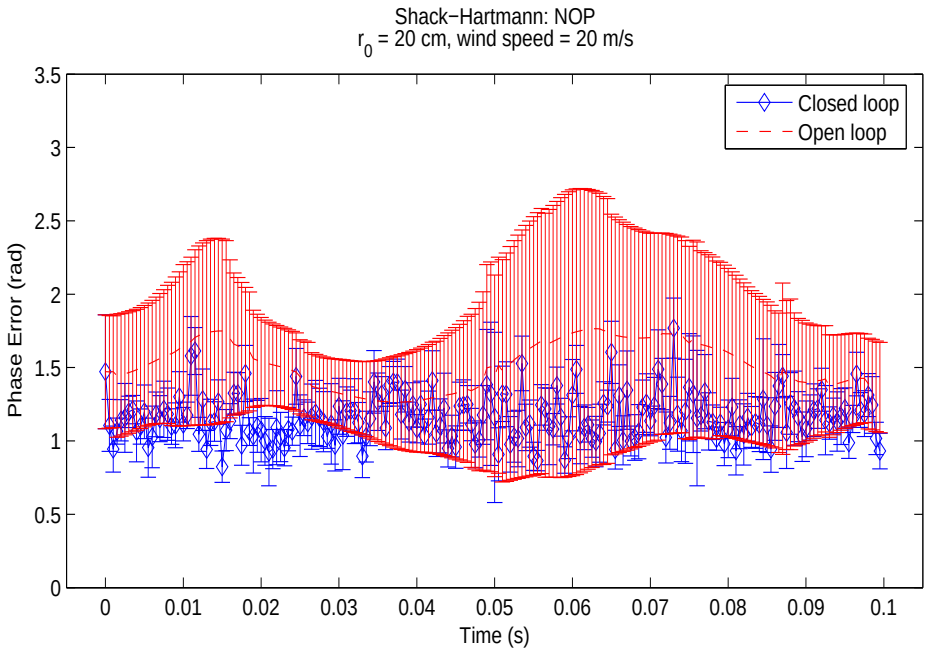

Figure B.22: Shack-Hartmann WFS, r_0 = 20 cm, wind speed = 20 m/s

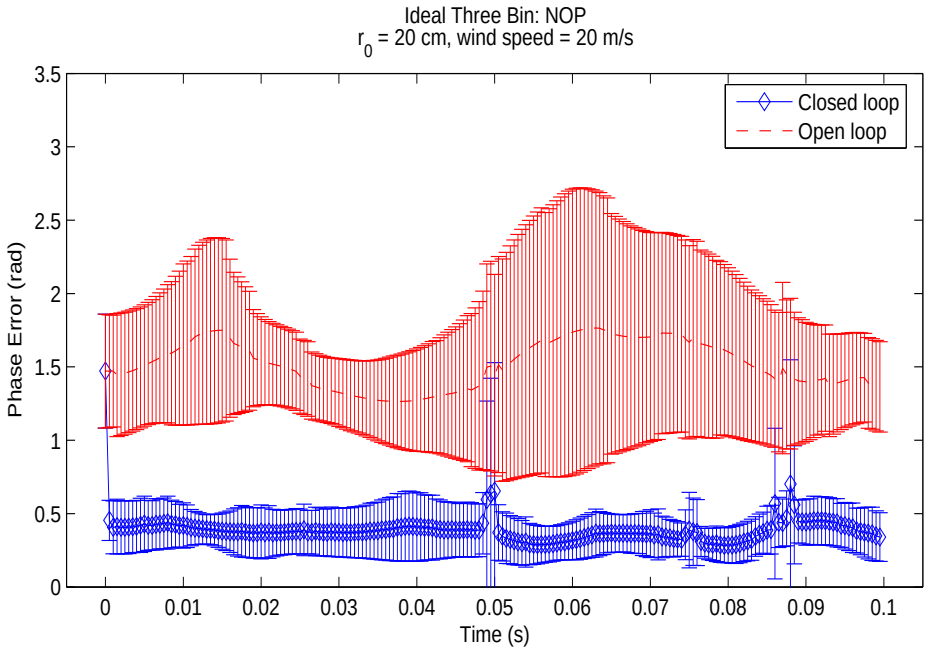

Figure B.23: Ideal Three Bin WFS, r_0 = 20 cm, wind speed = 20 m/s

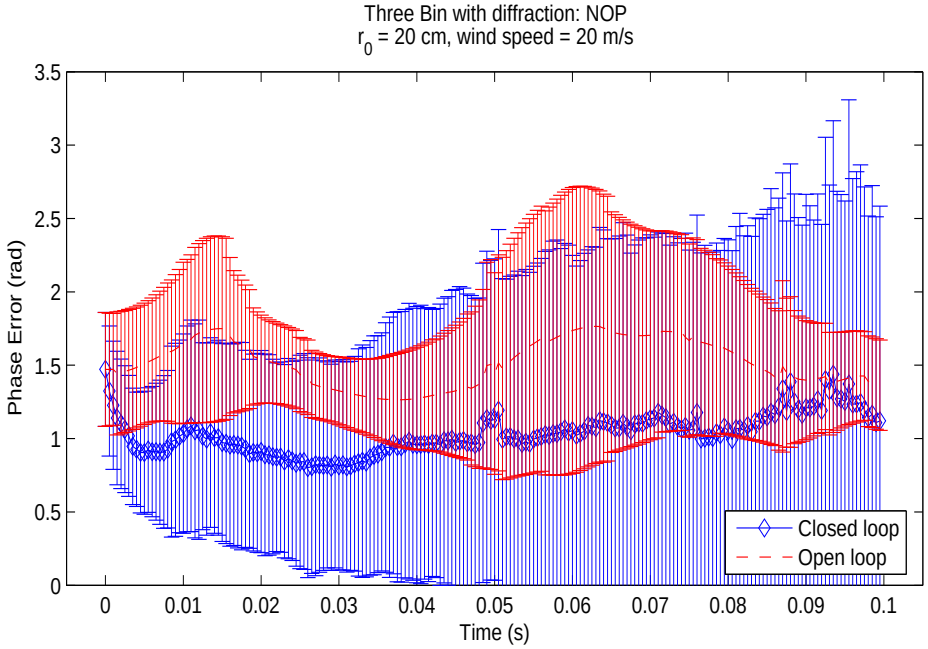

Figure B.24: Three Bin with diffraction WFS, r_0 = 20 cm, wind speed = 20 m/s

B.3 r_0 **=** 15 cm

With an r_0 value of 15 cm, the results for each of the three systems are fairly independent of wind speed: The Shack-Hartmann system is having problems due to low light levels; the ideal three bin loop is correcting well; and the three bin loop with diffraction starts to correct, but then runs into problems as measurement noise causes it to become unstable.

B.3.1 wind speed = 0 m/s

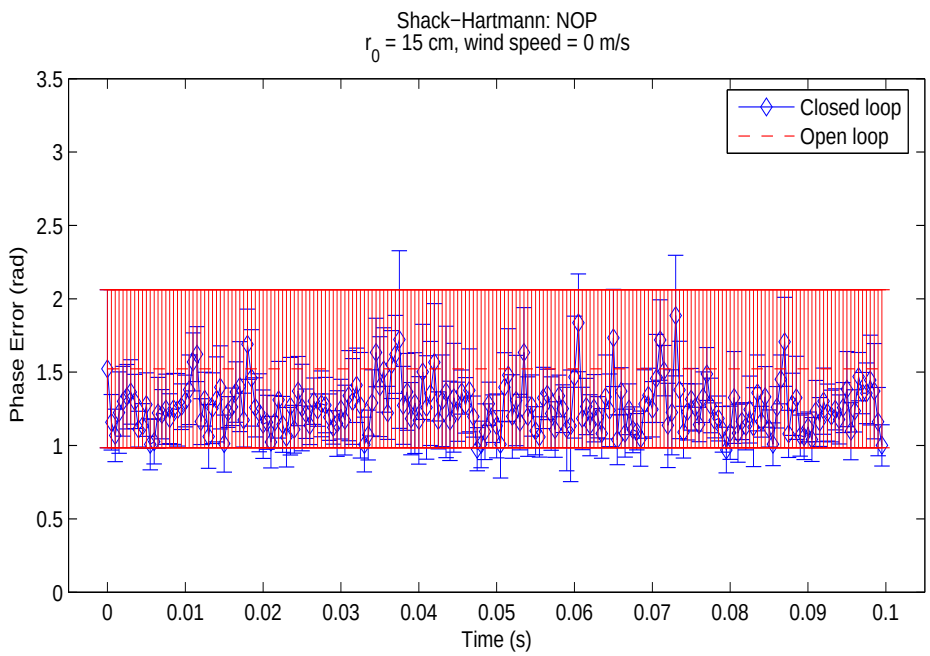

Figure B.25: Shack-Hartmann WFS, r_0 = 15 cm, wind speed = 0 m/s

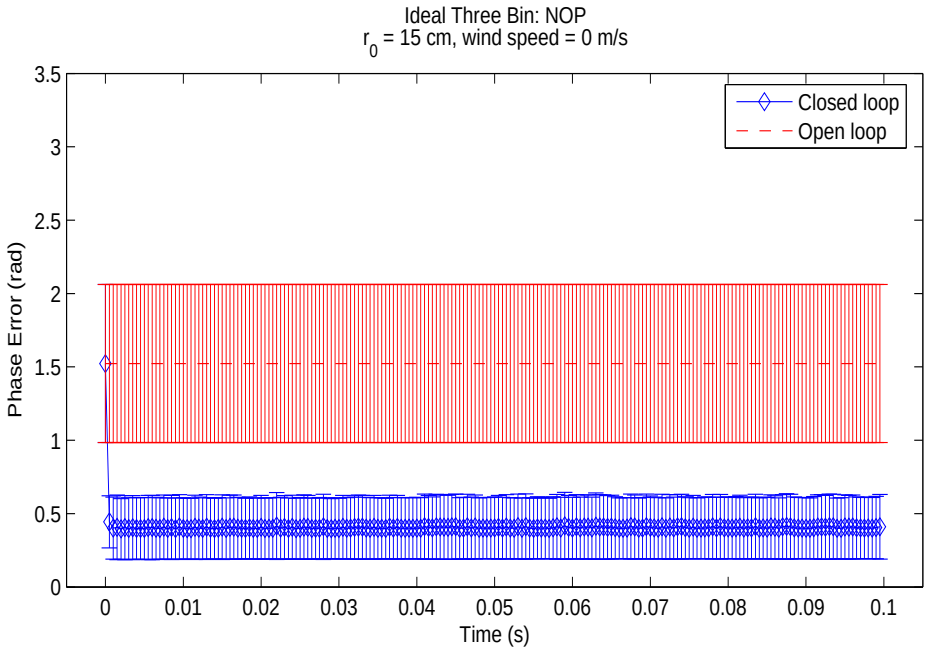

Figure B.26: Ideal Three Bin WFS, r_0 = 15 cm, wind speed = 0 m/s

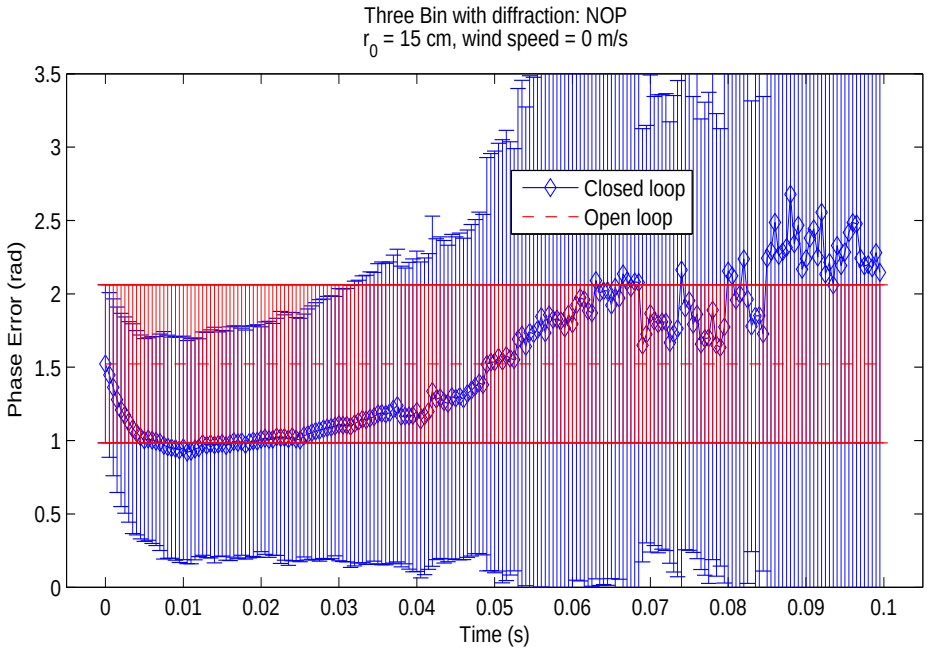

Figure B.27: Three Bin with diffraction WFS, r_0 = 15 cm, wind speed = 0 m/s

B.3.2 wind speed = 5 m/s

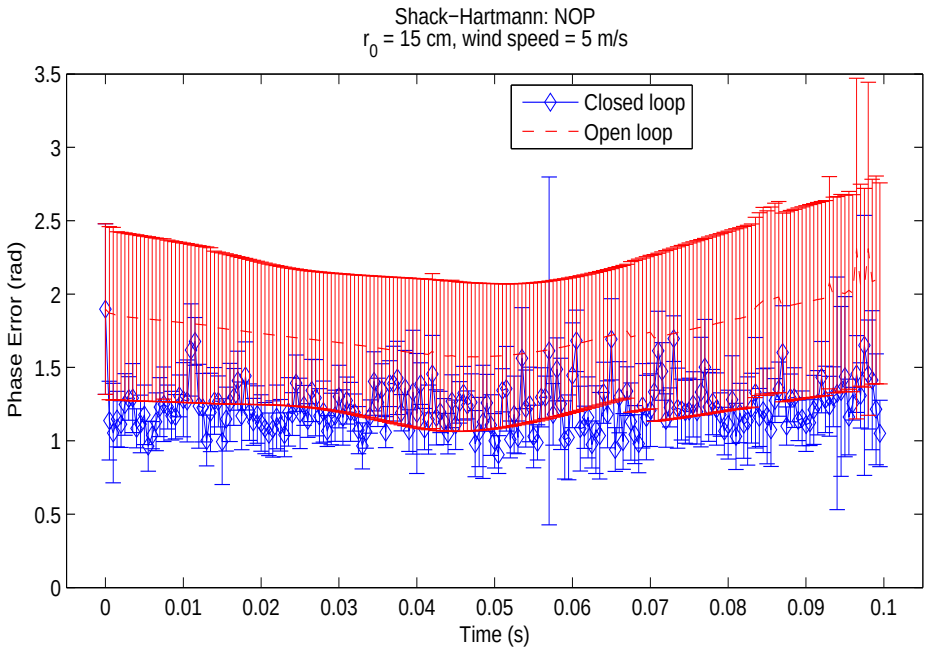

Figure B.28: Shack-Hartmann WFS, r_0 = 15 cm, wind speed = 5 m/s

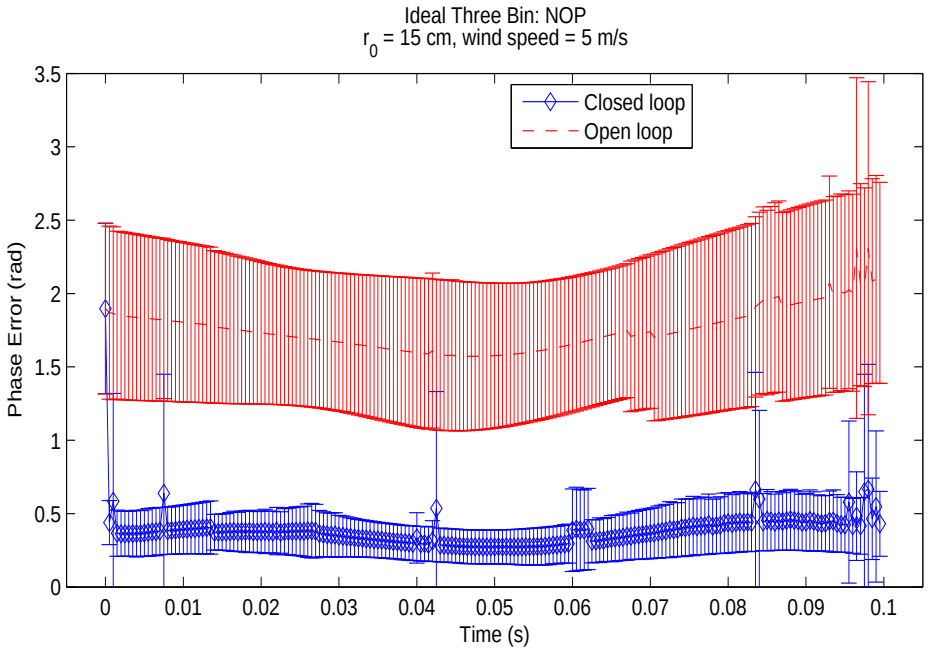

Figure B.29: Ideal Three Bin WFS, r_0 = 15 cm, wind speed = 5 m/s

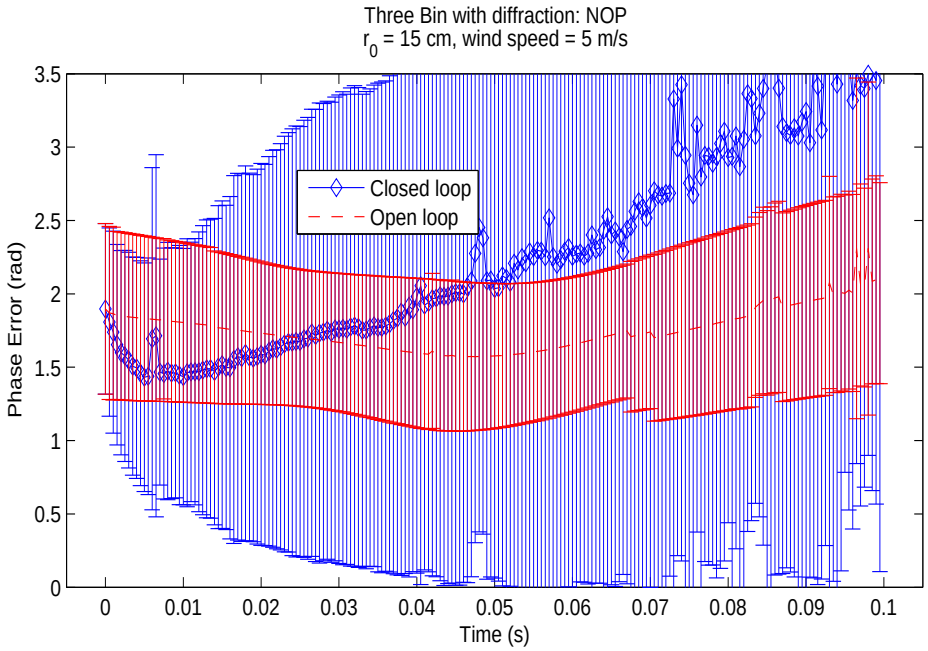

Figure B.30: Three Bin with diffraction WFS, r_0 = 15 cm, wind speed = 5 m/s

B.3.3 wind speed = 10 m/s

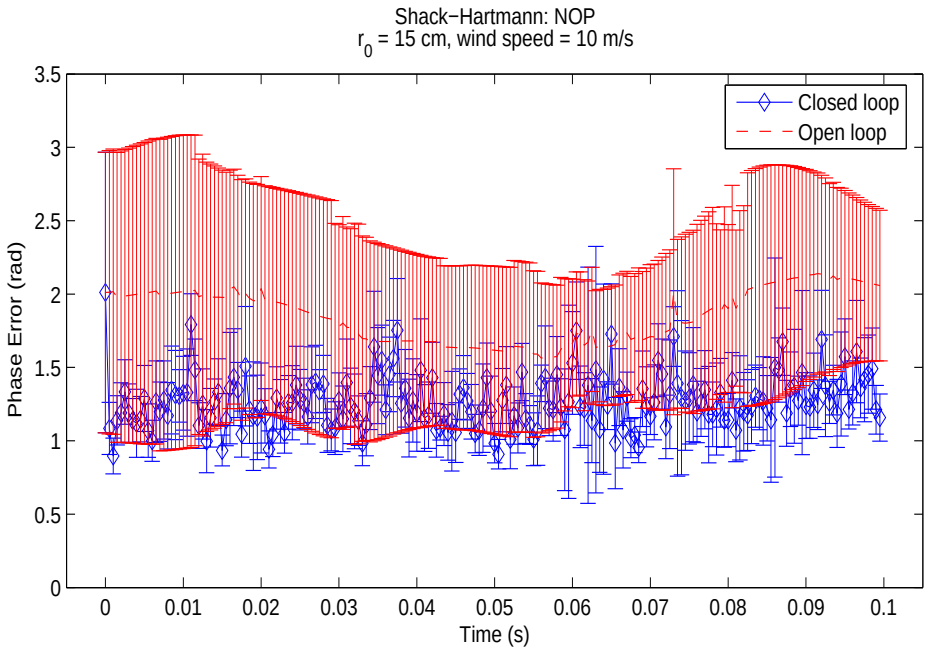

Figure B.31: Shack-Hartmann WFS, r_0 = 15 cm, wind speed = 10 m/s

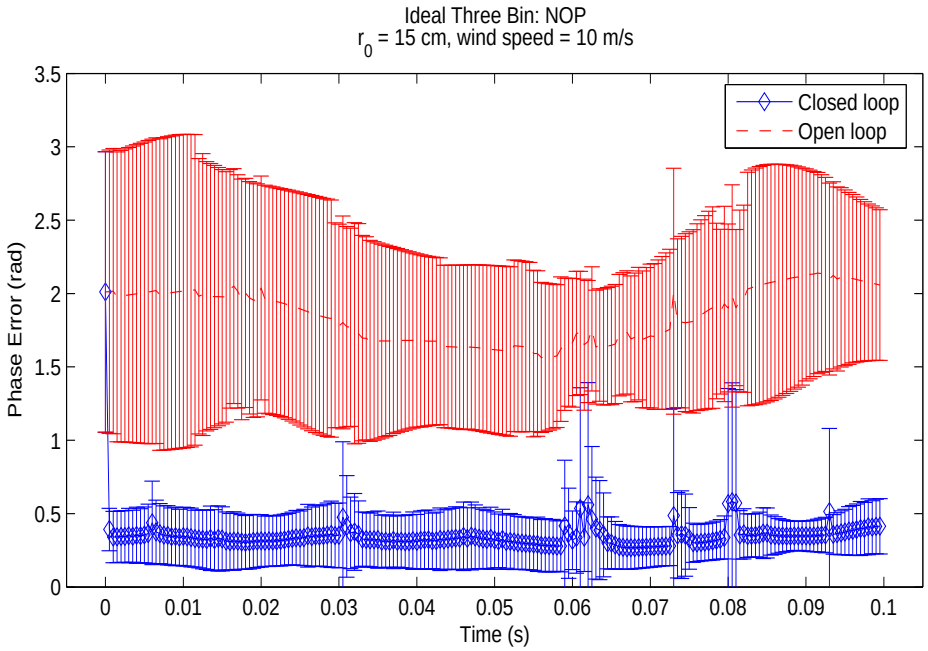

Figure B.32: Ideal Three Bin WFS, r_0 = 15 cm, wind speed = 10 m/s

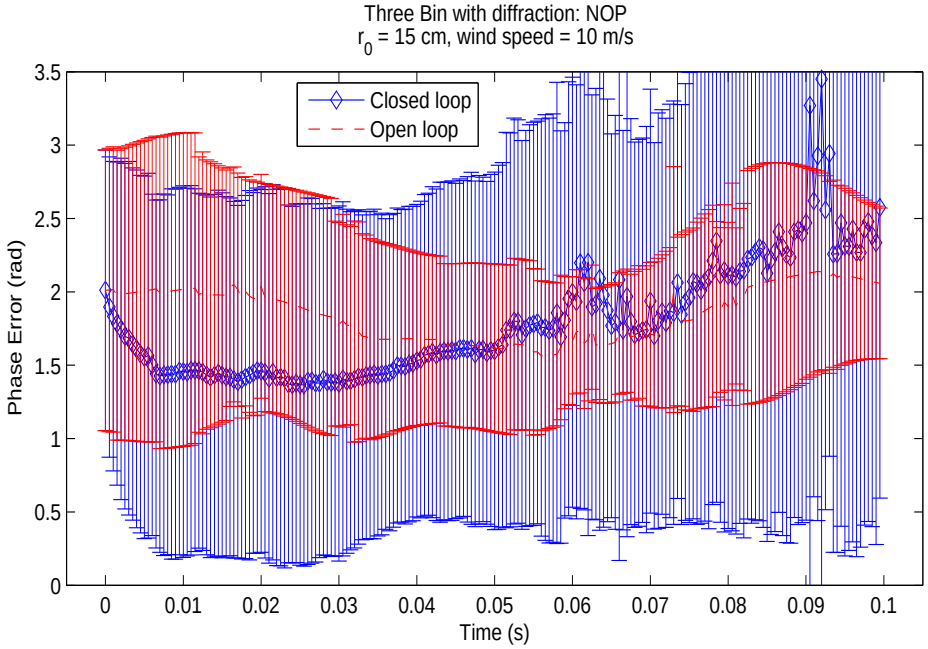

Figure B.33: Three Bin with diffraction WFS, r_0 = 15 cm, wind speed = 10 m/s

B.3.4 wind speed = 20 m/s

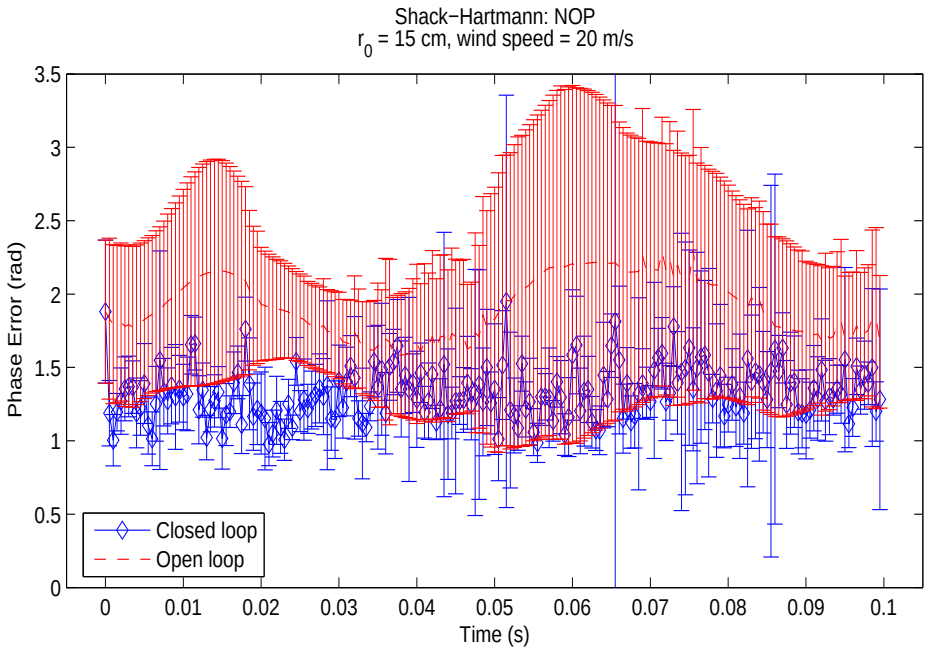

Figure B.34: Shack-Hartmann WFS, r_0 = 15 cm, wind speed = 20 m/s

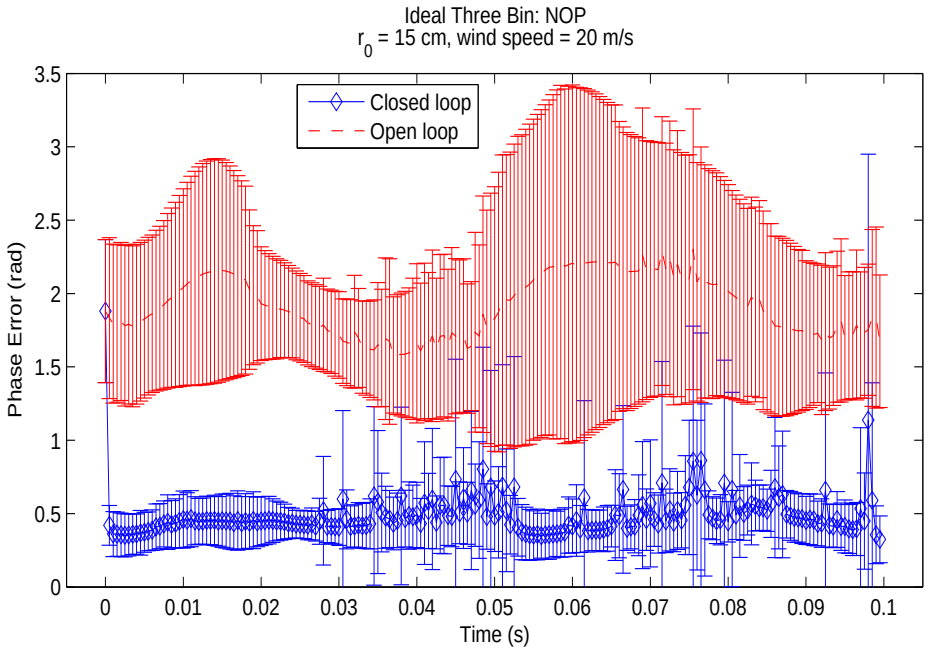

Figure B.35: Ideal Three Bin WFS, r_0 = 15 cm, wind speed = 20 m/s

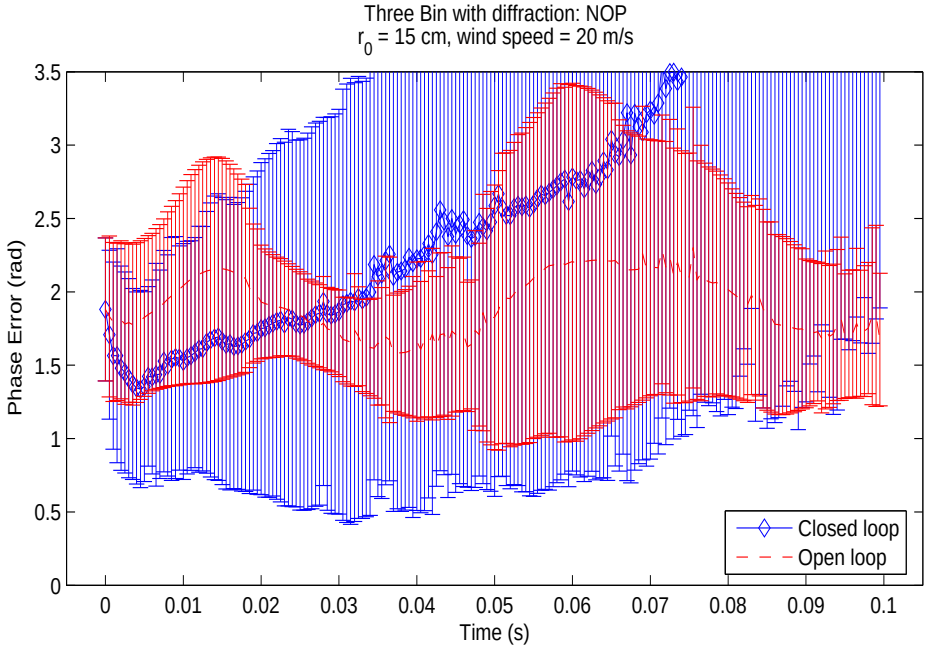

Figure B.36: Three Bin with diffraction WFS, r_0 = 15 cm, wind speed = 20 m/s

B.4 r_0 = 12 cm

With the atmosphere degrading to an r_0 of 12 cm, the ideal three bin corrector is beginning to have problems. The first case in which this shows up is where there is no wind. This is possibly due to problems that the phase unwrapping routines in the DiagnosticPlane system (see figure 8.2) have when the phase field is noisy. The unwrapping routines have fewer problems when there is at least a slight wind because the correlation in the underlying phase field tends to ensure that there are fewer misidentified breaks in the unwrapped field.

B.4.1 wind speed = 0 m/s

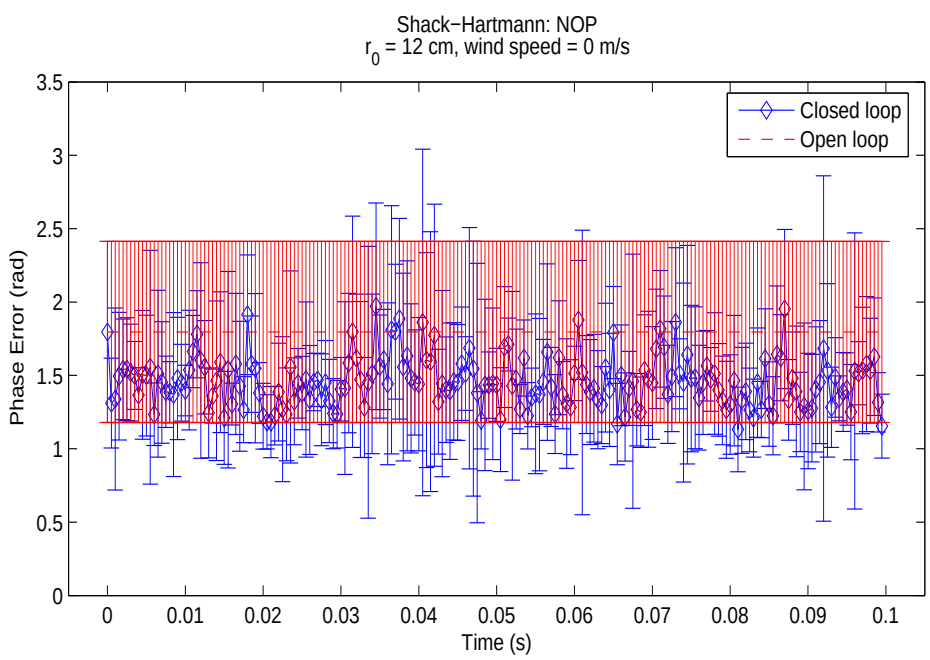

Figure B.37: Shack-Hartmann WFS, r_0 = 12 cm, wind speed = 0 m/s

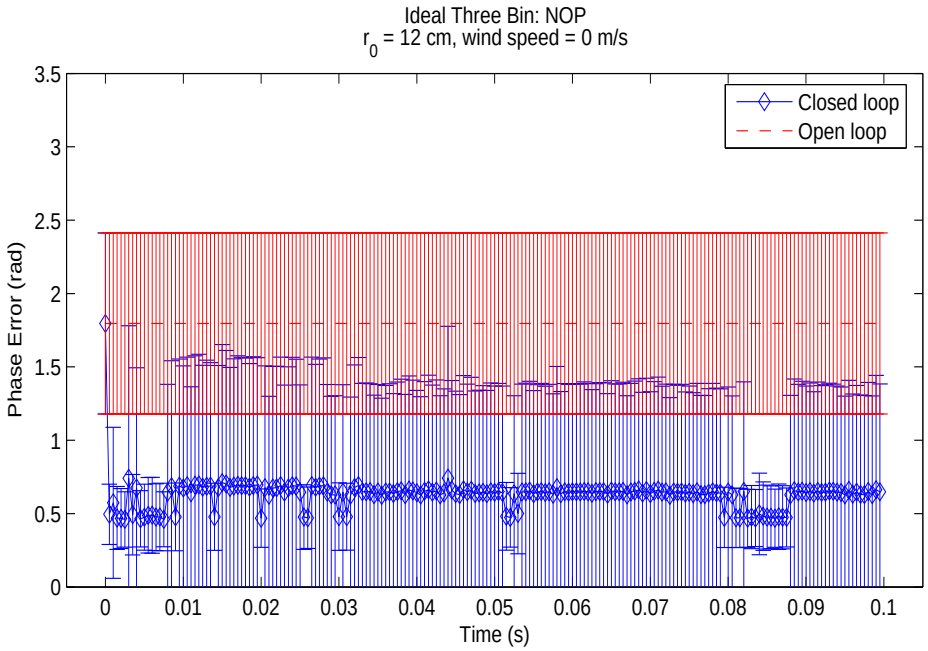

Figure B.38: Ideal Three Bin WFS, r_0 = 12 cm, wind speed = 0 m/s

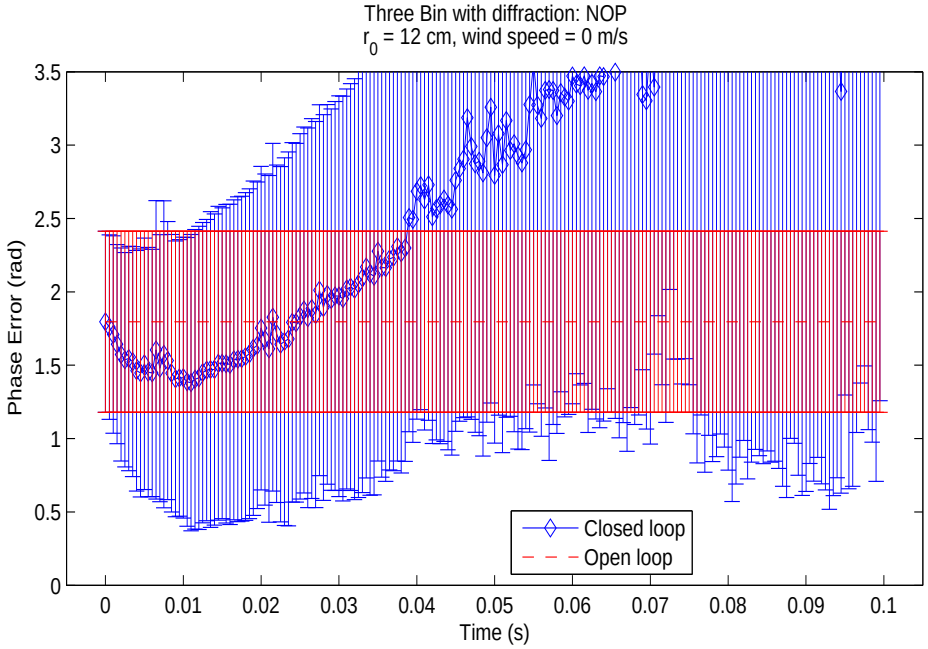

Figure B.39: Three Bin with diffraction WFS, r_0 = 12 cm, wind speed = 0 m/s

B.4.2 wind speed = 5 m/s

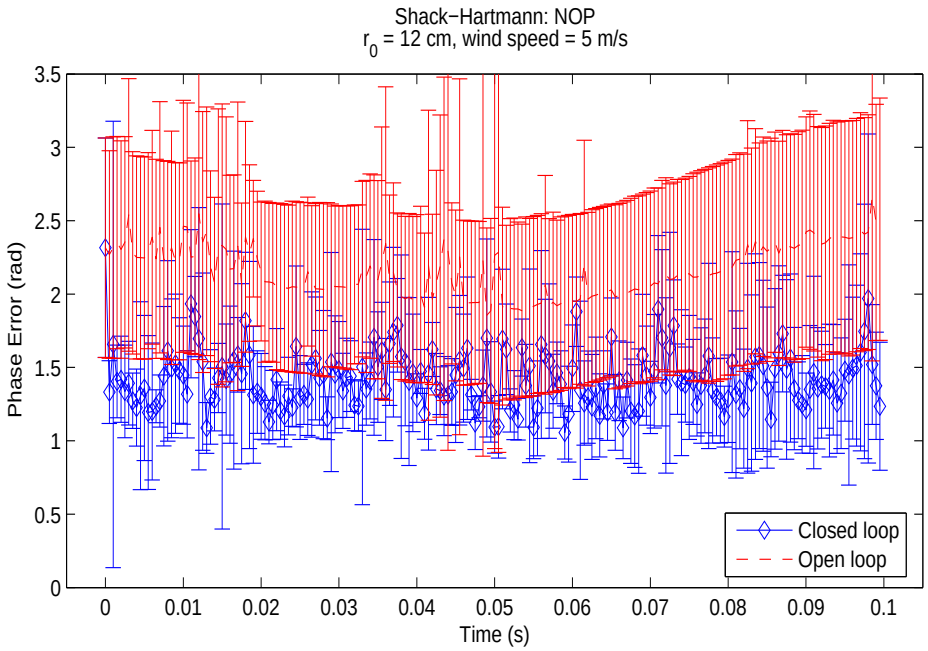

Figure B.40: Shack-Hartmann WFS, r_0 = 12 cm, wind speed = 5 m/s

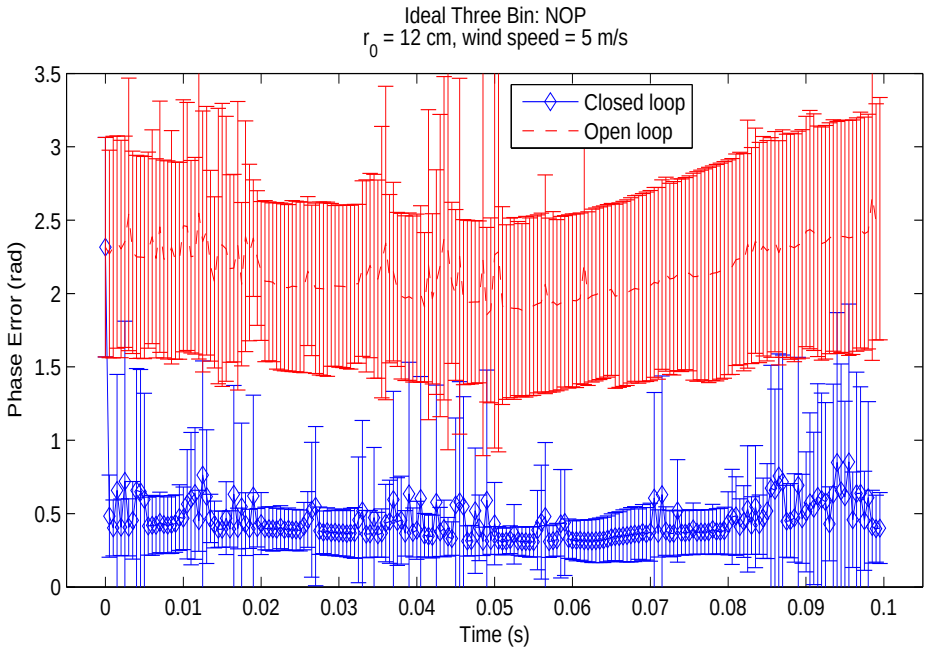

Figure B.41: Ideal Three Bin WFS, r_0 = 12 cm, wind speed = 5 m/s

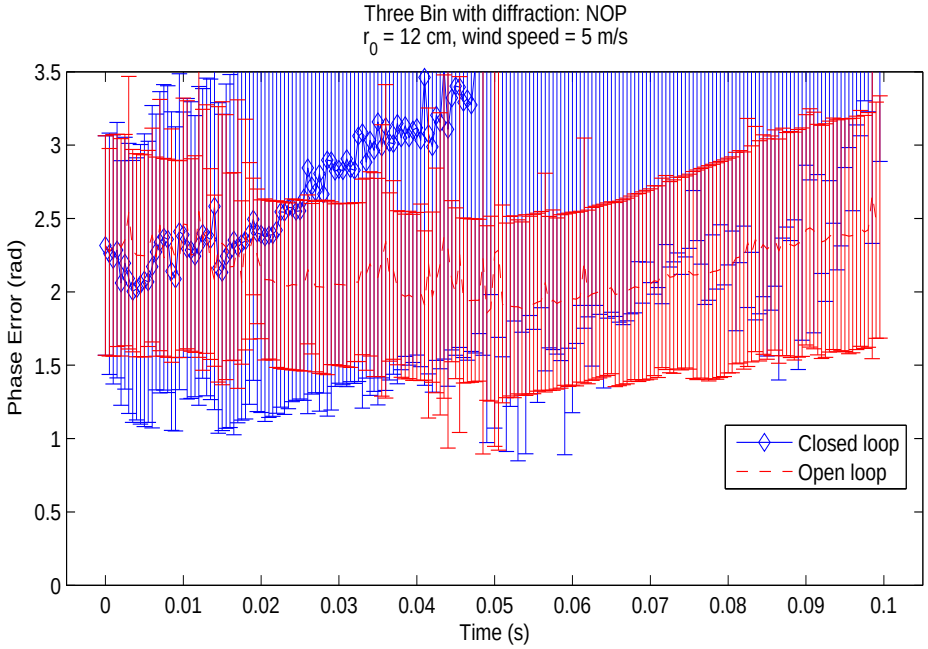

Figure B.42: Three Bin with diffraction WFS, r_0 = 12 cm, wind speed = 5 m/s

B.4.3 wind speed = 10 m/s

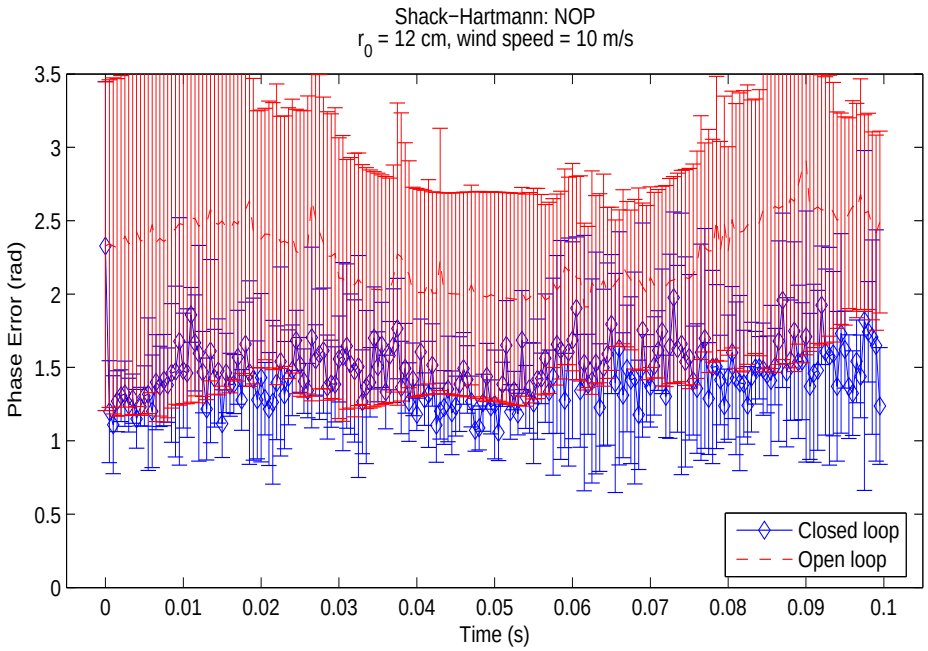

Figure B.43: Shack-Hartmann WFS, r_0 = 12 cm, wind speed = 10 m/s

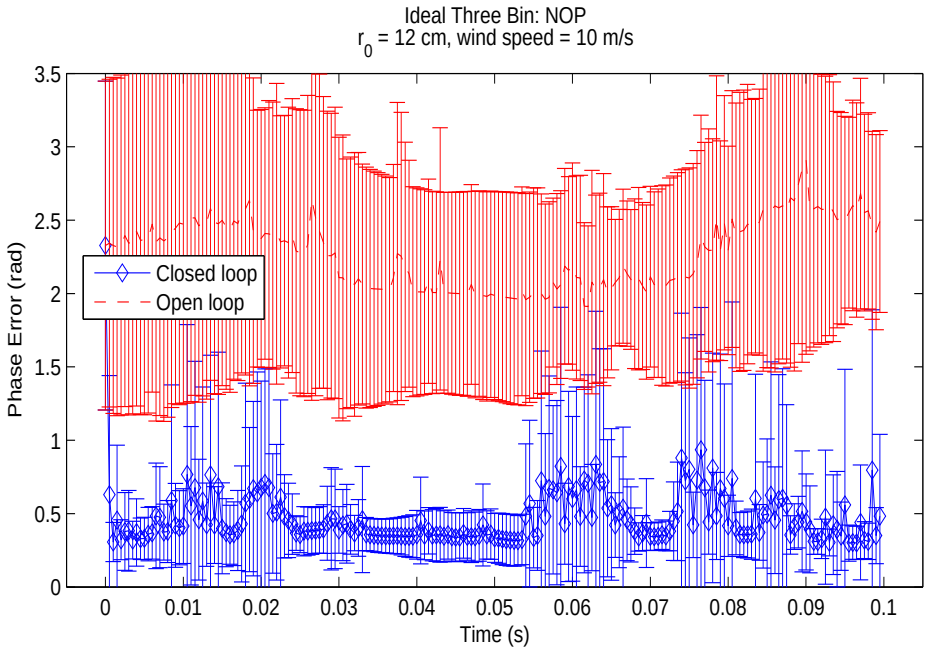

Figure B.44: Ideal Three Bin WFS, r_0 = 12 cm, wind speed = 10 m/s

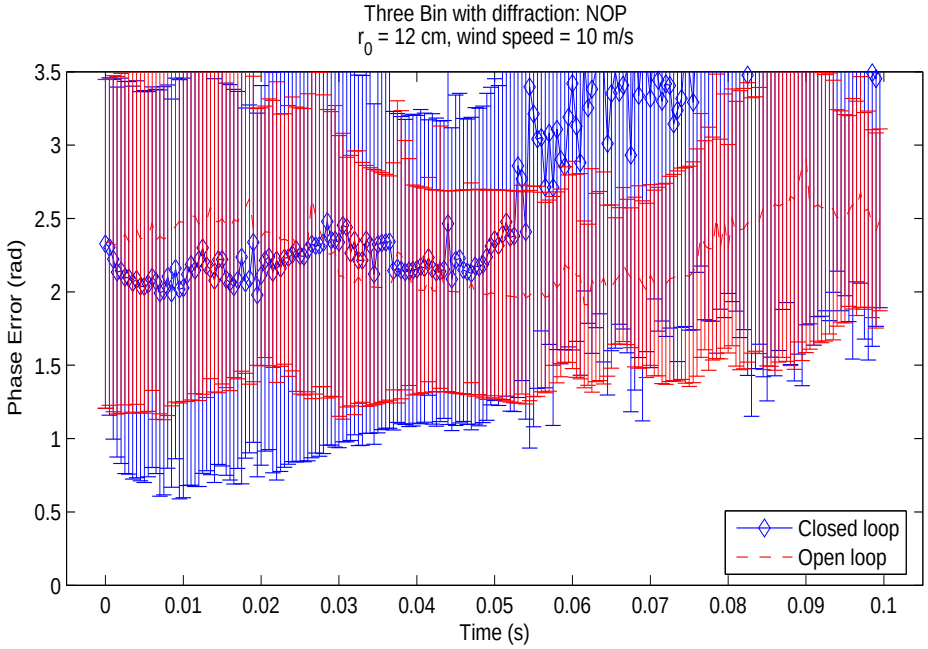

Figure B.45: Three Bin with diffraction WFS, r_0 = 12 cm, wind speed = 10 m/s

B.4.4 wind speed = 20 m/s

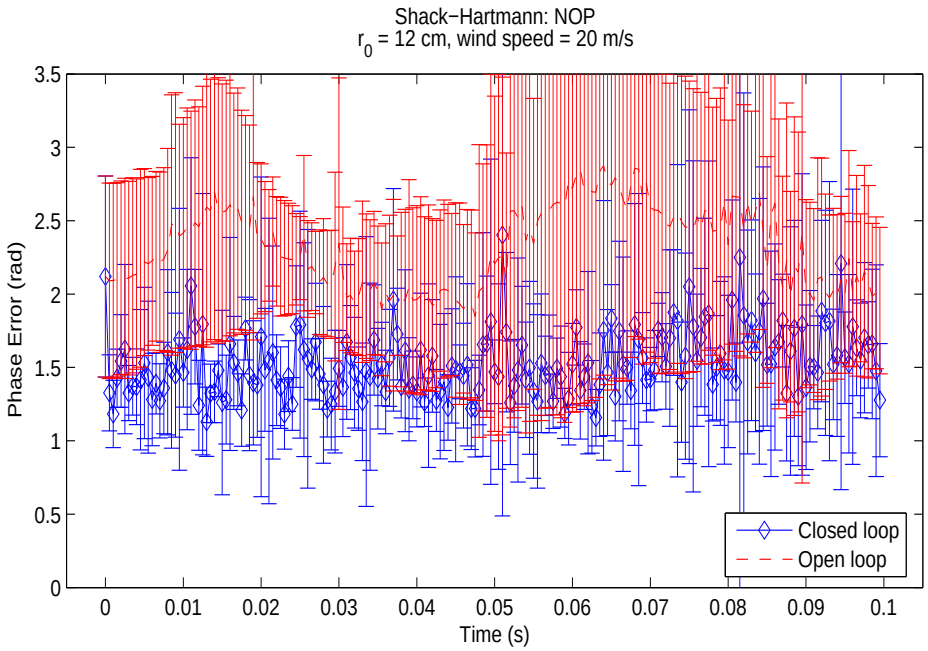

Figure B.46: Shack-Hartmann WFS, r_0 = 12 cm, wind speed = 20 m/s

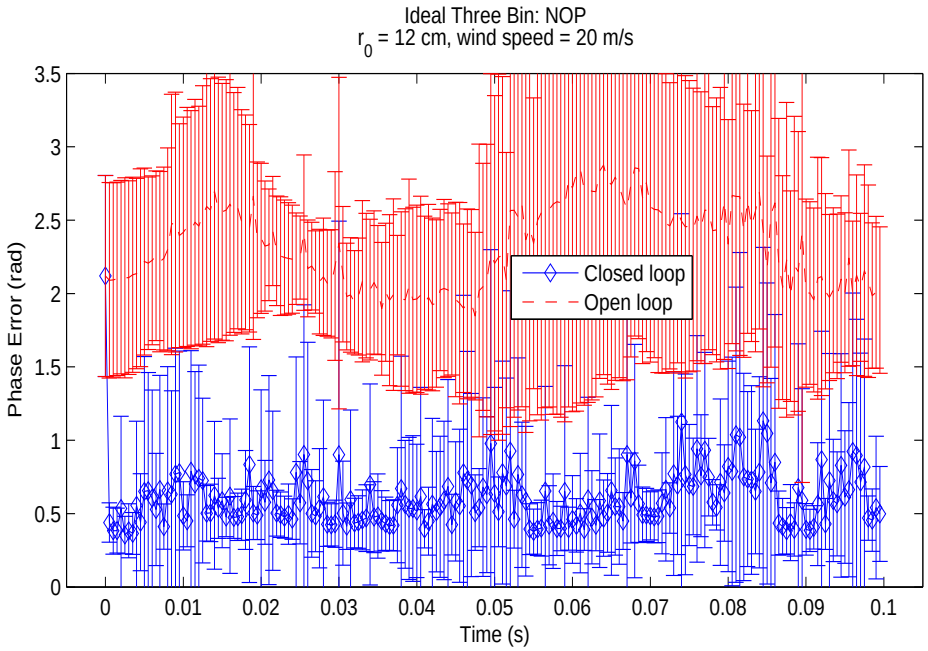

Figure B.47: Ideal Three Bin WFS, r_0 = 12 cm, wind speed = 20 m/s

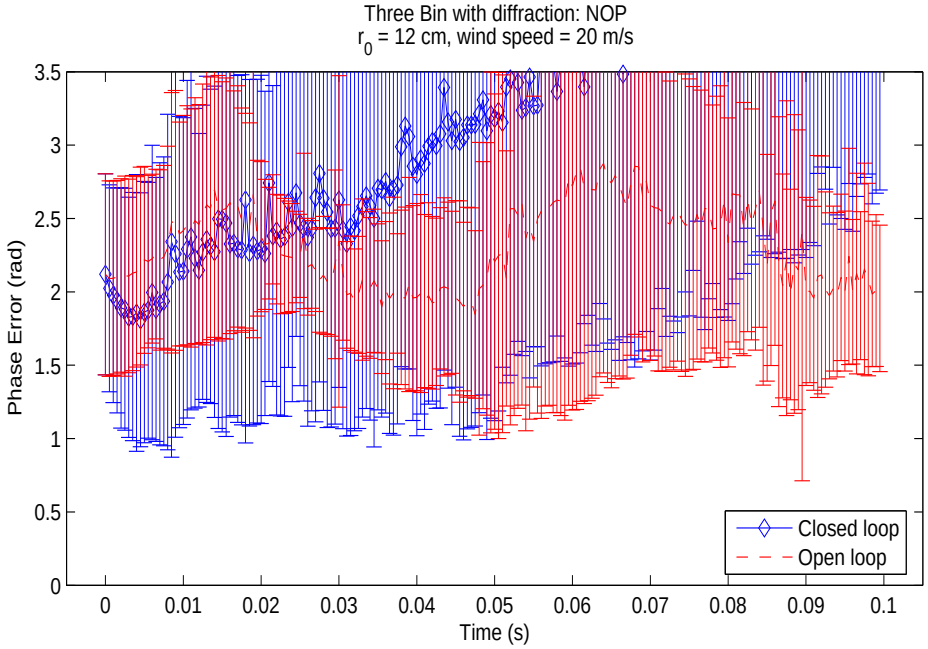

Figure B.48: Three Bin with diffraction WFS, r_0 = 12 cm, wind speed = 20 m/s

B.5 r_0 **=** 9 cm

An r_0 of 9 cm is the first case where the three bin loop with diffraction does not correct for a time before becoming unstable.

B.5.1 wind speed = 0 m/s

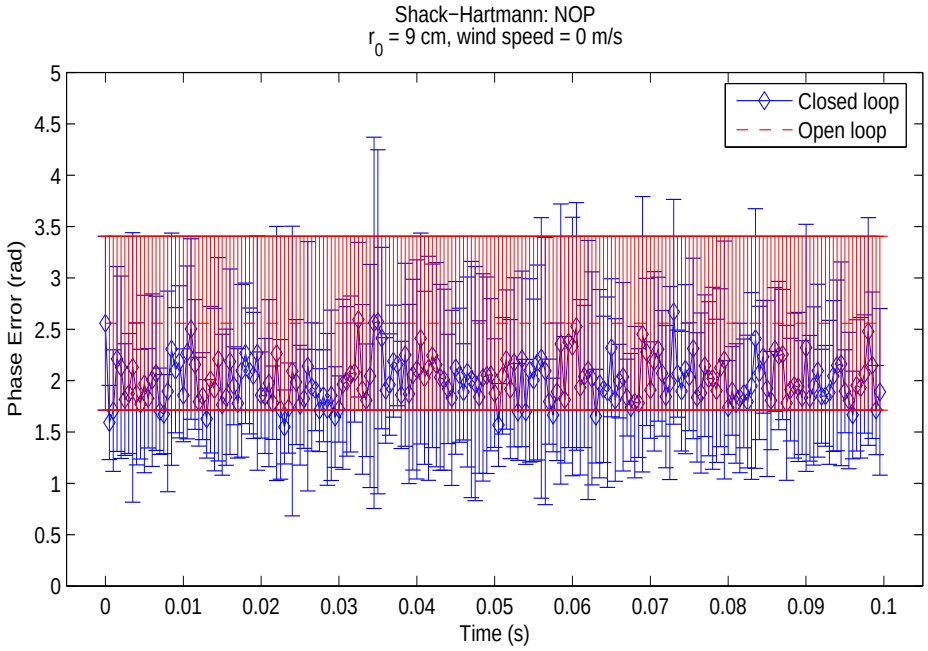

Figure B.49: Shack-Hartmann WFS, r_0 = 9 cm, wind speed = 0 m/s

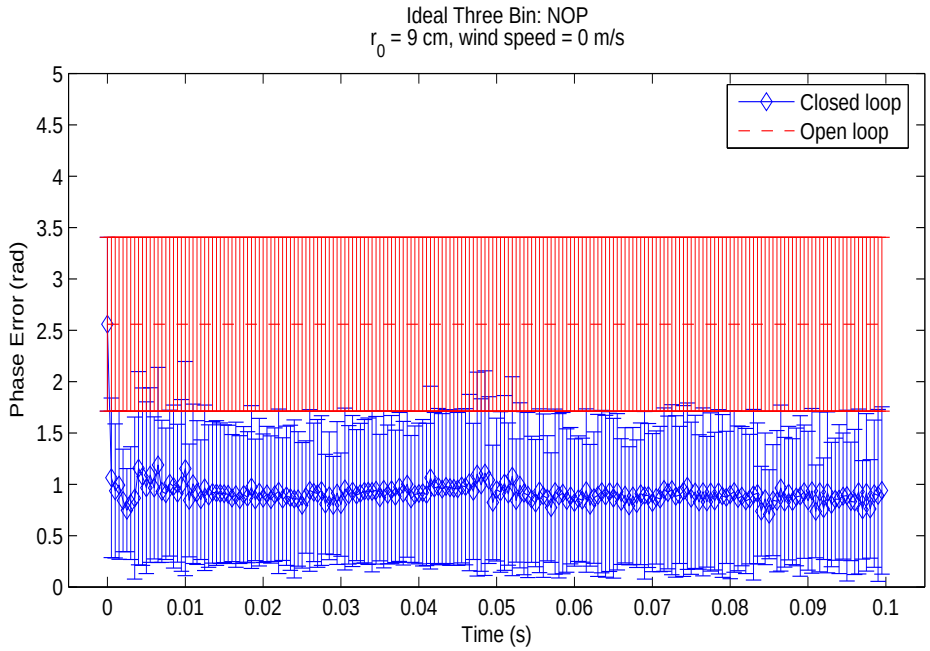

Figure B.50: Ideal Three Bin WFS, r_0 = 9 cm, wind speed = 0 m/s

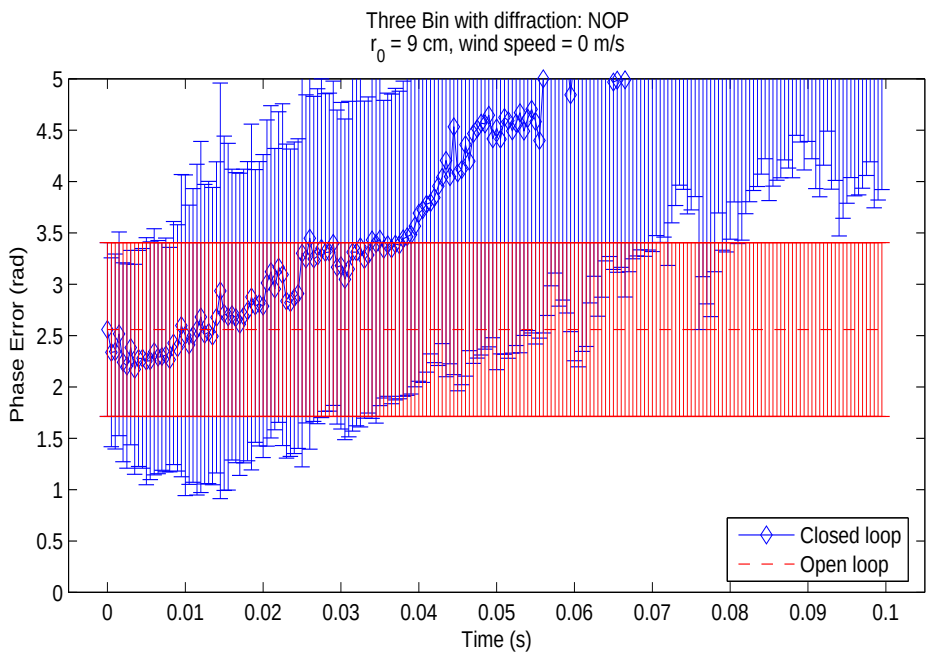

Figure B.51: Three Bin with diffraction WFS, r_0 = 9 cm, wind speed = 0 m/s

B.5.2 wind speed = 5 m/s

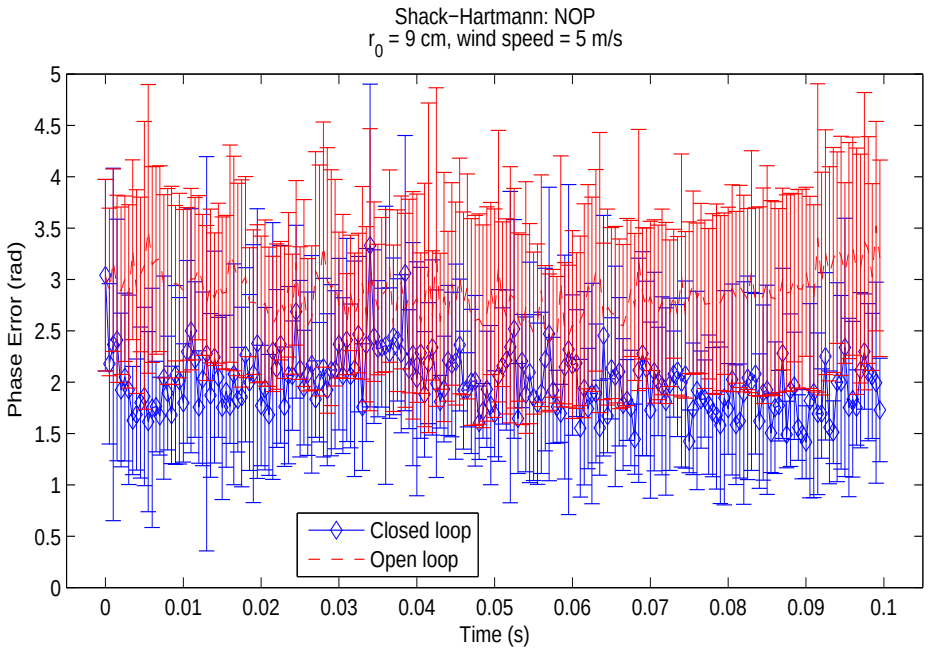

Figure B.52: Shack-Hartmann WFS, r_0 = 9 cm, wind speed = 5 m/s

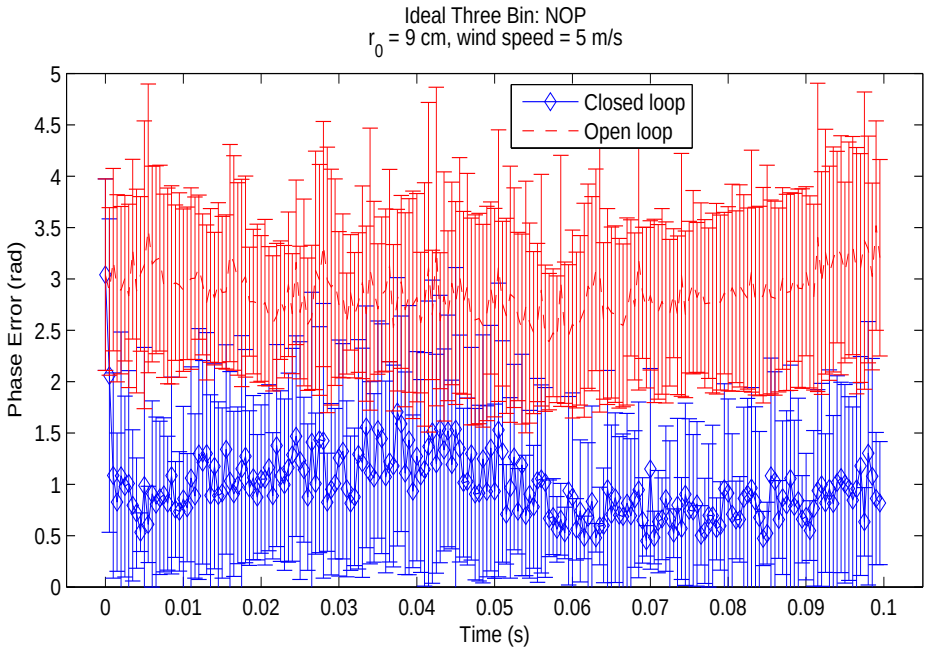

Figure B.53: Ideal Three Bin WFS, r_0 = 9 cm, wind speed = 5 m/s

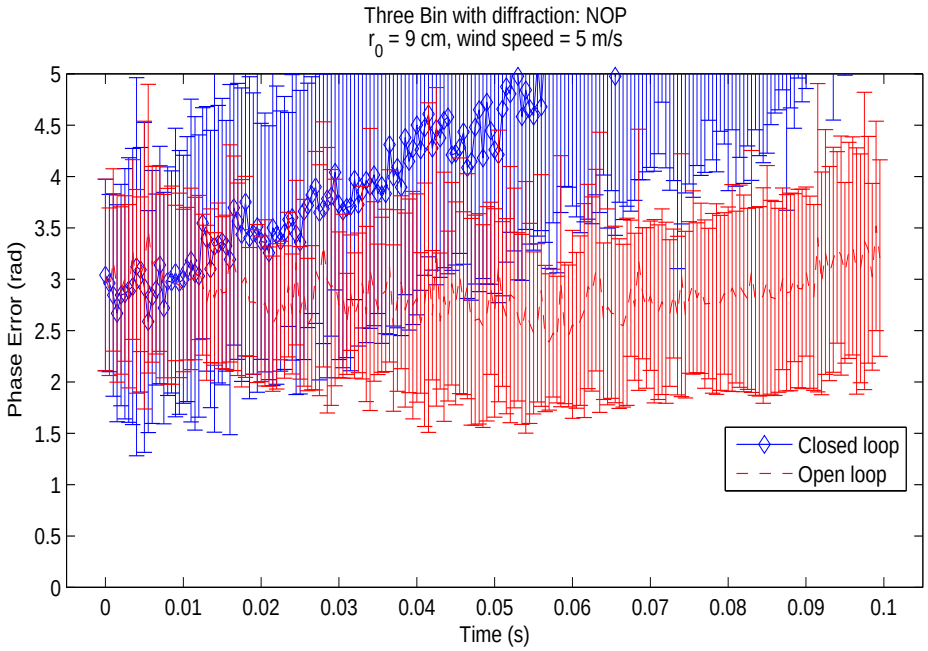

Figure B.54: Three Bin with diffraction WFS, r_0 = 9 cm, wind speed = 5 m/s

B.5.3 wind speed = 10 m/s

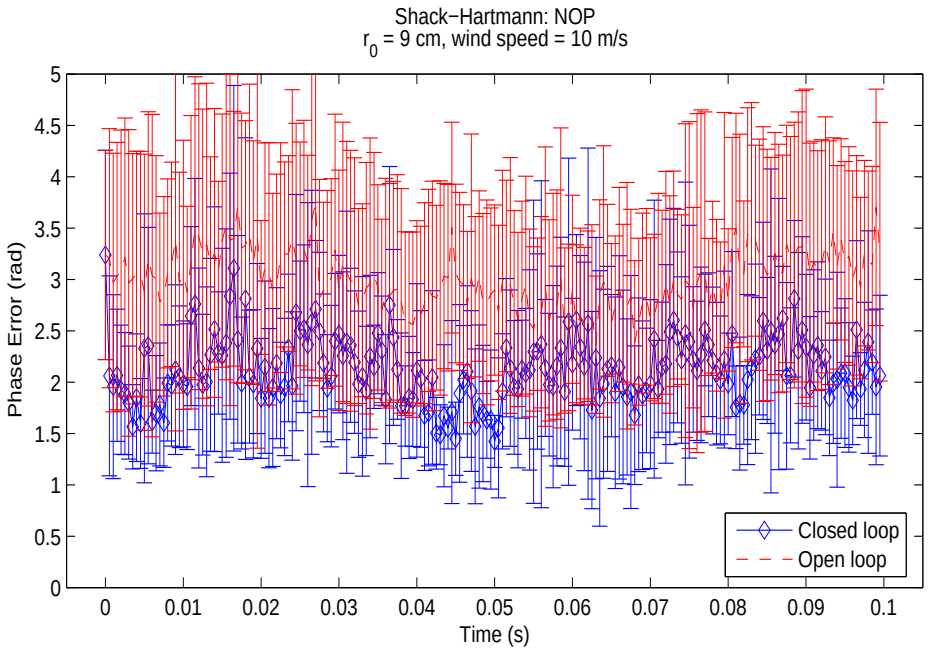

Figure B.55: Shack-Hartmann WFS, r_0 = 9 cm, wind speed = 10 m/s

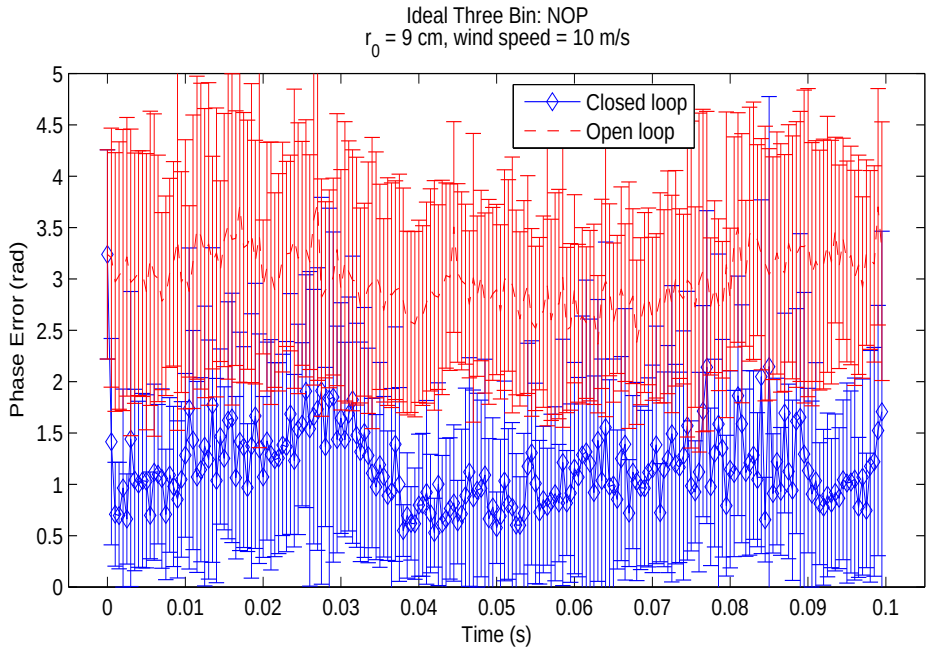

Figure B.56: Ideal Three Bin WFS, r_0 = 9 cm, wind speed = 10 m/s

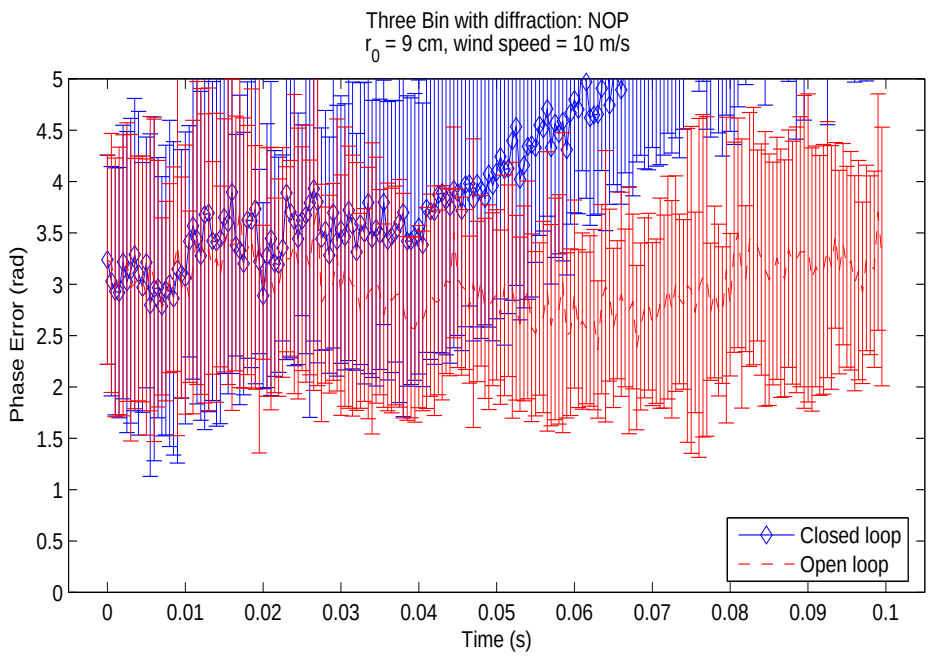

Figure B.57: Three Bin with diffraction WFS, r_0 = 9 cm, wind speed = 10 m/s

B.5.4 wind speed = 20 m/s

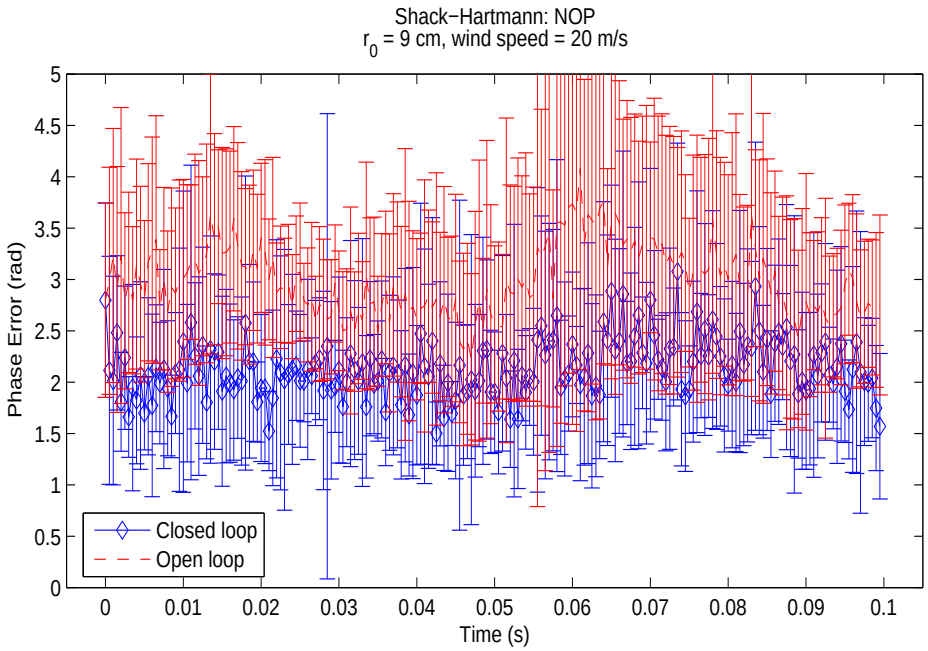

Figure B.58: Shack-Hartmann WFS, r_0 = 9 cm, wind speed = 20 m/s

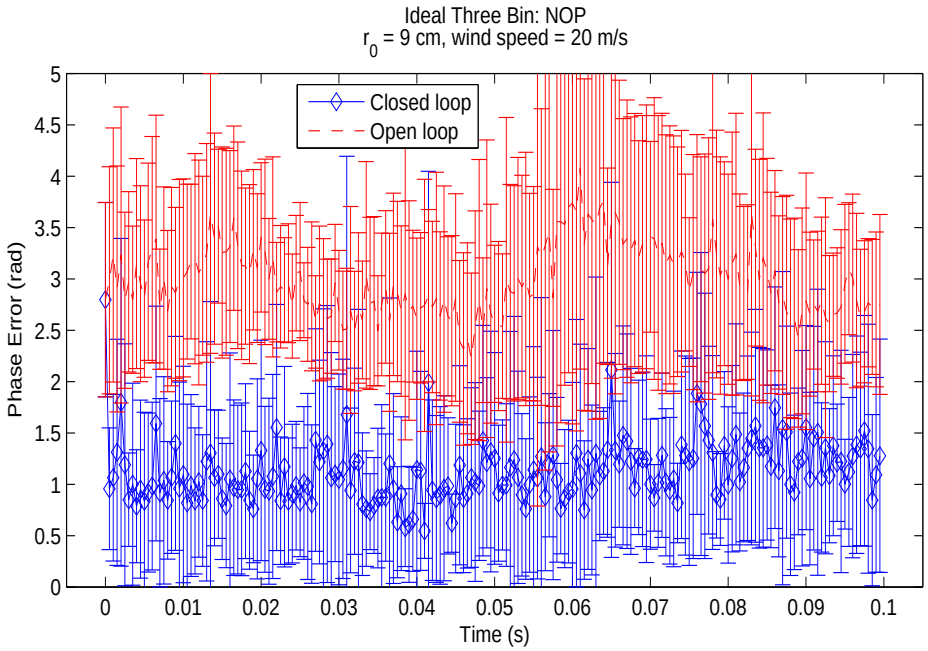

Figure B.59: Ideal Three Bin WFS, r_0 = 9 cm, wind speed = 20 m/s

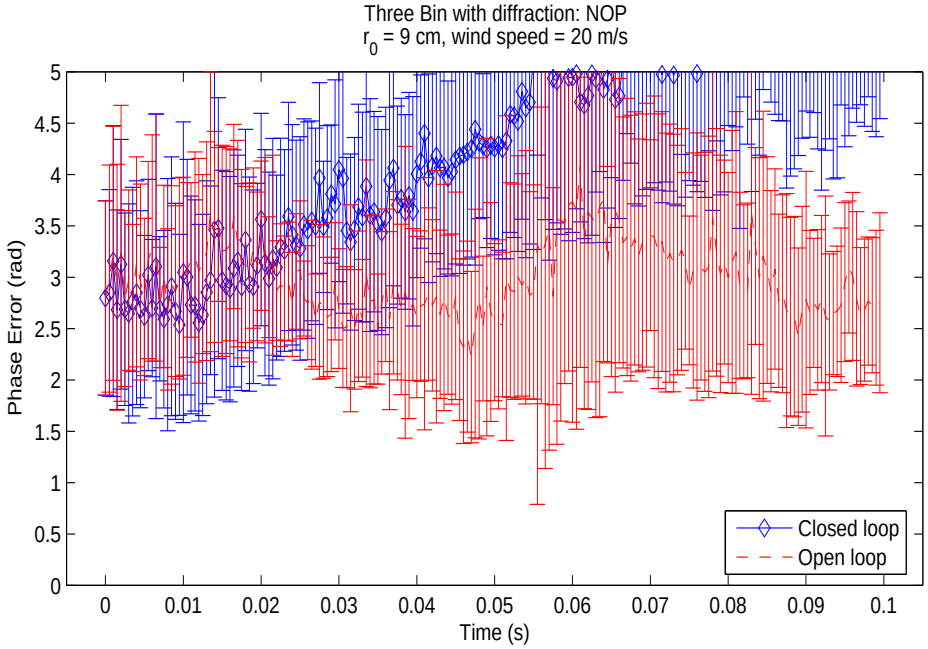

Figure B.60: Three Bin with diffraction WFS, r_0 = 9 cm, wind speed = 20 m/s

B.6 r_0 **=** 6 cm

The DM is almost at it's design limits when trying to correct for turbulence with an r_0 of 6 cm as it is for these runs.

B.6.1 wind speed = 0 m/s

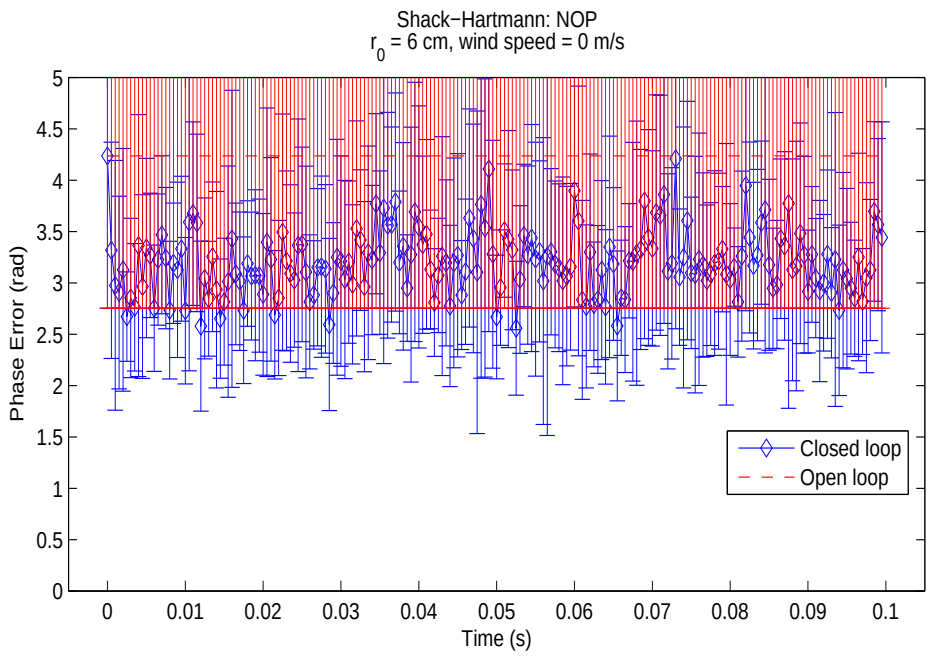

Figure B.61: Shack-Hartmann WFS, r_0 = 6 cm, wind speed = 0 m/s

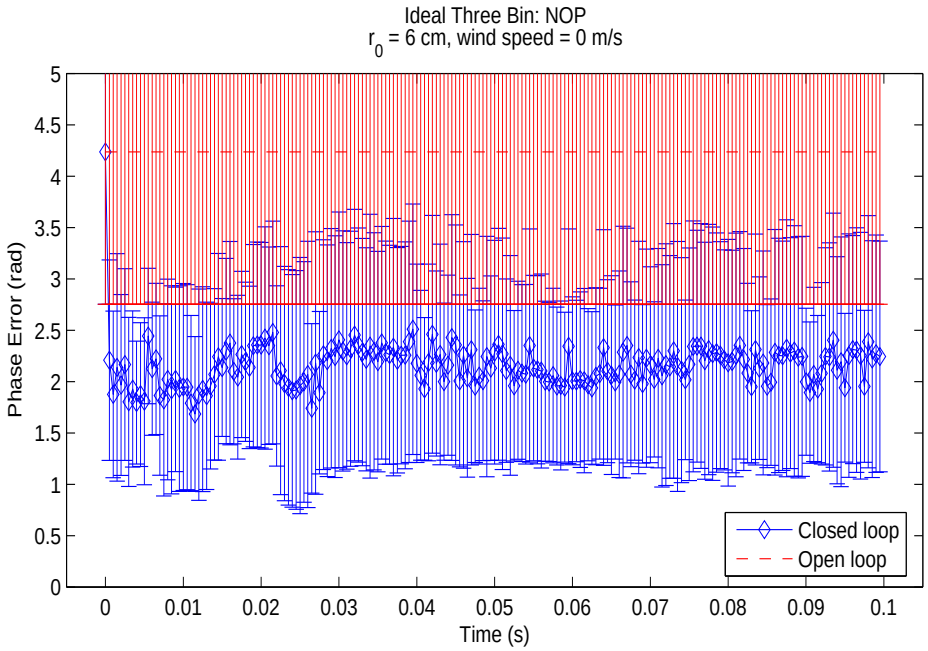

Figure B.62: Ideal Three Bin WFS, r_0 = 6 cm, wind speed = 0 m/s

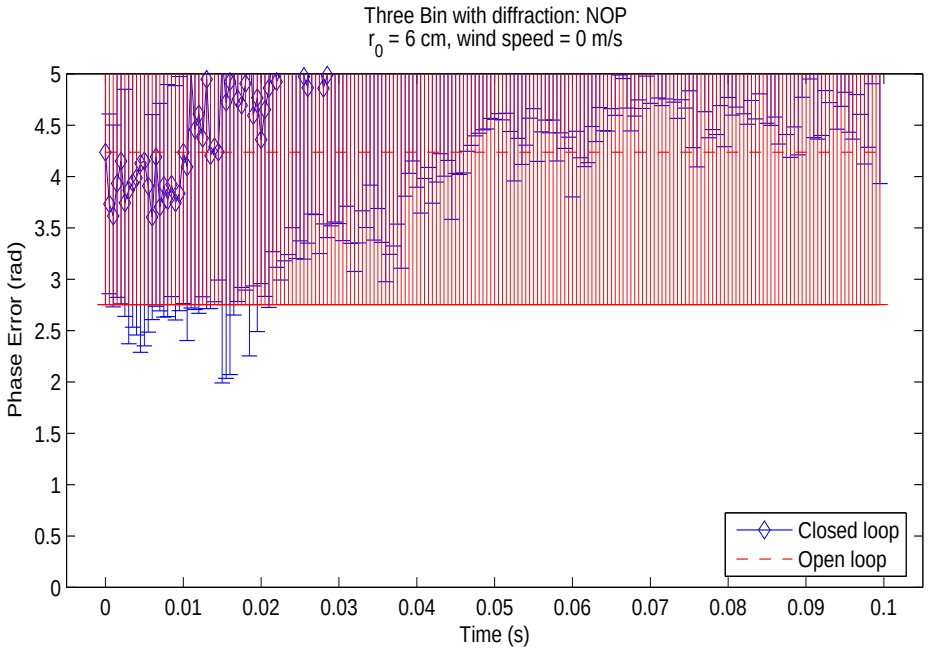

Figure B.63: Three Bin with diffraction WFS, r_0 = 6 cm, wind speed = 0 m/s

B.6.2 wind speed = 5 m/s

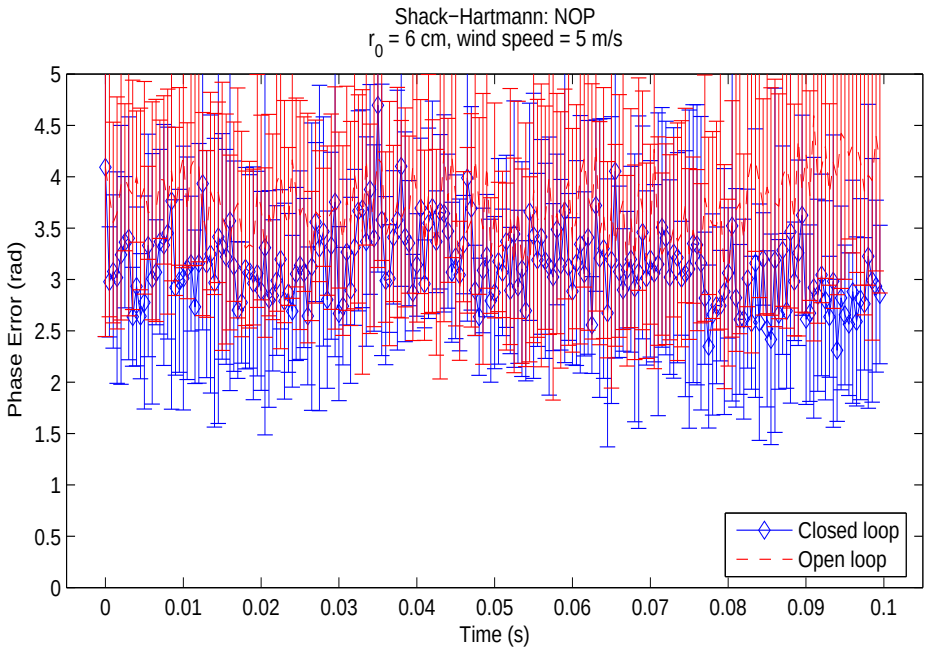

Figure B.64: Shack-Hartmann WFS, r_0 = 6 cm, wind speed = 5 m/s

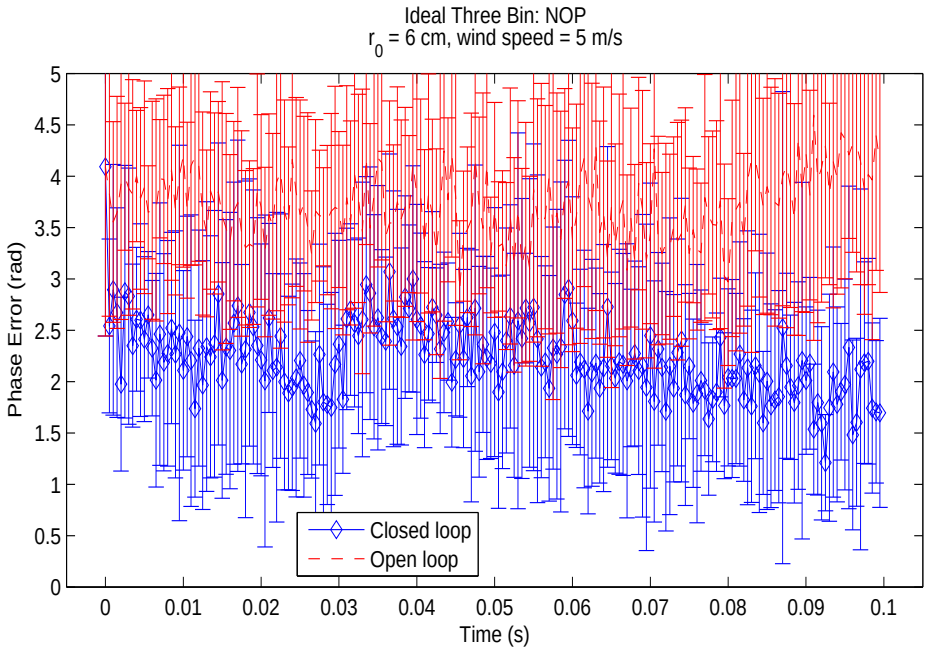

Figure B.65: Ideal Three Bin WFS, r_0 = 6 cm, wind speed = 5 m/s

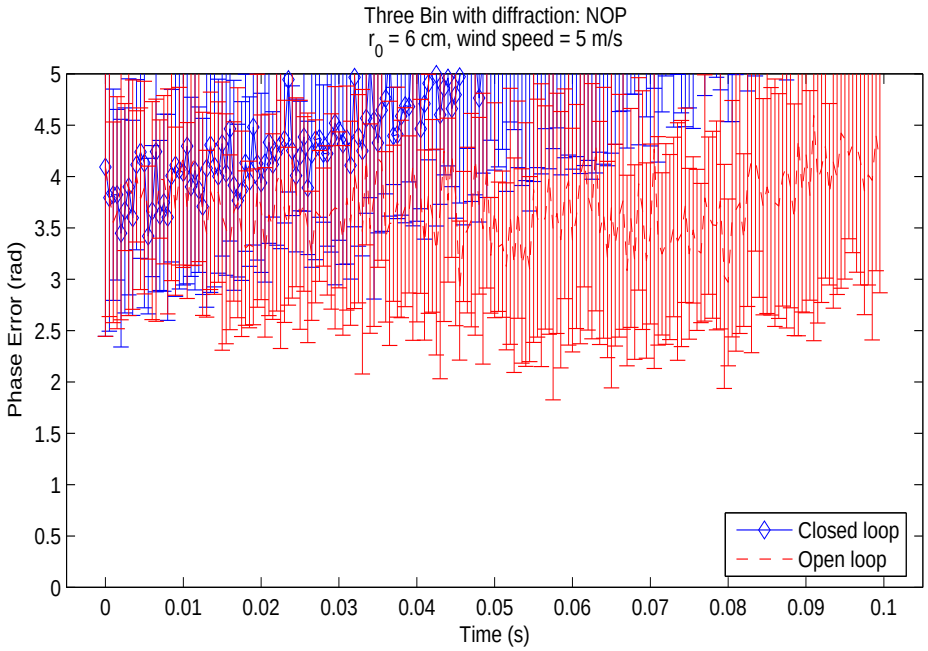

Figure B.66: Three Bin with diffraction WFS, r_0 = 6 cm, wind speed = 5 m/s

B.6.3 wind speed = 10 m/s

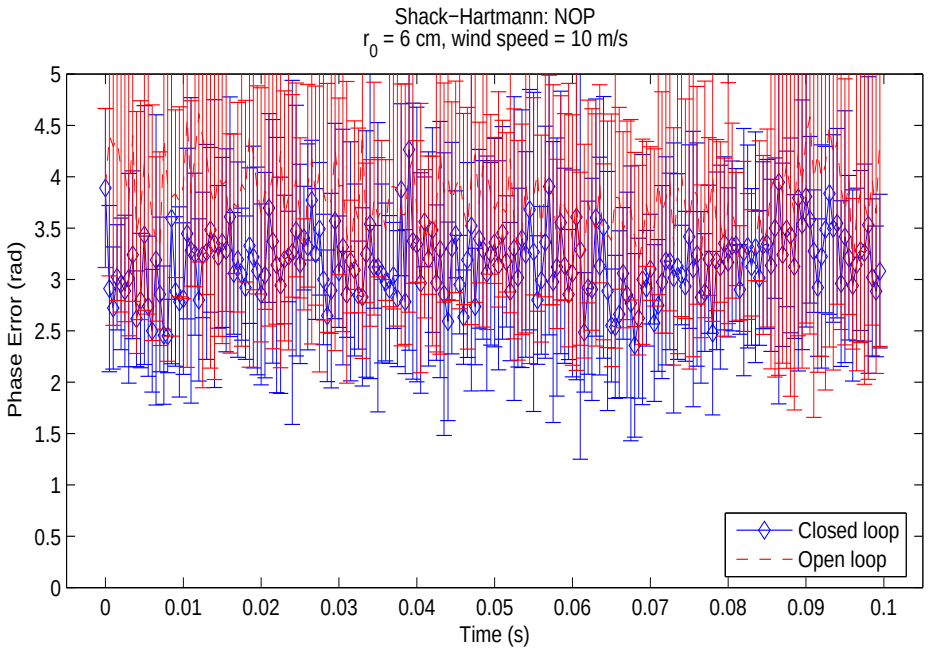

Figure B.67: Shack-Hartmann WFS, r_0 = 6 cm, wind speed = 10 m/s

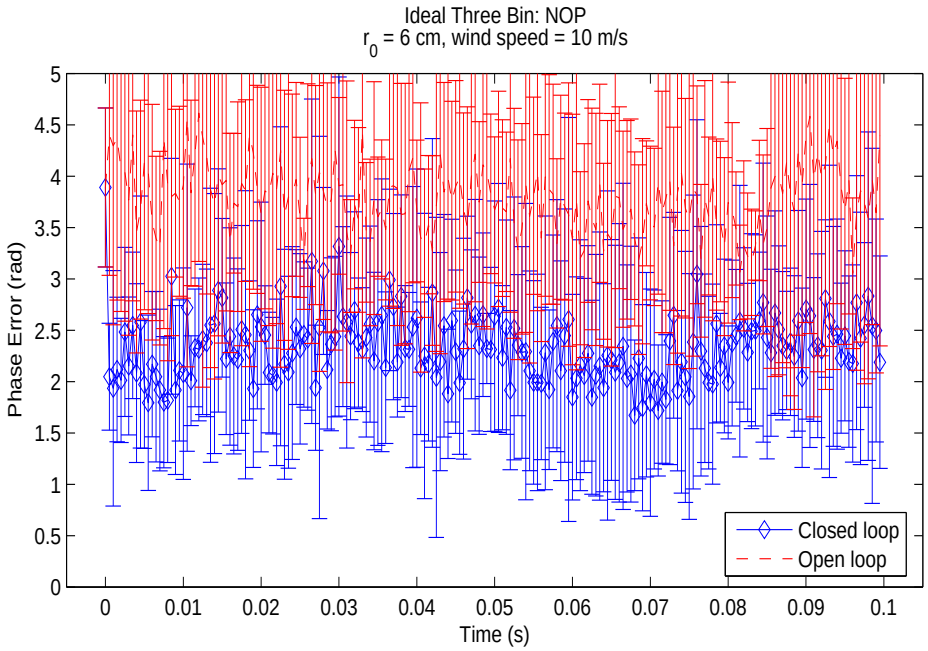

Figure B.68: Ideal Three Bin WFS, r_0 = 6 cm, wind speed = 10 m/s

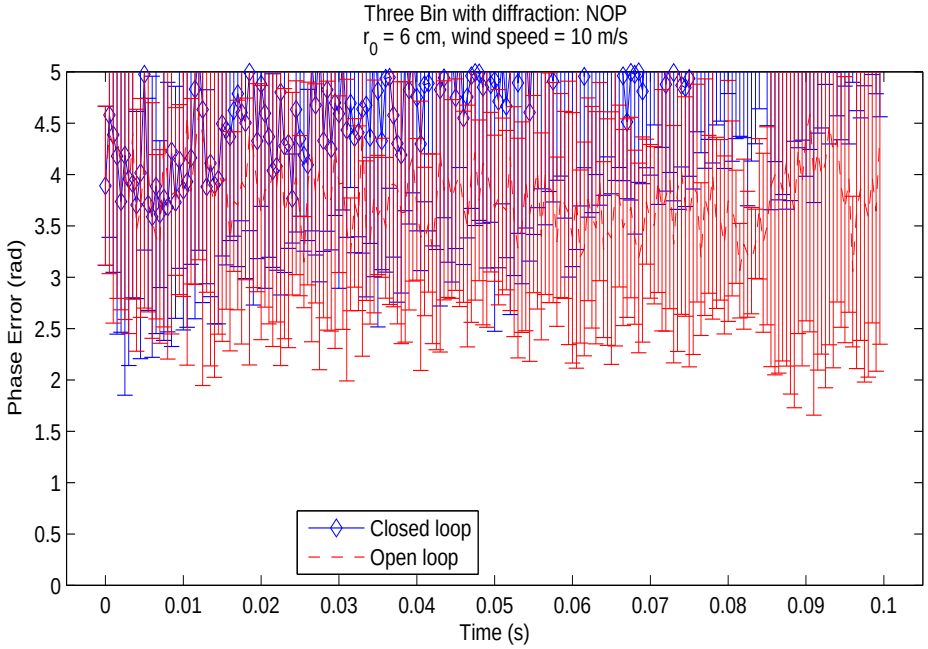

Figure B.69: Three Bin with diffraction WFS, r_0 = 6 cm, wind speed = 10 m/s

B.6.4 wind speed = 20 m/s

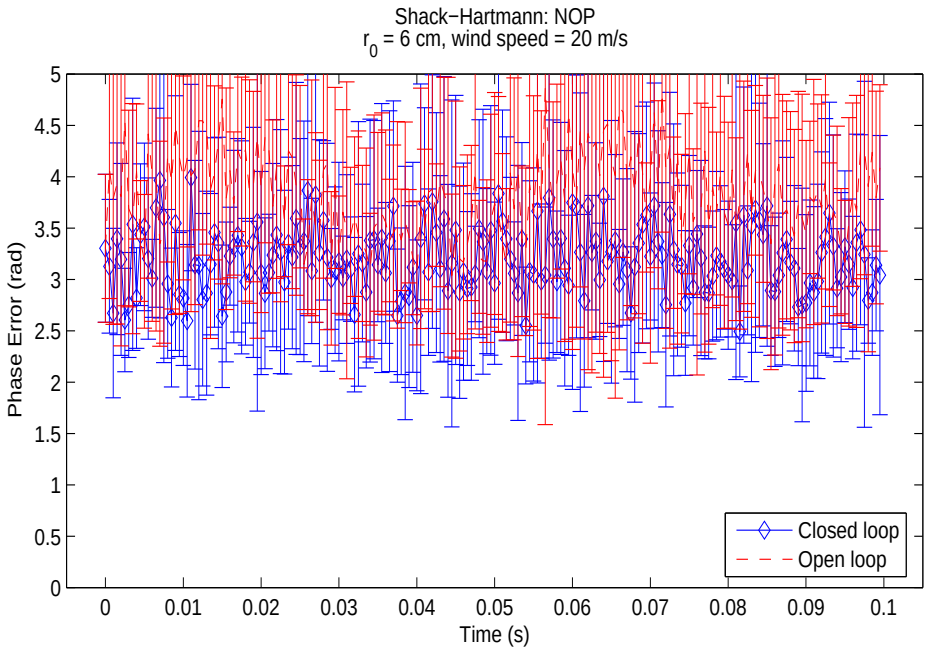

Figure B.70: Shack-Hartmann WFS, r_0 = 6 cm, wind speed = 20 m/s

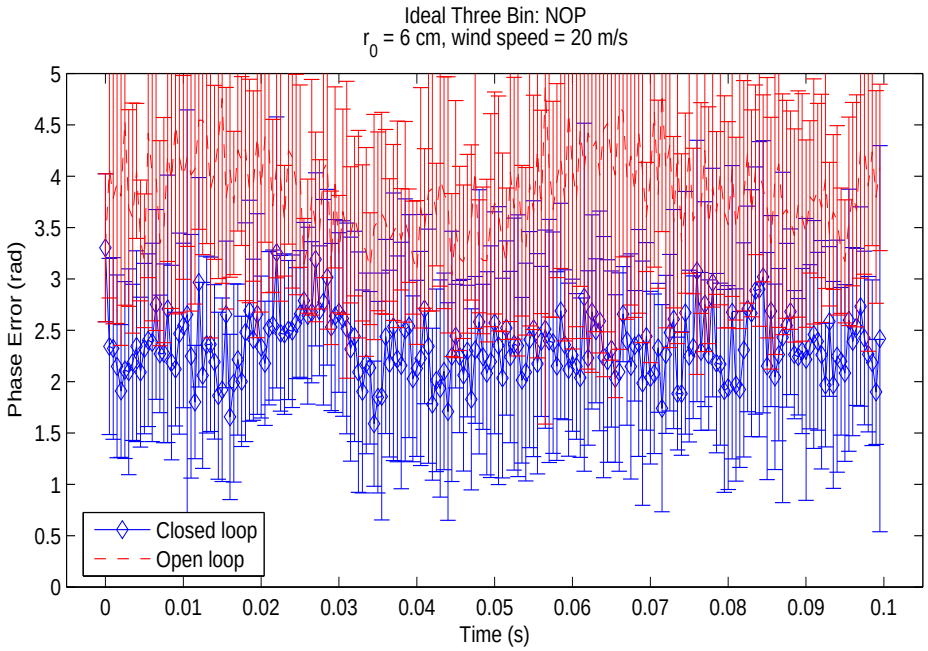

Figure B.71: Ideal Three Bin WFS, r_0 = 6 cm, wind speed = 20 m/s

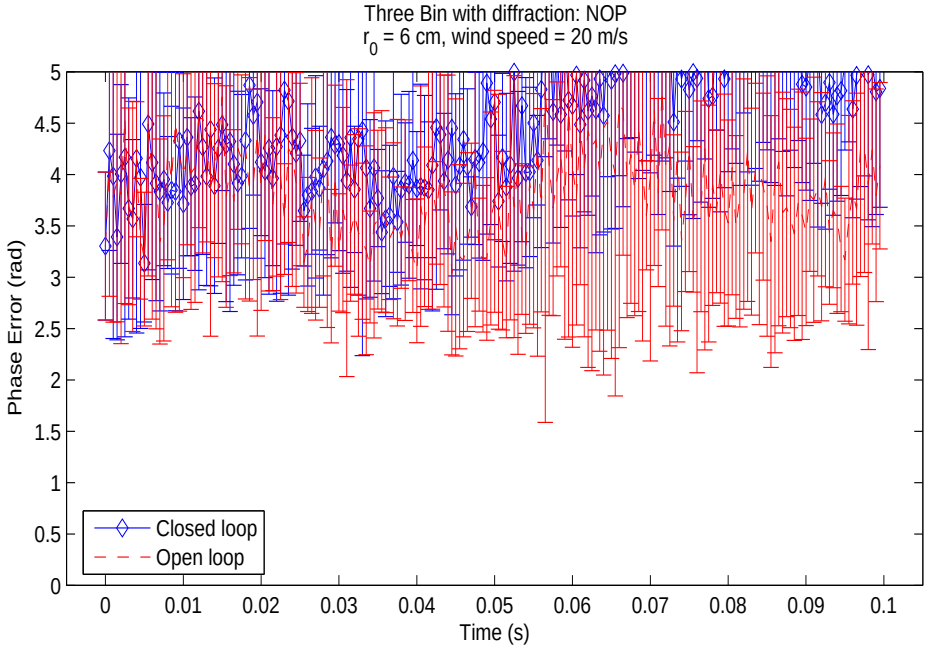

Figure B.72: Three Bin with diffraction WFS, r_0 = 6 cm, wind speed = 20 m/s

B.7 r_0 **=** 3 cm

At an r_0 of 3 cm, the system is beyond the limits of its design. What is surprising is that the ideal three bin loop is able to correct the slight amount that it does.

B.7.1 wind speed = 0 m/s

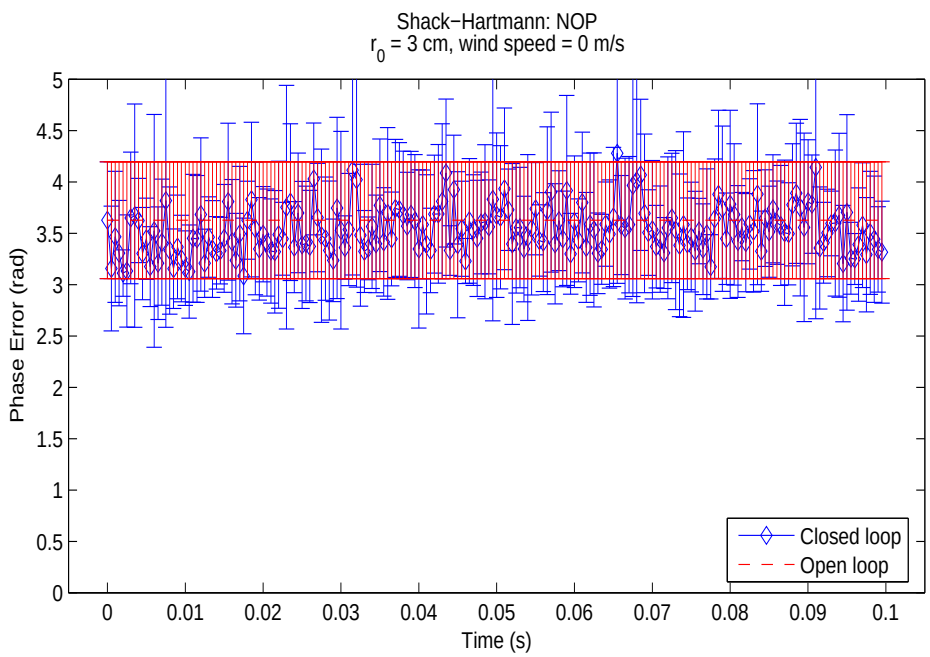

Figure B.73: Shack-Hartmann WFS, r_0 = 3 cm, wind speed = 0 m/s

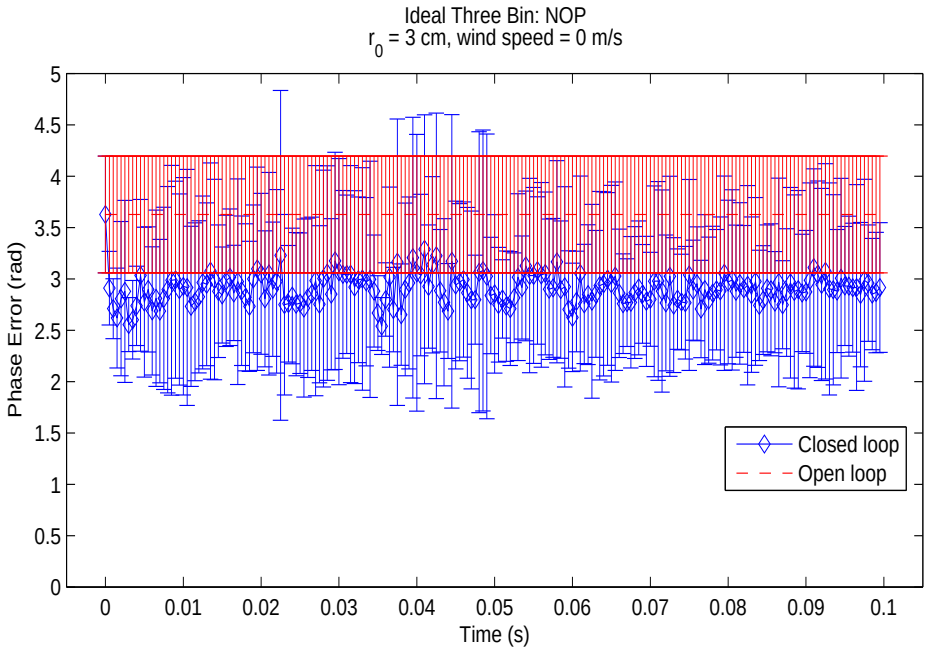

Figure B.74: Ideal Three Bin WFS, r_0 = 3 cm, wind speed = 0 m/s

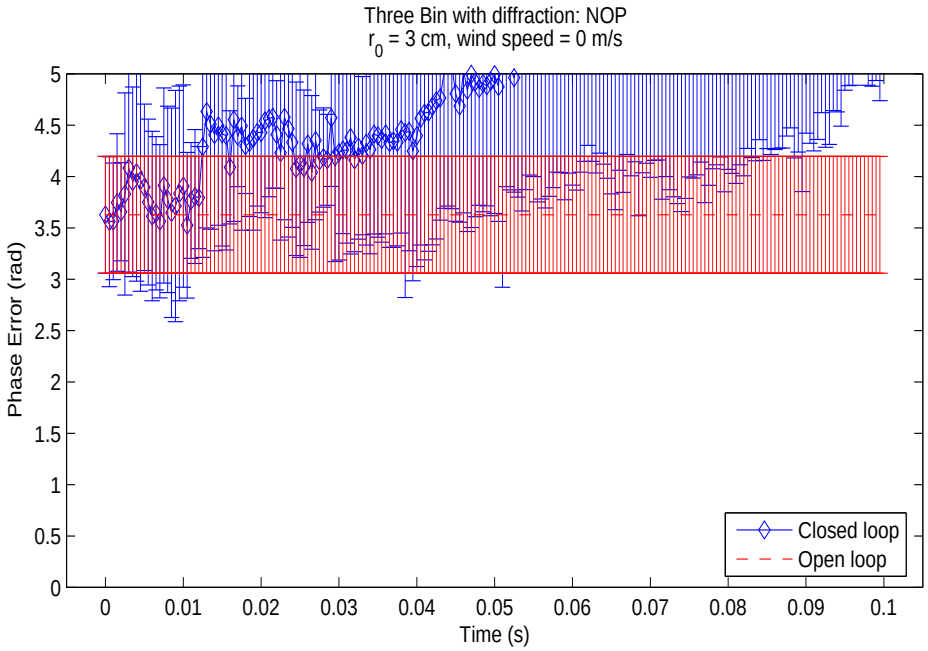

Figure B.75: Three Bin with diffraction WFS, r_0 = 3 cm, wind speed = 0 m/s

B.7.2 wind speed = 5 m/s

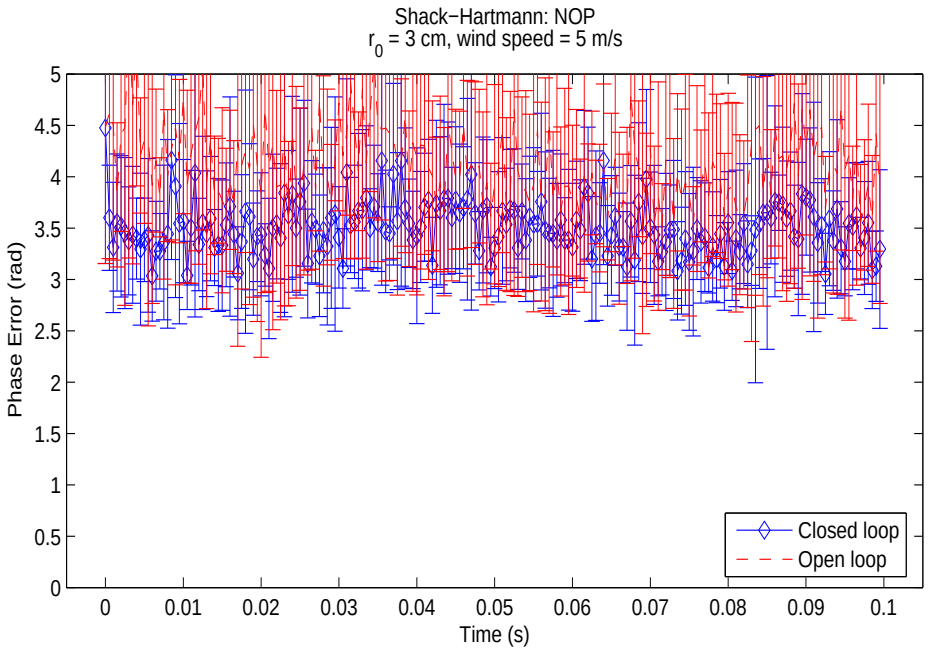

Figure B.76: Shack-Hartmann WFS, r_0 = 3 cm, wind speed = 5 m/s

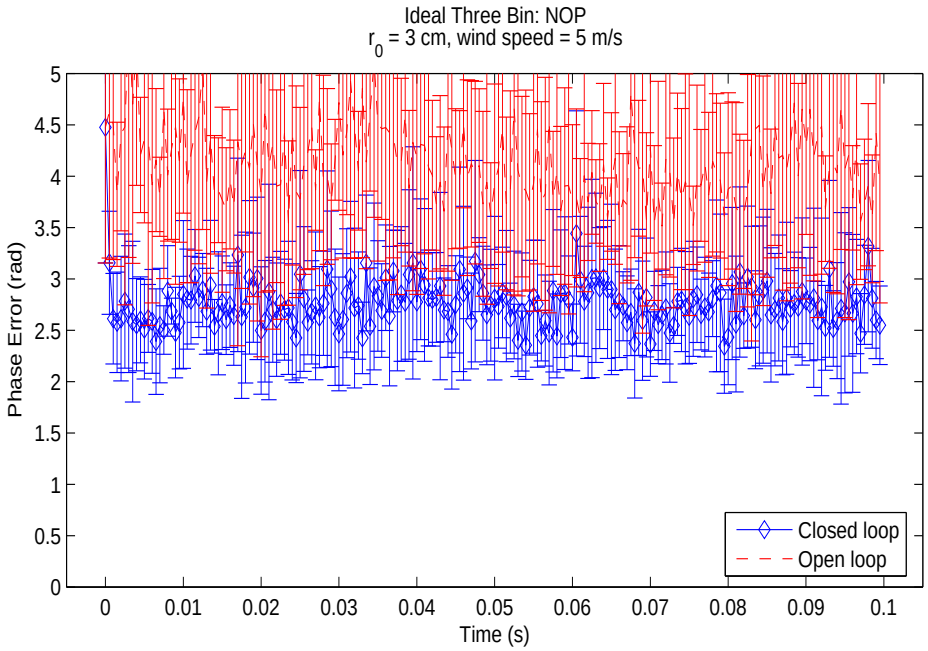

Figure B.77: Ideal Three Bin WFS, r_0 = 3 cm, wind speed = 5 m/s

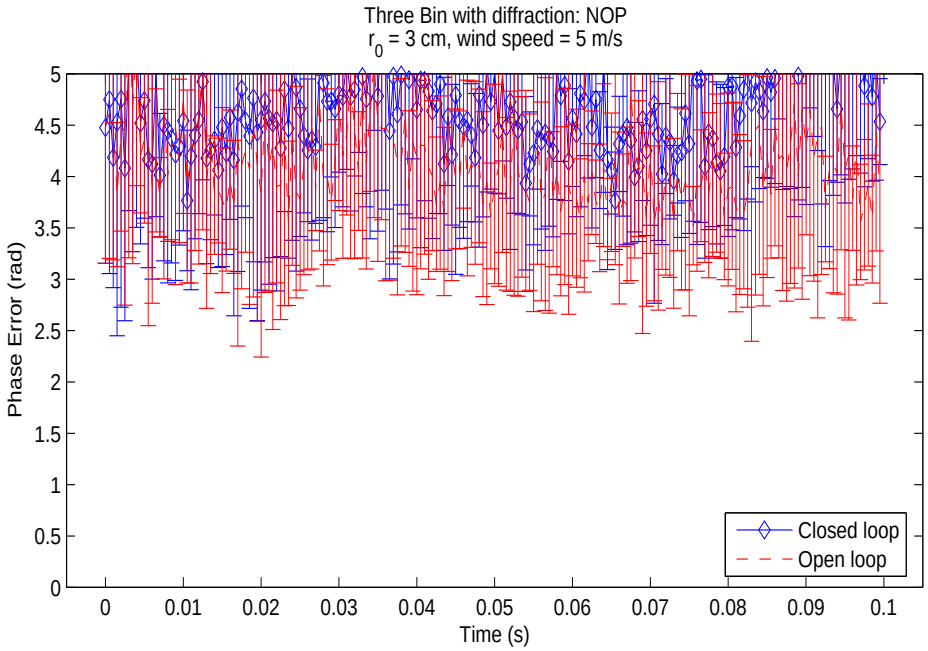

Figure B.78: Three Bin with diffraction WFS, r_0 = 3 cm, wind speed = 5 m/s

B.7.3 wind speed = 10 m/s

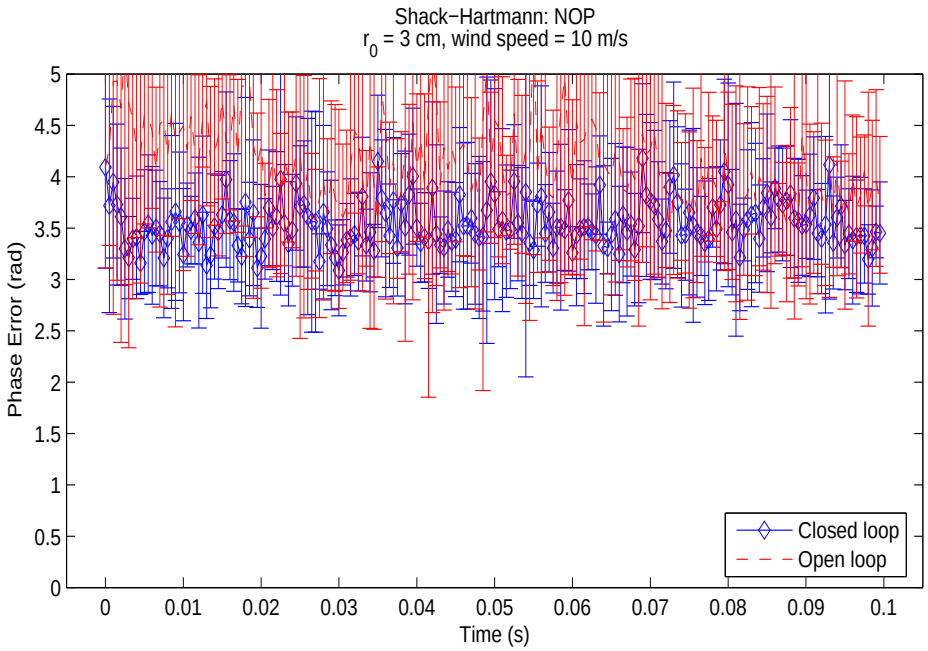

Figure B.79: Shack-Hartmann WFS, r_0 = 3 cm, wind speed = 10 m/s

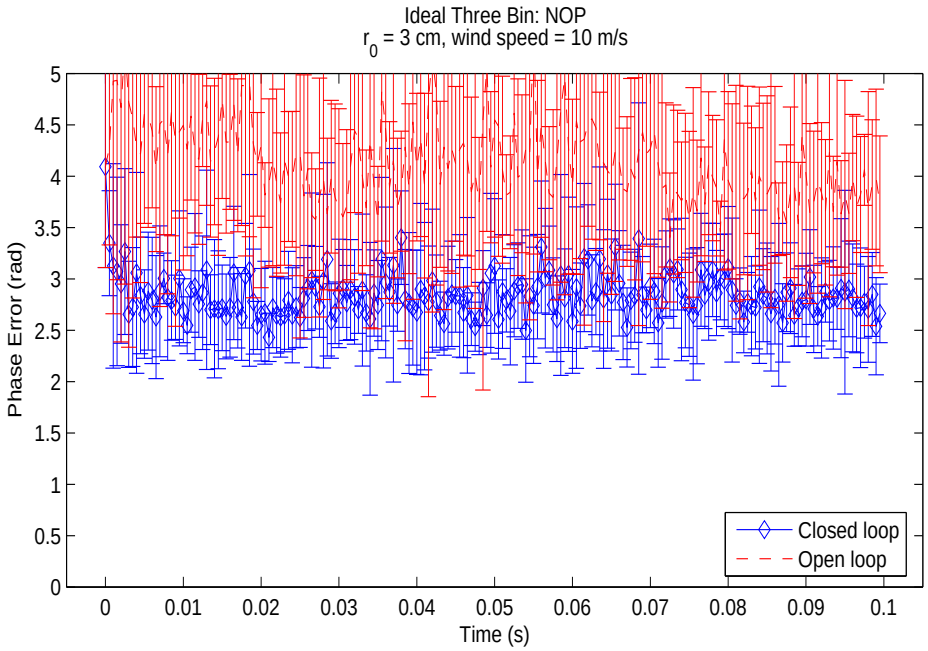

Figure B.80: Ideal Three Bin WFS, r_0 = 3 cm, wind speed = 10 m/s

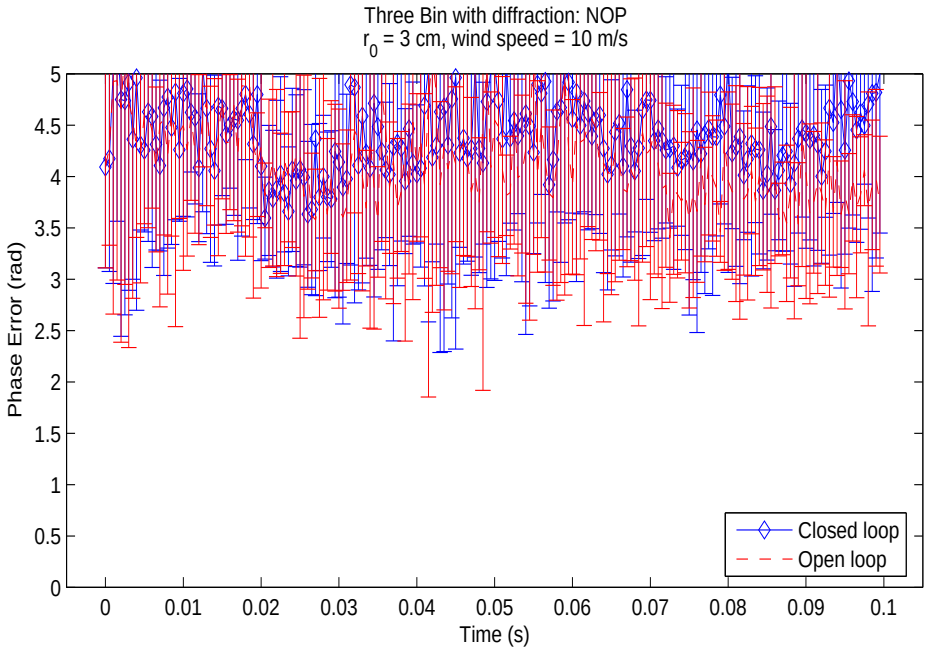

Figure B.81: Three Bin with diffraction WFS, r_0 = 3 cm, wind speed = 10 m/s

B.7.4 wind speed = 20 m/s

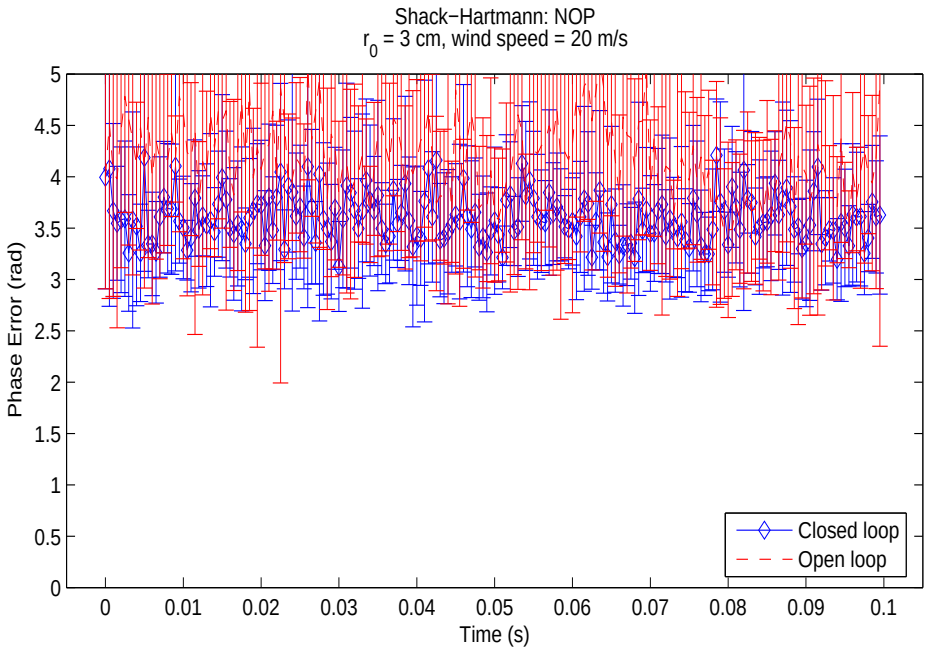

Figure B.82: Shack-Hartmann WFS, r_0 = 3 cm, wind speed = 20 m/s

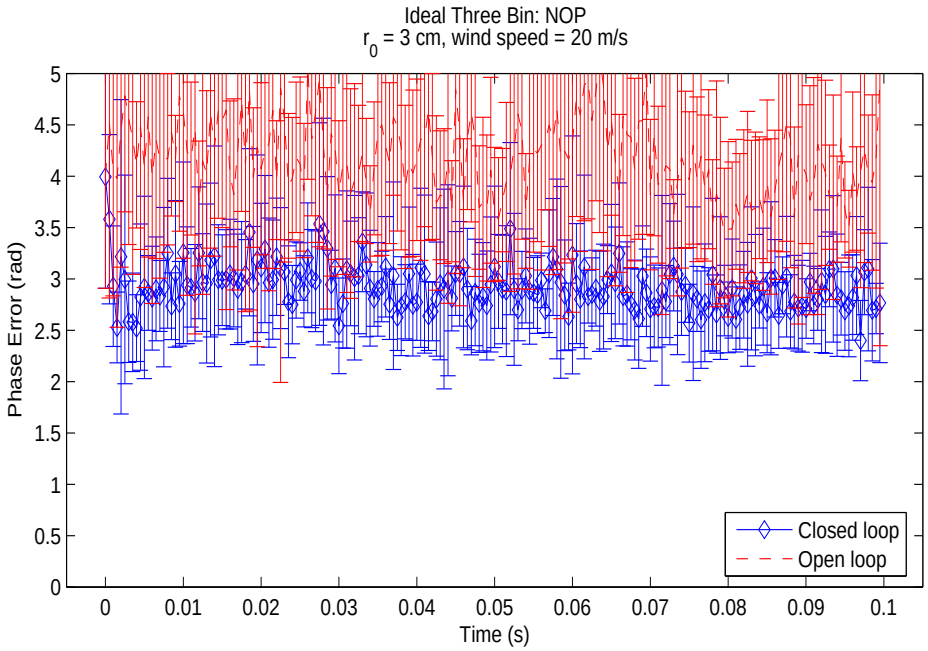

Figure B.83: Ideal Three Bin WFS, r_0 = 3 cm, wind speed = 20 m/s

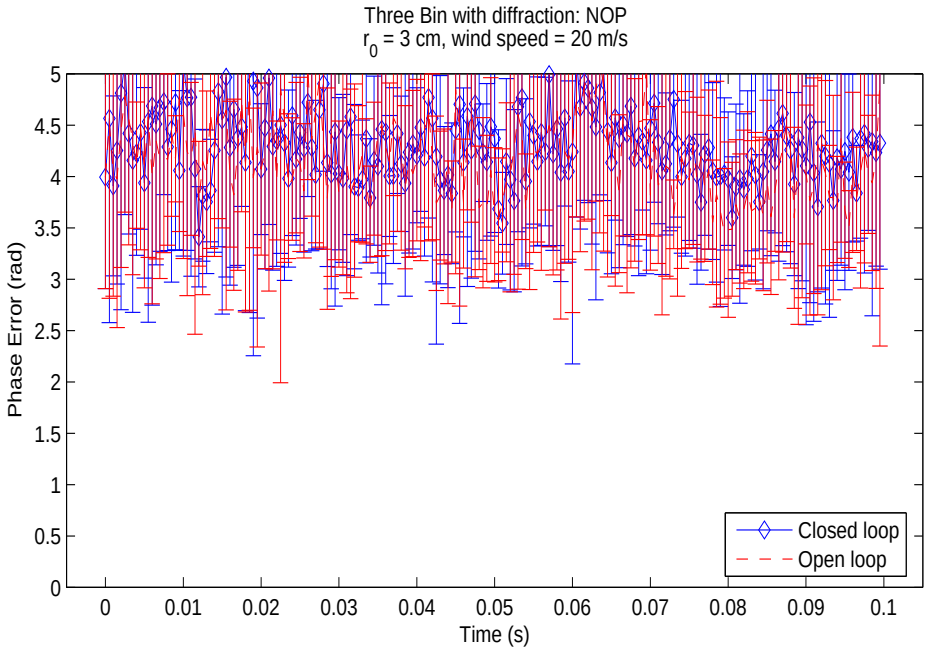

Figure B.84: Three Bin with diffraction WFS, r_0 = 3 cm, wind speed = 20 m/s

Appendix C

NOP CORRECTOR PLOTS II

This appendix collects the detailed plots resulting from the simulations run with the model of the continuous facesheet DM at NOP and with an aperture averaged power over the pupil of 8 μW. The text in section 8.4 sumarizes these results.

WIND SPEED = 0 m/s

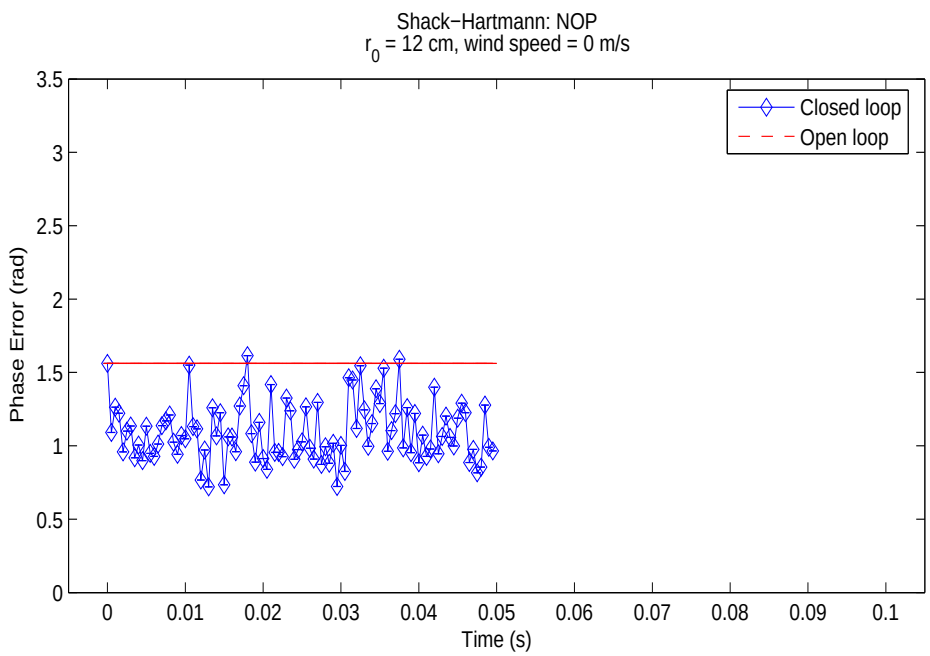

Figure C.1: Shack-Hartmann WFS, r_0 = 12 cm, wind speed = 0 m/s

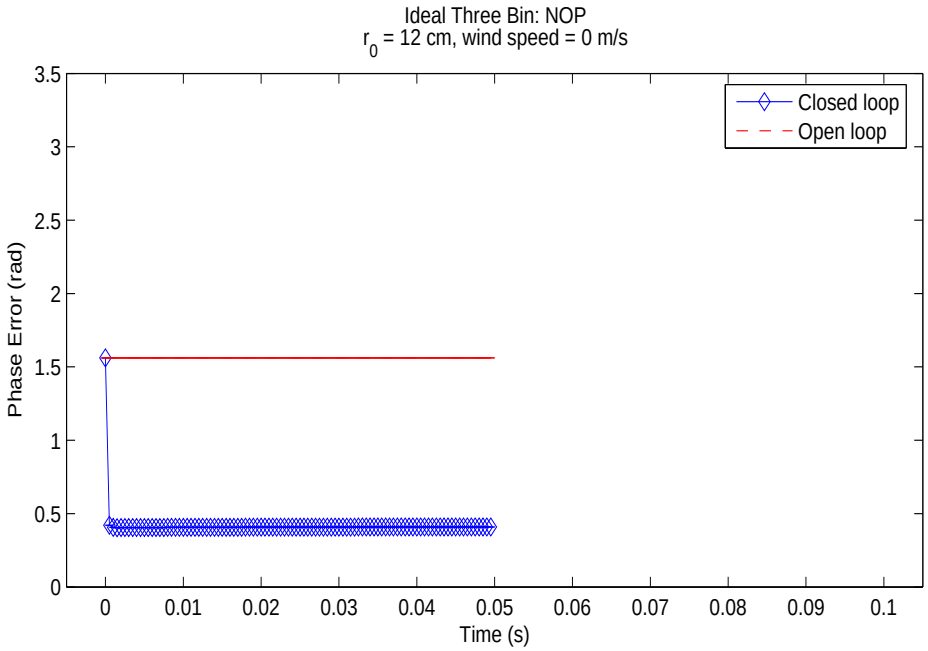

Figure C.2: Ideal Three Bin WFS, r_0 = 12 cm, wind speed = 0 m/s

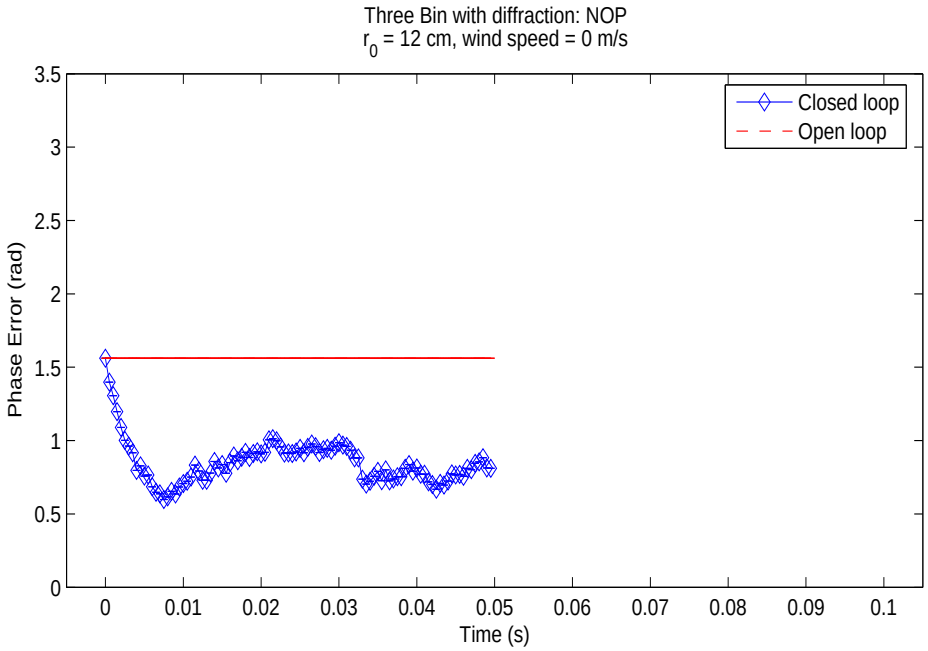

Figure C.3: Three Bin with diffraction WFS, r_0 = 12 cm, wind speed = 0 m/s

WIND SPEED = $5\ \mathrm{m/s}$

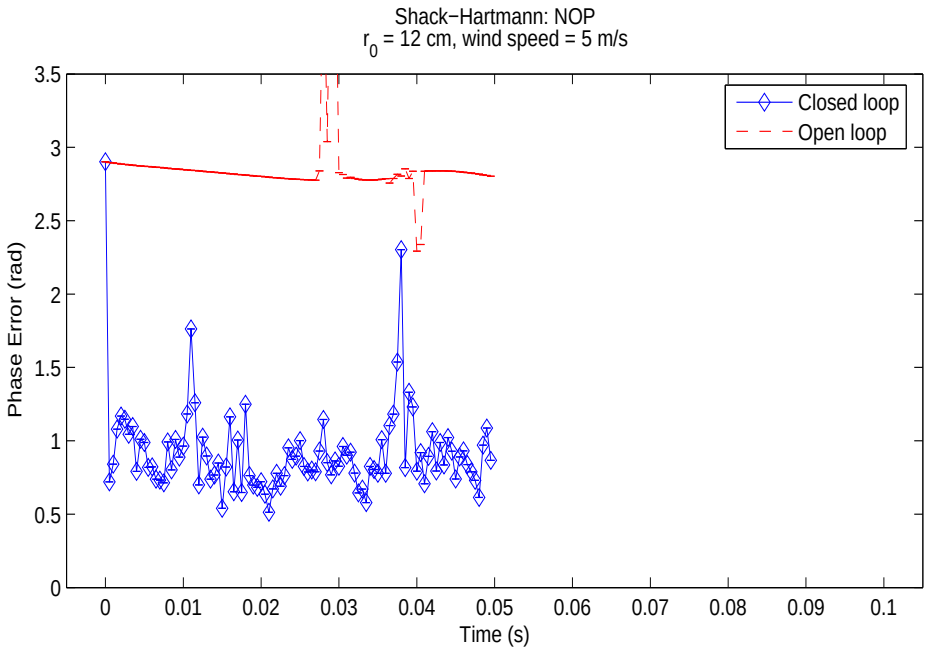

Figure C.4: Shack-Hartmann WFS, r_0 = 12 cm, wind speed = 5 m/s

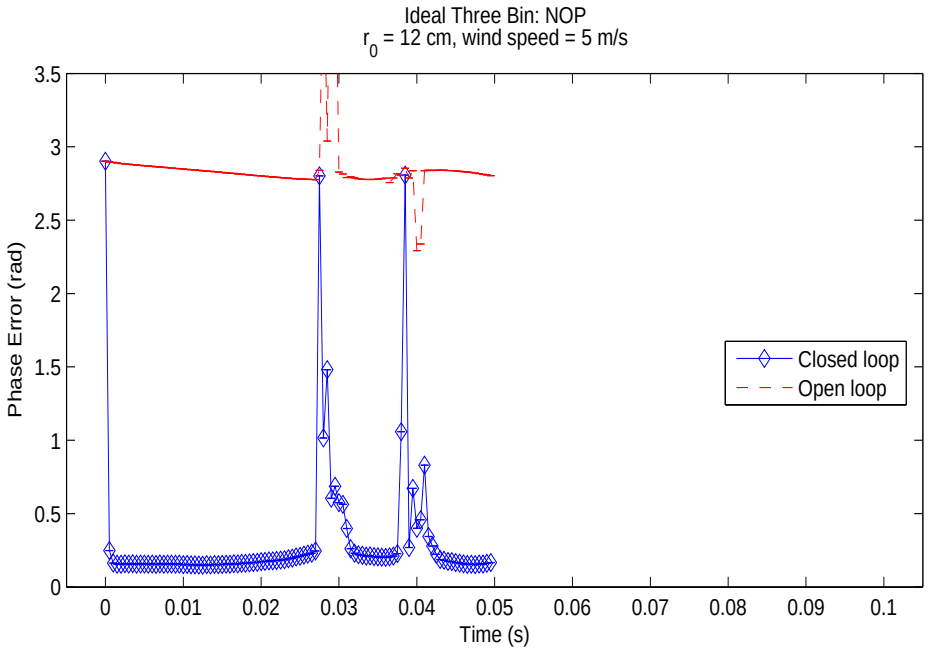

Figure C.5: Ideal Three Bin WFS, r_0 = 12 cm, wind speed = 5 m/s

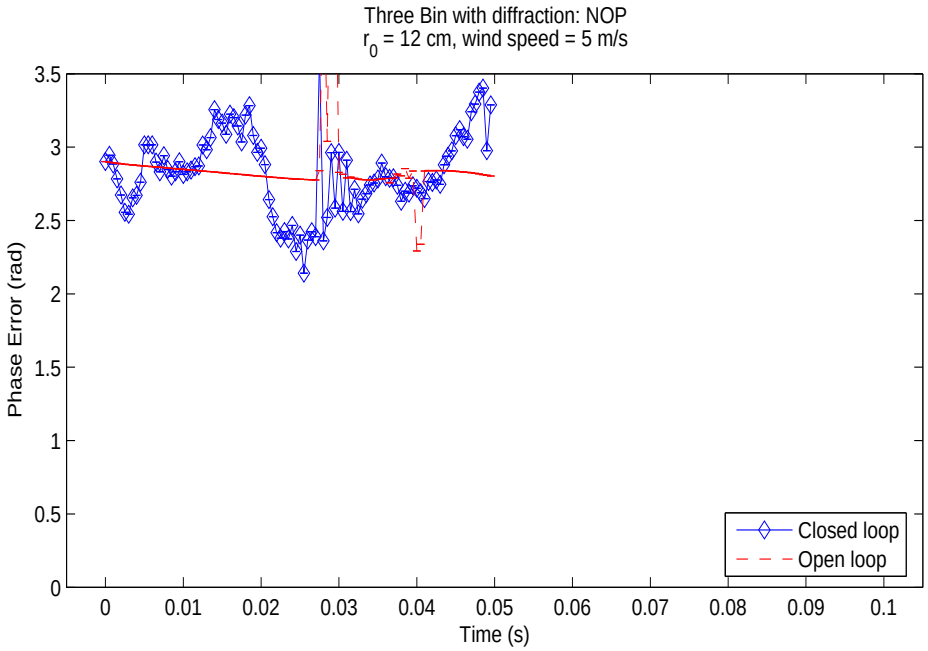

Figure C.6: Three Bin with diffraction WFS, r_0 = 12 cm, wind speed = 5 m/s

WIND SPEED = 10 m/s

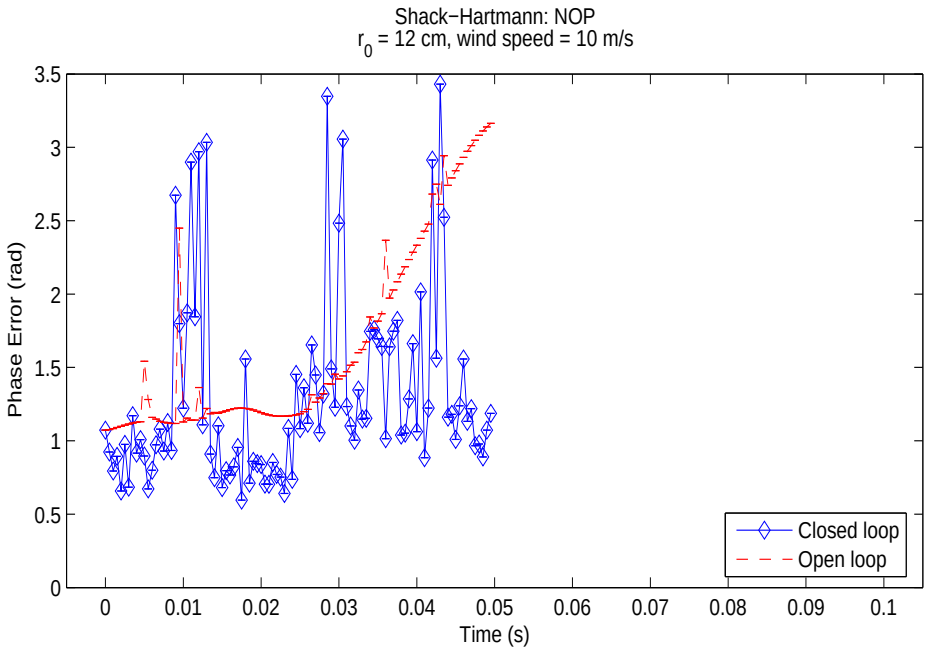

Figure C.7: Shack-Hartmann WFS, r_0 = 12 cm, wind speed = 10 m/s

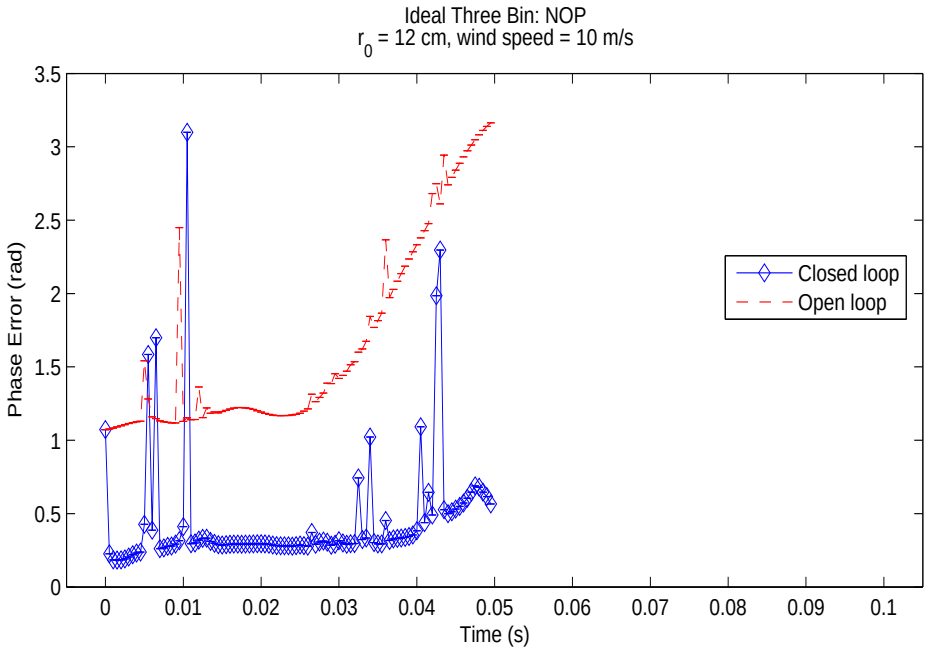

Figure C.8: Ideal Three Bin WFS, r_0 = 12 cm, wind speed = 10 m/s

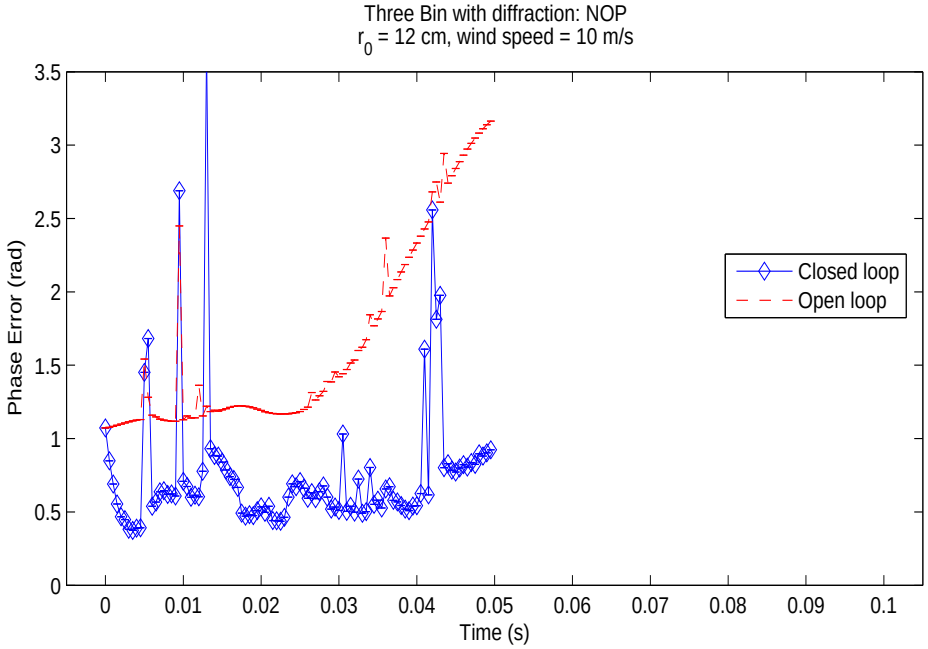

Figure C.9: Three Bin with diffraction WFS, r_0 = 12 cm, wind speed = 10 m/s

WIND SPEED = 20 m/s

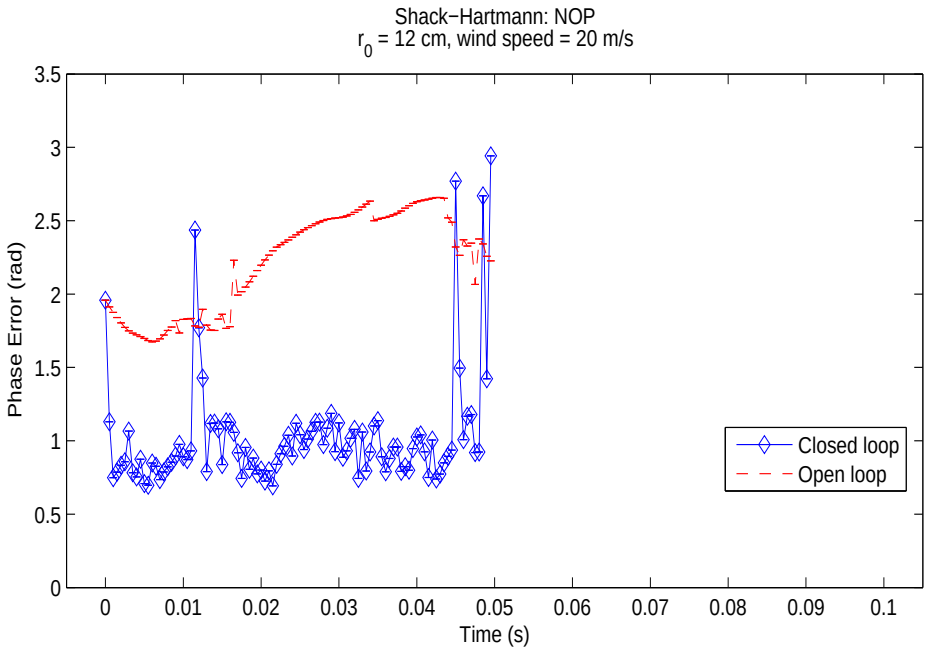

Figure C.10: Shack-Hartmann WFS, r_0 = 12 cm, wind speed = 20 m/s

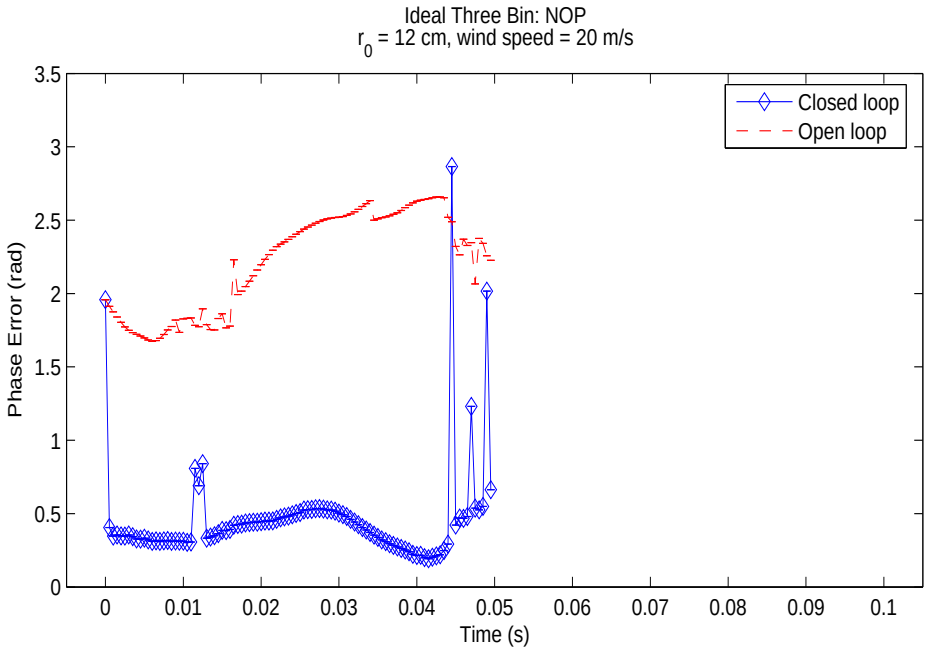

Figure C.11: Ideal Three Bin WFS, r_0 = 12 cm, wind speed = 20 m/s

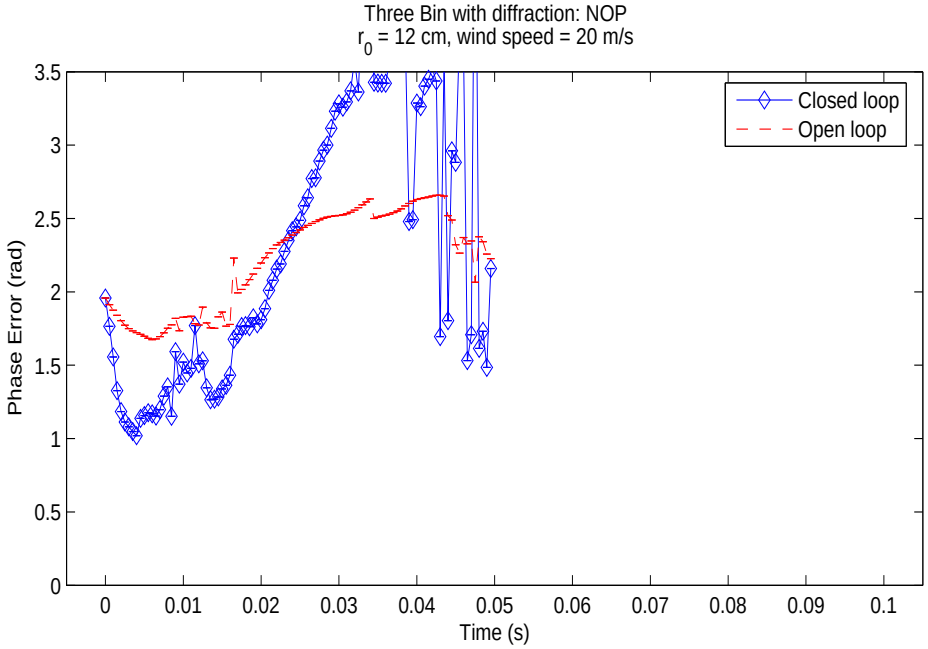

Figure C.12: Three Bin with diffraction WFS, r_0 = 12 cm, wind speed = 20 m/s

Appendix D

NOP CORRECTOR PLOTS III

This appendix collects the detailed plots resulting from the simulations run with the model of the continuous facesheet DM at NOP and with an aperture averaged power over the pupil of 13.5 μW. The text in section 8.5 sumarizes these results.

WIND SPEED = 0 m/s

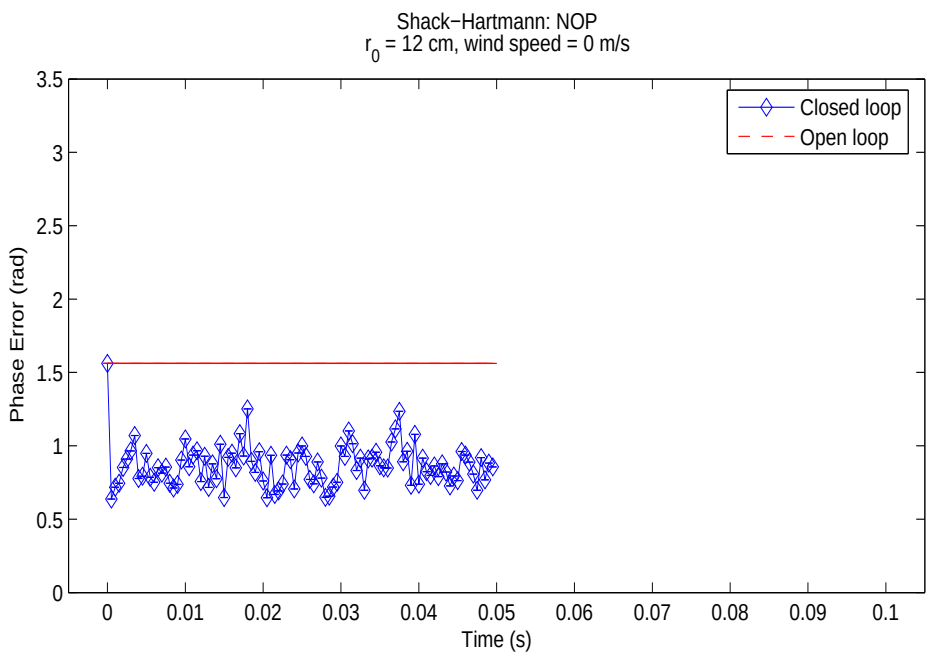

Figure D.1: Shack-Hartmann WFS, r_0 = 12 cm, wind speed = 0 m/s

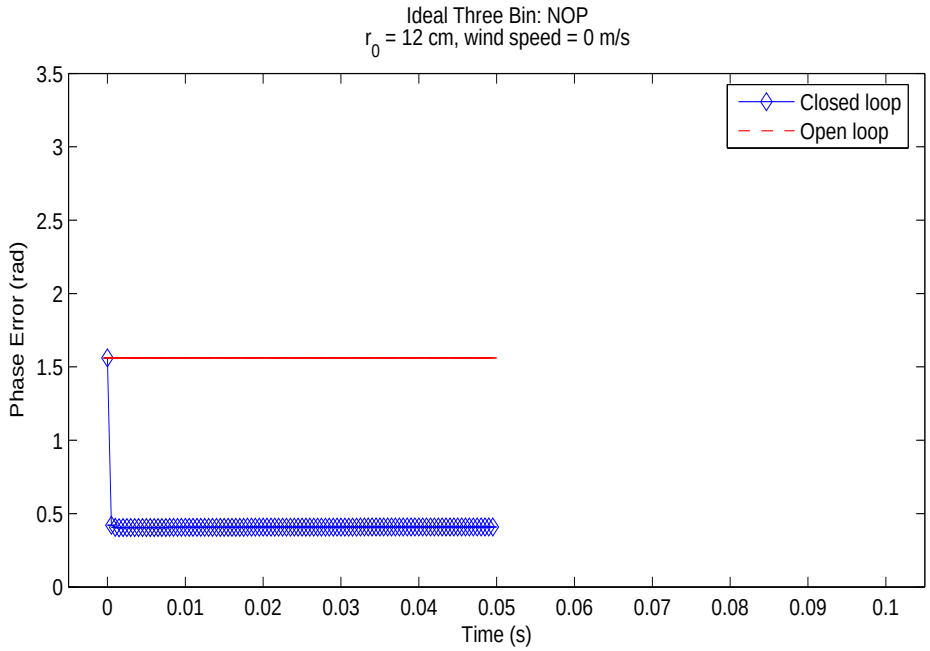

Figure D.2: Ideal Three Bin WFS, r_0 = 12 cm, wind speed = 0 m/s

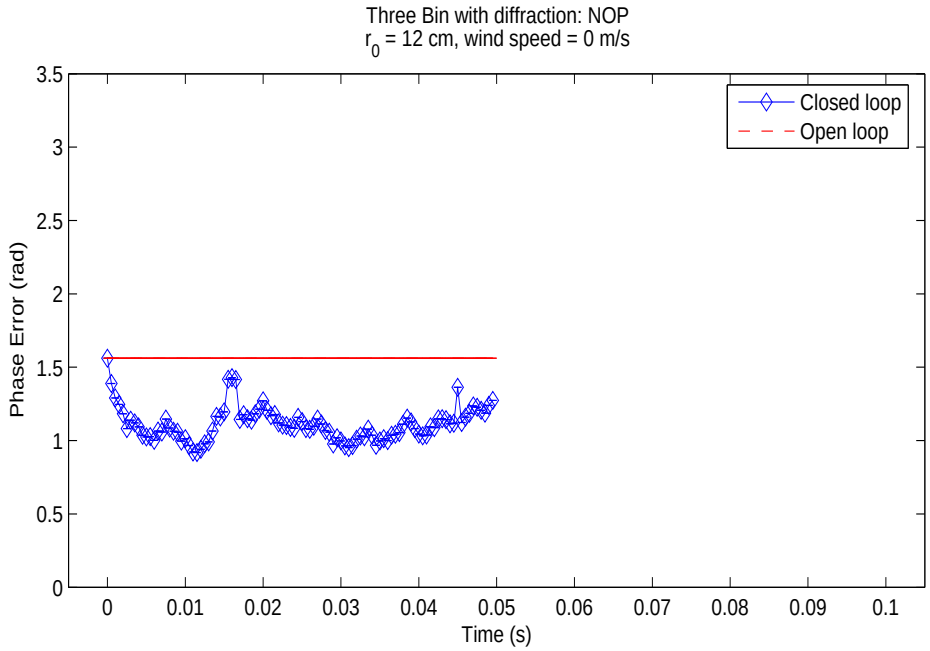

Figure D.3: Three Bin with diffraction WFS, r_0 = 12 cm, wind speed = 0 m/s

WIND SPEED = $5\ \mathrm{m/s}$

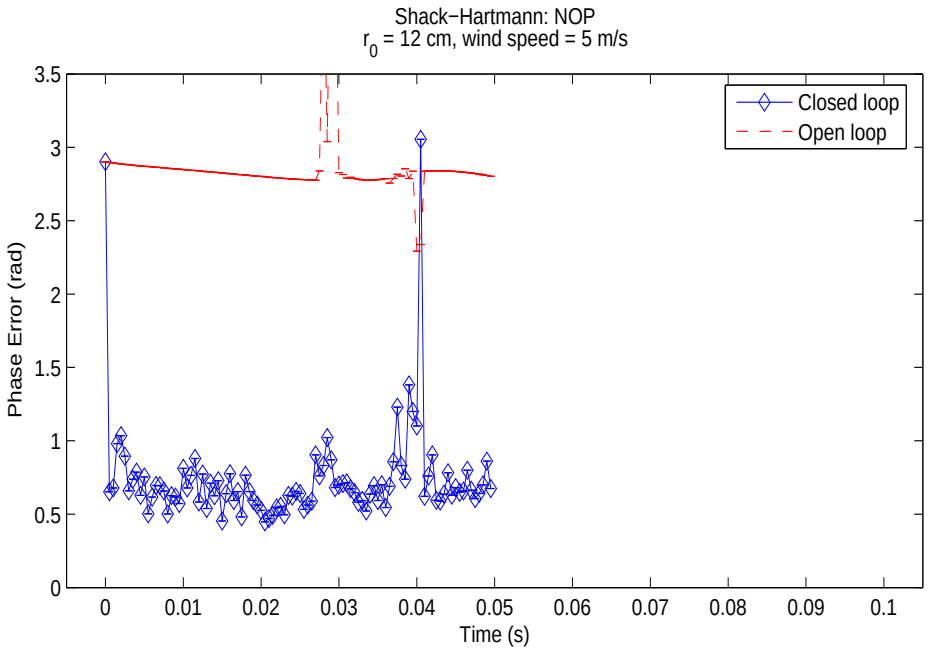

Figure D.4: Shack-Hartmann WFS, r_0 = 12 cm, wind speed = 5 $\mathrm{m/s}$

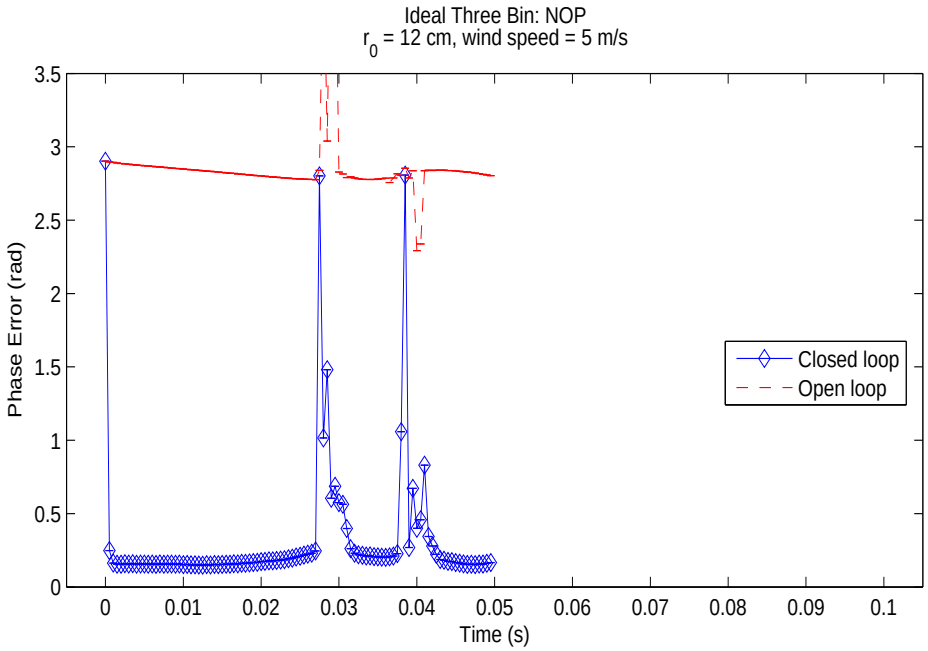

Figure D.5: Ideal Three Bin WFS, r_0 = 12 cm, wind speed = 5 m/s

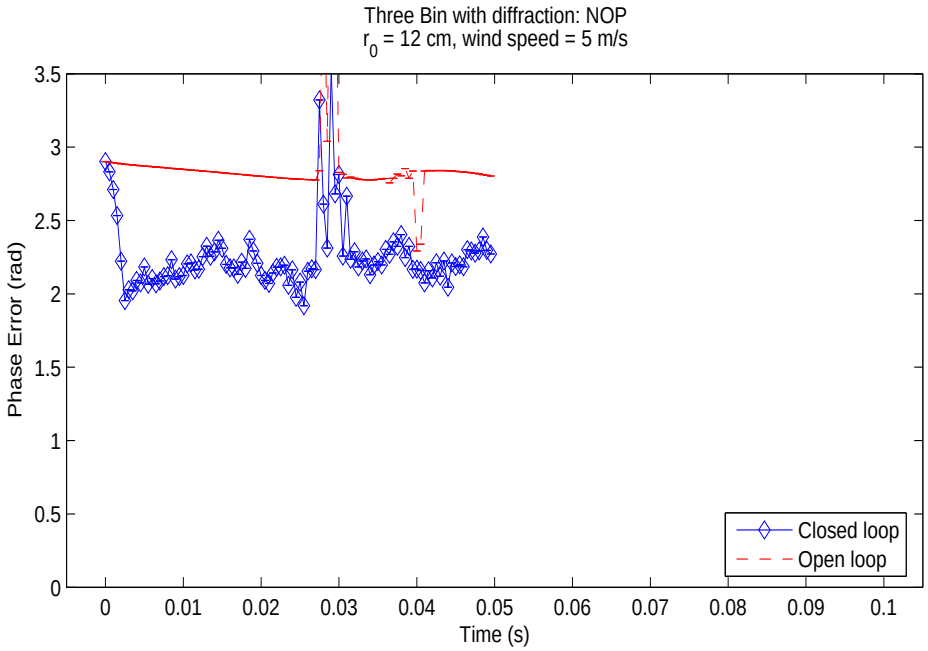

Figure D.6: Three Bin with diffraction WFS, r_0 = 12 cm, wind speed = 5 m/s

WIND SPEED = 10 m/s

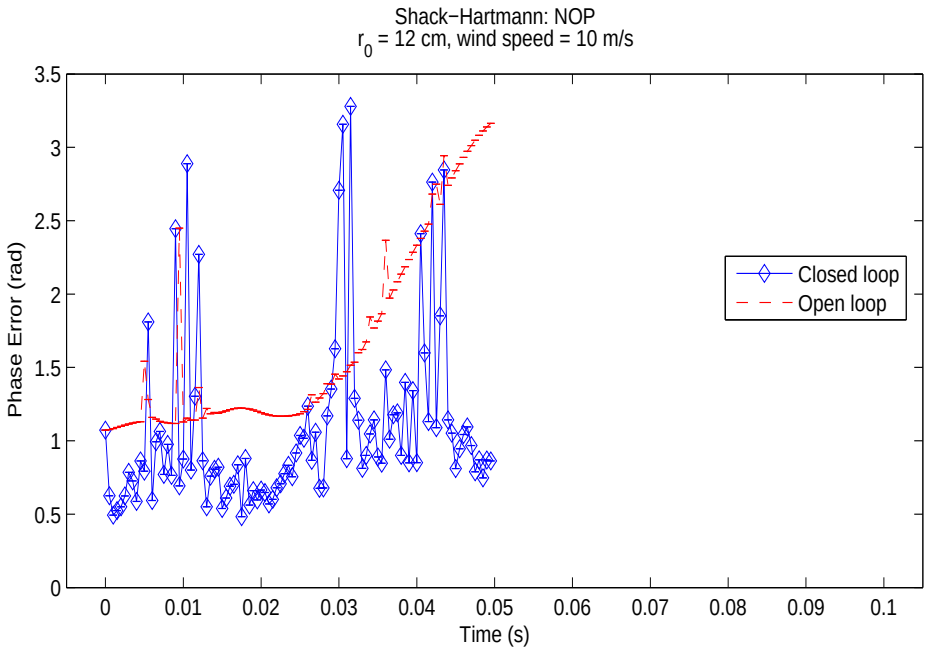

Figure D.7: Shack-Hartmann WFS, r_0 = 12 cm, wind speed = 10 m/s

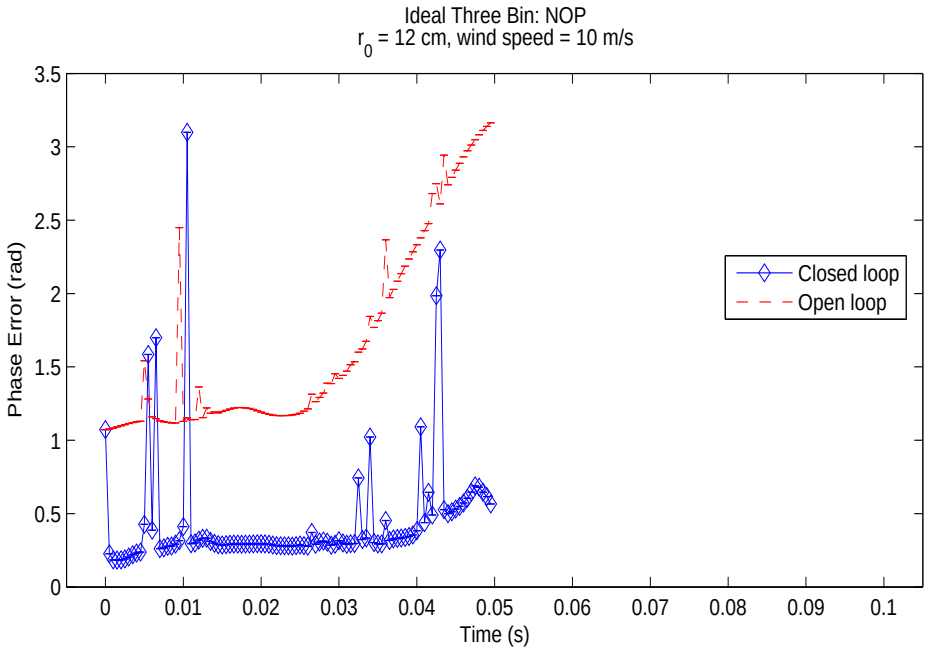

Figure D.8: Ideal Three Bin WFS, r_0 = 12 cm, wind speed = 10 m/s

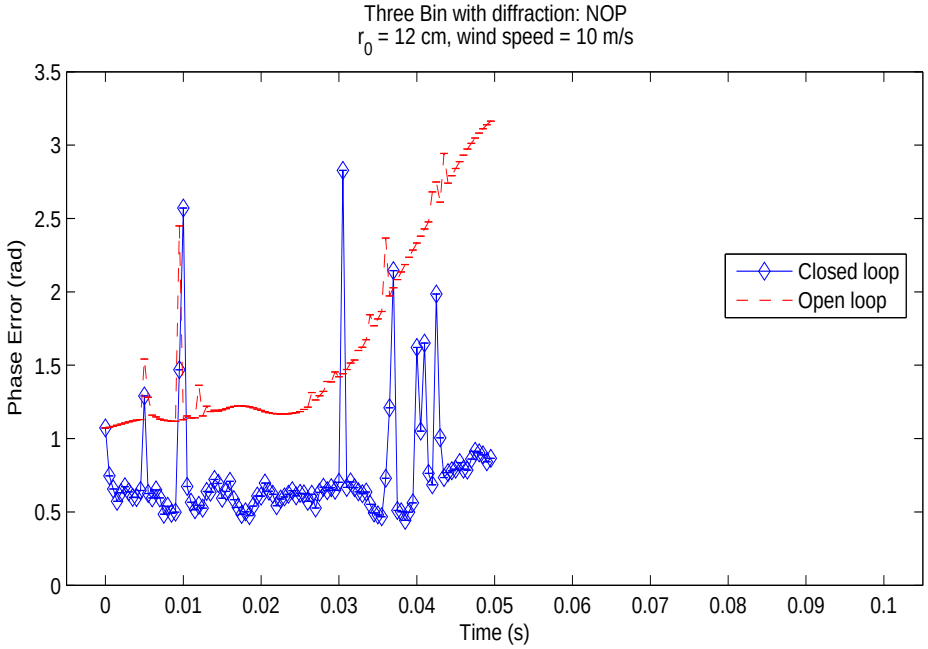

Figure D.9: Three Bin with diffraction WFS, r_0 = 12 cm, wind speed = 10 m/s

WIND SPEED = 20 m/s

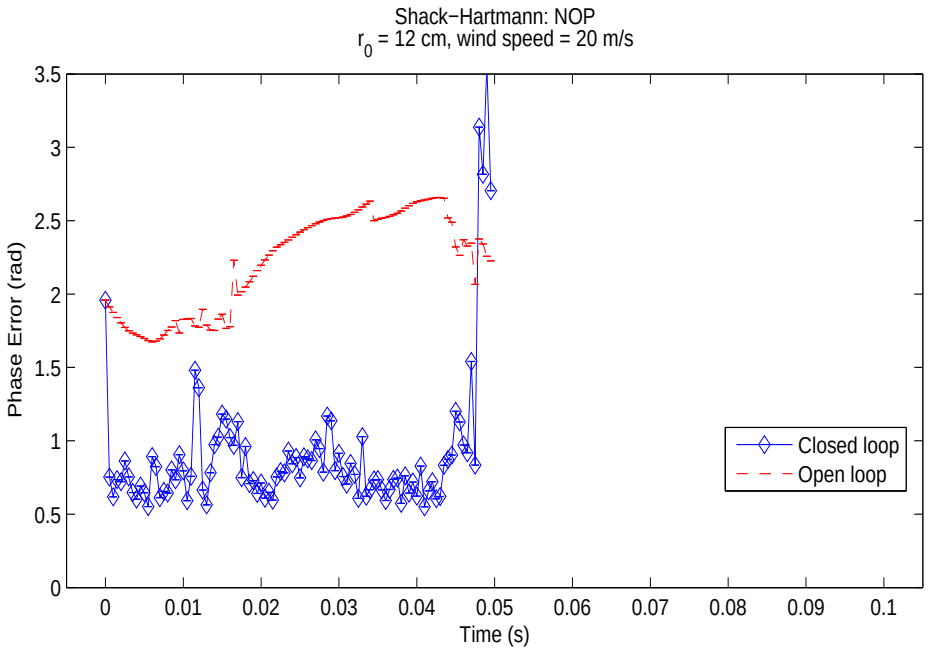

Figure D.10: Shack-Hartmann WFS, r_0 = 12 cm, wind speed = 20 m/s

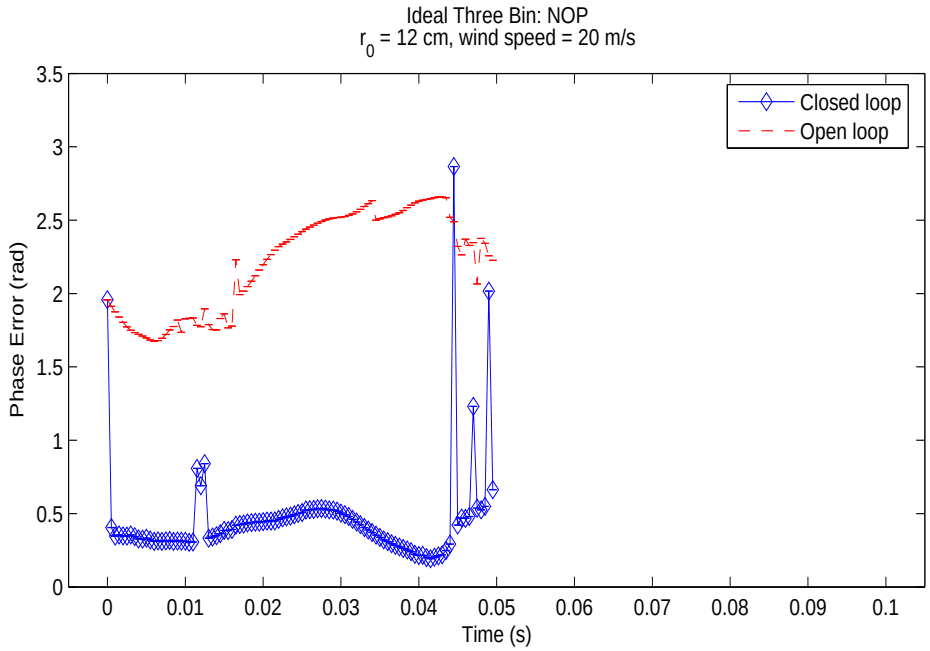

Figure D.11: Ideal Three Bin WFS, r_0 = 12 cm, wind speed = 20 m/s

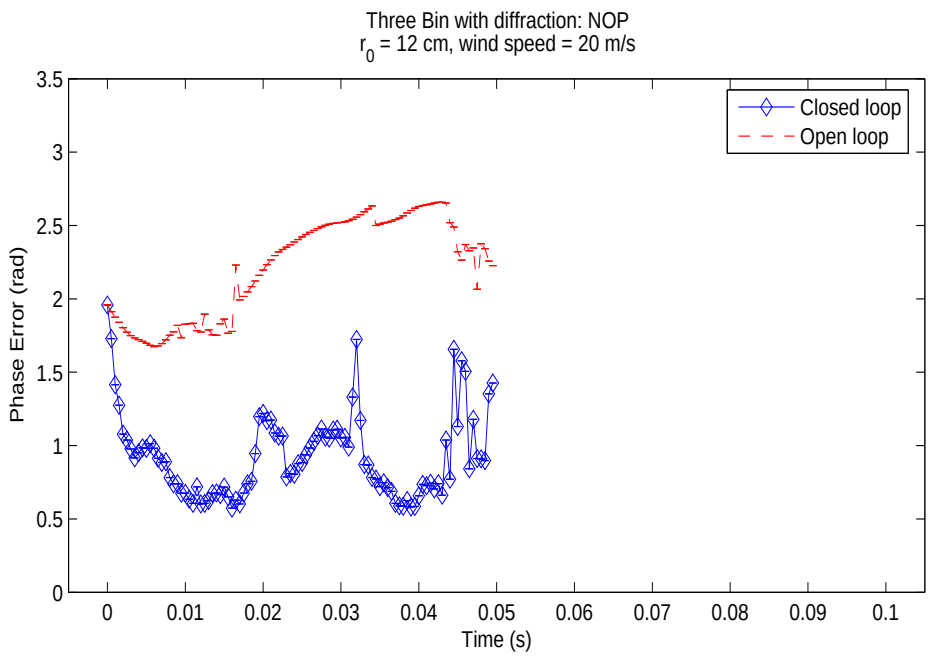

Figure D.12: Three Bin with diffraction WFS, r_0 = 12 cm, wind speed = 20 m/s

Appendix E

RESCALING

We can now characterize five major physical parameters of the system components in terms of the turbulence strength. In table (E.1) we see a summary of

Number of actuators	$N_0 = \left(\frac{D}{r_0}\right)^2$
Tip-Tilt magnitude	$\Delta_{tt} = \lambda \left(\frac{D}{r_0}\right)^{5/6}$
Full aperture dynamic range	$\Delta_{ap} = .22 \cdot \Delta_{tt}$
Inter-actuator dynamic range	$\Delta_{IA} = \frac{.36}{\sqrt[4]{N_0}} \cdot \Delta_{tt}$
System cutoff frequency	$f_c = \frac{.426}{\left(\sigma_t^2\right)^{3/5}} \sum_{l=1}^{layers} \frac{v_{wl}}{r_{0l}}$

Table E.1: System constraints

the parameters and how they can be evaluated. There are a few things to note. First, recall that in the discussion of the number of actuators noticeable gains in performance can be achieved if the number of actuators is increased from N_0 to anything up to about $4N_0$. However, an increase in the number of actuators will normally lead to corresponding increase in the numbers of detectors used by the wavefront sensor and thus to a decrease in the sensitivity of wavefront sensor (see page 41).

Second, note that the system cutoff frequency is, unlike the other parameters, independent of the entrance pupil diameter. It is also the only parameter

that requires some detailed knowledge of the vertical structure of the atmosphere at the site. The other parameters are characterized by the turbulence statistics at either the wavefront sensor plane or the wavefront corrector plane. This makes it difficult to parameterize a system's frequency response without careful study of a site. It also means that there aren't any simple rescaling formulas for changes in the site parameters or wavelength. For that reason the rest of the section will not consider rescaling of f_c.

E.1 A change in r_0

Since all four of the parameters of interest vary inversely with a power of r_0, the rescaling expressions are straightforward:

$$N_{0new} = N_{0old} \left(\frac{r_{0old}}{r_{0new}} \right)^2 \tag{E.1}$$

$$\Delta_{ttnew} = \Delta_{ttold} \left(\frac{r_{0old}}{r_{0new}} \right)^{5/6} \tag{E.2}$$

$$\Delta_{apnew} = \Delta_{apold} \left(\frac{r_{0old}}{r_{0new}} \right)^{5/6} \tag{E.3}$$

$$\Delta_{IAnew} = \Delta_{IAold} \left(\frac{r_{0old}}{r_{0new}} \right)^{5/6} \tag{E.4}$$

E.2 A change in λ_{ref}

A change in the reference wavelength is somewhat trickier, however, since a dependency on λ_{ref} is contained in r_0. The formula for rescaling r_0 versus λ_{ref} is shown in equation (3.5). This can be used directly in the expression for

scaling N_0 in terms of λ_{ref}:

$$N_{0new} = N_{0old} \left(\frac{\lambda_{ref_{old}}}{\lambda_{ref_{new}}} \right)^{12/5} \tag{E.5}$$

From equation (4.15), the equation for the tip-tilt magnitude versus a change in operating wavelength is

$$\begin{aligned}
\left(\frac{\Delta_{tt_{new}}}{\lambda_{ref_{new}}}\right)^{6/5} r_{0new} &= \left(\frac{\Delta_{tt_{old}}}{\lambda_{ref_{old}}}\right)^{6/5} r_{0old} \\
\frac{\Delta_{tt_{new}}}{\lambda_{ref_{new}}} &= \frac{\Delta_{tt_{old}}}{\lambda_{ref_{old}}} \left(\frac{r_{0old}}{r_{0new}}\right)^{5/6} \\
\Delta_{tt_{new}} &= \Delta_{tt_{old}} \frac{\lambda_{ref_{new}}}{\lambda_{ref_{old}}} \left(\frac{r_{0old}}{r_{0new}}\right)^{5/6} \\
\Delta_{tt_{new}} &= \Delta_{tt_{old}} \frac{\lambda_{ref_{new}}}{\lambda_{ref_{old}}} \frac{\lambda_{ref_{old}}}{\lambda_{ref_{new}}} \\
\Delta_{tt_{new}} &= \Delta_{tt_{old}} \quad .
\end{aligned} \tag{E.6}$$

So, unless there are chromatic effects caused by the particular wavefront corrector and tip-tilt correction system, if the dynamic range is sufficient at a given wavelength it is sufficient for all wavelengths. A change in wavelength will still affect the level of correction, however, since the number of actuators for a given level of correction is not invariant to the reference wavelength.

E.3 A change in D

Like changes with respect to r_0, these relations are simple:

$$N_{0new} = N_{0old} \left(\frac{D_{new}}{D_{old}} \right)^2 \tag{E.7}$$

$$\Delta_{ttnew} = \Delta_{ttold} \left(\frac{D_{new}}{D_{old}} \right)^{5/6} \tag{E.8}$$

$$\Delta_{ap_{new}} = \Delta_{ap_{old}} \left(\frac{D_{new}}{D_{old}} \right)^{5/6} \tag{E.9}$$

$$\Delta_{IAnew} = \Delta_{IAold} \left(\frac{D_{new}}{D_{old}} \right)^{5/6} \tag{E.10}$$

BIBLIOGRAPHY

[1] Anthony J. Seward, François Lacombe, and Michael K. Giles. Focal Plane Masks in Adaptive Optics Systems. In Robert K. Tyson and Robert Q. Fugate, editors, *Adaptive Optics Systems and Technology*, volume 3762 of *Proc. SPIE*, pages 283–293, September 1999.

[2] Michael K. Giles, Anthony J. Seward, Mikhail A. Vorontsov, Jungtae Rha, and Ray Jimenez. Setting up a liquid crystal phase screen to simulate atmospheric turbulence. In John D. Gonglewski, Mikhail A. Vorontsov, and Mark T. Gruneisen, editors, *High-Resolution Wavefront Control: Methods, Devices, and Applications II*, volume 4124 of *Proc. SPIE*, pages 89–97, November 2000.

[3] Michael K. Giles, Anthony J. Seward, and Todd M. Giles. Closed-loop phase contrast adaptive optics system using liquid crystal phase modulators: experimental results. In John D. Gonglewski, Mikhail A. Vorontsov, and Mark T. Gruneisen, editors, *High-Resolution Wavefront Control: Methods, Devices, and Applications III*, volume 4493 of *Proc. SPIE*, pages 174–183, February 2002.

[4] Michale C. Roggemann and Byron Welsh. *Imaging through turbulence*. CRC Press, Inc., 1996.

[5] Robert K. Tyson. *Principles of Adaptive Optics*. Academic Press, Inc., San Diego, 1991.

[6] Sir Issac Newton. *Opticks*. Dover Publications, Inc., New York, 1979.

[7] A. Labeyrie. Attainment of diffraction-limited resolution on large telescopes by Fourier analysing speckle patterns. *Astron. Astrophys.*, 6:85, 1970.

[8] Joseph W. Goodman. *Statisical optics*. Wiley Series in Pure and Applied Optics. John Wiley & Sons, New York, 1985.

[9] K. T. Knox and B. J. Thompson. Recovery of images from atmospherically degraded short exposure images. *Astrophysics Journal*, 193:L45–L48, 1974.

[10] A. W. Lohmann, G. Weigelt, and B. Wirnitzer. Speckle masking in astronomy: triple correlation theory and applications. *Applied Optics*, 22:4028–4037, 1983.

[11] Eric Gendron and Pierre Léna. Single-layer atmospheric turbulence demonstrated by adaptive optics observations. *Astronomy and Astrophysics*, 239(2):221–228, 1996.

[12] Dustin C. Johnston and Byron M. Welsh. Analysis of multiconjugate adaptive optics. *Journal of the Optical Society of America A*, 11(1):394–408, January 1994.

[13] Jean-Pierre Véran. *Estimation de la réponse impulsionnelle et restauration d'image en optique adaptative. Application au système d'optique adaptative du Télescope Canada-France-Hawaii*. PhD thesis, Ecole Nationale Supérieure des Télécommunications, November 1997.

[14] Olivier Lai. *L'optique adaptative du Télescope Canada-France-Hawaii et son utilisation pour l'etude des cœurs de galaxies à flambée d'étoiles*. PhD thesis, Université de Paris VII (Denis Diderot), 11 December 1996.

[15] David L. Fried. Optical resolution through a randomly inhomogeneous medium for very long and very short exposures. *Journal of the Optical Society of America*, 56:1372, 1966.

[16] David L. Fried. Limiting resolution looking down through the atmosphere. *Journal of the Optical Society of America*, 56:1380, 1966.

[17] Darryl P. Greenwood. Bandwidth specification for adaptive optics systems. *Journal of the Optical Society of America*, 67(3):390–393, March 1977.

[18] Nicolas Roddier. Atmospheric wavefront simulation and Zernike polynomials. In James B. Breckinridge, editor, *Amplitude and Intensity Spatial Interferometry*, volume 1237 of *Proc. SPIE*, pages 668–679, August 1990.

[19] Joseph Wincour. Modal compensation of atmospheric turbulence induced wave front aberrations. *Applied Optics*, 21(3):433–438, 1 February 1982.

[20] Robert J. Noll. Zernike polynomials and atmospheric turbulence. *Journal of the Optical Society of America*, 66(3):207–211, March 1976.

[21] Eric Gendron. *Optimisation de la commande modal en optique adaptative: applications à l'astronomie*. PhD thesis, Université Paris VII — Denis Diderot, 1995.

[22] Eric Gendron and Pierre Léna. Astronomical adaptive optics I: Modal control optimization. *Astronomy and Astrophysics*, 291:337–347, 1994.

[23] Scott S. Olivier and Donald T. Gavel. Tip-tilt compensation for astronomical imaging. *Journal of the Optical Society of America A*, 11(1):368–378, January 1994.

[24] W. Happer, G. J. MacDonald, C. E. Max, and F. J. Dyson. Atmospheric-turbulence compensation by resonant optical backscattering from the sodium layer in the upper atmosphere. *Journal of the Optical Society of America A*, 11(1):263–276, January 1994.

[25] David L. Fried. Anisoplanatism in adaptive optics. *Journal of the Optical Society of America*, 72(1):52–61, January 1982.

[26] Max Born and Emil Wolf. *Principles of Optics*. Pergamon Press, Oxford, sixth edition, 1980.

[27] Lewis J. Golden. Zernike test. 1: Analytical aspects. *Applied Optics*, 16(1): 205–213, January 1977.

[28] Jorge Ojeda-Castañeda. Foucalt, wire, and phase modulation tests. In Daniel Malacara, editor, *Optical Shop Testing*, Wiley Series in Pure and Applied Optics, pages 265–320. John Wiley & Sons, Inc., New York, second edition, 1992.

[29] Jack D. Gaskill. *Linear Systems, Fourier Transforms, and Optics*. Wiley Series in Pure and Applied Optics. John Wiley & Sons, Inc., New York, 1978.

[30] Dennis C. Ghiglia and Mark D. Pritt. *Two-Dimensional Phase Unwrapping: Theory, Algorithms, and Software*. Wiley-Interscience. John Wiley & Sons, Inc., New York, 1998.

[31] *Index to WaveTrain and tempus Documents*. MZA Associates Corporation, Albuquerque, New Mexico, 29 December 2004. URL `http://www.mza.com/doc/`.